2018

Circulation & Exchange Within Shelf & Estuarine Waters Driven by the Atmosphere, Tides and Buoyancy

Christina Anne Wertman
University of Rhode Island, caking@my.uri.edu

CIRCULATION & EXCHANGE WITHIN SHELF & ESTUARINE WATERS DRIVEN BY THE ATMOSPHERE, TIDES AND BUOYANCY

BY

CHRISTINA ANNE WERTMAN

A DISSERTATION SUBMITTED IN PARTIAL FULFILLMENT OF THE REQUIREMENTS FOR THE DEGREE OF

DOCTOR OF PHILOSOPHY

IN

OCEANOGRAPHY

UNIVERSITY OF RHODE ISLAND

2018

DOCTOR OF PHILOSPHY DISSERTATION

OF

CHRISTINA ANNE WERTMAN

APPROVED:

Dissertation Committee:

Major Professor Christopher Kincaid

Kathleen Donohue

Gopu Potty

David Ullman

Nasser H. Zawia
DEAN OF THE GRADUATE SCHOOL

UNIVERSITY OF RHODE ISLAND
2018

ABSTRACT

The proximity of human populations to the coast renders the studies of the coastal ocean important due to impacts by natural hazards, environmental management and material transport. This dissertation will quantify the impacts of the atmosphere, tides and buoyancy forces in Rhode Island Sound (RIS) and Narragansett Bay (NB) at a variety of scales. Observational analysis and numerical modeling provide comprehensive tools to study resonance between the atmosphere and ocean beneath synoptic storm systems; to describe circulation in RIS; and to study the effect of tides on stratification in NB.

The characterization of the shallow shelf circulation under various forcing mechanisms provides information useful for hazard monitoring. The study of momentum propagation over the East Coast continental shelf is discussed in Chapter 1. We determine the role of atmospheric pressure in creating high frequency surface gravity waves extending over a large geographic range. We find that shallow water waves are generated near the continental shelf break under long-lived squall lines.

Buoyancy, tides and wind driven circulation influencing RIS circulation and hydrography are examined using observations in Chapter 2. We find that the largest contributor to circulation are tides and the largest controller of stratification is solar insolation. At monthly time-scales we find a cyclonic coastal current present along the periphery of RIS, enhanced during the summer as a result of baroclinic and barotropic pressure gradients. During the winter the coastal current is reduced and, in some areas, not detectible. The reduction is thought to be caused by smaller baroclinic forces and barotropic forces that oppose the cyclonic circulation.

Chapter 3 expands beyond the spatial-temporal limitations of data moorings within NB by using numerical hydrodynamic models to reveal 4-D aspects of estuary dynamics. We find that much of NB has a maximum stratification during either low or high tide resulting from a combination of straining, advection and mixing. The predicted tidal change in stratification is confirmed by observations from buoys located in NB.

The coastal area of New England, an area of great economic, recreational, and environmental importance, is an ideal area to study contemporary hydrographic and dynamic processes. This dissertation applies innovative analytical and numerical techniques to investigate the relative roles of atmospheric, buoyancy, and tidal forcing in determining circulation in the shallow shelf sea of RIS and in the NB estuary.

ACKNOWLEDGMENTS

I would like to thank the academic community including the faculty, staff and students at the Graduate School of Oceanography who have helped facilitate my academic growth during my Ph.D. I would like to especially thank my advisor Christopher Kincaid for his help over the past several years. My dissertation would not have been the same without him.

I would like to especially thank my committee Kathleen Donohue, David Ullman, Gopu Potty, Robert Pockalny and Reza Hashemi**,** with their never-ending support and advice. Especially, Robert, Kathy and Dave, for their guidance, assistance, and encouragement. I would like to thank my lab group, Sara Swaja, Kevin Rosa, Tucker Sylvia, Christelle Balt and Anna Pfeiffer-Herbert for their assistance and advice. I would like to extend a special thank you to Yang Shen, James Miller, Brian Savage, Richard Yablonksy, John Merrill, Katie Kelly, Qianqian Liu, the seismic lab group and the URI Geology department, for their aid and support in my research. A big thank you to Rhonda Kenny for her patience and help over the last several years.

Lastly I would like to thank and express my gratitude to my family and friends. Especially, my sister Dr. Ashley King and husband Geoff Wertman, you have truly been compassionate and an inspiration in my life. To everyone mentioned above you have made the past several years of work worthwhile and wonderful.

.

PREFACE

The following dissertation examines and quantifies the roles of atmosphere, tides and buoyancy in coastal circulation and hydrography. This dissertation is written in manuscript format and is comprised of the following three manuscripts:

The first manuscript, "Mesoscale convective system surface pressure anomalies responsible for meteotsunamis along the U.S. East Coast on June 13th, 2013," describes storm generated tsunamis. We use observations to track and quantify the responsible pressure anomalies over the continental United States. Estimates of the generation zone of the meteotsunami where calculated along the continental shelf. This manuscript was published in *Scientific Reports* in November 2014.

The second manuscript, "Temporal and spatial variations of circulation and hydrography in Rhode Island Sound," describes observations made along the shallow inner shelf region using multiple data sets. We explore temporal variations from hours to seasons and link observations to possible forcing mechanisms. We plan to submit this manuscript to *Continental Shelf Research.*

The third manuscript, "Tidally driven stratification changes in Narragansett Bay," describes both observations and modeling of hydrographic changes in Narragansett Bay. We utilize numerical models to reproduce variations in stratification observed by buoys within the bay. We plan to submit this manuscript to the *Journal of Marine Systems.*

TABLE OF CONTENTS

LIST OF TABLES

LIST OF FIGURES

MANUSCRIPT I

Mesoscale convective system surface pressure anomalies responsible for meteotsunamis along the U.S. East Coast on June 13th, 2013

By

Christina A. Wertman[1], Richard M. Yablonsky[1], Yang Shen[1], John Merrill[1], Christopher R. Kincaid[1], & Robert A. Pockalny[1]

Published in ***Scientific Reports,*** Nov. 2014

[1]Graduate School of oceanography, University of Rhode Island, Narragansett, RI 02882, USA.

Abstract

Two destructive high-frequency sea level oscillation events occurred on June 13th, 2013 along the U.S. East Coast. Seafloor processes can be dismissed as the sources, as no concurrent offshore earthquakes or landslides were detected. Here, we present evidence that these tsunami-like events were generated by atmospheric mesoscale convective systems (MCSs) propagating from inland to offshore. The USArray Transportable Array inland and NOAA tide gauges along the coast recorded the pressure anomalies associated with the MCSs. Once offshore, the pressure anomalies generated shallow water waves, which were amplified by the resonance between the water column and atmospheric forcing. Analysis of the tidal data reveals that these waves reflected off the continental shelf break and reached the coast, where bathymetry and coastal geometry contributed to their hazard potential. This study demonstrates that monitoring MCS pressure anomalies in the interior of the U.S. provides important observations for early warnings of MCS-generated tsunamis.

Introduction

Tsunamis are most often caused by sudden movement of the seafloor due to submarine earthquakes, landslides, or volcanic activities. Tsunami-like events created by disturbances on the ocean surface are less well known, but their existence is well-documented in areas such as the Balearic Islands, the Adriatic Sea, South Japan, New Zealand, northeastern North America, the United Kingdom, and northwestern North America[1,2,3,4,5]. Common to all of these ocean surface-generated tsunami-like events is forcing by an atmospheric surface pressure anomaly moving over a relatively shallow body of water[3]. Hence, this type of tsunami-like event is typically classified as a "meteotsunami."

A large sea level anomaly associated with a meteotsunami can occur through a variety of atmosphere-ocean resonance mechanisms, including Greenspan, Shelf, and/or Proudman resonance[3]; for the meteotsunamis examined in the current study, Proudman resonance has the largest influence on the sea level anomaly. Proudman resonance exists when the ground speed of the atmospheric pressure anomaly (U) matches the phase speed of meteotsunami waves (C), which travel as shallow water waves so that $C = (gh)^{1/2}$, where g is the gravitational acceleration (9.8 m s^{-2}) and h is the water depth[6]. For an atmospheric pressure anomaly propagating at a common ground speed of 20-40 m s^{-1}, the corresponding resonant water depth is 40-160 m, within the depth range of most continental shelves.

Although, not widely known, meteotsunamis along the east coast of North America are not rare events. There have been at least two documented meteotsunami events each year with sea level oscillations of 0.1-1 m along the U.S. East Coast from 2006 to early 2012, although the atmospheric forcing for these meteotsunamis has not been investigated in detail[7,8]. Mercer et al.[2] describes two tropical cyclones, Helene (2000) and Jose (1999), which generated meteotsunamis (with wave heights up to 3m) as the low-pressure anomalies at the center of the tropical cyclones rapidly propagated across the Grand Banks. These meteotsunamis then reflected back toward the coast once the storms crossed the shelf break into deeper water. Since limited observations of the pressure distributions in the tropical cyclones were available, Mercer et al.[2] estimated the pressure distribution using a simple analytical model.

Tropical cyclones do not appear to be the most common cause of meteotsunamis along the U.S. East Coast. Churchill et al.[9] describes a mesoscale

convective system (MCS), which propagated southward along the east coast of Florida, generating a 3-m meteotsunami (recorded at Daytona Beach) that was forced by a high surface pressure anomaly under the squall line portion of the MCS. They used hourly radar reflectivity and barometric pressure readings from sparse stations to illustrate the relationship between radar reflectivity and the high atmospheric pressure anomaly. Churchill et al.[9] recorded a positive pressure anomaly of ~2 hPa, and through their estimations of atmospheric forcing, they concluded that, in addition to Proudman resonance, bathymetric effects (including wave refraction off an underwater ridge) may have played a large role in generating such a high amplitude meteotsunami.

Some MCSs include a fast-moving, long-lived, quasi-linear squall line (i.e., derecho), which produces strong winds and has a well-defined surface pressure anomaly signature (Fig. 1a). Derecho-producing MCSs are not uncommon in the interior of the U.S., numbering on average ~20 per year with a possible upward trend in frequency[10]. Most common in the months of May, June, and July, derechos frequently occur in groups along the eastern half of the U.S.[10,11]. On land, the most destructive impact of a derecho-producing MCS is typically straight-line wind damage, but as the MCS passes over the ocean, the potential initiation of a meteotsunami creates a different hazard.

On June 13, 2013, two high-frequency sea level oscillation (i.e., meteotsunami) events hit the U.S. East Coast. The maximum sea level oscillations recorded at National Oceanic and Atmospheric Administration (NOAA) tide gauges for the first and second meteotsunamis were 0.59 m at Providence, RI and 0.44 m at Atlantic City,

NJ, respectively (i.e., stations 27 and 19, respectively, in Table 1 and Supplementary Fig. 1). Earthquakes and landslides can be dismissed as the likely causes of these events because no earthquake was detected near the coast around the times of the events, and a subsequent offshore survey near Hudson Canyon by NOAA found no evidence of a significant submarine landslide (Jason Chaytor, personal communication). However, two derecho-producing MCSs propagated eastward off the U.S. East Coast that same day[12] (Fig. 2). Using recently available barometric pressure measurements from the USArray Transportable Array (TA) and radar reflectivity with high temporal sampling, this study builds upon previous studies (such as Churchill et al. [9]) by quantitatively documenting and analyzing the atmospheric surface pressure anomalies associated with MCSs that generate meteotsunamis along the U.S. East Coast. Similar concurrent MCS-meteotsunami pairs occurred along the U.S. East Coast on June 29-30, 2012 and April 10-11, 2013 (see Supplementary Figs. 2 and 3), but for brevity, the focus here is on the June 13, 2013 event.

Results

MCS atmospheric pressure anomalies. Two sets of instruments are used to measure the atmospheric pressure on the Earth's surface during the two eastward-propagating MCSs on June 13, 2013. Unlike previously documented U.S. East Coast meteotsunami events, barometers on the recently installed TA stations in the eastern U.S. were available to record atmospheric surface pressure anomalies over land at a sample rate of once per second[13]. These measurements provided the first detailed account of the magnitude, dimension, and duration of the atmospheric pressure anomalies that were ultimately responsible for the meteotsunamis along the U.S.

eastern seaboard, once the pressure anomalies moved offshore. Along the coast, NOAA tide gauges are used to monitor sea level, but many also measure coincident atmospheric sea level pressure, with 0.1 hPa precision and a six-minute sampling frequency[14] (Table 1 and Supplementary Fig. 1). All barometric pressure anomalies are calculated by demeaning the recorded pressure values and then high-pass filtering above five hours to highlight the high-frequency pressure anomalies (Fig. 1).

A derecho-producing MCS typically includes a quasi-linear group of thunderstorms, consisting of well-developed convective and stratiform cloud regions. Since radar measures reflectivity off water and ice particles, areas with the heaviest precipitation, such as beneath the convective towers (i.e., squall line) in a MCS, have the highest reflectivity, as shown in Fig. 1. In a well-developed MCS, the downdraft is often directly below this area of high reflectivity, creating a mesohigh[15]. In addition to high pressure under the convective towers, warm air preceding the convective towers is forced upwards in the gust front, creating a precursory mesolow ahead of the mesohigh[15,16]. Also, another mesolow often follows the convective line in the stratiform region of the MCS (i.e., wake low), resulting from adiabatic warming of the descending air mass in the rear of the MCS[17]. This mesolow/mesohigh/mesolow pressure combination is well illustrated by TA station P61A as the first MCS passed over the coastline (Fig. 1). Here, the first mesolow pressure anomaly of -0.5 hPa corresponds to a narrow area of stratiform precipitation, indicated by moderate radar reflectivity. Immediately behind this first mesolow is an area of strong reflectivity, up to 45 dBZ, with a corresponding pressure anomaly of 2.8 hPa. Finally, as the reflectivity decreases to 20 dBZ, the pressure anomaly associated with the wake low

reaches a minimum value of -1.8 hPa. The MCS creates a peak-to-trough anomaly of 4.6 hPa. Radar images from station KDOX show that the cross-sectional reflectivity of the first MCS extends about ~90 km front-to-back, roughly east-to-west, as the MCS passes over TA station P61A (Fig. 2e). While the highest reflectivity occurred concurrently with the highest positive pressure anomalies (Fig. 2a-d), the mesolow/high/low sequence may further enhance meteotsunami generation relative to a scenario whereby the precursor mesolow and wake low were not present. By examining many TA stations and NOAA tide gauges simultaneously, the highest pressure occurs beneath the MCS's convective squall line (Fig. 3), though interpolation of pressures at the stations broadens the apparent pressure anomaly along the convective line. The second MCS passed further south ~6 hours after the first MCS, arriving at Bishops Head, MD with an associated peak-to-trough pressure anomaly of ~5 hPa (Fig. 2d). The TA station O61A (Fig. 2a), which is located on the extreme northern fringe of the second MCS near the synoptic scale low pressure center, did not show significant atmospheric pressure anomalies and did not have reflectivity measurements above 40 dBZ.

The maximum peak-to-trough atmospheric pressure anomalies during the two MCSs at all of the TA stations and tide gauges are shown in Supplementary Fig. 4. The first MCS had a latitudinal footprint of 200 km. The maximum peak-to-trough pressure anomaly reached 6 hPa and remained stable at ~4 hPa as it passed over Delaware Bay. The second MCS had a larger latitudinal footprint of 500 km, and its largest maximum pressure anomaly recorded was far inland; as it traversed the Atlantic coast, the maximum pressure anomaly recorded by both TA stations and

NOAA tide gauges was ~3 hPa. The magnitude of pressure anomalies across the interior of the U.S. illustrates the long duration and wide spatial coverage of these MCSs. It should also be noted that these surface pressure anomalies may be enhanced by atmospheric ducting[18], but the thermodynamic profiles in advance of the MCSs do not support ducting being a dominant mechanism for pressure anomaly generation in this case (Supplementary Figs. 5 and 6).

The maximum atmospheric pressure anomalies at the TA stations and tide gauges correlate with the peak radar reflectivity (Figs. 1-3). Three different methods are used to further confirm this observation. First, the collocation of the center of radar reflectivity and atmospheric pressure anomaly is verified, as shown in Supplementary Fig. 7 and described in the Method section. As the first MCS on June 13th,2013 moves across the interior of the United States, the position of the center of the atmospheric pressure anomaly is never more than 150 km away from the center of the radar reflectivity values. Second, to confirm that the storm moves at the same velocity as the atmospheric pressure anomaly, the propagation velocity derived from both radar reflectivity and atmospheric pressure anomalies is shown in Supplementary Fig. 8 and described in the Method section. These velocity estimations are within 5 m/s of one another. The atmospheric pressure anomaly velocity was estimated by temporal averaging the atmospheric pressure anomalies observed on the 90 km spaced TA array. We believe that the discrepancy in the velocity estimations is due to the station spacing of the TA array, which spatially under samples the atmospheric pressure anomaly with an average wavelength of 150 km at any given time. The estimation of the atmospheric pressure anomaly velocity would be improved with the

increase of station spacing or modeling of the phenomena. Finally, over a given continental location (in this case at TA stations), it is shown that the arrival of the maximum observed atmospheric pressure anomaly and the arrival of the maximum observed radar reflectivity occur at the same time (Supplementary Fig. 9), verifying that the average velocities of the MCS and pressure anomalies must be similar. These observations of location, speed, and timing provide at least to first order the basis to infer MCS pressure anomalies offshore using radar reflectivity data, where direct atmospheric pressure measurements at sea level are currently lacking.

Once offshore, the propagation speeds and back-azimuths of the MCSs are estimated from radar reflectivity (Method). The first MCS maintained an average speed of 22 m/s as it propagated over the Atlantic Ocean at ~1500 UTC and dissipated by ~2000 UTC (Fig. 4). Conversely, the second MCS decelerated after ~0000 UTC on June 14 and was sustained for > 16 hours before the MCS propagated out of radar range.

Sea level response to atmospheric pressure anomalies. Spatial and temporal patterns in sea-surface elevation from 38 NOAA tide gauge stations are analyzed to reveal meteotsunami generation and transport characteristics. Twenty-four hours of sea level records starting at 1200 UTC on June 13, 2013 are examined after the NOAA tide predictions have been removed[19] and the resulting demeaned data have been five-hour, high-pass filtered (Fig. 5a). The first tide gauge that recorded the first MCS was station 17 (Ship John Shoal, NJ; Table 1). Sea level oscillations at this station were small (< 0.2 m peak-to-trough). Larger sea level oscillations associated with the first MCS started at a tide gauge located in Lewes, DE (station 16; Table 1) at 1500 UTC,

following within a few minutes of a ~3 hPa peak-to-trough pressure anomaly at the same location (Fig. 5; Supplementary Fig. 10). Stations to the south recorded more gradual pressure anomalies and undetectable sea level oscillations. To the north, station Cape May, NJ (station 18), also located in Delaware Bay, detected a sea level oscillation beginning at ~1500 UTC but with a peak-to-trough pressure anomaly of ~4 hPa arriving ~20 minutes earlier at ~1440 UTC (Supplementary Fig. 10). Sea level oscillation arrivals north of Cape May display a lag time of up to 3 hours relative to pressure anomalies. Such is the case at Atlantic City, NJ (station 19), for which a pressure anomaly arrived at 1500 UTC but the first sea level oscillation did not arrive until 1806 UTC. Stations north of the Montauk, NY (station 22) tide gauge did not measure a significant atmospheric pressure anomaly but had significant sea level oscillations. Newport, RI (station 29), for example, had a maximum peak-to-trough sea level oscillation of ~0.5 m but no significant atmospheric pressure anomaly. Maximum sea level oscillations and atmospheric pressure anomalies are displayed in Supplementary Fig. 11. Sea level oscillations were significant with a signal to noise ratio of >2 at tide gauges as far north as Portland, ME (station 36).

Within Delaware Bay, tide gauges at Lewes, DE, Ship John Shoal, NJ, and Cape May, NJ all have positive first arrivals of the observed sea level oscillation. With an average wavelength on the order of 150 km, the pressure anomaly may be too wide to exert its force fully on Delaware Bay, which has a maximum width of 60 km. The maximum water depth in the bay is 30 m[20], corresponding to a maximum shallow water wave speed of ~17.1 m s^{-1}. This speed is lower than the forward speed of the atmospheric pressure anomaly during the first MCS (~22 m s^{-1}) over the bay, implying

a supercritical flow regime, in which a positive sea level anomaly corresponds to a positive atmospheric pressure anomaly (Method), as observed at the tide gauges in the bay (Fig. 5, Supplementary Fig. 10, Supplementary Fig. 12). Further investigation, perhaps using a numerical model, is required to determine the relative importance of atmospheric pressure and wind forcing within Delaware Bay.

The second MCS propagated eastward over the continental U.S. and subsequently propagated across the Atlantic Ocean. Lewisetta, VA (station 9), well within Chesapeake Bay, was the first NOAA tide gauge to detect the second MCS atmospheric pressure anomaly and wind gusts (Supplementary Fig. 13). The MCS crossed over this gauge at 1942 UTC, with a sea level oscillation occurring shortly after at 2000 UTC. The longest delay time for the second meteotsunami occurred at the tide gauge at Wachapreague, VA (station 10), outside Chesapeake Bay, with an arrival of the atmospheric pressure anomaly and strong wind gusts at 2042 UTC, followed by a sea level oscillation arriving at 2242 UTC. However, most delay times between the second MCS atmospheric pressure anomaly (as well as wind gusts) and recorded sea level oscillations were less than an hour for stations south of Atlantic City, NJ (Fig. 5). This short delay time supports the working hypothesis that within Chesapeake Bay, sea level oscillations are created under direct forcing (in shallow water near the tide gauge stations), not reflections off the shelf break. Since the width of Chesapeake Bay (~25 km) is much less than the average wavelength of the atmospheric pressure anomaly (~150 km), the sea level oscillations are most likely the result of wind stress, not atmospheric pressure forcing.

Outside the two bays towards the open ocean, the increasing water depth on the continental shelf leads to a higher shallow water wave speed that approaches the propagation speed of the MCS near the continental shelf break, resulting in growing amplitude of the water wave. Mercer et al.[2] illustrate with a numerical model that a meteotsunami moving over a shelf break into deeper water has both transmitted and reflected wave energy. Once the meteotsunami is reflected, it travels as a free wave. Indeed, in the present study, sea level oscillation arrivals for stations 19-30 (north of and including Atlantic City) are consistent with the predicted travel times[21] of waves reflected from the shelf break (Supplementary Fig. 14; Method).

The first arrival of a sea level anomaly at NOAA Deep-ocean Assessment and Reporting of Tsunamis (DART) buoy 44402, east of the shelf break, is the first meteotsunami transmitted across the shelf break, moving at a shallow water wave speed that causes it to arrive before the atmospheric pressure anomaly (Fig. 6). DART instruments are ocean pressure sensors located on the seafloor that report ocean pressure as water column height[22]. The instruments record every 15 minutes unless the sea level oscillation exceeds one of two critical thresholds, at which time sampling increases to every minute or 15 seconds. Removing the mean water depth and high-pass filtering low-frequency oscillations over 5 hours reveals two sea level anomalies that passed over the station, the first at 1654 UTC and the second at 2006 UTC on June 13, 2013. Unlike the NOAA tide gauges, the first wave event occurred before high radar reflectivity of the first MCS passed over the station, suggesting that the leading edge of the meteotsunami propagated faster than the atmospheric forcing (Fig. 6b). The second arrival at DART buoy 44402 occurred three hours later, with a

reversed polarity. The first arrival is attributed to the transmitted wave from the continental shelf break, and the second arrival is attributed to a wave that was first reflected from the continental shelf break, then reflected again at the shoreline, and finally transmitted across the continental shelf break to DART buoy 44402. To estimate the time between the transmitted arrival at the buoy and the reflected arrival, a travel time model[21] is used with a shallow water velocity structure obtained using National Geophysical Data Center (NGDC) bathymetry[23] (Method). Results indicate that a majority of the energy reflected off the coastline would arrive back at the buoy ~3 hours after the transmitted meteotsunami arrives at the buoy (Supplementary Fig. 15), consistent with the observations of both the June 13, 2013 (Fig. 6b) and April 10, 2013 (Supplementary Fig. 16) meteotsunamis observed at DART buoy 44402.

Unlike the first MCS, the second MCS generated no significant meteotsunami reflection off the continental shelf break. Specifically, there were no significant sea level oscillations at stations north of Atlantic City, NJ, and no significant sea level oscillation was detected by DART Buoy 44402 or 41424 in response to the second MCS. The second MCS decelerated to a propagation speed of ~20 m s^{-1} and then to 15 m s^{-1} (Fig. 4) as it propagated towards the shelf break, which limited the region of Proudman resonance along the shelf and reduced the amplitude of the second meteotsunami in areas decoupled from the atmospheric pressure forcing.

Discussion

The observed correlation between radar reflectivity and atmospheric pressure anomalies recorded by TA and tide gauge stations (Figs. 2 and 3) indicates that the largest positive pressure anomalies occur where reflectivity is >40 dBZ. These areas

also experience mesolows before and after passage of the convective line of the MCS. The integrated area over the continental shelf that has reflectivity > 40 dBZ is 40,000 km^2 during five hours for the first MCS and 90,000 km^2 during 20 hours for the second MCS, as indicated by NOAA WSR-88D stations KDIX, KAKQ, and KMHX. Although the second MCS covered ~2 times the area of the first MCS, the duration of the second MCS was four times as long due to its slower propagation speed and larger spatial extent. This speed disparity causes the atmospheric pressure forcing by the second MCS to be less efficient than the first MCS for generating a large amplitude water wave along the continental shelf.

The absence of a detected shelf break meteotsunami reflection from the second MCS at coastal tide gauge stations suggests that there may be a minimum threshold for the size of the MCS forced area under Proudman resonance that is required to observe a meteotsunami reflected off the shelf break. To find where the meteotsunamis were most efficiently generated, the area where resonance is occurring is defined to be the area where the MCS propagation speed and the shallow water wave speed are similar ($0.707 < U/C < 1.225$), as indicated by the yellow-colored regions in Fig. 7. These values correspond to where the absolute amplitude of the water wave is ~2 times the magnitude of the response to a stationary pressure anomaly (Method). The second MCS covers a larger area over the continental shelf than the first MCS does. However, 35% of the area covered by the first MCS and a much smaller percentage of the area covered by the second MCS (10%) are resonant. The lower percentage for the second MCS indicates that the speed of the second MCS was not as optimal for generating a meteotsunami through Proudman resonance. For the

first MCS, the resonant region was a continuous strip at latitude 39-40°N near the continental shelf break. For the second MCS, the resonant region was distributed over a much larger latitude range (33-40°N) in relatively small patches. The smaller, noncontiguous patches may indicate a reduced pressure anomaly relative to the first MCS. In addition, those patches occurred at different times, further distributing the sea level oscillations over time and limiting their amplitudes.

By examining the entire MCSs as they pass over the Atlantic Ocean, the areas that are approximately resonant and the amount of time spent in resonance are estimated (Fig. 7; Supplementary Fig. 17). These areas provide constraints on the possible locations of the reflection of tsunami waves along the continental shelf break. The second MCS crossed over both a broad continental shelf break at ~33-34°N and a narrow shelf to the north, while the first MCS crossed over a narrow shelf break at ~39-40°N (Fig. 7). The broad shelf break traversed by the second MCS allowed more wave energy to be transmitted across the shelf break than reflected back towards the coast[24], contributing to a relatively weak reflected meteotsunami and negligible sea level oscillations being recorded at the South Carolina tide gauges in response to the forcing from the second MCS. Within local bays and harbors north of 34°N, detecting a signal associated with reflection of the second meteotsunami is difficult because the signal is embedded within the noise associated with the oscillations or seiches generated by the first meteotsunami.

Land-based radar reflectivity extends to ~230 km, limiting the extent that MCSs can be observed off the coast. However, for near-term meteotsunami prediction, radar-based observations (supplemented whenever possible by coincident

in situ atmospheric surface pressure measurements) only need to be made as an MCS passes over resonant areas, which are within this 230 km limit for MCS propagation speeds < 40 m s^{-1}. Most of the resonant areas for typical MCS propagation speeds of 20-40 m s^{-1} are within 200 km of the coast. Once the meteotsunami is in a subcritical regime, it outruns the atmospheric forcing, traveling at the local shallow water speed. At this point, predictions must rely on models to estimate reflections off the continental shelf and back towards the coastline. Radar is most helpful for tracking and estimating the MCS velocity as it propagates offshore.

One potential limitation of this study is the assumption that the wind stress forcing is negligible compared to the atmospheric pressure forcing[25]. Although wind stress is known to affect the magnitude of the shallow water wave, this effect is likely to be small relative to the atmospheric pressure forcing outside of shallow bays because the effect of wind stress is inversely proportional to water depth. Within Chesapeake Bay, due to the small crossing distance, wind forcing is likely the dominant mechanism for generating the observed sea level oscillations. Oscillation generation mechanisms within Delaware Bay are harder to determine. For example, stations at Lewes, DE and Cape May, NJ, located on opposite sides of Delaware Bay (Supplementary Fig. 12), support a primarily pressure-driven sea level oscillation, as indicated by the positive and equal amplitude of the initial sea level oscillations; if the wind stress contribution was significant, then the westerly wind stress associated with the eastward-propagating MCS should increase the sea level oscillation magnitude at Cape May, NJ relative to Lewes, DE. This increase, however, is not observed.

Since meteotsunamis generated by MCSs along the U.S. East Coast are damaging to property, hazardous to boats in shallow waters, and dangerous to public safety, predicting these events is of financial and social value. The U.S. East Coast continental shelf and bays are environments where two wave trains created by the same meteotsunami-producing event can be present. The first wave train is forced directly beneath an atmospheric pressure anomaly and strong wind gusts, as seen at the stations in Delaware and Chesapeake Bay on June 13, 2013, and the second wave train results from the reflection of the wave off the continental shelf break, seen at the stations along the Atlantic coast and in Narragansett Bay on that day. This double wave train phenomenon has not been observed in other areas of the world where meteotsunamis have been documented [1,2,3,4,5].

For near-term meteotsunami prediction along the U.S. East Coast, three stages in the forecast process are suggested: (1) using land-based pressure measurements to monitor the magnitude of the atmospheric surface pressure anomalies as a radar-indicated MCS propagates towards the coast from the interior of the U.S., (2) monitoring radar reflectivity as the MCS propagates off the coast to the potential geographical area where Proudman resonance may occur, and (3) modeling of the meteotsunami development and possible reflection off the shelf break back towards the coastline.

Developing and then operationally implementing accurate numerical models of meteotsunami waves under atmospheric pressure (and perhaps wind) forcing is the next step towards understanding and predicting when and where MCS-generated meteotsunamis may occur. Ports, harbors, and bays may all have varying risk, and

characterizing areas that may have extreme resonant mechanisms is also required. Places like Atlantic City, NJ, documented both in the present study and in others[7], appear to have an especially large ocean response to MCS forcing. Along with numerical modeling, monitoring high-frequency atmospheric pressure anomalies in the interior of the continental U.S. and along the coastline is essential for early warning of potentially hazardous meteotsunamis.

Method

Pressure and Radar Anomaly Location. Estimates of the center of the atmospheric pressure anomalies and radar reflectivity of the first MCS front were found using pressure data from the TA stations and NOAA/WSR-88D radar station KPBZ. Station KPBZ was used because of the dense coverage of TA stations surrounding it. Atmospheric pressure time series were demeaned, high pass filtered over 5 hours, and squared so positive and negative anomalies did not cancel. Pressure data were averaged a half an hour before and after a given time step and then linearly interpolated to a 10 km grid. Radar data were down-sampled to a 10 km by 10 km grid. Radar reflectivity >40 dBZ was used to isolate the MCS front. The centers of the pressure anomalies and radar reflectivity measurements were calculated at five-minute intervals using a gray-level-weighted average of values. Results are displayed in Supplementary Fig. 7.

MCS Propagation Speed. The propagation speed and back-azimuth of the two MCSs are based on NOAA WSR-88D radar reflectivity > 40 dBZ (primarily within the convective line) from station KDIX for the first MCS and KMHX for the second MCS. A 2-D cross-correlation of two successive reflectivity images is performed. To

obtain estimations errors, estimations are performed over multiple time steps ranging from 5 minutes to 1 hour. The MCS propagation direction is estimated from the spatial shift of the peak cross-correlation, and the speed is calculated from the distance of the peak cross-correlation shift divided by the time interval between the reflectivity images.

Propagation speed and back-azimuth of the atmospheric pressure anomalies are found using the center of the pressure anomalies described above. Instead of a 2-D cross correlation, the change in position of the center of the pressure anomaly over a known time is calculated to find velocity. To obtain error estimations, speeds and back-azimuths are calculated using multiple time steps ranging from 5 minutes to 2 hours. Results during the first MCS from the atmospheric pressure anomalies, as well as the radar reflectivity, are displayed in Supplementary Fig. 8.

Proudman Resonance. The sea level anomaly (N) due to an atmospheric pressure anomaly (P_o) moving at a constant speed (U), neglecting bottom friction and the Coriolis effect, is given by[24]:

$$\mathrm{N} = (\frac{\mathrm{P_o}}{\mathrm{g\rho}})/(Fr^2 - 1) \quad (1)$$

where Froude number $Fr = U/C$, g is gravitational acceleration, and ρ is the water density. From equation (1), a positive (negative) atmospheric pressure anomaly yields a positive (negative) sea level anomaly under the supercritical condition ($Fr > 1$), where the pressure anomaly is moving faster than the tsunami waves. In contrast, a positive (negative) atmospheric pressure anomaly yields a negative (positive) sea level anomaly under the subcritical condition ($Fr < 1$), where the pressure anomaly is moving slower than the tsunami waves. As Fr approaches 1 (the critical condition),

Proudman resonance occurs, resulting in a large sea level anomaly. The steady-state sea level anomaly becomes infinite when $Fr = 1$ in the idealized situation described by equation (1).

Reflected Travel Times. To estimate arrival times at tide gauges 19-30 (Supplementary Fig. 14), the travel time from positions on the shelf break underneath the first MCS to the tide gauges is calculated using a travel time model[21] with a shallow water velocity structure converted from NGDC bathymetry[22] and added to the time of reflection at the shelf break. NOAA WSR-88D radar reflectivity from station KDIX was used to estimate a reflection time of 1700 UTC for the meteotsunami (generated by and initially collocated with the first MCS) from the continental shelf break, defined as a depth of 140 m. The first MCS covered a latitudinal range from 39°-40° N.

Tsunami Travel Times. The travel time of rays from various back-azimuths and reflection points to the DART 44402 buoy are calculated using a travel time model[21] with a shallow water velocity structure obtained using NGDC bathymetry[22]. The time delay (T_D) between the transmitted and coast-reflected tsunami arrivals at the buoy is given by:

$$T_D = T_R - T_T \quad (2)$$

where T_R is the travel time from the continental shelf break to the shore and back to the buoy, and T_T is the travel time from the continental shelf break to the buoy. Here, the continental shelf break and the shore are defined as 140 m depth and 0 m depth, respectively.

References

1. Goring, D. G. Meteotsunami resulting from the propagation of synoptic-scale weather system. *Phy. Chem. Earth.* **34**, 1009-1015 (2009).

2. Mercer, D., Sheng J., Greatbatch, R. J., & Bobanović J. Barotropic waves generated by storms moving rapidly over shallow water. *J. Geophys. Res.* **107,** 1-17 (2002).

3. Monseratt, S., Vilibić, I. & Rabinovich, A. B. Meteotsunamis: atmospherically induced destructive ocean waves in the tsunami frequency band. *Nat. Hazards Earth Syst. Sci.* **6,** 1035-1051, (2006).

4. Thomson, R. E. *et al.* Meteorological tsunamis on the coasts of British Columbia and Washington. *Phy. Chem. Earth.* **34,** 971-988 (2009).

5. Haslett, S. K., Mellor H. E. & Bryant, E. A. Meteo-tsunami hazard associated with summer thunderstorms in the United Kingdom. *Phy. Chem. Earth.* **34,** 1016-1022 (2009).

6. Proudman, J. The effects on the sea of changes in atmospheric pressure. *Geophys. J. Int.* **2,** 197-209 (1929).

7. Pasquet S., Vilibić, I. & Šepić, J. A survey of strong high-frequency sea level oscillations along the US East Coast between 2006 and 2011. *Nat. Hazards Earth Syst. Sci.* **13,** 473-482 (2013).

8. Pasquet S. & Vilibić I. Shelf edge reflection of atmospherically generated long ocean waves along the central U.S. East Coast. *Cont. Shel Res.* **66,** 1-8 (2013).

9. Churchill, D. D., Houston, S. H. & Bond, N. A. The Daytona Beach wave of 3-4 July 1992: A shallow water gravity wave forced by a propagating squall line. *B. Am. Meteorol. Soc.* **76,** 21-32 (1995).

10. Bentley, M. L. & Sparks, J. A. A 15 yr climatology of derecho-producing mesoscale convective systems over the central and eastern United States. *Clim. Res.* **24,** 129-139 (2003).

11. Ashley, W. S. & Mote, T. L. Derecho hazards in the United States. *Bull. Amer. Meteor. Soc.* **86,** 1577-1592 (2005).

12. SPC severe weather event review for Thursday June 13, 2013, http://www.spc.noaa.gov/exper/archive/event.php?date=20130613 (2013) Date of access: 06/21/2013.

13. USArray Data at the DMC. http://www.iris.edu/earthscope/usarray (2013) Date of access: 07/22/2013.

14. CO-OPS specifications and deliverables for installation, operation, and removal of water level stations. http://beta.tidesandcurrents.noaa.gov/publications/CO-OPS_Specifications_and_Deliverables_for_installation_operation_and_removal_of_water_level_stations_updated_November2008.pdf (2008) Date of access: 10/15/2013**.**

15. Adams-Selin, R. D. & Johnson, R. H. Mesoscale surface pressure and temperature features associated with bow echoes. *Mon. Wea. Rev.* **138,** 212-227 (2010).

16. Houze Jr., R. A. Mesoscale convective systems. *Rev. Geophys.* **42,** 1-43 (2004).

17. Houze Jr., R. A., Rutledge, S. A., Biggerstaff, M.I. & Smull, B. F. Interpretation of Doppler weather radar displays of midlatitude mesoscale convective systems. *Am Meteor. Soc.* **70,** 608-619 (1989).

18. Vilibić, I. & Šepić, J. Destructive meteotsunamis along the eastern Adriatic coast: Overview. *Phys. Chem. Earth* **34,** 904-917 (2009).

19. Parker, B. B. Tidal analysis and predictions. http://beta.tidesandcurrents.noaa.gov/publications/Tidal_Analysis_and_Predictions.pdf (2008) Date of access: 10/15/2013.

20. Multibeam Bathymetry. http://www.ngdc.noaa.gov/mgg/bathymetry/ (2013) Date of access: 07/19/2013.

21. Margrave, G. F. Numerical methods of exploration seismology with algorithms in MATLAB. http://www.crewes.org/ResearchLinks/FreeSoftware/NumMeth.pdf (2003) Date of access: 10/27/2013.

22. Deep-ocean assessment and reporting of tsunamis (DART®) Description. http://www.ndbc.noaa.gov/dart/dart.shtml (2013) Date of access: 09/15/2013.

23. Amante, C. & Eakins, B. W. ETOPO1 1 Arc-minute global relief model: procedures, data sources and analysis. NOAA Technical Memorandum NESDIS NGDC-24. http://www.ngdc.noaa.gov/mgg/global/relief/ETOPO1/docs/ETOPO1.pdf (2009) Date of access: 07/19/2013.

24. Kowalik, Z. Introduction to Numerical Modeling of Tsunami Waves. https://www.sfos.uaf.edu/directory/faculty/kowalik/Tsunami_Book/book_sum.pdf (2012) Date of access: 01/10/2014.

25. Dean, R. G. & Dalrymple, R. A. *Water wave mechanics for engineers and scientists* (World Scientific Publishing Co., New Jersey 1991).

Acknowledgements

We thank NOAA for providing the buoy data and NSF for supporting the USArray Transportable Array. We also thank the various institutions who participated in the July 18, 2013 teleconference to discuss ideas and preliminary analysis of the June 13, 2013 tsunami event along the U.S. East Coast, which the URI team had previously identified as being caused by MCS pressure forcing. Materials from the July 18, 2013 teleconference are available online at: http://nctr.pmel.noaa.gov/eastcoast20130613/

Author Contributions

C.A.W. gathered and analyzed data. R.M.Y. analyzed radar data and identified MCSs as the most likely source for the tsunami-like oscillations. Y.S. analyzed seismic data and ruled out offshore earthquakes as a possible source for the tsunami-like sea-level oscillations. J.M. investigated the relevance of Proudman resonance as a key contributor to the magnitude of the sea-level oscillations. C.A.W., R.M.Y., Y.S., J.M. C.R.K. and R.A.P. discussed the results and implications and commented on the manuscript and Supplementary Information at all stages.

Competing financial interests

The authors declare no competing financial interests.

Table 1 | NOAA tide gauge and DART buoy locations and water depth. Gauge and buoy locations are mapped in Supplemental Figure 1.

Station	Lat (N)	Long (W)	Mean Water Depth (m)	Station number	Location
8411060	44.66	-67.21	12.66	38	Cutler Farris Warf, ME
8413320	44.39	-68.21	9.14	37	Bar Harbor, ME
8418150	43.66	-70.25	13.49	36	Portland, ME
8419317	43.32	-70.56	19.53	35	Wells, ME
8423898	43.07	-70.71	7.41	34	Fort Point, NH
8443970	42.20	-71.05	8.73	33	Boston, MA
8447386	41.70	-71.16	23.06	32	Fall River, MA
8447435	41.69	-69.95	6.48	31	Chatham, MA
8449130	41.29	-70.10	3.6	30	Woods Hole, MA
8452660	41.51	-71.31	3.6	29	Newport, RI
8452944	41.72	-71.34	20.6	28	Conimicut Light, RI
8454000	41.81	-71.40	5.74	27	Providence, RI
8454049	41.86	-71.41	24.9	26	Quonset Point, RI
8461490	41.36	-72.09	5.06	25	New London, CT
8465705	41.28	-72.91	21.7	24	New Haven, CT
8467150	41.17	-73.18	5.6	23	Bridgeport, CT
8510560	41.05	-71.96	5.1	22	Montauk, NY
8518750	40.70	-74.01	5.86	21	The Battery, NY
8531680	40.47	-74.01	5.09	20	Sandy Hook, NJ
8534720	39.36	-74.42	7.17	19	Atlantic City, NJ
8536110	38.97	-74.96	4.99	18	Cape May, NJ
8537121	39.31	-75.38	21.42	17	Ship John Shoal, NJ
8557380	38.78	-75.12	5.01	16	Lewes, DE
8570283	38.33	-75.09	9.31	15	Ocean City Inlet, MD
8571421	38.22	-76.04	29.95	14	Bishops Head, MD

8571892	38.57	-76.07	3.48	13	Cambridge, MD
8575512	38.98	-76.48	5.24	12	Annapolis, MD
8577330	38.32	-76.45	4.48	11	Solomons Island, MD
8631044	37.61	-75.69	4.6	10	Wachapreague, VA
8635750	38.00	-76.46	5.53	9	Lewisetta, VA
8636580	37.62	-76.29	2.96	8	Windmill Point, VA
8637689	37.23	-76.48	6.44	7	Yorktown USCG Training Center, VA
8638863	36.97	-76.13	4.7	6	Chesapeake Bay Bridge Tunnel, VA
8639348	36.78	-76.30	23.18	5	Money Point, VA
8651370	36.18	-75.75	20.35	4	Duck, VA
8654467	35.21	-75.70	27.66	3	USCG Station Hatteras, NC
8656483	34.72	-76.67	3.55	2	Beaufort, NC
8662245	33.35	-79.19	6.66	1	Oyster Landing, SC
44402	39.40	-70.94	2443		DART 44402
41424	32.922	-72.466	5284		DART 41424

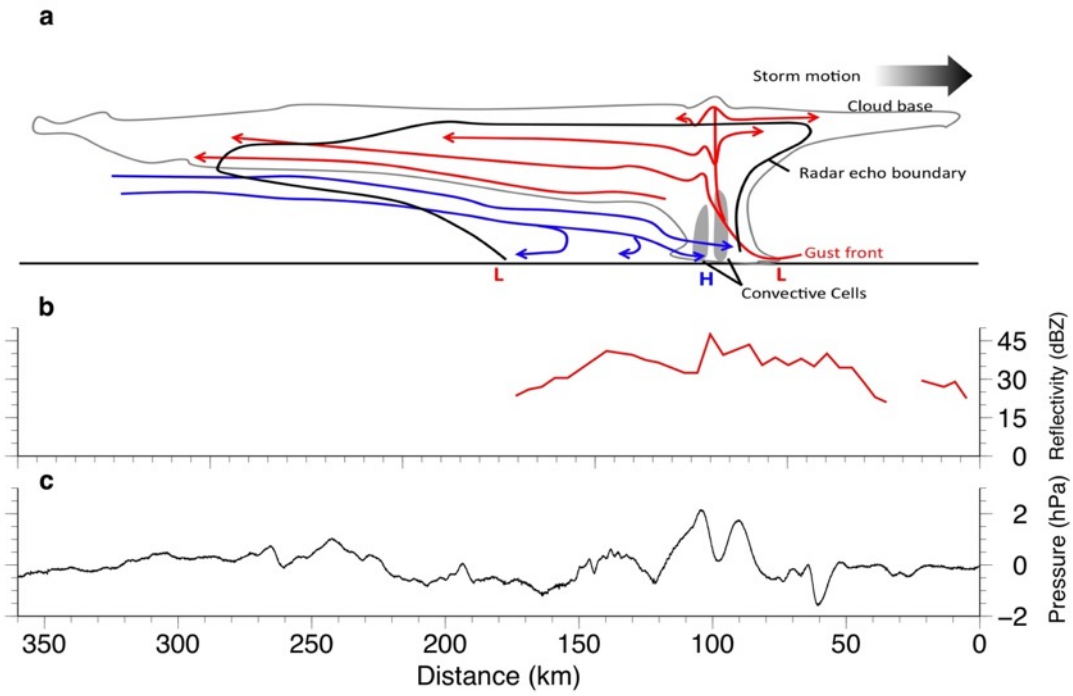

Figure 1 | Schematic, observed radar reflectivity, and observed surface pressure of the June 13, 2013 MCS at USArray station TA.P61A displayed in Figure 2 (Hammonton, NJ). (a) Vertical cross-section schematic of an MCS with a leading squall line and trailing stratiform region (adapted from Houze et al.[17]), where arrows indicate airflow, "L" markers indicate area of low surface pressure, and "H" marker indicates area of high surface pressure; (b) NOAA/WSR-88D radar station KDIX (Mt. Holly, NJ) base reflectivity (red) and (c) demeaned and five-hour high-pass filtered barometric pressure anomaly (black) from TA station P61A.

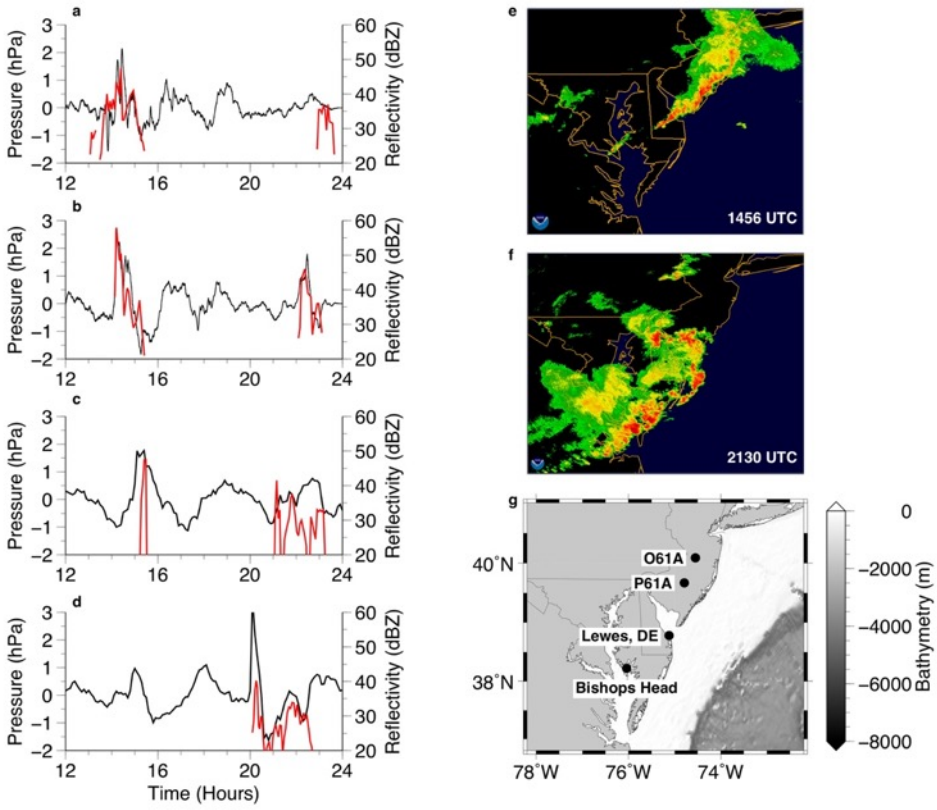

Figure 2| Radar reflectivity and pressure comparison. Base radar reflectivity (red) and demeaned and five-hour high-pass filtered atmospheric pressure anomaly (black) for USArray stations (a) TA.O61A and (b) TA.P61A, as well as NOAA tide gauges in (c) Lewes, DE and (d) Bishops Head, MD, on June 13, 2013 (with time indicated in UTC); NOAA/WSR-88D NEXRAD radar station KDOX base reflectivity at (e) 1456 UTC (first MCS) and (f) 2130 UTC (second MCS), obtained using the NOAA Weather and Climate Toolkit; (g) map displaying locations of time series in (a)-(d). Maps (e) and (f) were created with software NOAA's Weather and Climate Toolkit (WCT v3.7.4; http://www.ncdc.noaa.gov/wct/). Map (g) was created with software Generic Mapping Tools (GMT v4.5.12; http://gmt.soest.hawaii.edu).

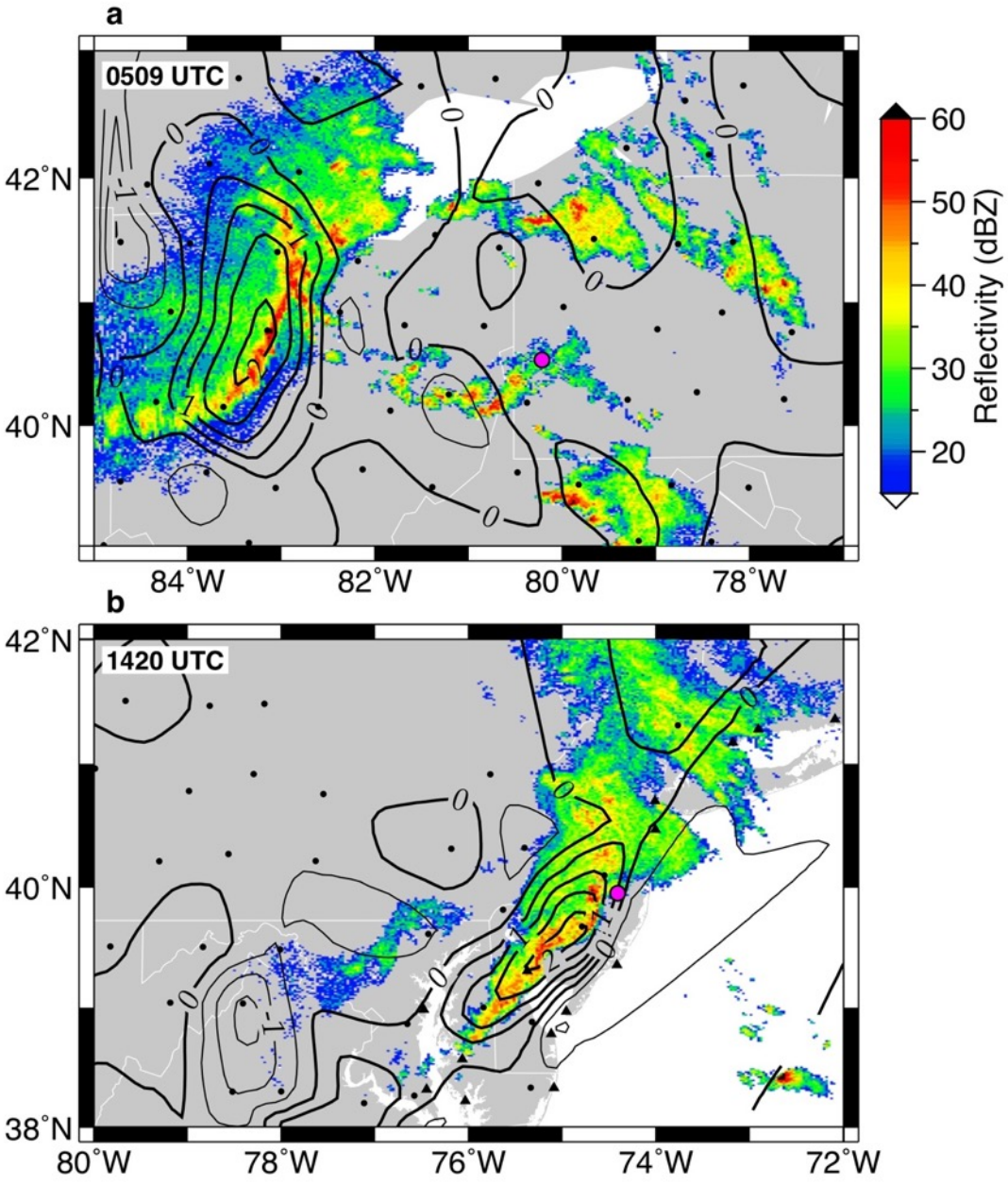

Figure 3| Snapshots of atmospheric surface pressure anomaly and radar reflectivity during the first MCS. Contours of atmospheric surface pressure anomalies cubically interpolated from TA (circle) and tide gauge (triangle) stations at (a) 0509 UTC and (b) 1420 UTC, overlaid on base radar reflectivity images from NOAA/WSR-88D radar stations (a) KPBZ and (b) KDIX, with radar locations indicated by magenta circles. Positive (negative) pressure anomalies (in hPa) displayed by thick (thin) black lines. Maps were created with software Generic Mapping Tools (GMT v4.5.12; http://gmt.soest.hawaii.edu).

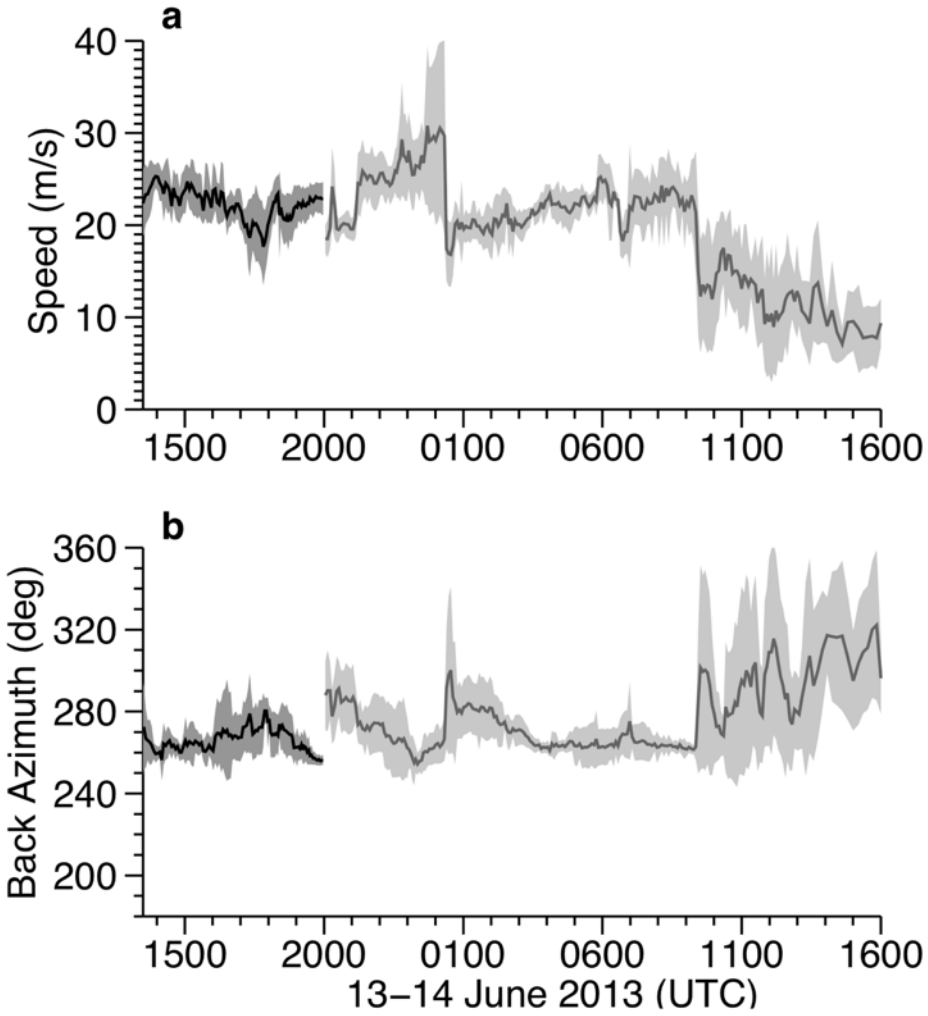

Figure 4| Estimated (a) propagation speed and (b) back-azimuth for both MCSs. The speeds of the first MCS (black) and second MCS (gray) are calculated starting when the MCS moves over Chesapeake Bay and ending when the MCSs dissipate or are out of the range of land based radar. Time is in hours from 0000 UTC on June 13. The meteorological convention is used here, whereby the back-azimuth is the direction from which the disturbances originate.

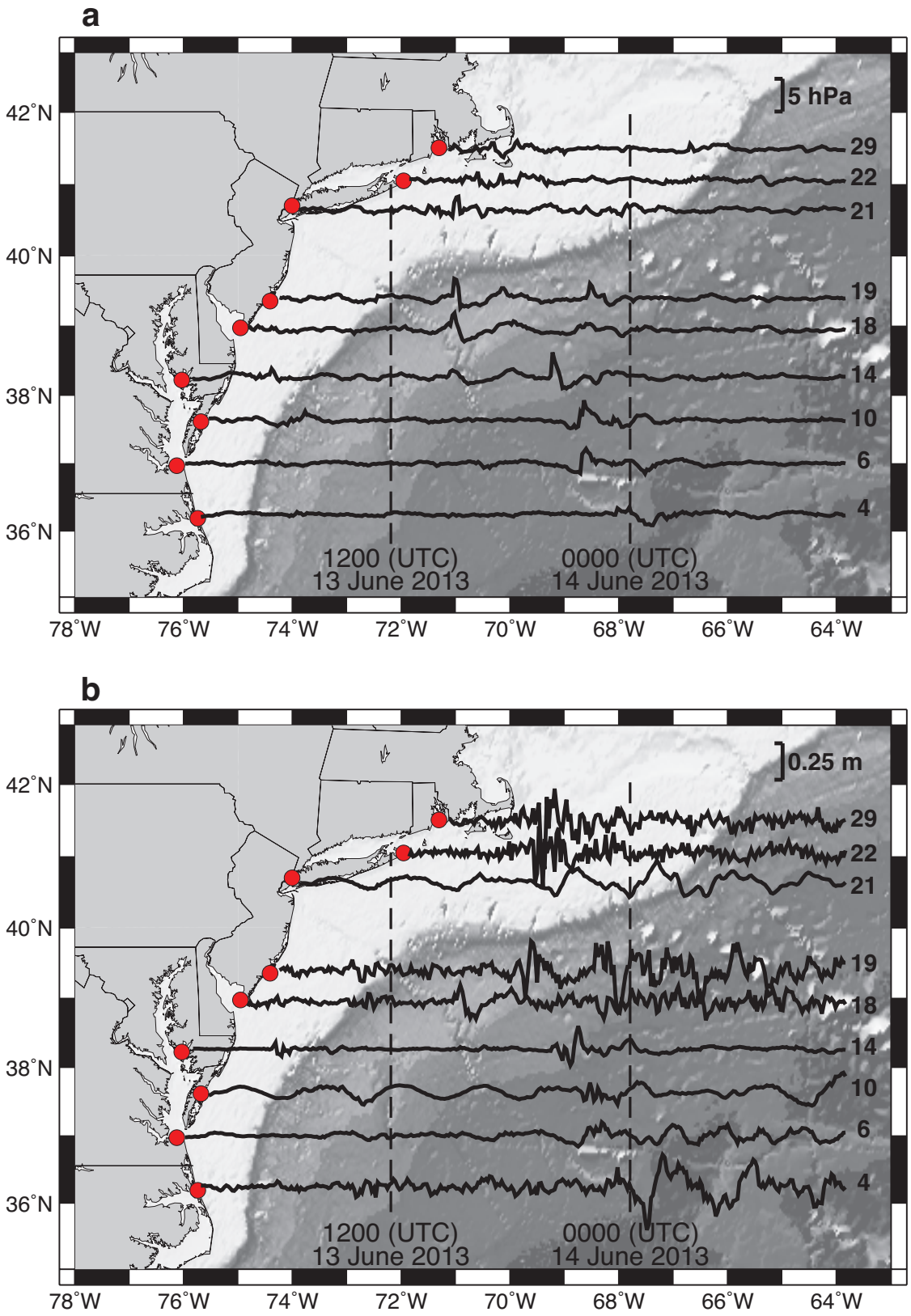

Figure 5| (a) Atmospheric surface pressure anomalies and (b) corresponding sea level oscillations for all 38 NOAA tide gauge stations. Tide gauge station locations

(red circles) and numbers are listed in Table 1 and displayed here. Maps were created with software Generic Mapping Tools (GMT v4.5.12; http://gmt.soest.hawaii.edu).

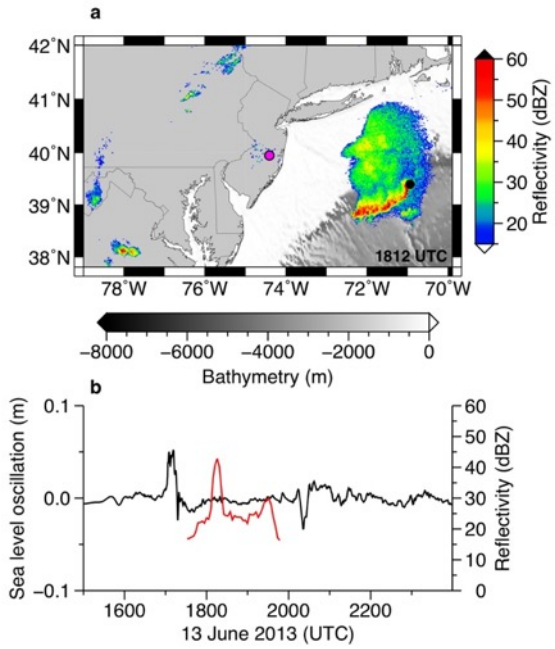

Figure 6| Response to atmospheric forcing observed at DART buoy 44402. (a) NOAA WSR-88D KDIX radar reflectivity at 1812 UTC on June 13, 2013 near DART buoy 44402 (black circle) and the location of KDIX (magenta); (b) sea level oscillation (black) and radar reflectivity (red) time series on June 13, 2013, where the sea-surface height is interpolated to every 1 minute, demeaned, and five-hour high-pass filtered. Map was created with software Generic Mapping Tools (GMT v4.5.12; http://gmt.soest.hawaii.edu).

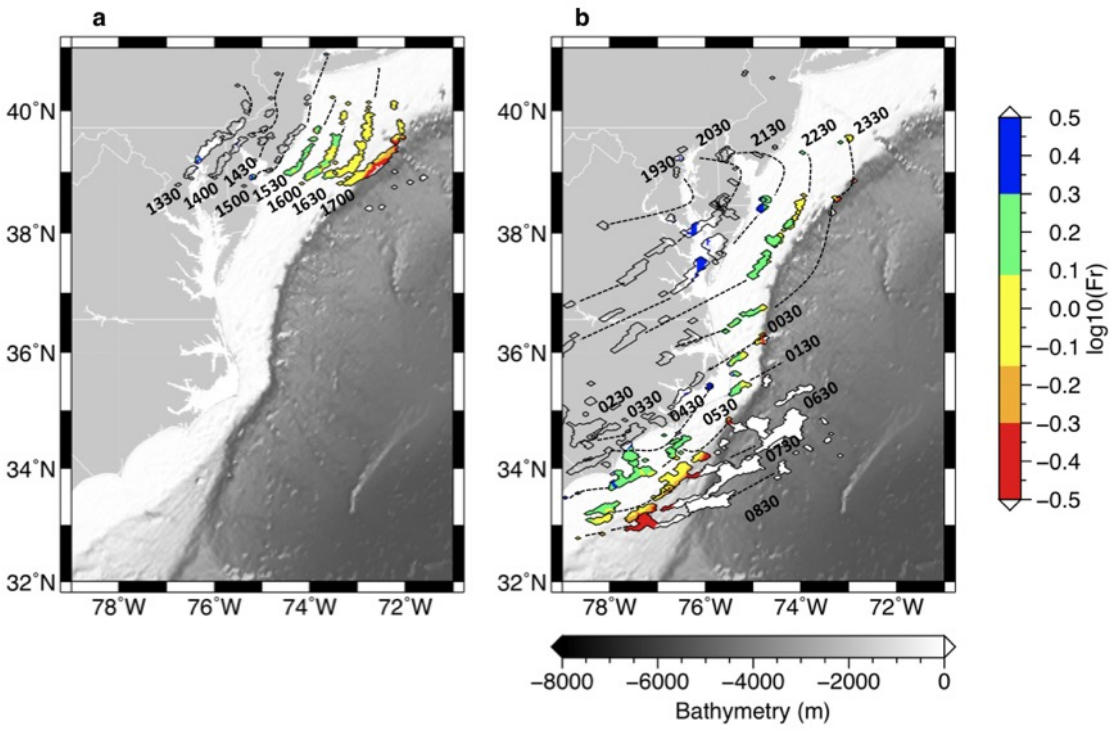

Figure 7 | Location of Proudman resonance and high radar reflectivity for the meteotsunami generated by the first and second MCS. Contours of reflectivity above 40 dBZ, determined from NOAA WSR-88D stations KDIX, KAKQ and KMHX, are colored according to the corresponding $\log_{10}(U/C)$. Time (UTC) on June 13-14, 2013 is contoured for the (a) first MCS and (b) the second MCS. Maps were created with software Generic Mapping Tools (GMT v4.5.12; http://gmt.soest.hawaii.edu).

Supplementary Material

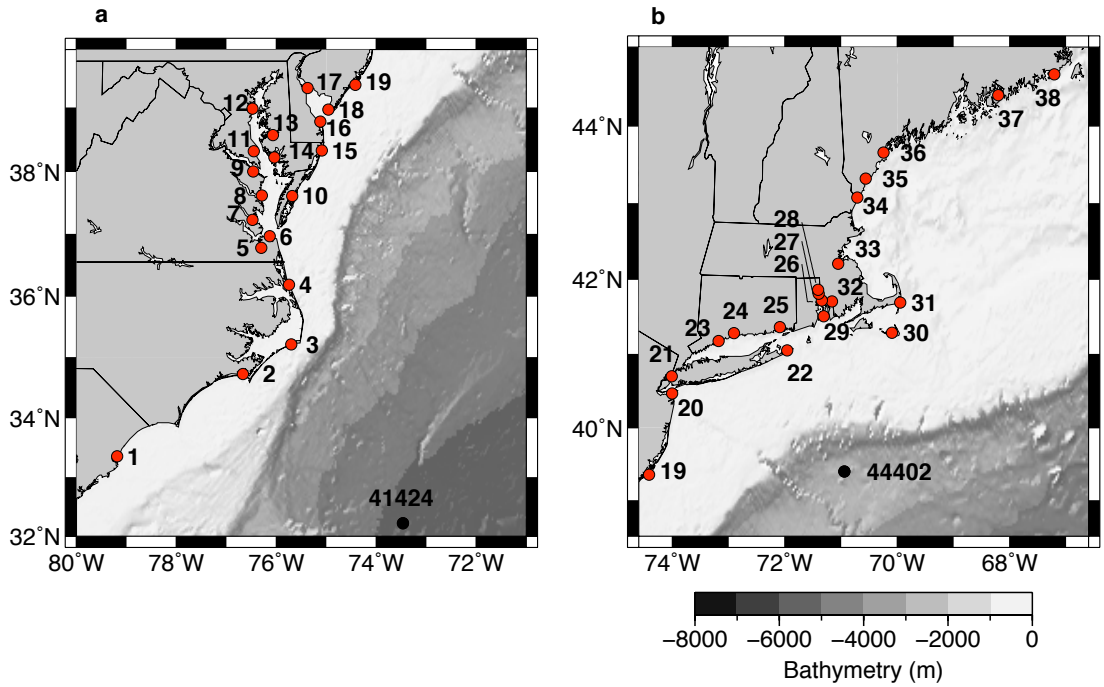

Figure 1| Locations of NOAA tide gauges (red) and DART buoys (black). Maps were created with software Generic Mapping Tools (GMT v4.5.12; http://gmt.soest.hawaii.edu).

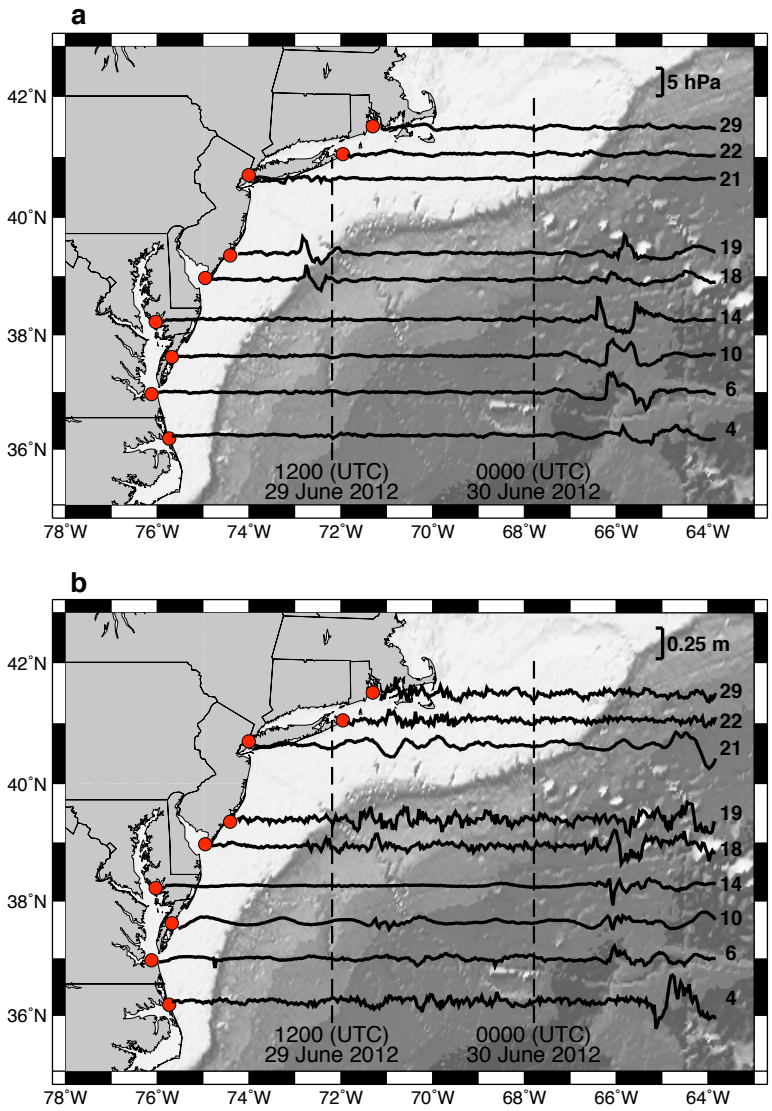

Figure 2 | June 29-30, 2012 meteotsunami (a) atmospheric surface pressure anomalies for select NOAA tide gauge stations and (b) corresponding sea level oscillations. Tide gauge station locations (red circles) and numbers are listed in Table 1 and displayed here. Maps were created with software Generic Mapping Tools (GMT v4.5.12; http://gmt.soest.hawaii.edu).

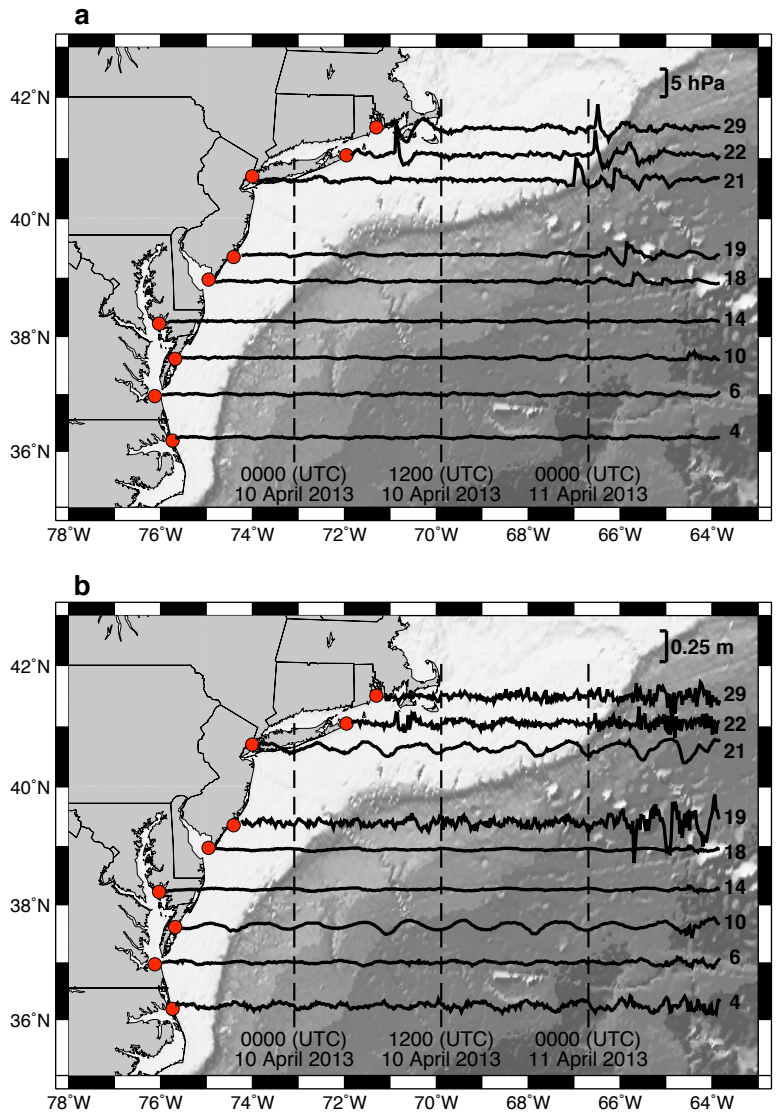

Figure 3| Same as Supplemental Figure 2 but for the April 10-11, 2013 meteotsunami. Maps were created with software Generic Mapping Tools (GMT v4.5.12; http://gmt.soest.hawaii.edu).

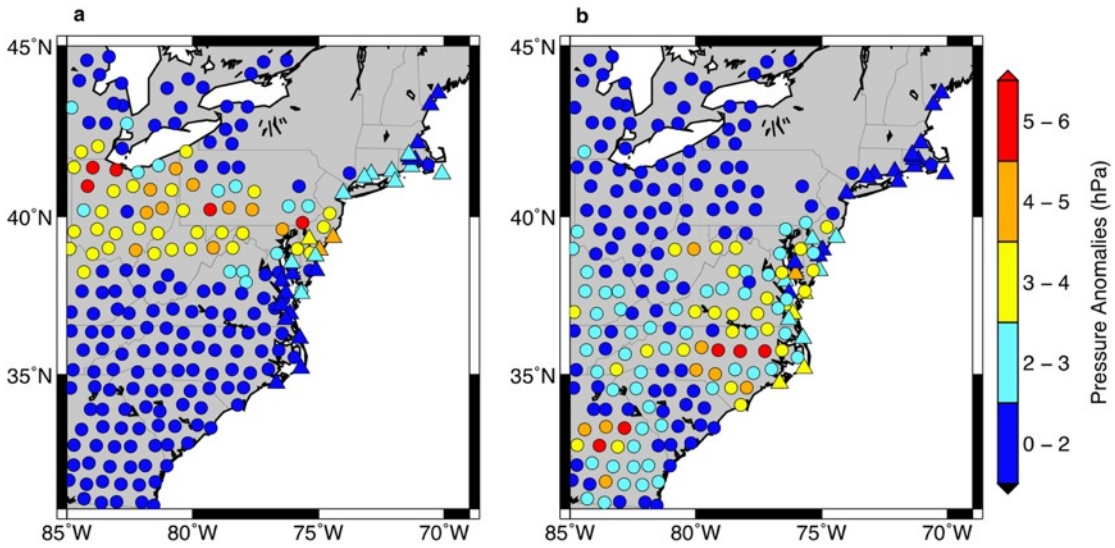

Figure 4| Maximum peak-to-trough atmospheric surface pressure anomalies. Pressure anomalies recorded by TA stations (circles) and NOAA tide gauges (triangles) for (a) the first MCS and (b) the second MCS. Maps were created with software Generic Mapping Tools (GMT v4.5.12; http://gmt.soest.hawaii.edu).

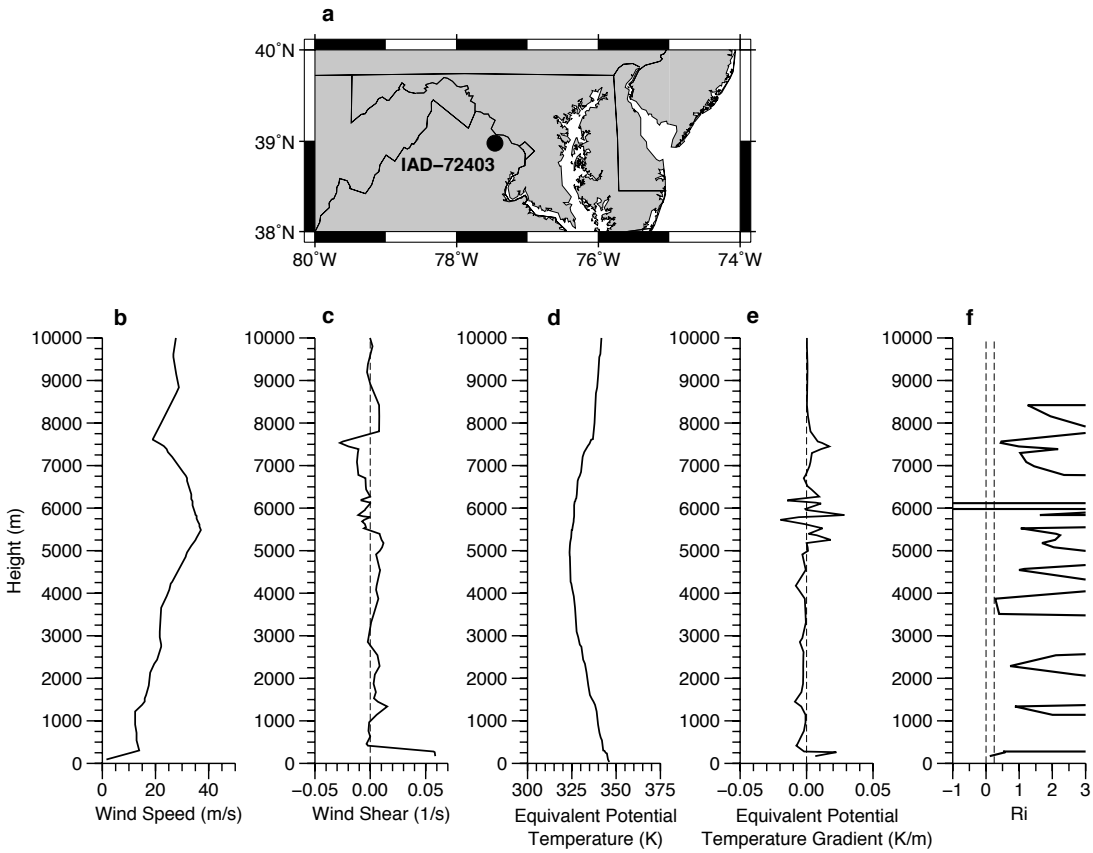

Figure 5 | Upper air sounding for station 72403 IAD at 12 UTC on June 13th, 2013. (a) Station location marked in black, (b) wind speed, (c) wind shear, (d) equivalent potential temperature, (e) equivalent potential temperature gradient, and (f) Richardson number (Ri), calculated using central difference estimations. Map was created with software Generic Mapping Tools (GMT v4.5.12; http://gmt.soest.hawaii.edu).

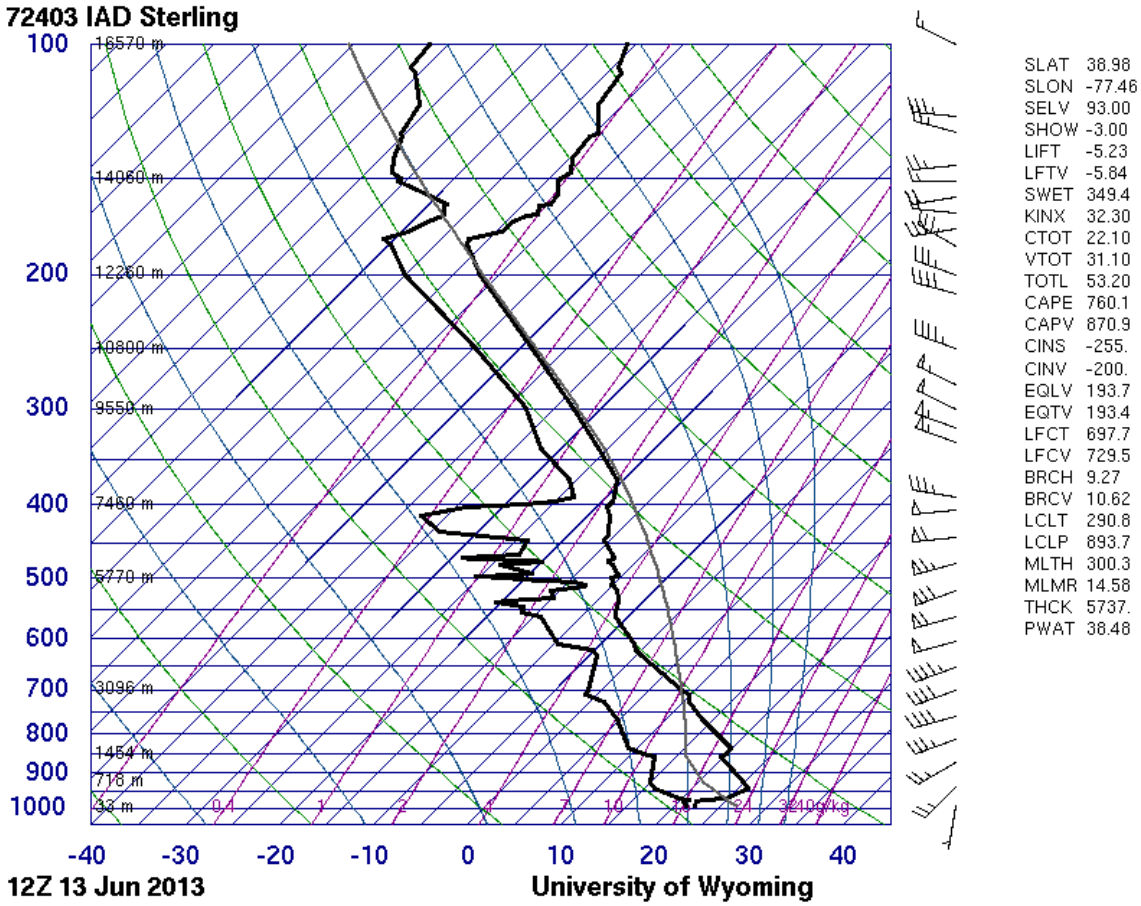

Figure 6 | SkewT diagram for station 72403 IAD at 12 UTC on June 13, 2013 (courtesy of the University of Wyoming).

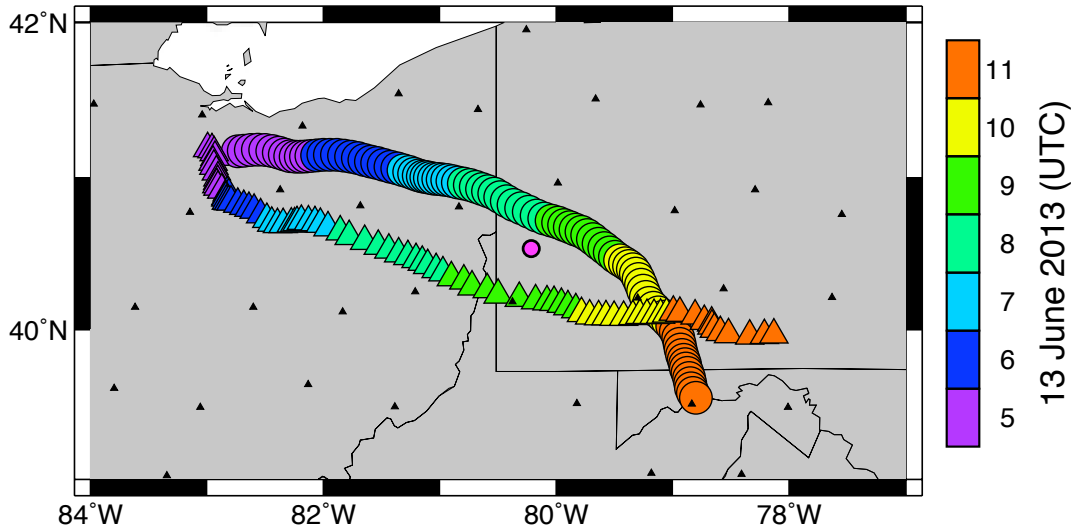

Figure 7| Center of radar measurements (circles) and pressure anomalies (triangles). Colors represent the time of the center location of radar reflectivity measurements and pressure anomalies. Small black triangles are locations of TA stations, and the magenta circle is the location of NOAA/WSR-88D radar station KPBZ (Pittsburgh, PA). Map was created with software Generic Mapping Tools (GMT v4.5.12; http://gmt.soest.hawaii.edu).

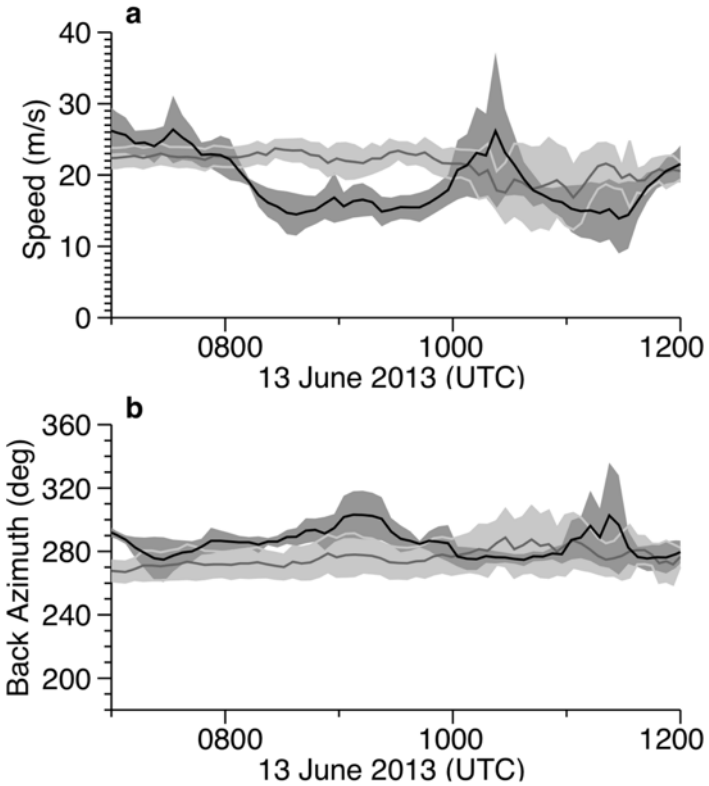

Figure 8 | First MCS (a) speed and (b) back azimuth with 95% confidence intervals. NOAA/WSR-88D radar station KPBZ (Pittsburgh, PA) was used to estimate the first MCS velocity (grey line). Estimations based on center of mass of atmospheric surface pressure measured on the TA station (black line).

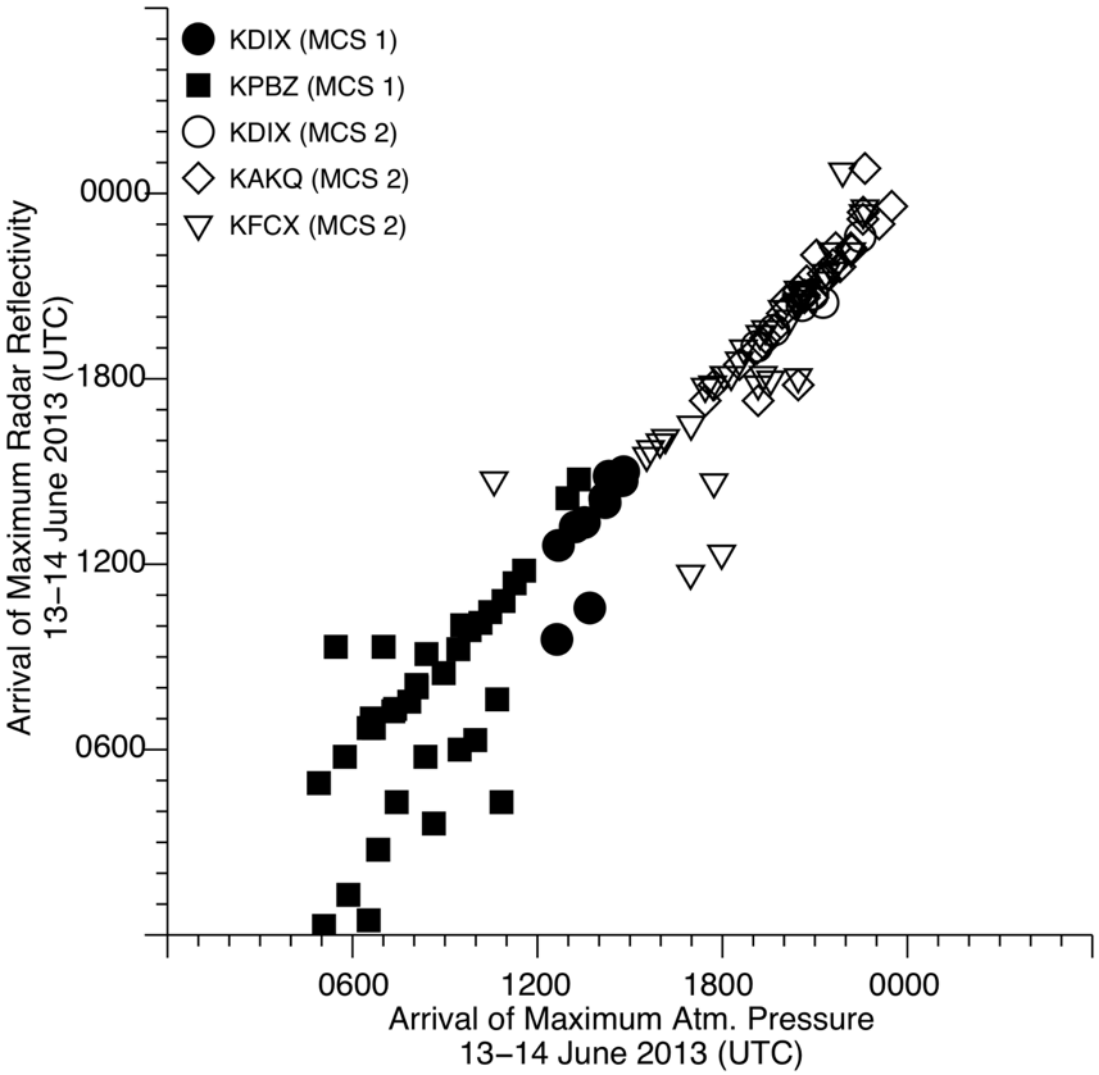

Figure 9 | Arrival times of maximum atmospheric pressure measured on TA stations and arrival time of maximum radar reflectivity over concurrent locations of TA stations for the first (filled markers) and second (open markers) MCSs. Radar reflectivity was limited to with in 250 km of NOAA/WSR-88D radar stations, listed by symbol in figure and to with in 6 hours of maximum pressure anomalies to limit the effect of radar reflectivity not associated with the two MCSs. Best-fit line through the data yields $R_{max} = 1.08\ P_{max} - 1.73$ with an R^2 value of 0.926.

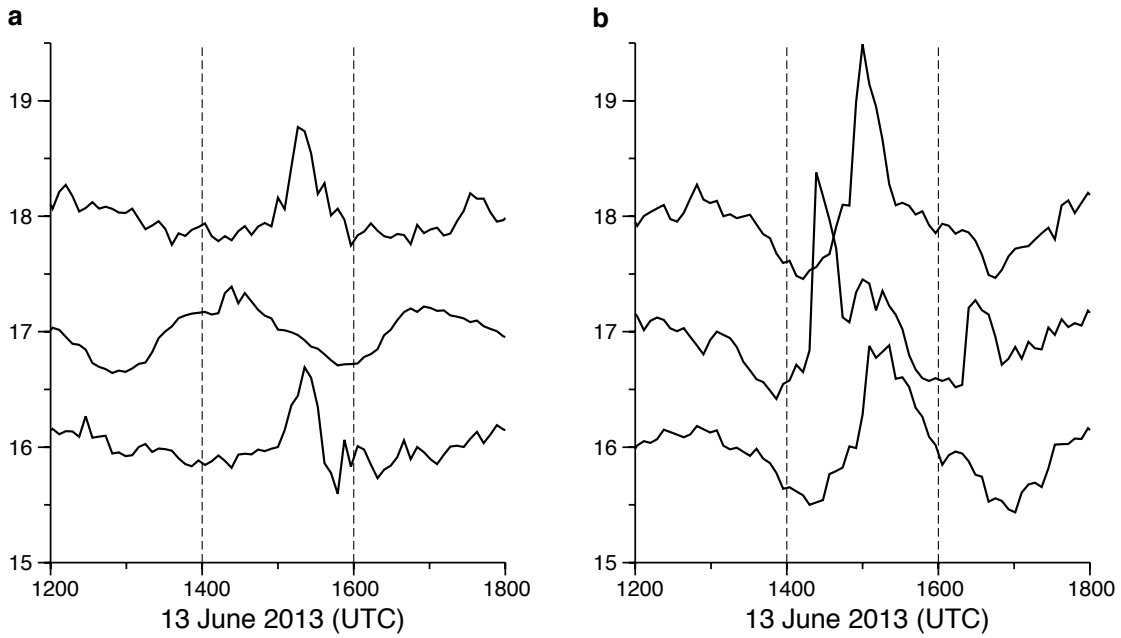

Figure 10| Selected NOAA tide gauges located in Delaware Bay. (a) Sea level oscillations and (b) atmospheric pressure anomalies for tide gauge stations Lewes, DE (16), Ship John Shoal, NJ (17), and Cape May, NJ (18). Y-axis tick marks represent (a) +/- 0.1 m and (b) +/- 1 hPa. Station locations are listed in Table 1 and displayed in Supplementary Fig. 1.

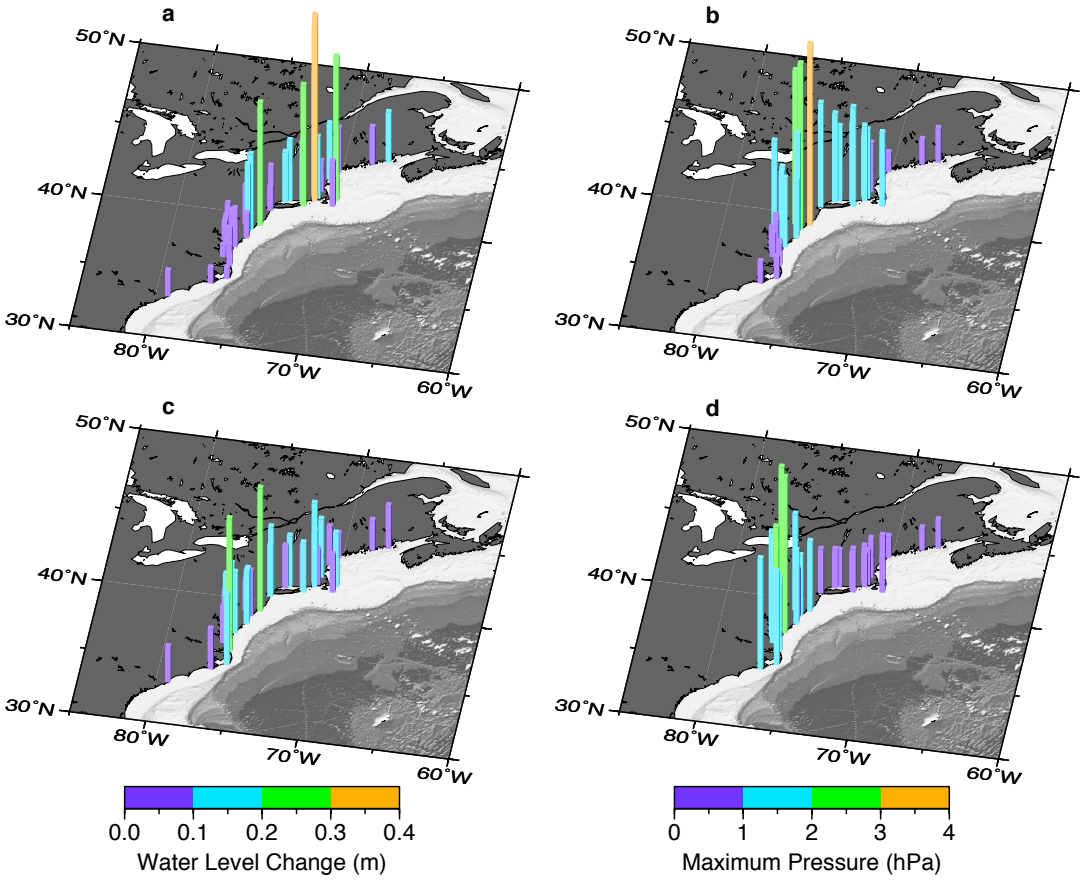

Figure 11| Maximum absolute (a, c) sea level oscillations and (b, d) atmospheric pressure anomalies at all 38 NOAA tide gauges for the (a, b) first and (c, d) second meteotsunamis. Maps were created with software Generic Mapping Tools (GMT v4.5.12; http://gmt.soest.hawaii.edu).

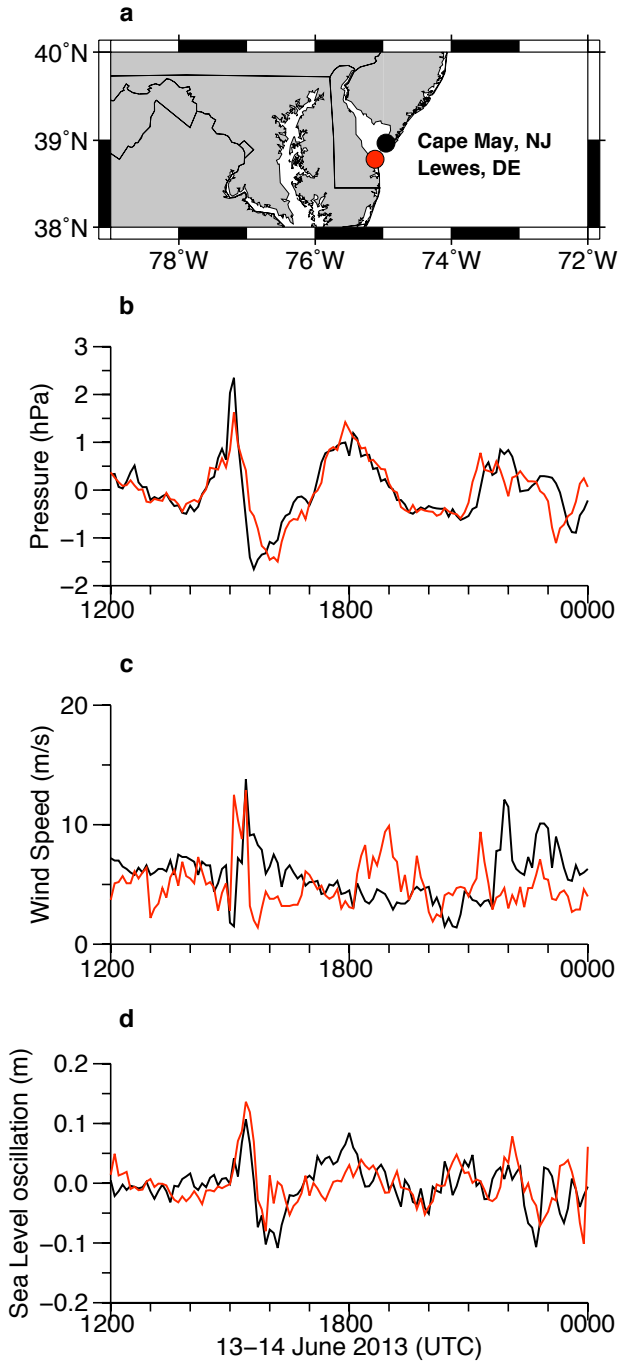

Figure 12| Atmospheric and sea level measurements for tide gauges at Cape May, NJ (black) and Lewes, DE (red) on June 13, 2013. (a) tide gauge locations; (b) atmospheric pressure, (c) wind speed, and (d) sea level oscillation. Map was created with software Generic Mapping Tools (GMT v4.5.12; http://gmt.soest.hawaii.edu).

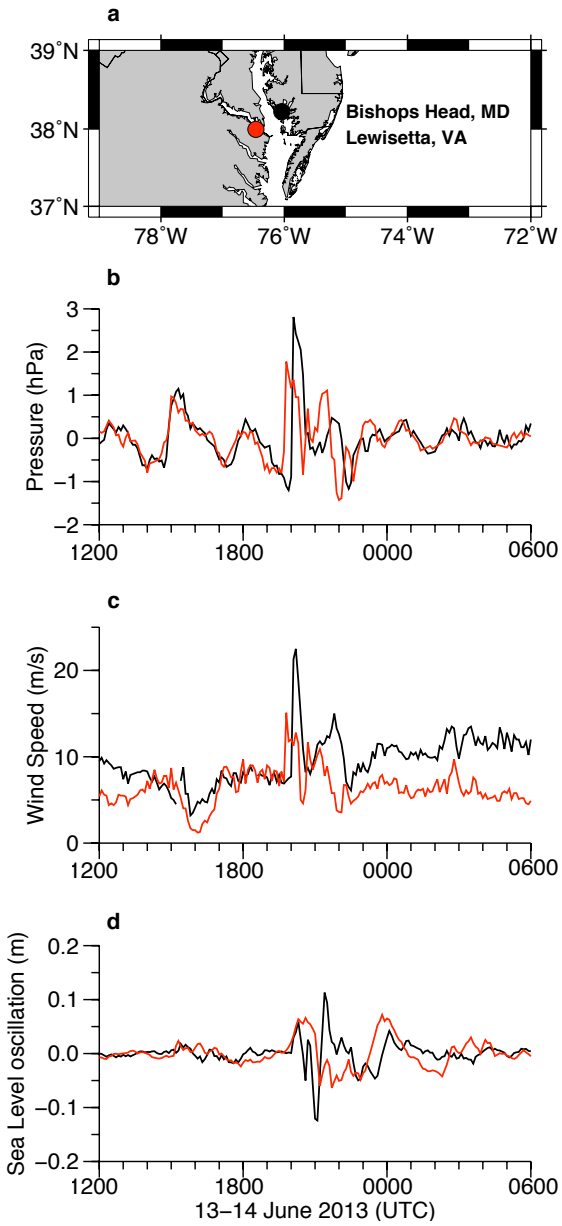

Figure 13 | Atmospheric and sea level measurements for tide gauges at Bishops Head, MD (black) and Leweisetta, VA (red) on June 13 and 14, 2013. (a) tide gauge locations; (b) atmospheric pressure, (c) wind speed, and (d) sea level oscillation. Map was created with software Generic Mapping Tools (GMT v4.5.12**;** http://gmt.soest.hawaii.edu).

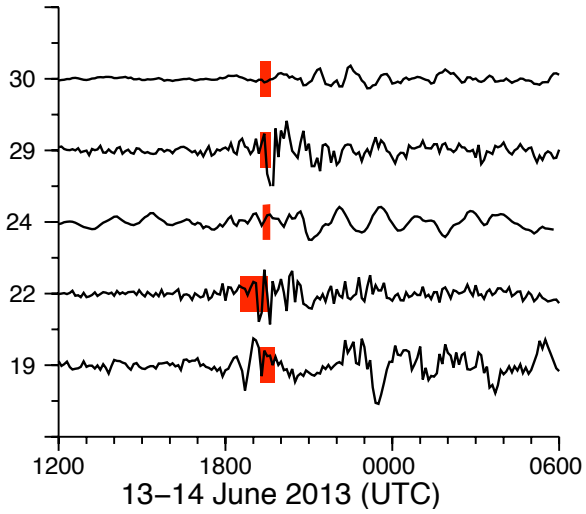

Figure 14 | Estimated arrival times (red) and measured sea level oscillations (black) at selected tide gauge stations. Y-axis tick marks represent +/- 0.1 m. Station locations are listed in Table 1 and displayed in Supplementary Fig. 1.

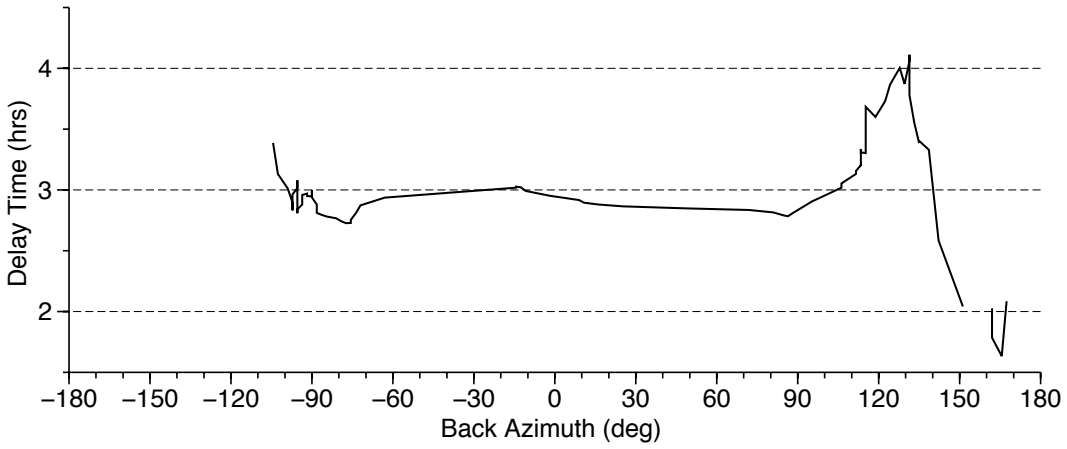

Figure 15| Time lag between first water wave arrival and second water wave arrival at DART buoy 44402. Angle corresponds to back azimuth relative to the DART buoy, where 0° is from the north and 90° is from the east.

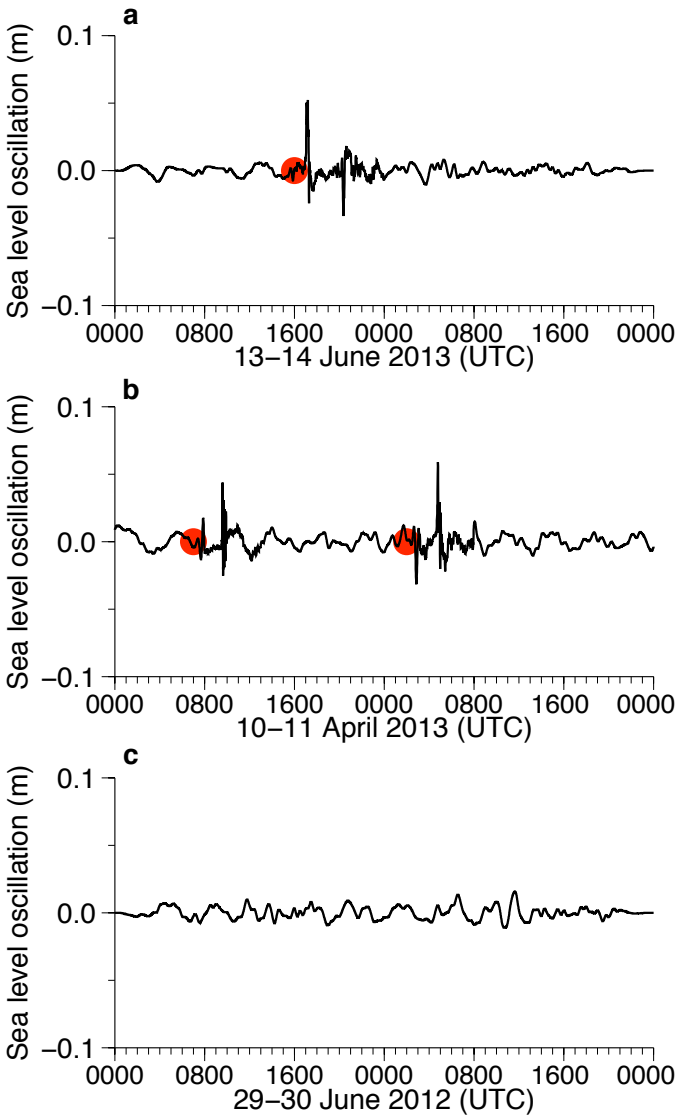

Figure 16 | Sea level response at DART buoy 44402. Time series are five-hour high-pass filtered and displayed for (a) June 13-14, 2013; (b) April 10-11, 2013; and (c) June 29-30, 2012. Estimate arrivals are highlighted in red.

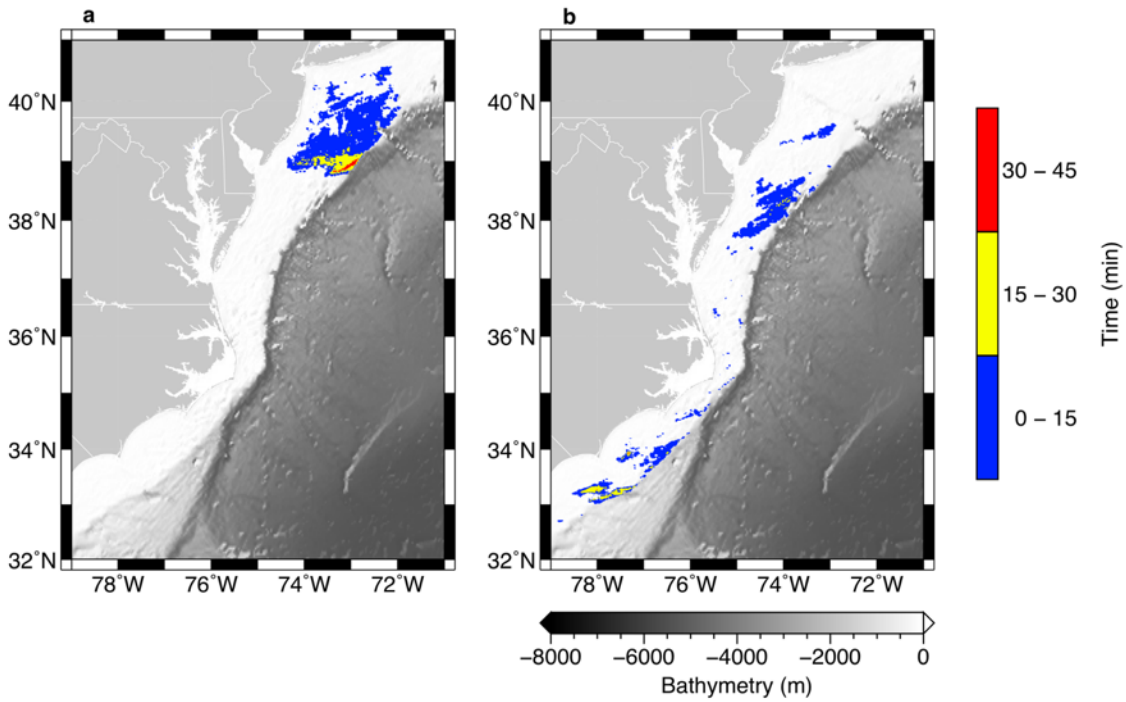

Figure 17 | Resonance time for areas near critical resonance for meteotsunamis on June 13-14, 2013. Locations for the most efficient generation of meteotsunamis generated by the (a) first and (b) second MCS, based on critical Fr. NOAA WSR-88D stations KDIX and KMHX were used to find reflectivity > 40 dBZ, as well as the propagation speed of the two MCSs. Maps were created with software Generic Mapping Tools (GMT v4.5.12**;** http://gmt.soest.hawaii.edu).

MANUSCRIPT II

Temporal and Spatial Variations of Circulation and Hydrography in Rhode Island Sound

By

Christina A. Wertman[1], David Ullman[1], Christopher R. Kincaid[1], Kathleen Donohue[1], Robert A. Pockalny[1], Anna Pfeiffer-Herbert[2]

To be submitted to ***Continental Shelf Research***

---

[1]Graduate School of oceanography, University of Rhode Island, Narragansett, RI 02882, USA.
[2]Stockton University, Galloway, NJ 08205, USA.

Abstract

Velocity profiles and hydrographic measurements were collected over a period of approximately two-years, throughout Rhode Island Sound, in order to characterize the environment and general coastal current. A coastal current was characterized as an intensification of cyclonic circulation along the periphery of Rhode Island Sound. The current strengthened during the summer (2-8 cm s^{-1}) and weakened during the winter (1-5 cm s^{-1}). We quantify the relative contributions through estimation of the depth-averaged momentum equation. The current is driven by a combination of tidal rectification, density gradients, and sea-surface setup. Over much of Rhode Island Sound, the Coriolis term is balanced by both barotropic and baroclinic pressure gradients. In addition, we find that there is a seasonal difference in the driving mechanisms. During the summer, baroclinic gradients enhance the cyclonic flow that is already established by tidal rectification and possibly wind-driven setup. During the winter, baroclinic and barotropic gradients are both small.

1. Introduction

Coastal currents are responsible for the transportation of water along the inner shelf. In Rhode Island Sound (RIS), the coastal current transports water in a cyclonic motion primarily parallel to local isobaths. This connects Vineyard Sound, Buzzards Bay, Narragansett Bay and Block Island Sound with the continental shelf. The summer intensification and winter dissipation of this current is thought to be a result of three general mechanisms: tidal rectification, density gradients, and sea-surface setup. Luo et al. (2013) and Liu (2015) numerically estimate that cyclonic circulation is doubled due to the development of a bottom cold pool during summer months. This

drives a baroclinic flow that adds to already present tidally rectified flow. Studies done on either side of RIS in Block Island Sound (Ullman and Codiga, 2004) and south of Martha's Vineyard (Fewings and Lentz, 2010), find that a wind driven sea-surface setup plays a dominant role at various times of the year in driving barotropic flow. The goal of this study is to determine what the relative contributions of the tidally rectified to the depth-average coastal current in RIS are. To address this question, we will quantify coastal circulation in RIS, document temporal and spatial distributions and estimate the mechanisms that contribute to the sustained cyclonic circulation.

Since the 1970s, many studies have been conducted along the North American continental shelf, which are adjacent to our study area (e.g. Bumpus, 1973; Brown et al., 1985; Beardsley et al., 1985; Chapman et al., 1986; Beardsley and Winant, 1979). The water along the middle and outer shelf, southeast of RIS, originates from the Scotian shelf (Beardsley and Winant, 1979). Large scale wind stress and heat fluxes over the continental shelf generate an alongshore pressure gradient (Beardsley et al., 1985). The alongshore pressure gradient drives persistent flow to the southwest. In contrast in the inner shelf we expect the circulation to vary significantly over seasonal times-scales due to stratification changes, sea-surface setup and wind-forcing.

Previous observational studies of RIS have focused on the description of seasonal variations of hydrography and to a limited extent of coastal jets. We define the coastal jets in this area as specific sub-regions of a coastal current, often 10's of km long. These studies have a scattered temporal and spatial distribution of observations. Ship-based measurements made over several days throughout the year indicate seasonal stratification develops in the summer and dissipates in the fall and

winter months (Shonting and Cook, 1970; Armstrong, 1998; Hicks and Campbell, 1953). The relatively strong current flows to the west at the mouth of Narragansett Bay. The current was observed with acoustic Doppler current profiler (ADCP) surveys (Kincaid et al., 2003). Kincaid et al. (2003) attribute this development to lateral density differences that extend from central RIS to the shoreline, resulting from differential heating and mixing. Ullman and Codiga (2004), Edwards (2004) and Ullman and Cornillon (2001) also identified a strong spring and summer coastal jet around Block Island, in the western region of RIS. They attributed the jet, observed with High Frequency Radar, satellites and numerical models, to a seasonal freshwater plume extending from Long Island and Block Island Sound into RIS. Observations of the coastal current in central and eastern sides of RIS are lacking and represent a gap in our understanding.

General studies of circulation along inner shelf regions suggest generation by tides, buoyant plumes, surface gravity waves, across-shelf wind stress, along-shelf wind stress and pressure gradients (Lentz and Fewings, 2012). Two recent numerical studies of RIS, have illustrated the importance of both tidal rectification and buoyancy driven flow in the RIS basin wide cyclonic circulation. Liu (2015) and Luo et al. (2013) find that in addition to tidal rectification, circulation is enhanced by density gradients developing primarily in the summer. They also find that surface currents are affected by seasonal wind forcing in the winter.

Despite the early hydrographic studies and recent modeling, the response of the whole water column to wind forcing, variability of sub-tidal currents across RIS and observational confirmation of tidal rectification, are not well measured and

lacking in this inner shelf region. From late 2009 to late 2011, multiple moored ADCP and hydrographic instruments were deployed in RIS over multiple months, providing an unprecedented view of the sub-mesoscale circulation and fluctuations. In addition, spatially dense hydrographic surveys were performed during multiple seasons to further illuminate the regional variability of the hydrographic environment. The resulting time series and hydrographic distribution allows us to explore the variability and dynamics of the coastal current.

We intend to improve on the knowledge in RIS by analyzing hydrographic and current measurements over seasonal time periods. We estimate the depth-averaged momentum equation, allowing us to compare measured flow with appropriate forcings. With better understanding of the physical processes important to RIS, we address the following questions: First, what are the magnitude and direction of tidal and sub-tidal circulation in RIS? Second, does tidal rectification, wind stress or pressure gradients dominate and explain the sub-tidal circulation observed? Our last question is what role does the RIS geometry play in the subtidal circulation?

2. Regional Characteristics

RIS is an inner shelf environment, connecting surf zones with the deeper middle and outer shelf. It is the region where the shelf circulation adjusts to the presence of the coastal boundary conditions, in both the horizontal and vertical (Lentz, 1995). The inner shelf extends to a depth of 10's of meters depending on wind strength, waves and vertical stratification. Often the inner shelf is defined as the region where surface and bottom boundaries interact (Lentz and Fewings, 2012). Assuming a typical eddy viscosity (A) of 0.01 $m^2 s^{-1}$, a characteristic Ekman boundary

layer ($\delta_E = \sqrt{2A/f}$) at the latitude of 41° would extend 15 m. Much of RIS is less than double this depth, indicating that the surface and bottom boundary layers should overlap. Therefore, RIS is classified as an inner shelf region.

Bathymetry and the coastal configuration plays a part in governing circulation in RIS. RIS is located outside the mouth of Narragansett Bay and bounded to the east and west by Buzzards Bay and Block Island Sound, respectively. RIS makes a bowl shape with deeper bathymetry in the center and southern edges, with depths averaging between 30-40 m. In the center, there is a long trough running northeast-southwest reaching depths of up to 55 m. RIS is open to the continental shelf to the south. We next discuss the major known mechanisms driving circulation and hydrography.

2.1 Tidal Flows

The tidal velocities in RIS range from 0.1 to 1 m s^{-1} (Luo et al., 2013), with the largest velocities observed around Block Island (Edwards, 2004). Tides are primarily semidiurnal and corresponding tidal ellipses are oriented along the northwest-southeast direction (Shonting and Cook, 1970). The M2 is the largest constituent (Codiga and Ullman, 2010), accounting for over 85% of the tidal constituent energy (Liu, 2015).

Modeling done by He and Wilkin (2006) found tides in RIS are co-oscillatory with the open ocean. In this area, ocean tides in deep water force tidal amplitudes onto the shelf. The resulting tidal amplitudes increase with distance away from the shelf break due to the onshore progression of the tidal wave (He and Wilkin, 2006; Moody et al., 1984). The resultant orientations of the major tidal axes are primarily perpendicular to the shelf break and do not vary substantially across RIS. For any

constituent, the ensuing high and low tides occur approximately uniformly across the shallow sound.

2.2 Residual Flows and Forcing Conditions

Circulation longer than tidal periods (e.g. > 33 hours) occurs primarily parallel to the shore. Large vertical changes in bathymetry over a relatively short distance cause cross-shelf circulation to decrease toward the shore. Any induced cross-shelf exchange creates vertical velocities, i.e. upwelling and downwelling. Vertical velocities are key to transporting larvae, nutrients, sediment, pollutants, and oxygen in the inner shelf (Lentz and Fewings, 2012). As such, we focus on the local forcing conditions in RIS in an aim to understand the drivers that influence the residual circulation.

2.2.1 Winds

Winds influence circulation through direct shear stress, induced sea-surface height gradients, and through mixing. During the winter season, winds blow to the east-southeast averaging less than 12 m s^{-1}. However, strong variation in both magnitude and direction are observed as storms pass through the area reaching up to 25 m s^{-1} (e.g. Codiga and Ullman, 2010). Summer winds are less variable, with average wind directions to the northeast and magnitudes averaging less than 7.5 m s^{-1}. At shorter time-scales, the New England inner shelf is susceptible to sea breezes, on the order of 2-5 m s^{-1}, created by differential heating of the land and sea (Fisher, 1960).

Winds in the area have an average eastward component during both the winter and summertime, commonly generating upwelling conditions in RIS (Codiga and

Ullman, 2010). Although, wind magnitude and direction have been documented for the southern coast of New England, the effects on circulation have not been well reported in RIS.

2.2.2 Tidal Rectification

Tidally rectified flow is thought to be more important than wind influenced circulation for periods longer than synoptic scales (3-5 days) in RIS (Liu, 2015). The resulting residual flow can be produced by tidal rectification created by exchanging momentum from tidal frequency motions to lower frequency motions in areas with sloped bathymetry (Wright and Loder, 1985). Tidally rectified flow is usually along isobaths with shallow bathymetry to the right of flow. When looking at the shore from RIS, circulation is counterclockwise or down-shelf. The resulting tidal rectification is on the order of 3 cm s^{-1} and predominantly along the periphery of RIS (Luo et al., 2013). The rectified flow is cyclonic with negligible flow in the center of RIS (Luo et al., 2013).

2.2.3 Solar Insolation

In the summer, numerical models suggest RIS residual flow is intensified and is almost doubled along the periphery (Liu, 2015). The increase is thought to be created by the presence of a bottom thermal front. The front starts when solar insolation overcomes tidal mixing in warmer months, leading to a well-developed pycnocline (Rosenberger, 2001; Shonting and Cook, 1970). The horizontal variations in vertical mixing creates a tidal mixing front and induces strong lateral density gradients (e.g. Holt and Umlauf, 2008). A numerical model supports stronger mixing along the shallow edges of RIS, and a resulting summertime bottom thermal front

(Liu, 2015). In addition to numerical models, measurements near the mouth of Narragansett Bay (Kincaid et al., 2003) have confirmed the intensification of residual flow associated with increased stratification during summer months.

2.2.4 Non-Local Forces

Non-local forces are thought to be small but could have limited effect on residual flow in RIS. Large-scale pressure gradients along the continental shelf remotely forces flow from the northeast to the southwest (Luo et al., 2013). However, idealized studies such as Chapman et al. (1986), indicate that along-shore flow remains mostly near the shelf break, limiting the effect on our region of interest. It is unclear the magnitude of the non-local forcing in this area.

3. Data

In order to further assess the forcings and local circulation properties in RIS, we focused on five key measurements: temperature, salinity, water velocity, tidal height, and wind velocity. We used moored acoustic Doppler current profilers (ADCPs), thermistors, conductivity, temperature and depth (CTD) instruments, underway hydrographic surveys, tide gauges, and weather buoys to best characterize these properties in RIS.

Moored instruments, measuring water velocity and hydrography were placed in and around RIS. Stations of moored instruments are described with a three-letter abbreviation given in Table 1. All stations had a moored ADCP (Fig. 2). Most stations had a chain of thermistors or CTD sensors located within 100-200 meters of the ADCP location. Therefore, the location of the hydrographic measurements is also referred to as the three letter station abbreviations of the ADCPs. Four deployments

were undertaken, each lasting at least a month (Table 1). Finally, four dense underway hydrographic surveys were collected in RIS. Location of the hydrographic measurements are illustrated in Fig. 2.

3.1 Velocities

Observations of velocity were made using RDI broadband 300 kHz and 600 kHz ADCPs moored on the seafloor. The ADCP data consisted of four deployments starting in November 2009 and ending December 2011. Instruments had a 6, 10 or 60-minute sampling rate and sampled the water column in 1 m or 2 m bins. Each ADCP used four beams to determine velocity. We eliminated the near surface data, usually about 6% of the water depth, because of side-lobe contamination of the signal. Velocities were transformed into components directed in the along- and across-shore directions at each station, illustrated schematically in Fig. 3a. Up and down-shelf are defined as an observer looking from RIS at the shore with up-shelf to the right and down-shelf to the left (Fig. 3a). These coordinates are oriented, so the across-shore coordinates point down slope toward deeper bathymetry (Fig. 1 & 3).

3.2 Temperature and Salinity

To measure hydrography, we used HOBO Water Temperature Pro instruments and HOBO Pendant Temperature thermistor chains as well as Seabird MicroCat CTD chains. Exact locations are shown in Fig.1 and the deployment times are listed in Table 1. Seven to nine thermistor instruments were evenly spaced along a chain with one pressure sensor below the surface float. These pressure sensors were used to estimate the depth of the thermistors during the deployments. The known distance between pressure sensors and thermistors was used to estimate the depths of each

thermistors throughout the deployment. Similarly, five or six CTDs were attached to chains near moored ADCPs. The duration of the thermistor and CTD deployments are listed in Table 1. In addition to measurements in the water column, bottom temperatures were recorded during the entire experiment, with thermistors attached to the bottom mounted ADCPs.

Higher resolution spatial measurements of hydrography were obtained with CTD surveys. Multiple vertical measurements are averaged to 1m depth intervals on September 22-24**,** 2009; December 7-8, 2009; March 9-11, 2010; and June 16-18, 2010. The locations are displayed in Fig. 2, and are the same for the four surveys.

3.3 Tidal Height

We use tidal range to compare variations of observations with the spring-neap tidal cycle. Our reference tidal range is from tidal height at Newport, RI from NOAA tide gauge 8452660 (Fig. 1). This is the closest tide gauge to our study area. In addition, we use tide gauges located at Newport, RI; Montauk, NY; New London, CT and Woods Hole, MA to estimate sea-surface height gradients over RIS.

Sea level heights were recorded every 6 minutes during this experiment and measured from mean lower low water. Data is available from the start to the end of

Table 1: Deployment periods and depth for stations.

Instrument	Station	Depth (m)	Number of Instruments	Start Date	End Date
ADCP Moored	Block Island North (BIN)	25.7	-	11/10/09	4/2/10
		26.8	-	5/15/10	10/20/10
	Sakonnet River (SAK)	26.3	-	7/14/10	10/5/10
		26.6	-	9/10/11	11/29/11
	Block Island East (BIE)	31.4	-	11/10/09	4/2/10
		30.7	-	5/15/10	10/7/10
	Martha's Vineyard 7 (MV7)	31.9	-	7/14/10	9/28/10
		33.3	-	10/8/10	2/10/11
	Central Rhode Island Sound (CRS)	34.5	-	9/10/11	12/12/11
	Woods Hole Oceanographic Institution Buoy Farm (WBF)	41.1	-	11/10/09	4/2/10
		39.3	-	5/16/10	10/6/10
		41.2	-	10/8/10	2/17/11
		41.2	-	9/10/11	12/12/11
	Cox Ledge Central (CLC)	44.8	-	11/10/09	4/2/10
		45.8	-	5/15/10	10/6/10
		44.8	-	10/8/10	2/17/11
CTD Chains	SAK	-	6	7/14/10	10/5/10
		-	5	9/10/11	11/27/11
	MV7	-	5	7/14/10	10/5/10
		-	5	10/8/10	2/13/11
	CRS	-	6	9/10/11	11/27/11
	CLC	-	6	10/8/10	2/13/11
Thermistors Chains	BIN	-	7	5/15/10	9/27/10
	WBF	-	9	5/16/10	9/27/10
		-	7	9/10/11	12/6/11
	CLC	-	9	5/16/10	9/27/10

our experiment. The tidal range, the difference between high and low tide, varied from 0.7 m to 1.5 m at the tide gauge in Newport, RI.

3.4 Wind Velocity

Wind data was collected at station BUZM3, a NOAA weather station, located in the northeast corner of RIS (Fig. 1). This station records hourly wind speed and direction. This station measures wind 24.8 m above mean sea level. Data is recorded in m s^{-1} and is available from the start to the end of our experiment. Wind velocities were measured from 0 m s^{-1} to over 25 m s^{-1} with an average northeastward component in the summer and a southeastward component in the winter.

4. Results

Analysis of the moored ADCPs, moored hydrographic instruments and underway hydrographic surveys provides information at a variety of temporal and spatial scales in RIS. Due to the sampling rate of our instruments and the multiple year duration of the experiment, we analyze RIS data at time-scales from hours to seasons. The spatial resolution of velocities is limited to the seven locations of the moored instruments. These instruments are 5 to 10 km apart and therefore sample a wide range of environments in and around RIS. The hydrographic surveys provide more detailed observations of hydrography between the moored stations but limited temporal evolution. Below we discuss in detail our observations.

4.1 Tidal Circulation

Temporal and spatial variations within RIS, are first analyzed with a spectral analysis of the velocity time series data to determine the most prominent frequencies of interest. Data was linearly detrended and we use the Welch method, utilizing the

Fast Fourier transforms of the auto-correlated time series, to create a power spectrum (Emery and Thomson, 2001). Overlap of the time series is set at 50% to reduce variance. Gaps in the data are filled with station averages (Emery and Thomson, 2001). It is important to note that padding the data may bias some of the high frequency signal close to the sampling frequency. We produce power spectra of our depth-averaged velocities and depth-averaged shear (Fig. 4 & 5).

Strong power spectral density peaks are observed for depth-averaged flow in the diurnal (1 cpd), M2 (1.93224 cpd) and M4 (3.86448 cpd) frequencies at all stations (Fig. 4). We separate depth-averaged spectral analysis into along- and across-shore directions. Similar magnitudes in power spectra are observed between stations and in each direction. Station BIN has the highest power spectrum and station SAK has the lowest.

In addition to depth-averaged velocities, we also explore depth-averaged shear. Depth-averaged shear is calculated by differencing the near-surface and near-bottom velocities and dividing by the separation distance of the two measurements. Power spectral density analysis of depth-averaged shear flow indicates strong peaks at the M2 and diurnal frequency (Fig. **5**). This is true for both the along and across-shore directions. The M2 has the strongest peak at all stations. Some stations such as BIN, WBF, and MV7 have peaks at the M4 tidal frequency, but this is not consistent across all stations.

In addition to spectral analysis described above, we utilize the MATLAB toolbox *t_tide* to quantify the tidal components in our velocity measurements (Pawlowicz et al., 2002). *T_tide* provides estimates of the significant tidal

constituents, the amplitude of the major and minor axis of the tidal ellipse, inclination and phase. The tidal ellipse is a way to describe the current vector for tidal velocities, with the current vector tip tracing out the path of the ellipse. Inclination and phase describe how and where the vector rotates around the ellipse. Specifically, the inclination is the direction of the semi-major axis and is measured counterclockwise from due east. Phase is the orientation of the vector relative to a specific time (Pawlowicz et al., 2002).

Depth-averaged analysis of tidal constituents shows the M2, the principal lunar semidiurnal constituent, is the largest constituent by a factor of 4 for all stations. Results are listed in Table 2. M2 tidal ellipses are primarily oriented perpendicular to the shelf break, except for station BIN (Fig. 6). Magnitude of the major axis primarily increases as the depth of the stations decreases. Consistent with the theory that momentum must be conserved as the tidal wave approaches shore. The second two largest semidiurnal frequencies are the N2 and S2, the larger lunar elliptic and principal solar semidiurnal constituents, respectively. These constituents have comparable magnitudes to one another at each station (Table 2**).** The two largest diurnal frequencies are the K1 and O1, both lunar diurnal constituents. The major axis of these diurnal frequencies is primarily oriented parallel to isobaths and the shoreline (Fig. 7). Our observations support the analysis of He and Wilkin (2006) who modeled the barotropic amplitude of tidal constituents and found that the semi-diurnal constituents dominate this area over diurnal frequencies.

Table 2: Tidal constituents for depth-averaged velocities at moored stations. Largest four constituents are listed.

Constituents	**Major ($m\ s^{-1}$)**	**Minor ($m\ s^{-1}$)**	**Inc (deg)**	**Phase (deg)**	**Constituents**	**Major ($m\ s^{-1}$)**	**Minor ($m\ s^{-1}$)**	**Inc (deg)**	**Phase (deg)**
BIN					SAK				
M2	0.39	-0.02	9	207	M2	0.08	-0.03	115	303
N2	0.09	0.00	10	192	N2	0.02	-0.01	98	283
S2	0.07	0.00	7	236	S2	0.01	0.00	109	301
K1	0.04	0.00	14	261	M4	0.01	0.00	78	302
BIE					MV7				
M2	0.16	-0.04	126	2	M2	0.16	-0.09	83	339
N2	0.04	-0.01	122	339	N2	0.04	-0.02	84	309
S2	0.03	0.00	129	27	K1	0.03	-0.01	87	56
K1	0.02	-0.02	59	169	S2	0.03	-0.01	91	341
CRS					WBF				
M2	0.09	-0.02	124	323	M2	0.10	-0.06	117	311
N2	0.02	0.00	113	303	N2	0.03	0.02	99	300
K1	0.02	-0.01	17	223	K1	0.02	0.01	154	26
S2	0.02	0.00	118	329	S2	0.02	-0.01	116	330
CLC									
M2	0.08	-0.03	115	337					
K1	0.02	-0.01	11	199					
N2	0.02	-0.01	104	308					
O1	0.01	0.00	33	144					

Applying *t_tide* to individual depths reveals the depth dependence of tidal ellipses. To explore velocity variation with depth, we divide the water column at each station into three levels. The top level uses the closest measurement available to the surface, usually around 5 m below the surface. The middle level uses measurements closest to the midpoint between the surface and the sea floor. The bottom level uses measurements closest to the sea floor, usually 2 m above the bottom. The top and middle measurements agree well in both magnitude and orientation and therefore we only plot the top and bottom measurements (Fig. 7). Bottom ellipses tend to be about 10 % smaller in magnitude and more circular than the overlying layers. The reduction in tidal amplitudes is indicative of bottom friction (e.g. Edwards and Seim, 2008). The bottom layer is also dissimilar in that the phase marker for the largest tidal component, the M2, (Fig. 7) is rotated relative to the overlying layers. All stations except BIN and BIE have bottom tidal ellipse phases that are rotated clockwise from the surface phase. This indicates the bottom layer velocities slightly precede the overlying layer velocities, as the rotation at these stations is clockwise.

4.2 Residual Circulation

Depth- and deployment-averaged horizontal velocities are largest closest to shore. Deployment-averaged moored ADCPs provide a mean current field for RIS (Fig. 8). Central stations of CLC, CRS, SAK and WBF have residual velocities on the order of 1 cm s^{-1}, that are within the corresponding variance ellipses. Stronger flow was measured closer to shore on the order of 5 cm s^{-1} at stations BIN, BIE and MV7, primarily parallel to the local shoreline (Fig. 8).

Inflow into RIS, comes in around the east, near Martha's Vineyard as indicated by deployment-averaged velocities at station MV7 (Fig. 8). Outflow appears to be divergent around Block Island leaving RIS to the west, north of Block Island (BIN) and exiting to the southwest on the southeastern side of Block Island (BIE) (Fig. 8). Station BIN displays outflow from RIS into Block Island Sound, counter to observations of surface High-Frequency Radar measurements (Ullman and Codiga, 2004), suggesting complex depth-dependent flow. The northern end of Block Island creates a sharp bathymetric point that likely causes the generation of two headland eddies. It is likely that the flow measured at this station is the result of a headland eddy as seen in model results by Sun et al. (2016).

We plot depth-averaged velocities filtered with a 33-hour low-pass filter for all four deployments to explore shorter time variations (Fig. 9-12). The strongest depth-average velocities are observed around Block Island at stations BIE and BIN. Two major time-scale variations are apparent from the residual velocities (Fig. 9-12). One is that there is a lot of variation across all stations at synoptic time-scales. However, velocities at stations are not necessarily coherent or in the same direction as the wind measured at BUZM3 during our experiment (Fig. 9-12). The second time-scale is on the order of months, indicated by an intensification of velocity magnitudes at several stations during different seasons. For example, during deployment 2 (Fig. 10), throughout summer months, the velocities at stations BIN and BIE are qualitatively larger than velocities measured at the same stations during the 1st deployment (Fig. 9), i.e. during winter months**.**

Subtidal velocities are variable across stations. We quantify of how coherent the subtidal circulation is across RIS with correlation coefficients of the complex depth-averaged velocities. The complex depth-averaged velocity vectors lead to a complex correlation coefficient. The magnitude (Fig. 13a) is used to quantify the linear similarity of the two-time series. An angle (Fig. 13b) is calculated from the resulting complex value, representing the rotation of one station relative to another.

For all correlations we consider a method that utilizes effective degrees of freedom to determine statistical significance (Fig. 13c) described by MacKenzie and Schiedek (2007). Using the Student's t-distribution we determine if our correlation is significant. If the computed t-value based on the correlation coefficient (C) is greater than a critical value of a Student's t-distribution for a probability of 95% with a specific effective degrees of freedom (n), than the correlation is considered significant (Hald, 1976):

$$t_{val} = C\frac{\sqrt{n}}{\sqrt{1-C^2}} > t_{crit}(95\%, n) \quad (1)$$

Effective degrees of freedom are based on the autocorrelation of the time series of interest and accounts for the fact that filtering data reduces independence of samples.

Although, many of the correlations are significant between stations, (Fig. 13c) we find stations MV7 and SAK have limited significant correlations. MV7 is not significantly correlated with any station and SAK is not significantly correlated with stations BIE and BIN, around Block Island. In addition, correlation coefficients are relatively low. Only correlations between stations WBF and CLC are greater than 0.6 (Fig. 13a). Low and insignificant correlations between stations, suggests smaller scale forcing is important to circulation over our stations at synoptic time-scales. We

explore longer time periods, starting with seasonal averages, in hopes of finding larger scale patterns consistent over all stations.

Seasonal averages indicate stronger flow along the periphery of RIS during summer. We divide data into two major time intervals (Fig. 14). Periods during well-mixed hydrography in RIS and periods during stratified hydrography with a well-developed pycnocline. During the end of fall and throughout winter, measured during November through April, RIS is well-mixed. Throughout spring and summer, May through October, RIS is usually stratified. We find the largest depth-averaged velocities in shallow water during the well-mixed season. Stations BIN, BIE and MV7 have average velocities around 5 cm s^{-1} (Fig. 14). These velocities are larger than the standard deviation of the depth-averaged flow for these stations. Station MV7's and BIE's average velocities suggest a cyclonic flow, parallel to isobaths, around RIS that is persistent during the well-mixed season. Central stations of CLC and WBF have smaller seasonal averages (~ 1 cm s^{-1}). The variance of these stations suggests no significant net flow during the well-mixed season as the variability is larger than the mean (Fig. 14). The largest feature in the flow pattern is the increase in cyclonic magnitude at periphery stations compared to central stations.

Depth-average velocities during stratified periods (May-October) show similar velocity averages to well-mixed seasons. However, periphery stations of BIN, BIE and MV7 have a greater magnitude by at least 3 cm s^{-1} during the stratified season (~8 cm s^{-1}). Central stations of CLC and WBF do not show meaningful changes from well-mixed averages with magnitudes reaching ~2 cm s^{-1}.

Mean monthly depth-averaged flow indicates a persistent negative circulation in the along-shore direction at all stations (Fig. 15b &e). Along-shore flow is maximized during June and July of 2010 and minimized during November and December for most stations (Fig. 15b & e). We discuss the possible mechanisms for the along-shore flow in section 5.

4.3 Regional Hydrography

The four CTD surveys made during the experiment illustrate the seasonal changes in density and stratification in RIS. Depth-averaged density increases from north to south during all four deployments, mostly a function of the increasing depth (Fig. 16). In addition to the latitudinal trend in average densities, there is also a low-density anomaly to the west of Block Island in Block Island Sound, the result of freshwater input from the Connecticut river. Largest densities are recorded during the March 2010 deployment on the order of 25.5 kg m^{-3}. Lightest densities are recorded during the September 2009 deployment, approximately 22 kg m^{-3} (Fig. 16).

Cross-sections of the CTD surveys indicate a dense central bottom pool present throughout the year (Fig. 17). The eastern side of RIS is less dense than central RIS measurements. As a result, isopycnals intersect bathymetry on the eastern side of RIS. Isopycnals dip toward bathymetry on the western side of RIS as well, but not as strongly. The structure of the isopycnals creates a central bottom dense pool, most well defined during the June 2010 deployment (Fig. 17e).

Temperature and salinity measurements from CTD deployments indicate that density distribution is dependent on both properties. During the September, December and March surveys, temperature is fairly homogenous (Fig. 18a, b, c), indicating that

salinity is controlling the density differences observed. In December 2009, interestingly the survey measures a warm salty bottom (Fig. 19b), with a temperature inversion (Fig. 18b). Ullman et al. (2014) have documented the temperature inversion in this area as a warm salty intrusion from the shelf break. The survey in June 2010 indicates a spatial salinity gradient (Fig. 19d) that coincides with spatial temperature gradients (Fig. 18 d), creating the largest spatial density gradients. Strongest density differences both vertically and horizontally are measured during this survey.

We quantify the vertical distribution of density with stratification measurements. Stratification can be measured as a potential energy anomaly (ϕ) of a given water column. Simpson and Bowers (1981) describe potential energy anomalies as the amount of work required to completely mix the water column:

$$\phi = \frac{1}{H}\int_{-H}^{0}(\bar{\rho} - \rho)gzdz, \quad \bar{\rho} = \frac{1}{H}\int_{-H}^{0}\rho dz \tag{2}$$

where H is the water depth, ρ is the density, g is 9.8 m s^{-2} and z is depth below sea level. When CTD data are available we can directly estimate the density at various depths and calculate ϕ.

Stratification increases from north to south, similar in trend to the density measurements (Fig. 16). A local maximum occurs in the trough that runs nearly northeast to southwest in central RIS in September 2009 and June 2010. A local maximum is also observed west of Block Island in March 2010, the result of freshwater input from the Connecticut river, similar in position to the density anomaly in March. Strongest stratification is measured during the June 2010 deployment over 120 J m^{-3} (Fig. 16). Stratification is minimized and close to zero across RIS during the December 2009 and March 2010 CTD deployments (Fig. 16).

We further explore temporal changes in hydrography with monthly averages of density, temperature, salinity and potential energy anomalies at moored stations (Fig. **20).** A clear seasonal cycle is observed over the four variables measured, however, the phase among the variables differs. Density and salinity are maximized during winter (Jan-Mar) and fall (Oct-Dec) months respectively (Fig. 20a & c). Values for density and salinity are minimized during late spring (June) and summer (July-Sept). Salinity variations between stations are much greater (> 1 psu) for CTD surveys (marked with *) when compared with moored CTD sites (Fig. 20). The surveys have been interpolated to the moored station location for consistency, except for station MV7, which is outside the survey area.

Temperature and potential energy anomalies are out of phase with density measurements (Fig. 20b & d). Both variables are maximized during late spring and summer. Minimum values occur during winter (Jan-Mar) for temperature and late fall (Nov-Dec) for potential energy anomalies. Unlike the other 3 variables, measured at moored stations, the timing of temperature maximums varies between stations. Deeper central stations of WBF and CLC are maximized during September 2010, while the rest of the stations, in shallower water, are maximized during August 2010. Large variations between stations are also observed in the potential energy anomaly measurements. We find that for the moored CTDs monthly averages approach zero in the fall and winter of 2010, indicating a well-mixed state. We discuss the potential effects of stratification development on the depth-averaged momentum balance in section 5.

4.4 Wind and Freshwater Influences

Before the discussion of the depth-averaged momentum balance in section 4.5, we explore two regional environmental parameters that impact the momentum balance. Winds and freshwater can directly influence the inner shelf dynamics through wind stress, sea-surface setup and baroclinic effects. We describe the first order trends of monthly averages of wind and river runoff during our experiment.

The seasonal cycle of monthly mean wind has peak magnitudes during November through January (Fig. 21) of 10 m s^{-1} measured at BUZM3. Summer magnitudes decrease to around 5 m s^{-1}. Primarily the eastward component of the wind measured in RIS is always positive, increasing in magnitude during late fall and early winter months. The northward component of the wind is negative during fall and winter months and positive during summer months. Therefore, wind blows to the southeast during winter and to the northeast during summer. The later part of 2011, during the fall, shows some deviation from the general seasonal pattern with a smaller magnitude northward component (Fig. 21).

The seasonal cycle, in monthly mean freshwater river inputs into RIS, can be qualitatively viewed from the transport of two major rivers in the area. Transport of water masses comes into RIS from Long Island Sound, Narragansett Bay, Buzzards Bay and Vineyard Sound. The largest transport, by a factor of 10, is the transport from Long Island Sound followed by Narragansett Bay (Codiga and Ullman, 2010). We use the Connecticut river, the major source of freshwater into Long Island Sound and the Blackstone river, a major source for Narragansett Bay to illustrate the seasonal variation in freshwater input into RIS (Fig. 22). River transport into Buzzards Bay and Vineyard Sound is tiny and therefore not highlighted in this study.

Both the Blackstone and the Connecticut rivers have a peak in river discharge during February and March (Fig. 22). Although, the Blackstone is the largest of several tributaries into Narragansett Bay, the magnitude is much smaller than the Connecticut river. The size discrepancy illustrates that freshwater influence of Narragansett Bay is of secondary importance compared to freshwater coming into RIS from Long Island Sound. Similar to Long Island Sound and Narragansett Bay, the freshwater input into RIS likely increases during spring. Studies of Long Island Sound suggest that much of the freshwater exits Long Island Sound in-between Block Island and Montauk Point, not entering RIS (Edwards, 2004). Therefore, we do not expect freshwater plumes to play the largest role in governing circulation through the entire RIS.

4.5 Depth-averaged Momentum Balance

The monthly depth-averaged flow provides insight into what is driving circulation in RIS. The relationship between flow and forcing conditions is observed through analysis of the depth-averaged momentum balance. The resulting momentum balance in each direction is:

$$0 = -\frac{\partial \bar{u}}{\partial t} + f\bar{v} - \frac{\tau_s^x}{\rho_o H} - \frac{\tau_b^x}{\rho_o H} - \langle \overline{U\frac{\partial U}{\partial x} + V\frac{\partial U}{\partial y} + W\frac{\partial U}{\partial z}} \rangle - \frac{1}{\rho_o H}\int_{-H}^{0} \frac{\partial P}{\partial x} dz \qquad (3)$$

$$0 = -\frac{\partial \bar{v}}{\partial t} - f\bar{u} - \frac{\tau_s^y}{\rho_o H} - \frac{\tau_b^y}{\rho_o H} - \langle \overline{U\frac{\partial V}{\partial x} + V\frac{\partial V}{\partial y} + W\frac{\partial V}{\partial z}} \rangle - \frac{1}{\rho_o H}\int_{-H}^{0} \frac{\partial P}{\partial y} dz \qquad (4)$$

where $(\bar{u}, \bar{v})$ are the residual depth-averaged velocities, (U, V) are the tidal velocities, f is the Coriolis parameter, ρ_o is a reference density, P is pressure, H is the depth, (τ_s^x, τ_s^y) are the surface wind stresses, (τ_b^x, τ_b^y) are the bottom friction stresses and $\langle\ \rangle$ denotes averaging over a tidal cycle. The $\hat{x}$ (eq. 3) direction is across-shore and the $\hat{y}$

(eq. 4) direction is along-shore. The first two terms in the above equations are the local acceleration and the Coriolis term. These terms can be estimated directly for the moored ADCP velocity measurements. The next four terms of the eq. 3 & 4 describe the wind stress, bottom stress terms, advective tidal stresses and the pressure gradient respectively (Ullman and Codiga, 2004; Visser et al., 1990). The advective tidal stress describes the momentum exchange from tidal frequencies to subtidal frequencies in areas where tidal ellipses change shape.

Monthly averages of the momentum terms calculated from deployment velocities and wind speed are displayed in Fig. 23. These include the acceleration term, the Coriolis term, wind stress and bottom stress. The magnitude illustrates the terms that are of primary importance in the momentum equation.

4.5.1 Local Acceleration and Coriolis terms

We calculated the local acceleration from a forward difference method of 33-hour low pass filtered velocities. In both the across and along-shore directions, the acceleration term has small magnitudes measured over all stations, relative to other momentum terms.

The Coriolis term, found by multiplying the observed depth-average velocities by the Coriolis parameter, has magnitudes in both eq. 3 and 4 on the order of 5×10^{-6} m s^{-2}. Monthly averages of the Coriolis term indicate there is always a negative across-shore (fv) term measured at all stations. This reveals a cyclonic flow around RIS. The monthly time series shows a maximum magnitude near June and July and a minimum across stations during December and January (Fig. 23). Station BIN does not fit this pattern as well as the other stations. The along-shore monthly-averaged time-series of

eq. 3 shows the Coriolis terms also has a large magnitude but smaller than the across-shore direction. Stations in RIS (BIE, CLC, CRS, MV7, SAK and WBF) have values close to zero while the station north of Block Island (BIN) is positive.

4.5.2 Wind Stress

The wind stress can be estimated using the depth of each station and drag coefficient estimated from the wind speed. The wind stress is calculated using

$$\boldsymbol{\tau_s} = \rho C_d |U_{10}| \boldsymbol{U_{10}}, \tag{5}$$

where $\boldsymbol{U_{10}}$ is the wind vector at 10 m above sea level and ρ is the density of air. We use a drag coefficient as defined by Garratt (1977):

$$C_d = \frac{1}{1000}\left(\frac{3}{4} + \frac{1}{15}|U_{10}|\right) \qquad |U_{10}| < 26.25\ m\ s^{-1} \tag{6}$$

$$C_d = 0.0025 \qquad |U_{10}| \geq 26.25\ m\ s^{-1} \tag{7}$$

Station BUZM3 measures wind at 24.8 m above sea level. We calculate the $\mathbf{U_{10}}$ by using a logarithmic relationship:

$$\boldsymbol{U}(z) = \frac{\sqrt{C_d}\boldsymbol{U_{10}}}{\kappa} \ln\left(\frac{z}{z_0}\right), \tag{8}$$

where $\boldsymbol{U}(\boldsymbol{z})$ is the wind velocity vector measured at height z, κ is the Von Karman constant and z_0 is the surface roughness length scale. To calculate the wind stress, we start with an initial guess in eq. 6 to calculate C_d, found from approximating U_{10} with U_{25}. We calculate z_0 at 10 m height, where $z_0 = (10m)/e^{\kappa/\sqrt{C_d}}$, found from rearranging eq. 8. Next, we solve for a new $\mathbf{U_{10}}$ by dividing eq. 8 solved at z = 10 m, by eq. 8 solved at z = 25 m, providing the relationship between **U**(10 m) and **U**(25 m):

$$\boldsymbol{U}(10\ m) = \boldsymbol{U}(25\ m)\frac{\ln\left(\frac{10m}{z_0}\right)}{\ln\left(\frac{25m}{z_0}\right)} \tag{9}$$

Finally, we update C_d with the new U_{10} velocity. We iterate this process until a solution for U_{10} and C_d converge, and changes are less than 0.01 %, usually 5 iterations. The wind stress is calculated instantaneously and averaged over a month.

The wind stress terms have small magnitudes, less than 1 x 10^{-6} m s^{-2} (Fig. 23), when averaged over a month. This is true for both the along- and across-shore directions. Magnitudes do increase during winter months when wind speed is largest. However, the wind stress is not large enough to balance the observed Coriolis term at any station over monthly time-scales.

4.5.3 Bottom Stress

The bottom stress is highly uncertain due to poorly estimated drag coefficients. We, therefore, use two estimates to calculate bottom friction and provide a range of possible estimates. First, we use a quadratic bottom stress, defined as:

$$\boldsymbol{\tau_b} = \rho_o C_d |u_b| \boldsymbol{u_b}, \tag{10}$$

where $\boldsymbol{u_b}$ is a near bottom velocity vector. Bottom velocities are approximated with the deepest measurements recorded at our ADCPs. C_d is set to 2.5 x 10^{-3}, a commonly used value along the continental shelf (e.g., Hofmeister et al., 2009; Lund-Hansen et al., 1996; Edwards, 2004; Pu et al., 2015; Simpson et al., 1981; Sylaios et al., 2013).

The second method we use is the linear drag bottom stress, defined as:

$$\boldsymbol{\tau_b} = \rho_o r \overline{\boldsymbol{u}}, \tag{11}$$

where $\overline{\boldsymbol{u}}$ is the depth-averaged velocity and we use a value of 4 x 10^{-4} m s^{-1} for r, similar to Liu and Weisberg (2005). Both methods calculate bottom stress instantaneously and values are averaged monthly.

Monthly-averaged bottom stress term in eq. 3 &4 is small on the order of 1 x 10^{-6} m s^{-2} for most stations, around the same order of magnitude as the wind stress. The one exception to this is station BIN. This station has positive bottom stress on the order of 2 x 10^{-6} m s^{-2} throughout the year in both the across- and along-shore directions. In Fig. 23, we only display the quadratic estimate of bottom stress as there was little difference between the quadratic and linear bottom stress estimates.

4.5.4 Advective Tidal Stress

We use the Regional Ocean Modeling System (ROMS) to estimate advective tidal stress. Commonly used for estuarine and coastal ocean processes, ROMS is a free-surface, terrain-following, primitive equation ocean model. Our ROMS domain includes Narragansett Bay and extends south to 41° N (Fig. 24). The eastern boundary cuts across Buzzards Bay and Martha's Vineyard Sound. The western boundary extends into Block Island Sound, terminating at the northern end of Long Island.

The grid consists of 750 by 900 nodes with 15 vertical terrain-following levels. Resolution is maximized in Narragansett Bay around 40 meters in each the ξ and η directions. The grid cells become larger in the southern part of the grid in RIS, around 150 m in each direction. Bathymetry data was obtained from the Coastal Relief Model and NOS Hydrographic Survey of Narragansett Bay from the National Oceanic and Atmospheric Administration's Geophysical Data Center. Bathymetry data sets had a resolution of 30 m within the bay and increased to 90 m outside of the bay.

Specific parameters important for mixing of momentum were specified as follows. We choose to use the Mellor Yamada Level 2.5 mixing scheme with vertical minimum mixing coefficients held at 10^{-7} m^2 s^{-1}. Horizontal diffusivity and viscosity

coefficients were set to 10 m^2 s^{-1} and 5 m^2 s^{-1} respectively and we use a logarithmic drag for bottom stress. Bottom roughness (z_o) was set to 0.001 m for the computation of momentum stress. Solving for C_d with a logarithmic approximation:

$$C_d = \frac{k^2}{\ln^2(\frac{z}{z_o})},$$

where k is the von Karman constant, and z is the height of the first node above the ocean bottom. Our numerical experiments produce coefficients averaging 0.0029 within RIS, on the same order of magnitude as the C_d we used in our quadratic approximation of bottom stress.

We use a prescribed tidal constituent, constant rivers to force the model and uniform density. Along the boundaries, we use the M2 tidal constituent obtained from the ADvanced Circulation Model (ADCIRC) of the Atlantic Ocean. The two largest rivers, located in Narragansett Bay, are held constant at yearly averages. The Blackstone and Taunton rivers introduce a flux of 22 m^3 s^{-1} and 14 m^3 s^{-1} respectively. Estimates of river daily discharge were obtained from the United States Geological Survey (USGS).

Our numerical experiment had surface fluxes held to zero, Chapman and Flather boundary conditions for 2-D properties and radiative boundary conditions for 3-D properties. We allow the model to run until it comes to steady state and velocities are not changing from one tidal cycle to the next. Output from the numerical experiment is used to calculate advective tidal stresses at the moored station locations.

The numerical experiment is verified against the measured tidal components at each moored station. Fig. 25 displays the depth-average tidal ellipse at each of the seven moored ADCPs. In general, the ROMS numerical model predicted tidal ellipses

that have a slightly larger eccentricity but the same general magnitude, rotation direction and phase as the ADCP measurements. The one exception is station BIN. At this station, the amplitude predicted by the ROMS model is comparable to observations, but the orientation and phase are off by about 20 degrees (Fig. 25). The rotation at this station is also not well modeled, as ROMS predicts a counterclockwise rotation instead of the observed clockwise rotation. Despite the discrepancy at station BIN, the rest of the stations agree well with observations and we precede to use the model output to estimate the advective tidal stress.

Studies such as Ullman and Codiga (2004) and Visser et al. (1990) have calculated the advective tidal stress using depth-average tidal velocities. We improve upon this estimate by depth-averaging the depth-dependent advective tidal stress:

$$-\langle\overline{U\frac{\partial U}{\partial x}+V\frac{\partial U}{\partial y}+W\frac{\partial U}{\partial z}}\rangle=-\langle\frac{1}{H+\eta}\sum_{i=1}^{15}(U\frac{\Delta U}{\Delta x}+V\frac{\Delta U}{\Delta y}+W\frac{\Delta U}{\Delta z})_i\,\Delta z_i\rangle \quad (12)$$

$$-\langle\overline{U\frac{\partial V}{\partial x}+V\frac{\partial V}{\partial y}+W\frac{\partial V}{\partial z}}\rangle=-\langle\frac{1}{H+\eta}\sum_{i=1}^{15}(U\frac{\Delta V}{\Delta x}+V\frac{\Delta V}{\Delta y}+W\frac{\Delta V}{\Delta z})_i\,\Delta z_i\rangle \quad (13)$$

Tidal velocities are found by subtracting the depth-averaged residual velocity from the instantaneous velocities in our numerical model. Reorientation of the curvilinear grid is preformed first on all components converting ξ, η to east, north directions at each grid cell. Depth-averaged instantaneous calculations of eq. 12 & 13 are then averaged over a M2 tidal cycle. Terms are mapped in Fig. 26. Central RIS had small advective tidal stress magnitudes, less than $|10^{-6}|$ m^2 s^{-1}. Only near the eastern and western sides of RIS and near Block Island, do values of advective tidal stress become substantial (> $|5 \times 10^{-6}|$ m^2 s^{-1}).

The ROMS numerical experiment allows for the calculation of advective tidal stresses at our moored station locations. Although, multiple tidal constituents contribute to tidal velocities in RIS, the model provides a first order estimate of the advective tidal stress, as the M2 is the largest constituent in the region. These estimates are displayed in Fig. 27 and indicate only stations BIN and MV7 have substantial advective tidal stresses contributing to the momentum balance. It is likely the numerical model does not accurately predict the advective tidal stresses present at station BIN, as the tidal ellipse is misaligned and rotates in the opposite direction (Fig. 25).

4.5.5 Advective Tidal Stress Sensitivity

We test the sensitivity of the tidal advective stress calculation by changing z_o to 0.01 m and 0.0001 m. Changing z_o by a factor of 10 to 0.01 m increases the average Cd to 0.0062. We estimate the effect the change in bottom roughness has on the tidal advective stress and quantify it as a percent difference:

$$\Delta T = \overline{\frac{\left|T_x(z_o{=}0.01) - T_x(z_o{=}0.001) + (T_y(z_o{=}0.01) - T_y(z_o{=}0.001)\,)\hat{j}\,\right|}{\left|T_x(z_o{=}0.001) + T_y(z_o{=}0.001)\;\hat{j}\right|}} \times 100\,\%$$

where T_x and T_y are the east and north components of tidal advective stress. The percent difference of the average tidal advective stress is 22%. This value was found by averaging ΔT over a tidal cycle and over the RIS domain.

To determine if the magnitude of the tidal advective stress has decreased or increased we look at the difference in magnitudes between the two experiments. We use a best fit linear regression between the change in magnitude and the original magnitude:

$$\Delta|T| = (\left|T_x(z_o = 0.01) + T_y(z_o = 0.01)\,\hat{j}\right| - \left|T_x(z_o = 0.001) + T_y(z_o = 0.001)\,\hat{j}\right|) \backslash \left|\left|T_x(z_o = 0.001) + T_y(z_o = 0.001)\,\hat{j}\right|\right| \times 100\ \%$$

The change in magnitude of the tidal stress is found to be -19%, over the RIS domain. The negative value indicates the magnitude of the tidal advective stress is smaller for the experiment with $z_o = 0.01\ m$.

Reducing $z_o\ to\ 0.0001\ m$, we find ΔT and $\Delta|T|$ to be 18 % and 13%, respectively. With decreased bottom roughness the tidal advective stress magnitude increases slightly. Therefore, we find that changing the bottom roughness by orders of magnitude from 0.01 to 0.0001 m, changes the tidal advective stress by $\pm$ 20 %.

4.5.6 Pressure Gradient

The last term in the depth-averaged momentum equation changes the momentum balance through the addition or reduction of mass and changes in density distributions. Particularly, pressure gradients can create depth-average momentum force, through changes in volume (steric) or through changes in mass (non-steric). We use the method described by Ullman and Codiga (2004), who separate the pressure gradient into a steric and non-steric contributions, which we will call baroclinic and barotropic respectively:

$$-\frac{1}{\rho_o H}\int_{-H}^{0}\frac{\partial P}{\partial x}dz = \overbrace{-g\frac{\partial \eta_{ns}}{\partial x}}^{barotropic} \overbrace{-\frac{g}{H}\frac{\partial}{\partial x}\int_{-H}^{0}\epsilon z dz + g\frac{\partial}{\partial x}\int_{-H_m}^{-H}\epsilon dz}^{baroclinic} \quad (14)$$

$$-\frac{1}{\rho_o H}\int_{-H}^{0}\frac{\partial P}{\partial y}dz = -g\frac{\partial \eta_{ns}}{\partial y} - \frac{g}{H}\frac{\partial}{\partial y}\int_{-H}^{0}\epsilon z dz + g\frac{\partial}{\partial y}\int_{-H_m}^{-H}\epsilon dz \quad (15)$$

where ϵ is defined as $\rho = \rho_o[1 + \epsilon(x, y, z, t)]$, ρ_o is the maximum density, and H_m is a reference depth. The steric (η_s) and non-steric (η_{ns}) sea-surface heights are defined as:

$$\eta_{ns} = \eta - \eta_s, \qquad \eta_s = -\int_{-H_m}^{0} \epsilon dz. \tag{16}$$

H_m is defined as 52 m, the deepest survey position in our study. The last term in eq. 14 and 15 are found by integrating ϵ along the bottom from the deepest point ($-H_m$) to the bottom of the survey ($-H$) (Csanady, 1979). We use the four hydrographic CTD surveys to estimate the steric contributions of the pressure gradients for the month the survey was taken.

If we assume only a geostrophic balance, we can calculate the depth-mean velocity induced by baroclinic pressure gradients. The results of these calculations are displayed in Fig. 28 for all four CTD surveys assuming no flow normal to the bottom. Two major features are apparent from this analysis. First, there are strong geostrophic currents produced in-between Block Island and Long Island. The predicted velocities are consistently to the southwest and over 10 cm s^{-1} in all four surveys. Second, there is almost always a counter-clockwise generated flow in RIS, which we will call the coastal current. The predicted baroclinic induced coastal current varies in magnitude and position during the four deployments. Baroclinic estimates predict the current to be strongest during the June 2010 survey and almost nonexistent during March 2010 survey (Fig. 28). In September 2010, the coastal current is furthest south, while in the other three surveys the geostrophic coastal current is located closer to the northern shoreline and Block Island.

The baroclinic pressure gradient is interpolated to each moored station to estimate the contribution to the depth-averaged momentum balance. We apply the baroclinic pressure gradients to the months the survey deployments was taken in. In the across-shore direction, we find that most of the estimates of the baroclinic pressure gradients are positive indicating larger densities in deeper water, as the positive $\hat{x}$ direction points down slope at all stations. Average values for the baroclinic contribution over the stations are above 0.5 x 10^{-5} m^2 s^{-1}. There is only one exception to stations having a positive across-shore estimate of baroclinic pressure gradients, with a small negative value (Fig. 27); at station CLC during the December 2009.

In the along-shore direction, the magnitude of the baroclinic terms are centered around zero. The positive gradients reveal that there is dense water up-shelf. For example, station BIN has a large positive gradient (~ 0.5 x 10^{-5} m^2 s^{-1}) indicating denser water on the RIS side of Block Island and less dense water located towards Block Island Sound. This is consistent with freshwater influence entering Block Island Sound from the Connecticut river. Negative gradients indicate there is dense water down-shelf. This is the case for station BIE, which indicates denser water is located closer to the middle shelf and less dense water located closer to the mouth of Narragansett Bay.

The last component of the momentum balance is the barotropic pressure gradient. Estimations were made with tidal height measurements from NOAA tide gauges surrounding our study area: Newport, RI; Montauk, NY; New London, CT and Woods Hole, MA (Fig. 29a). Sea surface height (SSH) relative to NAVD88 was used without correcting for the inverse barometer effect. Collocated with the tide gauges

were atmospheric pressure measurements available from NOAA. There are many gaps longer than several days in the pressure measurements, especially during the summer of 2010. The advantage to not using the inverse barometer correction is that the SSH can be used to find the total sea surface set up and does not limit the amount of SSH data available.

A 4th order Butterworth 33-hour low pass filter was used to remove the tidal signal of the SSH and calculate the difference between stations. The sea surface slope was calculated using a linear least-squares fit to the four tide gauge stations SSH and results are shown in Fig. 29b.

Comparing the monthly averaged SSH gradient across the four tide gauges with wind indicates a similarity between the two data sets (Fig. 30). As wind changes direction from southeastward blowing in winter to northeastward blowing in summer (Fig. 30 b), the SSH gradient changes from increasing heights to the south (positive slope) during winter periods to increasing heights to the north (negative slope) during the summer (Fig. 29b). The change in SSH gradients shows a seasonal variation contemporaneous with wind direction changes across RIS.

The SSH gradient across tide gauges was used to calculate the barotropic gradients at each station. Specifically, the SSH gradient ($\nabla_H \eta$) is the combination of baroclinic and barotropic gradients:

$$\nabla_H \eta_{ns} = \nabla_H \eta - \nabla_H \eta_s$$

where ∇_H is the horizontal gradient. $\nabla_H \eta_s$ is calculated using spatial distribution of η_s found from the CTD surveys. Due to the fact that we only have a relative η_s we subtract the averages from both η and η_s to find the relative η_{ns} shown in Fig. 31.

In December 2009, when the average wind direction is to the southeast, sea-surface highs are to the south. When monthly average wind magnitudes are small (September, 2009 and March 2010) as well as when winds are to the northeast (June 2010), sea-surface highs are more along the eastern side of RIS. The resulting barotropic gradient is displayed for each moored ADCP station and rotated into the along- and across-shore directions in Fig. 27 e&f.

The barotropic term in the across-shore direction is negative with magnitude comparable to the baroclinic across-shore term (Fig. 27 c & e). Barotropic magnitudes are strongest in winter, indicative of SSH increasing offshore at the moored stations. Barotropic averages over all stations for September 2009 and December 2009 are around -0.5×10^{-5} m s^{-2} (Fig. 27 e). Weaker barotropic gradients are observed during March and June 2010 but still increase SSH offshore. Barotropic averages over stations are around -0.25×10^{-2} m s^{-2} during these stratified months (Fig. 27 e).

The along-shore barotropic term was observed to be both positive and negative across stations. Magnitudes ranged from -1.2 to 1.2 x 10^{-5} m s^{-2} across all stations (Fig. 27 f). Spatial distribution of the barotropic term (Fig. 31), show a persistent SSH low to the west of Block Island.

Residuals of the momentum equation provides some indication of error of our estimates. Residuals in the across-shore direction are the summation of eq. 3. The residuals of the across-shore momentum equation have negative values with magnitudes as large as the Coriolis, baroclinic and barotropic terms (Fig. 27). It is likely that the barotropic term is over estimated. We have approximated a linear sea-surface setup created by wind. Most likely the SSH gradient has steeper slopes closest

to land. It is likely we have overestimated the barotropic contribution at each station, as our stations are in deeper water far from the shoreline.

In the along-shore directions residual estimations have the same order of magnitude as other terms in eq. 4. However, there are both positive and negative residuals, unlike the across-shore residuals estimates (Fig. 27 h). It should be noted that residuals in the along-shore direction all have the same sign as the barotropic estimates, except BIN. This again is consistent with the barotropic term being over estimated.

5. Discussion

The coastal boundary causes a restriction in cross-shelf flow and forces subtidal, depth-averaged flows to be stronger in the along-shore direction (Lentz and Fewings, 2012). The sloping bathymetry as well as the geographic shape governs how and where circulation can occur. We discuss the impacts the three-dimensional shape of RIS has on circulation, in the following sections.

5.1 Tidal Rectification

Bathymetry directly influences the depth-averaged dynamics through tidal rectification. In order for tidal rectification to occur, the tidal excursions must be on the same order of magnitude as the bathymetric features. Tidal excursion is the total distance a parcel of water travels from flood to ebb tide. The distance captures the horizontal Lagrangian motion (Parsa and Shahidi, 2010). Tidal rectification studies characterize the topographic length scale as $(\frac{h}{\frac{dh}{dx}})$, where h is the water depth and $\frac{dh}{dx}$ is the slope of the bathymetry (Wright and Loder, 1985; Loder, 1980).

We calculate the tidal excursion with the M2, the largest constituent across RIS. Defined here as $l=2V/\omega$, where V is the amplitude of the M2 major axis of the depth-averaged tidal velocity and ω is the M2 angular frequency. This results in excursions ranging from 1.1 km at SAK up to 5.5 km at BIN (Table **3)**. The average excursion over the 7 stations is 2 km, slightly smaller than the tidal excursions of Narragansett Bay (Bergondo et al., 2005).

Table 3: Tidal excursion estimates for the M2 tidal component calculated from depth-average velocities.

Station	**M2 major (m/s)**	**Tidal excursion (km)**
BIN	0.39	5.5
SAK	0.08	1.1
BIE	0.16	2.2
MV7	0.16	2.3
CRS	0.09	1.2
WBF	0.11	1.5
CLC	0.08	1.2

We calculate the topographic length scale near our moored stations by using the depth and local slope. The local slope is found by finding the change in height over 1 km in the across isobath direction, centered at the station of interest (Table 4). Our estimates of topographic length scale suggest that only near station BIN, where the tidal excursion (5 km) is large, would tidal rectification play a role in driving residual flow (Table 3 & 4). We also suspect possible influences near station MV7 where the tidal excursion is only a factor of 5 smaller than the topographic length scale. Due to the shape of RIS, with the bathymetric slope increasing into shallower water, it is very likely that tidal rectification is important shoreward of our stations.

Table 4: Topographic slope and length scale calculated from the depth of stations and bathymetric slope.

Station	**dh/dx (m/km)**	**Topographic length scale (km)**
BIN	4.1	6
SAK	1.2	22
BIE	1.7	18
MV7	2.8	11
CRS	2.1	16
WBF	0.9	45
CLC	4.2	11

Liu (2015) modeled the effects of tidal rectification in RIS also using ROMS and only the M2 tides. They found a persistent tidally rectified flow over most of RIS with stronger velocities towards the shore. Compared with our ROMS experiment, both Liu (2015) and our model predict tidal rectification generates a cyclonic flow on the order of 1 cm s^{-1}, with higher velocities measured in shallower waters, as well as a clockwise flow around Block Island (Fig. 32). Predictions of tidally induced flow from our numerical model should be taken with caution as the boundaries of our model are close to the domain of interest. However, the fact that our ROMS results are similar to Liu (2015), provides confidence that our estimates are reasonable.

Our model deviates from Liu (2015) in that our coastal current is narrower on the order of 5-10 km wide instead of around 20 km. This agrees with our analysis of tidal excurison and topographic length scale, which suggests only BIN and MV7 should be influenced by tidal rectification. We predict stronger residual flow on the order of 1-2 cm s^{-1} at the mouth of Narragansett Bay, not present in the Liu (2015) model (Fig. 32). In addition, our model predicts two headland eddies north of Block

Island and a horizontal detachment of the coastal current from the eastern side of Block Island also found by Sun et al., (2016). The differences between our and Liu (2015) ROMS models are thought to be a result of resolution, since tidal rectification is strongly dependent on the bathymetric gradients. Liu (2015) has a grid resolution of 800 m, close to the tidal excursion length, and ours is around 100 m.

Our ROMS numerical model experiment illustrates the largest advective tidal stress occurs around the periphery of RIS (Fig. 26) within 5 km of the shoreline. In RIS, advective tidal stresses create cyclonic flow adjacent to shoreline. Our numerical modeling suggests only stations BIN and MV7 has advective tidal stresses of O (1 x 10^{-5}) m^2 s^{-1} and O($1x10^{-6}$) m^2 s^{-1}, respectively. The rest of the stations' estimates are very small (Fig. 27).

5.2 Pressure Gradients

Bathymetry also affects pressure gradients through mixing. With increased velocities and decreased water depths, more mixing can occur. Mixing specifically effects baroclinic gradients by changing the horizontal density gradients. Therefore, mixing influences the pressure gradients in the momentum term. Often the boundary of the tidal mixing front is defined with the Simpson-Hunter criterion (h/U^3). The water depth (h) and the tidal velocities (U) are used define the position of tidal mixing fronts and the degree of mixing in shallow coastal waters (Simpson and Hunter, 1974). Liu (2015) estimated this parameter and did not expect a tidal mixing front to be extended to the surface in RIS. Their numerical analysis however, did reveal a bottom thermal front.

5.2.1 Presence and Modification of the Bottom Thermal Front

Bottom thermal fronts in RIS have been modeled to estimate the influence of buoyancy driven flow in RIS driven by mixing due to the M2 tidal constituent. Liu (2015) found that a bottom central cold pool creates a bottom thermal front that enhances the cyclonic flow around RIS. Their numerical model suggests that the resulting rectified flow could be almost doubled in the warmer months. Observational studies such as Shonting and Cook (1970) as well as our observations, have documented that there is in fact a bottom cold pool in the spring and summer in RIS.

RIS is subject to not only the M2 but other tidal constituents that create variable tidal mixing over fortnightly periods. The fortnightly intensification of tidal mixing fronts has been theorized (Dong et al., 2015; Sharples, 2007) but few studies have documented this phenomenon. We look for direct evidence for the enhancement of the coastal current due to either tidal rectification or tidal mixing within our dataset.

Over many tidal periods, we expect tidal rectified flow to have a spring-neap cycle as the M2 is not the only tidal constituent present in RIS. To test this variation, we quantify the correlation of the along and across-shore velocities with tidal range measured at Newport, RI. Particularly, we expect the along-isobath at BIN and MV7 flow to be correlated with the spring-neap cycle as tidal.

We use a 7 day to 3-month bandpass to filter the tidal range and depth-averaged velocities to identify the spring-neap signal. Filtering aids in the removal of the semidiurnal and diurnal tidal frequencies as well as synoptic (3-5 days) and seasonal (yearly) variations. Frequency analysis does not produce peaks at the fortnightly time-scale of interest because it is a result of the linear combination of

multiple frequencies. We rely on cross correlations to highlight the fortnightly relationship.

Correlations are performed by using the MATLAB function *xcorr*. Significance is determined with a Student's t-distribution, comparing a calculated t-value (eq. 1) with a critical value found by using the effective degrees of freedom and a 95% confidence level.

For this correlation analysis, we use all depth-averaged velocity data available from November 2009 to December 2011. All but the two deepest stations (WBF and CLC) have significant correlations with tidal range in the along-shore direction (Table **5**). Stations SAK, BIE, MV7 and CRS all have negative correlations, indicating an increase in cyclonic flow in the negative $\hat{y}$ direction, during spring tides. For these stations, we found that our numerical estimates of the advective tidal stress are small. Therefore, the correlation is hypothesized to be a result of baroclinic pressure gradients changing as tidal mixing increases during spring tides.

Table 5: Correlation coefficients and lag between tidal range measured at Newport, RI and velocity measurements. Velocity measurements are broken up into along and across-shore depth-average velocities and velocity shear. Data is used from all available periods and bandpass filtered from 7 days to 3 months. Significant correlations marked with * and lag (days) of velocity behind tidal range is indicated in parenthesis.

	Depth-averaged Velocity		**Depth-averaged Shear**	
Station	Across	Along	Across	Along
BIN	0.43* (0)	0.33* (2.1)	0.13 (0)	0.01 (0)
SAK	-0.15 (0)	-0.37* (5.1)	0.08 (0)	0.15 (0)
BIE	0.01 (0)	-0.56* (0.6)	0.16 (0)	0.19 (0)
MV7	-0.06 (0)	-0.35* (0)	0.05 (0)	0.06 (0)
CRS	0.40* (1.5)	-0.54* (4.2)	0.30 (0)	0.06 (0)

WBF	0.02 (0)	-0.06 (0)	0.02 (0)	0.07 (0)
CLC	-0.17 (0)	0.02 (0)	0.13 (0)	-0.01 (0)

Station BIN has depth-averaged along- and across-shore velocities, positively correlated with tidal range, resulting from onshore flow being minimized during spring tide and maximized during neap tide. As BIN is likely located in an area influenced by a headland eddy, we did not necessarily predict a negative correlation with spring neap tidal cycle. It is unclear if this change in velocity is consistent with a headland eddy as we would expect velocity to increase during spring tide. However, if migration of the eddy occurs as tidal velocities increase, there could be a reduction of velocity over the station as the eddy moves further offshore. This station has large advective tidal stress ($|1|x10^{-5}$ ms^{-2}) and the change in velocities is likely a combination of tidal rectification and tidal mixing.

The increase in tidal velocities creates more mixing in shallow areas and we look for evidence of this in our hydrographic data. The horizontal resolution of hydrographic measurements is limited in our study and we therefore, look for temporal changes at moored stations. We use the moored hydrographic measurements collocated at the ADCP to examine fortnightly trends and potential mixing. Three days after spring tide, local minimums in potential energy anomalies (eq. 2) are observed at BIN, WBF, SAK and MV7 (Fig. 33d). This is a reduction of stratification after the spring tide.

Concurrently examining bottom temperatures recorded at the ADCPs illustrates an increase in bottom temperature at stations ranging from 1 to 5 ^{o}C. The

reduction of stratification along with the increase in bottom temperatures are consistent with increased mixing in the bottom boundary layer (Fig. **33e)**. The tidal velocities increase turbulent mixing, entraining warmer water into the bottom boundary layer. Bottom velocities vary in direction and are not consistently up or down-shelf during spring tides, supporting the idea that advection is not a large contribution to the periodic stratification change at fortnightly scales.

Variations in the strength of mixing, allows us to hypothesize the coastal current depth-average velocities are affected by the change in horizontal density gradients. Consequently, as mixing increases, gradients along the mixing front become steeper, increasing the geostrophic velocities. Observations of fortnightly changes of stratification and bottom temperature are consistent with bottom mixing increasing during spring tides. Further observations are required to characterize whether the thermal font moves into deeper water, becomes narrower or some combination of the two processes, resulting in the increased tidal velocities.

Non-significant correlations between depth-averaged velocities and tidal range at stations WBF and CLC are the result of the position of the stations. These stations are not directly under a strong tidally rectified current or near the bottom thermal front. We find no significant correlation with depth-averaged shear and tidal range at any station.

Unlike Liu (2015), we have found through observations of the coastal current and hydrographic measurements, that the baroclinic effect of a central cold pool does not completely balance the Coriolis term. Evidence from nearby studies of Ullman and Codiga (2004) and Fewings and Lentz (2010) support our hypothesis that first order

effects of wind generated sea-surface setup is important for flow in the along-shore direction.

5.2.2 Wind Driven Sea-Surface Setup

Nearby studies of depth-averaged momentum have documented along-shore flow created by wind generated sea-surface setup, as well as baroclinic gradients. To the west of our study area, at the outflow of Long Island Sound, a coastal jet was found to be primarily in geostrophic balance with an across-shore pressure gradient (Ullman and Codiga, 2004). They define the coastal jet as a strong persistent circulation located close to shore. This pressure gradient, which was intensified during summer months, resulted from buoyancy driven flow. During winter months, the coastal jet was reduced as a result of sea-surface setup by upwelling-favorable winds, i.e. the surface tilt created a pressure gradient that opposed the jet flow.

East of our study area, off the southern coast of Martha's Vineyard, a similar depth-averaged momentum balance was performed by Fewings and Lentz (2010). These authors found local wind generated sea-surface tilting was an important mechanism along the inner shelf. Upwelling winds in this area, hindered the along-shore westward flow and downing-welling winds enhanced the along-shore westward flow. It is likely, given the influence of pressure gradients in nearby areas, that both buoyancy and sea-surface tilt play an important role in governing circulation in RIS.

We explore the effect of wind generated sea-surface setup by quantifying the correlation between wind and velocity. All available data, both depth-averaged velocities and depth-averaged shear measurements, is bandpass filtered at 33-hours to 3 months, exploring the synoptic timescale to compare to wind. At each station, for

both the across- and along-shore directions, we calculate the correlation coefficient and lag time for 5^{o} increments in wind directions. In Table 6, we list the maximum correlation coefficient, the lag time of velocities behind the wind and direction of the wind relative to north of the maximum correlation coefficient. The along-shore direction has the least variation in wind direction with stations BIN, SAK, BIE correlated with winds blowing towards 70^{o} east of north and the rest of the stations correlated with winds 180^{o} in the opposite direction, blowing to the southwest. This direction is parallel to the larger scale northeast orientation of the southern New England coastline.

Although, wind stress and sea-surface tilt effect all stations, each station may be more sensitive to one of these forcings. We suspect that wind blowing to the northeast forcing water directly at stations BIN, BIE and SAK through shear stress, causes flow in the same direction as the wind (Table 6), has a larger impact on depth-averaged momentum at this synoptic timescale. This hypothesis is supported by high correlations for winds blowing in the southwest direction (Table 6). Along the eastern side of RIS, northwestward blowing winds create a pressure gradient through tilting sea-surface that induces flow in the negative $\hat{y}$ direction, that is dominant over wind shear at these timescales. This hypothesis is supported by high correlations for winds blowing in the northeast direction for stations CLC, CRS, MV7 and WBF (Table 6). Wind directions found for maximum correlations with the across-shore direction have a greater variation than the along-shore estimates. Strong variations in wind direction were also found for both the along- and across-shore depth-averaged shear comparison with wind.

We further postulate on the relationship between wind and sea level during the summer season. Longer than synoptic timescales, we have found wind stress to be small in the depth-averaged momentum equation (Fig. 23). Fig. 31 displays the barotropic estimation of sea-surface setup as well as the monthly average wind magnitude and direction. Throughout all seasons the wind is parallel to the coastline in this area and should create upwelling conditions. For example, the SSH are low near shore for all estimations except March 2010 (Fig. 31). At our moored stations this creates a negative across-shore barotropic gradient that indicates sea level increases offshore (Fig. 27e).

Table 6: Correlation coefficients of depth-averaged velocity and shear with wind. Significant correlations are marked with * and lag of velocities behind wind are in parenthesizes with units of days. The direction of the wind with the highest correlation to velocity measurements is denoted in degrees from north, rotating clockwise. No shear measurements we estimated at station WBF for shear as part of the deployment no near surface velocities were recorded.

	Stations	BIN	SAK	BIE	MV7	CRS	WBF	CLC
Depth-Averaged Velocity	Along	0.57* (0)	0.72* (0.6)	0.36* (0.3)	0.47* (0.2)	0.68* (0.2)	0.54* (0.6)	0.66* (0.4)
	Angle from North	65	85	60	275	245	280	260
	Across	0.38* (0.4)	0.13 (0)	0.42* (0)	0.72* (0.1)	0.55* (0.3)	0.42* (0.8)	0.56* (0.6)
	Angle from North	220	125	55	265	285	85	280
Depth-Averaged Shear	Along	0.58* (0)	0.15 (0)	0.18* (0.5)	0.18* (1.8)	0.70* (0)	-	0.32* (0)
	Angle from North	245	30	115	40	230	-	210
	Across	0.51* (0)	0.38* (0.6)	0.32* (0)	0.24* (0)	0.67* (0.2)	-	0.15 (0)
	Angle from North	315	110	50	240	100	-	290

However, RIS is more geographically complicated than a northeast trending coastline and is bounded to the east with a bend at the northeast corner. We hypothesize the bend on the eastern side of RIS retains water, creating a sea-surface slope that enhances the coastal current and reduces the barotropic across-shore term during the summer. The June 2010 barotropic estimate (Fig. 31d) illustrates the northeastward blowing average summertime wind. The June estimate shows a SSH high along the eastern side of RIS and a reduced southward gradient. This is illustrated through more north-south trending contours of constant SSHs. Further observations are required to verify this hypothesis.

5.3 Seasonal Setup

To review all the contributions to the cyclonic coastal current, we summarize the relative size of the momentum terms averaged over stratified (summer) and well-mixed (winter) periods in various regions of RIS. We calculate momentum term averages during stratified periods, by taking the mean magnitude of the terms calculated by eq. 3 and 4. Well-mixed estimates were averaged over November through March. We characterize the magnitude of the momentum terms into three categories: strong ($>|0.5 \times 10^{-5}$ m $s^{-2}|$), moderate ($|0.1\text{-}0.5 \times 10^{-5}$ m $s^{-2}|$) and weak ($<|0.1 \times 10^{-5}$ m $s^{-2}|$). The pressure term is divided into the baroclinic contribution, estimated from the CTD deployment in summer and winter months, and barotropic estimates. Results for each term in various regions of RIS are listed in Table **7** and shown in Fig. 34.

Table 7: Characterization of the magnitude of momentum terms averaged over stratified (June-September) and well-mixed (Dec-March) seasons. We characterize the

absolute magnitude as strong (>|0.5 x10^{-5} m s^{-2}|), moderate (|0.1-0.5 x10^{-5} m s^{-2}|) or weak (<|0.1 x10^{-5} m s^{-2}|). * Indicates terms which we could not calculate and are making predictions based on nearby estimates from our experiment.

	Regions	Coriolis	Baroclinic	Tidal Advection	Barotropic
Stratified	1	Strong	Strong*	Moderate	Strong/Moderate
	2	Strong/Moderate	Strong	Weak	Strong/Moderate
	3	Strong	Strong	Strong	Strong/Moderate
	4	Moderate	Moderate	Weak	Strong/Moderate
Well-mixed (Dec-Mar)	1	Moderate	Moderate*	Moderate	Strong/Moderate
	2	Moderate	Moderate	Weak	Strong/Moderate
	3	Strong	Strong	Strong	Strong/Moderate
	4	Weak	Weak	Weak	Strong/Moderate

Region 1, along the eastern side of RIS, is most uniquely defined by the moderate tidal advection magnitudes. Station MV7 is on the deeper edge of this region. Topographic length scale comparison with tidal excursions at this station suggest that this region may be influenced by tidal rectification. Our numerical model predicted regions shallower than this site, closer to land, have moderate values of tidal advective stress (Fig. 26). In this region we predict the strongest coastal current to be closest to land, persistent all times of the year.

Region 3 is also influenced by strong tidal advection. Residual flow was strongest around Block Island measured at stations BIE and BIN. This region is heavily influenced by Block Island and the intensified tidal flow around the island. Our numerical model suggests that in region 3 tidally advective stresses are strong (Fig. 26). Flow to the north of Block Island is complicated. Our numerical model (Fig. 32) as well as recent modeling done by Sun et al. (2016), suggests two persistent headland eddies. It is likely that the ADCP station BIN is capturing part of this

circulation on presumably the western cyclonic eddy and is not representative of the entire flow for the area north of Block Island.

Additional momentum terms are variable across seasons. The coastal current, present in regions 1 and 2, is defined by a strong Coriolis term ($>|0.5 \times 10^{-5}$ m $s^{-2}|$) in stratified periods and moderate in well mixed periods, measured at our moored stations. Although, the mouth of Narragansett Bay had no current measurements during our experiment, we estimate this region to have a strong summer coastal current based on the observational study done by Kincaid et al. (2003). Thus, we extend region 2 to the mouth of Narragansett Bay. Strong baroclinic gradients enhance the cyclonic flow in regions 1 and 2, as the bottom cold pool develops during stratified periods. During well-mixed periods, density gradients are weak and have limited effect on the coastal current in these regions.

In regions 1, 2 and 3, seasonal changes in the barotropic component of pressure gradient was observed through the use of tide gauges. When the monthly average wind was blowing to the southeast (Fig. 31 b), the wind-driven sea-surface gradients impose a force that inhibits the cyclonic flow. Similarly, Kincaid et al. (2003) found that the coastal current was minimal or non-existent during winter seasons, also supporting our theory that the wind set-up of the sea-surface inhibits the coastal current. During stratified months (Fig. 31 d), the sea-surface slope, which normally increases to the south, is reduced. This reduces the effect of the barotropic force on the cyclonic coastal current.

The last area considered is region 4, which is characterized by weak momentum terms. The three moored instruments in this area (Fig. 34) showed the least

variation throughout the year. The flow in region 4 is sluggish and weak at seasonal timescales (Table 7).

6. Conclusion

Circulation in RIS is dominated by tides. Tidal velocities range from 0.10 to 0.40 m s^{-1} with the M2 being the largest tidal constituent measured at all stations. Largest velocities are measured in shallow water and near Block Island. The length of the tidal excursions, along with the size of bathymetric features, strongly suggests that tidal rectification should occur in shallow areas close to shore. Along-shore depth-averaged velocities were found to have a fortnightly oscillation when correlated with tidal range.

At longer periods than tidal frequencies, residual circulation in RIS has a general cyclonic flow pattern that is weak in central RIS and intensifies toward the periphery. Primarily RIS circulates water from near Martha's Vineyard and Buzzards Bay. Water is then transported to the mouth of Narragansett Bay and into Block Island and Long Island Sound. The measured residual velocities range from 1-5 cm s^{-1} during well-mixed periods and 2-8 cm s^{-1} during stratified seasons. Advective tidal stresses were estimated to be substantial for stations BIN and MV7.

Our observations suggest that a modification of the coastal current is a result of seasonal intensification of density gradients as well as wind set up. The seasonal spin-up or down of the coastal current is a result, in part, from the presence or absence of a central bottom cold pool in RIS, creating a buoyancy driven flow. Hydrographically, RIS is well-mixed during fall and winter months and stratified during spring and summer months. The buoyancy force, is maximized during summer months and

intensifies the cyclonic flow. Although present throughout the year, the gradients are created by a bottom cold pool in the summer and salinity gradients in the winter. Summer time spring-neap variations in tidal strength are thought to change horizontal density gradients. This causes fortnightly variations in potential energy anomalies, bottom temperature and residual velocities for several stations.

The barotropic pressure gradients are induced, in part, by wind driven sea-surface gradients. It is likely that the northeastward blowing wind limits the barotropic force in the summer. The northeastward blowing winds should create upwelling conditions for a shoreline oriented to the northeast-southwest. However, the geometry of RIS aids in the retention of water to the northeast, reducing the negative SSH gradient and barotropic pressure gradients. The southeastward wind increases this north-south SSH gradient and opposes the cyclonic flow in the winter. Pressure estimates were made from temporally sparse hydrographic data and tide gauge SSH. Further studies of dynamics in RIS would benefit from longer temporal measurements of both varying density fields and sea-surface heights to constrain pressure variations more accurately.

References

Armstrong, R.S., 1998. Water Temperatures and Climatological Conditions South of New England, 1974-83 (NOAA Technical Report NWFS No. 134). NOAA/National Marine Fisheries Service.

Beardsley, R.C., Chapman, D.C., Brink, K.H., Ramp, S.R., Schlitz, R., 1985. The Nantucket Shoals Flux Experiment (NSFE79). Part I: A Basic Description of the Current and Temperature Variability. J. Phys. Oceanogr. 15, 713–748. https://doi.org/10.1175/1520-0485(1985)015<0713:TNSFEP>2.0.CO;2

Beardsley, R.C., Winant, C.D., 1979. On the Mean Circulation in the Mid-Atlantic Bight. J. Phys. Oceanogr. 9, 612–619. https://doi.org/10.1175/1520-0485(1979)009<0612:OTMCIT>2.0.CO;2

Bergondo, D.L., Kester, D.R., Stoffel, H.E., Woods, W.L., 2005. Time-series observations during the low sub-surface oxygen events in Narragansett Bay during summer 2001. Mar. Chem. 97, 90–103. https://doi.org/10.1016/j.marchem.2005.01.006

Brown, W.S., Pettigrew, N.R., Irish, J.D., 1985. The Nantucket Shoals Flux Experiment (NSFE79). Part II: The Structure and Variability of Across-Shelf Pressure Gradients. J. Phys. Oceanogr. 15, 749–771. https://doi.org/10.1175/1520-0485(1985)015<0749:TNSFEP>2.0.CO;2

Bumpus, D.F., 1973. A description of the circulation on the continental shelf of the east coast of the United States. Prog. Oceanogr. 6, 111–157. https://doi.org/10.1016/0079-6611(73)90006-2

Chapman, D.C., Barth, J.A., Beardsley, R.C., Fairbanks, R.G., 1986. On the Continuity of Mean Flow between the Scotian Shelf and the Middle Atlantic Bight. J. Phys. Oceanogr. 16, 758–772. https://doi.org/10.1175/1520-0485(1986)016<0758:OTCOMF>2.0.CO;2

Codiga, D.L., Ullman, D.S., 2010. Characterizing the physical oceanography of coastal waters off Rhode Island, Part 1: Literature review, available observations, and a representative model simulation (Technical Report No. 2), Appendix to Rhode Island Ocean Special Area Management Plan. Rhode Island Coastal Resource Mangaement Council, Wakefield, R.I.

Csanady, G.T., 1979. The pressure field along the western margin of the North Atlantic. J. Geophys. Res. 84, 4905. https://doi.org/10.1029/JC084iC08p04905

Dong, C., Chen, D., Ou, H.-W., 2015. Numerical Study on Tidally Induced Cross-Frontal Mean Circulation. Atmosphere-Ocean 53, 363–375. https://doi.org/10.1080/07055900.2015.1056082

Edwards, C.A., 2004. Spring-summer frontogenesis at the mouth of Block Island Sound: 1. A numerical investigation into tidal and buoyancy-forced motion. J. Geophys. Res. 109. https://doi.org/10.1029/2003JC002132

Edwards, C.R., Seim, H.E., 2008. Complex EOF Analysis as a Method to Separate Barotropic and Baroclinic Velocity Structure in Shallow Water. J. Atmospheric

Ocean. Technol. 25, 808–821. https://doi.org/10.1175/2007JTECHO562.1

Emery, W.J., Thomson, R.E., 2001. Data analysis methods in physical oceanography, 2nd and rev. ed. ed. Elsevier, Amsterdam ; New York.

Fewings, M.R., Lentz, S.J., 2010. Momentum balances on the inner continental shelf at Martha's Vineyard Coastal Observatory. J. Geophys. Res. 115. https://doi.org/10.1029/2009JC005578

Fisher, E.L., 1960. An observational study of the sea breeze. J. Meteorol. 17, 645–660. https://doi.org/10.1175/1520-0469(1960)017<0645:AOSOTS>2.0.CO;2

Hald, A., 1976. Statistical theory with engineering applications, A Wiley publication in applied statistics. Wiley, New York u.a.

He, R., Wilkin, J.L., 2006. Barotropic tides on the southeast New England shelf: A view from a hybrid data assimilative modeling approach. J. Geophys. Res. 111. https://doi.org/10.1029/2005JC003254

Hicks, S.D., Campbell, R., 1953. Physical oceanographic cruises No. 6 and 7, Narragansett Bay and its approaches, July-September 1952 (Narragnsett Marine Laboratory Report No. 52–16). University of Rhode Island, Narragansett, RI.

Hofmeister, R., Burchard, H., Bolding, K., 2009. A three-dimensional model study on processes of stratification and de-stratification in the Limfjord. Cont. Shelf Res. 29, 1515–1524. https://doi.org/10.1016/j.csr.2009.04.004

Holt, J., Umlauf, L., 2008. Modelling the tidal mixing fronts and seasonal stratification of the Northwest European Continental shelf. Cont. Shelf Res. 28, 887–903. https://doi.org/10.1016/j.csr.2008.01.012

Kincaid, C., Pockalny, R.A., Huzzey, L.M., 2003. Spatial and temporal variability in flow at the mouth of Narragansett Bay. J. Geophys. Res. Oceans 108, 3218. https://doi.org/10.1029/2002JC001395

Lentz, S.J., 1995. Sensitivity of the Inner-Shelf Circulation to the Form of the Eddy Viscosity Profile. J. Phys. Oceanogr. 25, 19–28. https://doi.org/10.1175/1520-0485(1995)025<0019:SOTISC>2.0.CO;2

Lentz, S.J., Fewings, M.R., 2012. The Wind- and Wave-Driven Inner-Shelf Circulation. Annu. Rev. Mar. Sci. 4, 317–343. https://doi.org/10.1146/annurev-marine-120709-142745

Liu, Q., 2015. Dynamics of Rhode Island Coastal Water (PhD). University of Rhode Island.

Liu, Y., Weisberg, R.H., 2005. Momentum balance diagnoses for the West Florida Shelf. Cont. Shelf Res. 25, 2054–2074. https://doi.org/10.1016/j.csr.2005.03.004

Loder, J.W., 1980. Topographic Rectification of Tidal Currents on the Sides of Georges Bank. J. Phys. Oceanogr. 10, 1399–1416. https://doi.org/10.1175/1520-0485(1980)010<1399:TROTCO>2.0.CO;2

Loder, J.W., Wright, D.G., 1985. Tidal rectification and frontal circulation on the sides of Georges Bank. J. Mar. Res. 43, 581–604. https://doi.org/10.1357/002224085788440367

Lund-Hansen, L.C., Skyum, P., Christiansen, C., 1996. Modes of Stratification in a Semi-enclosed Bay at the North Sea–Baltic Sea Transition. Estuar. Coast. Shelf Sci. 42, 45–54. https://doi.org/10.1006/ecss.1996.0004

Luo, Y., Rothstein, L., Liu, Q., Zhang, S., 2013. Climatic variability of the circulation in the Rhode Island Sound: A modeling study: Circulation in The Rhode Island Sound. J. Geophys. Res. Oceans 118, 4072–4091. https://doi.org/10.1002/jgrc.20285

MacKenzie, B.R., Schiedek, D., 2007. Long-term sea surface temperature baselines—time series, spatial covariation and implications for biological processes. J. Mar. Syst. 68, 405–420. https://doi.org/10.1016/j.jmarsys.2007.01.003

Moody, J.A., Survey, U.D. of the I.G., Daifuku, P., Butman, B., 1984. Atlas of tidal elevation and current observations on the Northeast American continental shelf and slope, Bulletin US Geological Survey. U.S. Government Printing Office.

Parsa, J., Shahidi, A.E., 2010. Prediction of tidal excursion length in estuaries due to the environmental changes. Int. J. Environ. Sci. Technol. 7, 675–686. https://doi.org/10.1007/BF03326177

Pawlowicz, R., Beardsley, B., Lentz, S., 2002. Classical tidal harmonic analysis including error estimates in MATLAB using T_TIDE. Comput. Geosci. 28, 929–937. https://doi.org/10.1016/S0098-3004(02)00013-4

Pu, X., Shi, J.Z., Hu, G.-D., Xiong, L.-B., 2015. Circulation and mixing along the North Passage in the Changjiang River estuary, China. J. Mar. Syst. 148, 213–235. https://doi.org/10.1016/j.jmarsys.2015.03.009

Rosenberger, K., 2001. Circulation patterns in Rhode Island sound: Constraints from a bottom mounted acoustic Doppler current profiler. University of Rhode Island, Narragansett, RI.

Sharples, J., 2007. Potential impacts of the spring-neap tidal cycle on shelf sea primary production. J. Plankton Res. 30, 183–197. https://doi.org/10.1093/plankt/fbm088

Shonting, D.H., Cook, G.S., 1970. On the Seasonal Distribution of Temperature and Salinity in Rhode Island Sound1. Limnol. Oceanogr. 15, 100–112. https://doi.org/10.4319/lo.1970.15.1.0100

Simpson, J.H., Bowers, D., 1981. Models of stratification and frontal movement in shelf seas. Deep Sea Res. Part Oceanogr. Res. Pap. 28, 727–738. https://doi.org/10.1016/0198-0149(81)90132-1

Simpson, J.H., Crisp, D.J., Hearn, C., 1981. The Shelf-Sea Fronts: Implications of their Existence and Behaviour [and Discussion]. Philos. Trans. R. Soc. Math. Phys. Eng. Sci. 302, 531–546. https://doi.org/10.1098/rsta.1981.0181

Simpson, J.H., Hunter, J.R., 1974. Fronts in the Irish Sea. Nature 250, 404–406. https://doi.org/10.1038/250404a0

Sun, Y., Chen, C., Beardsley, R.C., Ullman, D., Butman, B., Lin, H., 2016. Surface circulation in Block Island Sound and adjacent coastal and shelf regions: A FVCOM-CODAR comparison. Prog. Oceanogr. 143, 26–45. https://doi.org/10.1016/j.pocean.2016.02.005

Sylaios, G., Kamidis, N., Anastasiou, S., Tsihrintzis, V.A., 2013. Hydrodynamic response of Thassos Passage (N. Aegean Sea) to Nestos River discharge and meteorological forcing. Cont. Shelf Res. 59, 37–51. https://doi.org/10.1016/j.csr.2013.04.003

Ullman, D.S., Codiga, D.L., 2004. Seasonal variation of a coastal jet in the Long Island Sound outflow region based on HF radar and Doppler current observations. J. Geophys. Res. 109. https://doi.org/10.1029/2002JC001660

Ullman, D.S., Codiga, D.L., Pfeiffer-Herbert, A., Kincaid, C.R., 2014. An anomalous near-bottom cross-shelf intrusion of slope water on the southern New England continental shelf. J. Geophys. Res. Oceans 119, 1739–1753. https://doi.org/10.1002/2013JC009259

Ullman, D.S., Cornillon, P.C., 2001. Continental shelf surface thermal fronts in winter off the northeast US coast. Cont. Shelf Res. 21, 1139–1156. https://doi.org/10.1016/S0278-4343(00)00107-2

Visser, A.W., Bowman, M.J., Crawford, W.R., 1990. Dynamics of Tidally Forced Basin-wide Coastal Eddies, in: Cheng, R.T. (Ed.), Residual Currents and Long-Term Transport. Springer New York, New York, NY, pp. 64–78. https://doi.org/10.1007/978-1-4613-9061-9_6

Wright, D.G., Loder, J.W., 1985. A depth-dependent study of the topographic rectification of tidal currents. Geophys. Astrophys. Fluid Dyn. 31, 169–220. https://doi.org/10.1080/03091928508219269

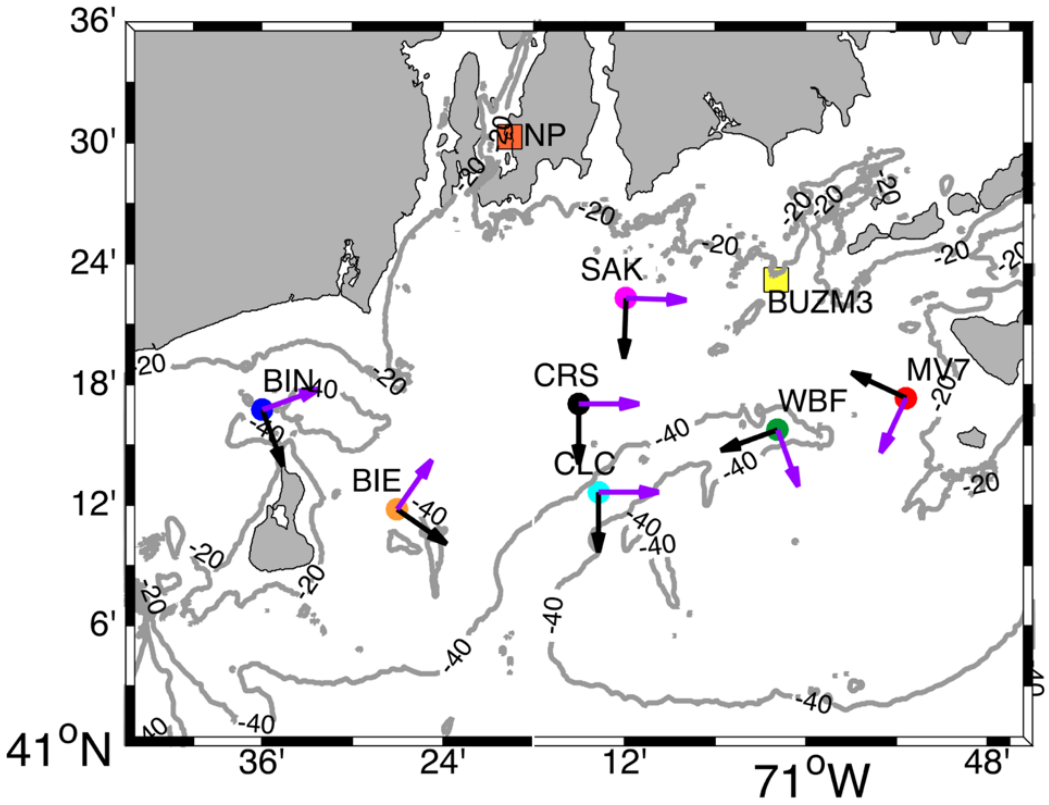

Figure 1: Map of Rhode Island Sound and moored station locations. Stations are marked with colored circles. Along- (purple) and across-shore (black) axis are illustrated with arrows. Bathymetric contours (grey) are labeled every 20 m. All maps use Mercator projections.

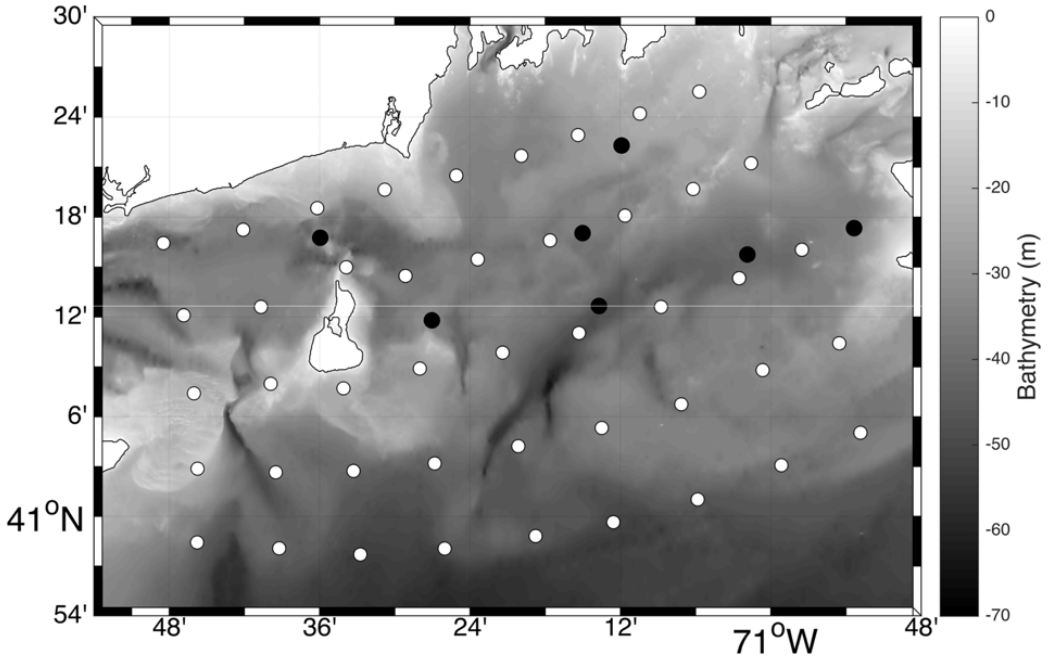

Figure 2: Locations of CTD casts (white circles) on September 22-24, 2009; December 7-8, 2009; March 9-11, 2010; and June 16-18, 2010 overlain on bathymetry. Moored stations indicated by black circles.

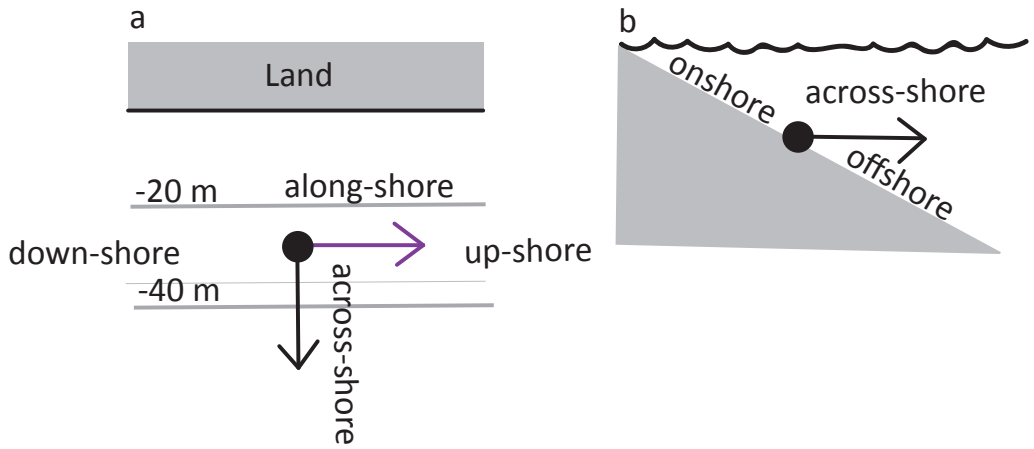

Figure 3: Orientations of horizontal axes at ADCP locations. Along-shore (purple arrow) and across-shore (black arrow) directions are parallel and perpendicular to isobaths respectively. (a) Map-view of orientation. (b) Vertical profile view of station taken perpendicular to isobaths.

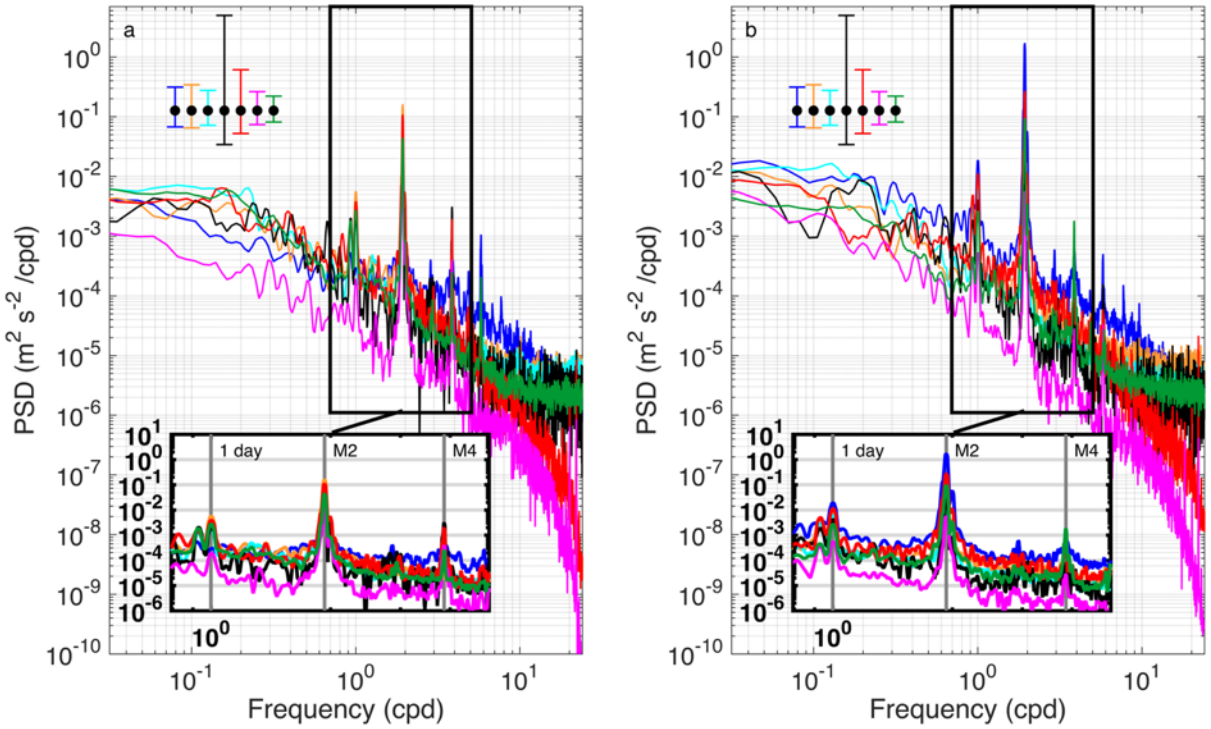

Figure 4: Power spectral density of depth-averaged velocity in (a) across- and (b) along-shore directions. Synoptic, diurnal and tidal frequencies indicated by grey vertical lines in subplot. Station colors are the same as Fig. 1. Error bars indicated in top left corner for each station.

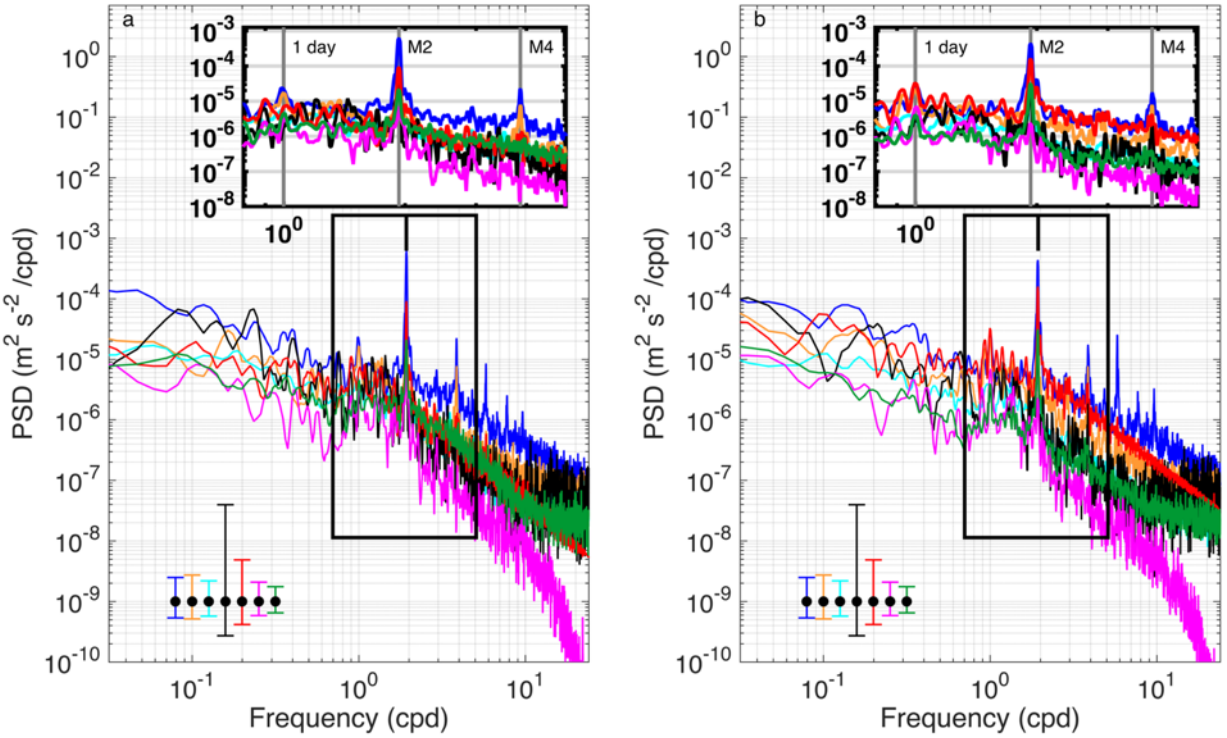

Figure 5: Power spectral density of depth-averaged velocity shear in the (a) across- and (b) along-shore directions. Synoptic, diurnal and tidal frequencies indicated by grey vertical lines in subplot. Station colors are same as Fig. 1. Error bars indicated in bottom left corner for each station.

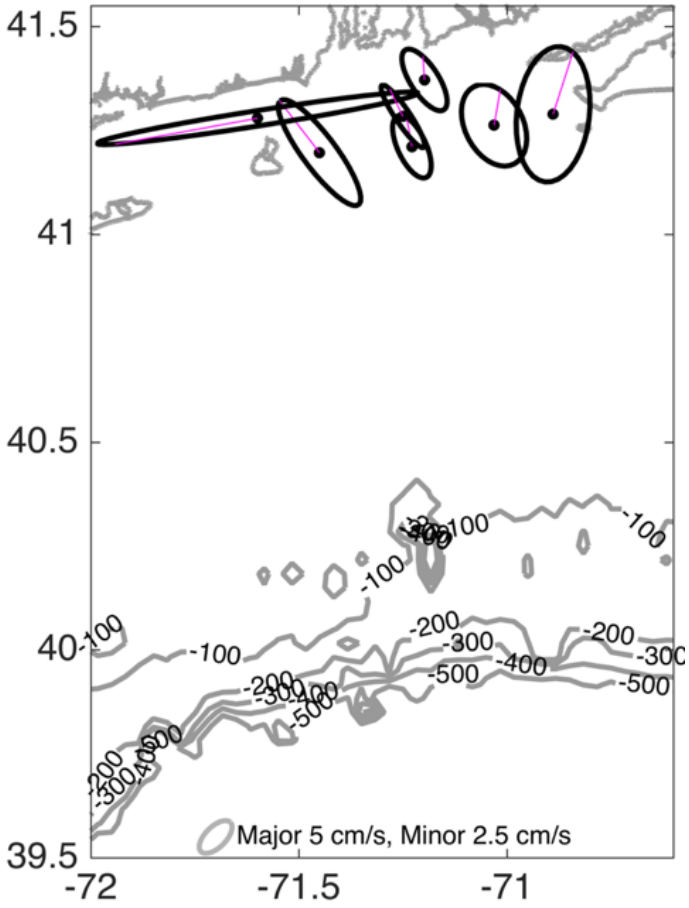

Figure 6: Depth-averaged M2 tidal ellipses overlain on bathymetry contoured every 100 m from 0-500 m. Station locations are indicated by black dots. Ellipses rotate clockwise and the relative phases are indicated by magenta line.

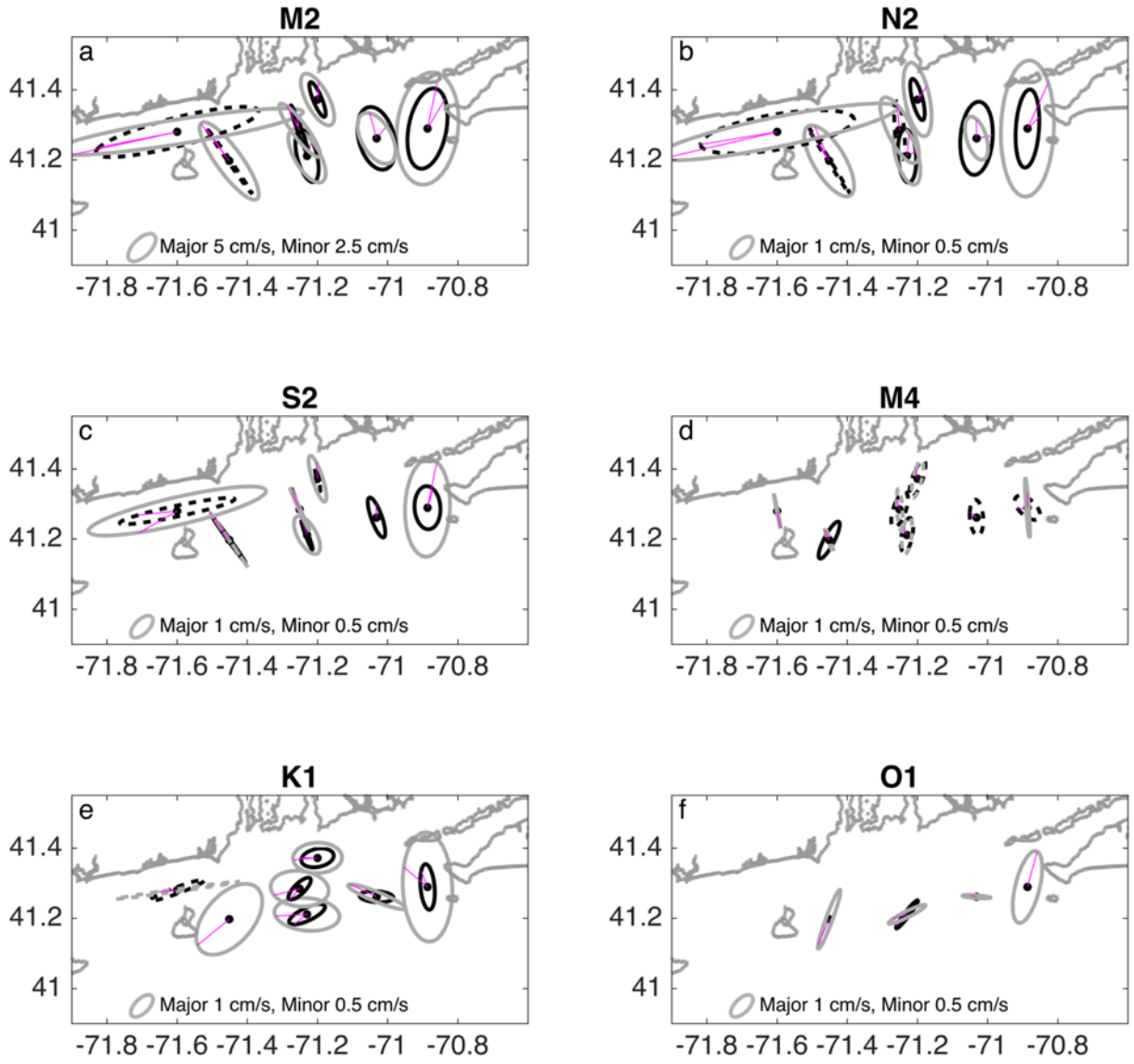

Figure 7: The six major tidal consituents are displayed. Two profiles are displayed at each station: near surface (grey), and near bottom (black). Middle water column tidal ellipses were also calculated but are very similar to surface tidal ellipses and not plotted. Pink lines indicate the phase orientation. Solid ellipses indicate a clockwise rotation of the tidal ellipse and dashed line indicates a counterclockwise rotation. Frequencies that are not significant are not plotted. The S2 frequency was not significant for WBF surface velocites. The O1 frequency was not significant at stations BIN and SAK. The O1 frequncy is also not significant for BIN, MV7 and WBF bottom velocities and the K1 frequency is not significant for BIE bottom velocities.

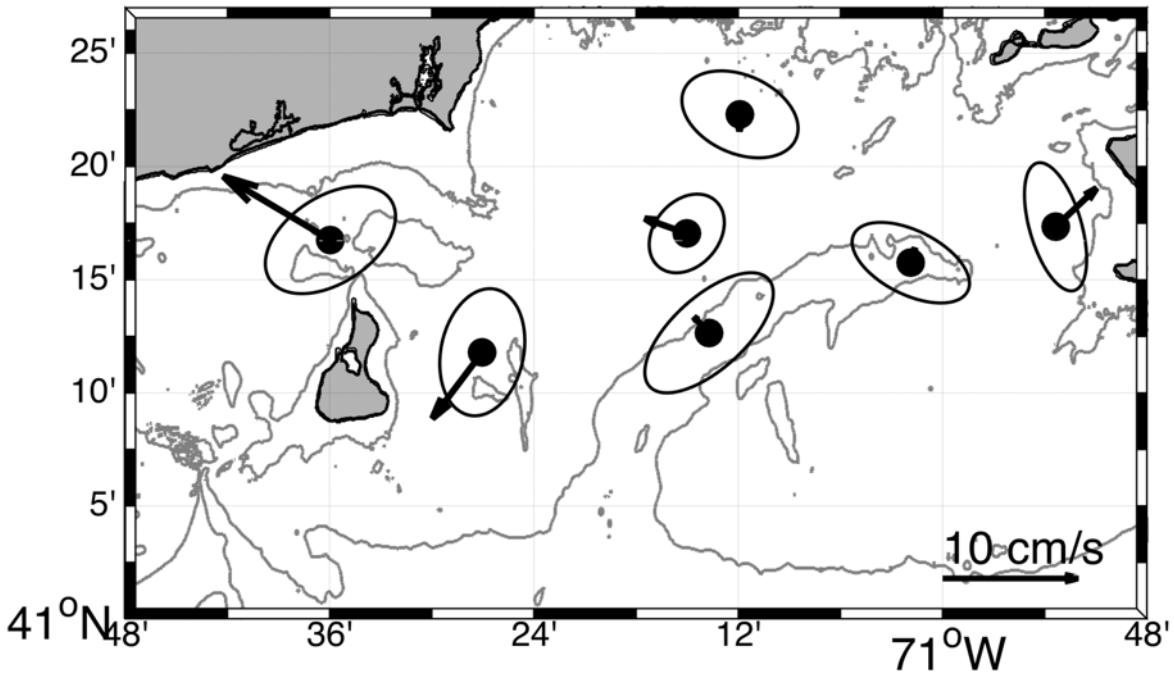

Figure 8: Depth- and deployment-averaged velocity vectors measured at each moored ADCP. Ellipse encapulates 60% variance of the depth avearged data centered at the station. Bathymetry contoured every 20 m.

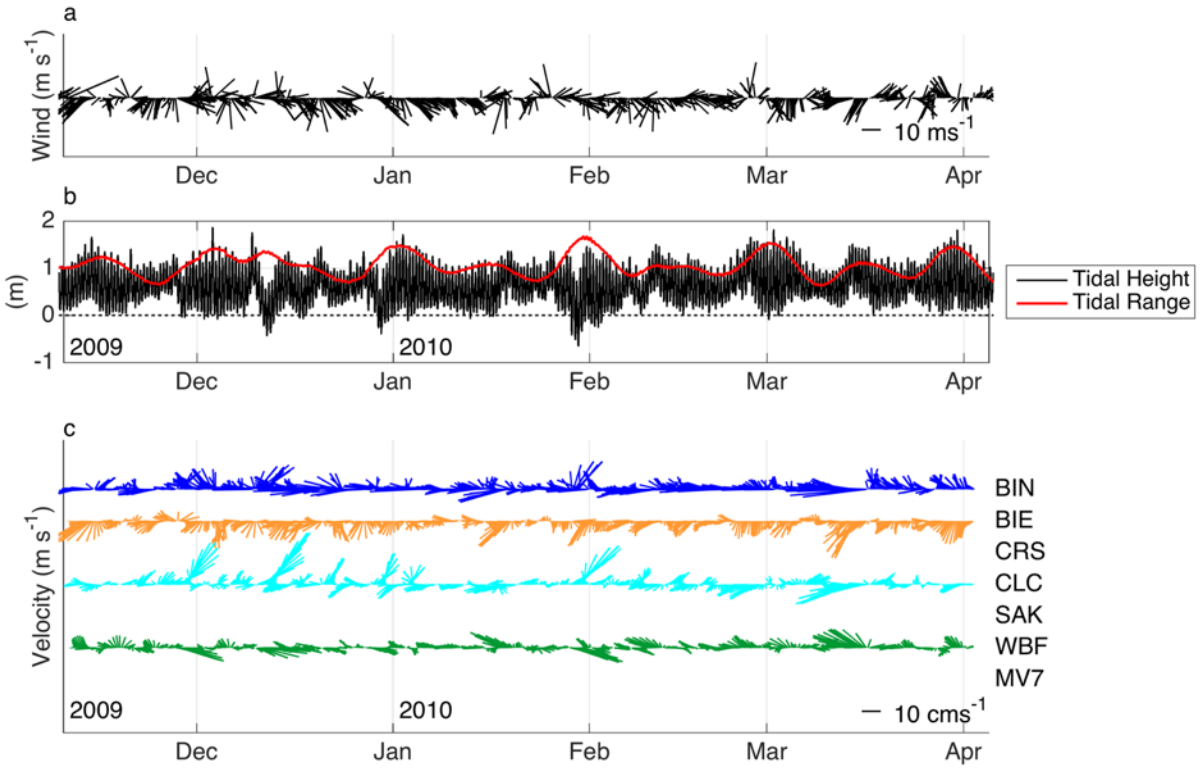

Figure 9: Observations plotted for deployment 1. (a) Wind speed measured at BUZM3 is illustrated as a vector pointing to where the wind is blowing. (b) Tidal height is plotted for the Newport, RI tide gauge and tidal range is indicated with a red line. (c) Station depth-average velocities pointing to where the water is flowing too. Stations are listed on the right side of the figure. Months labeled at the start of every month.

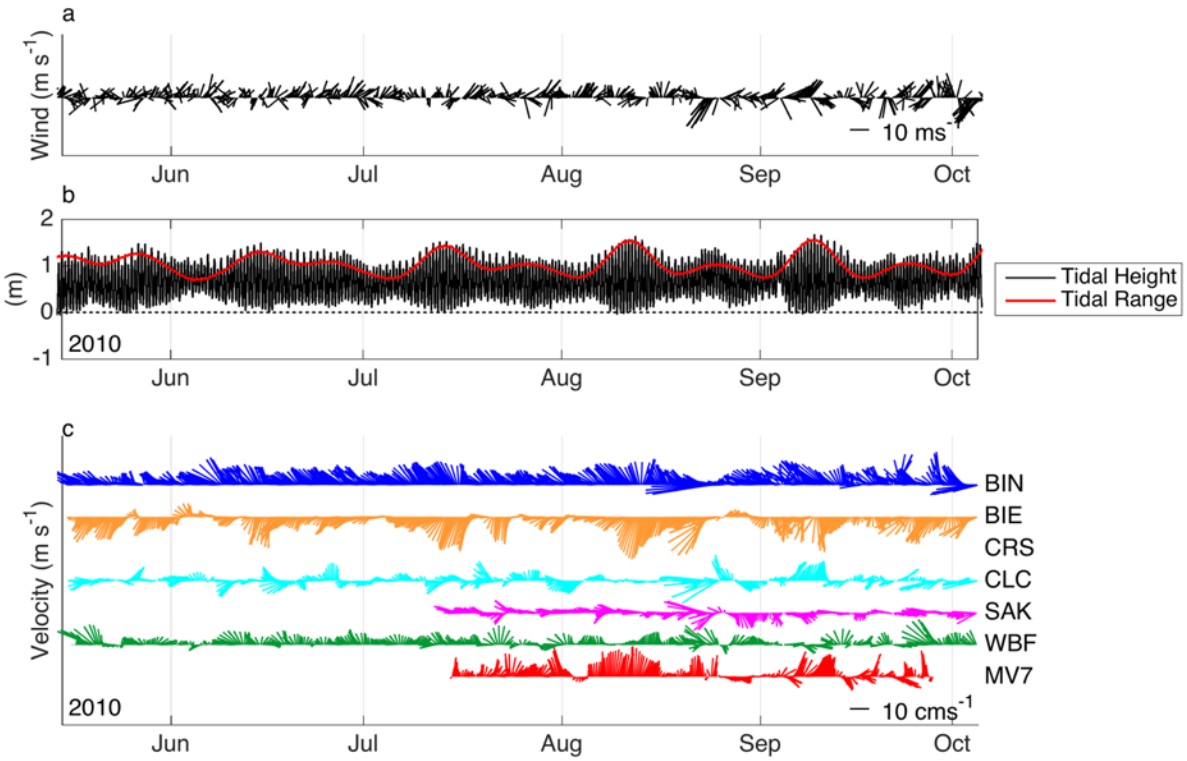

Figure 10: Observations plotted for deployment 2. (a) Wind speed measured at BUZM3 is illustrated as a vector pointing to where the wind is blowing. (b) Tidal height is plotted for the Newport, RI tide gauge and tidal range is indicated with a red line. (c) Station depth-average velocities pointing to where the water is flowing too. Stations are listed on the right side of figure. Months labeled at the start of every month.

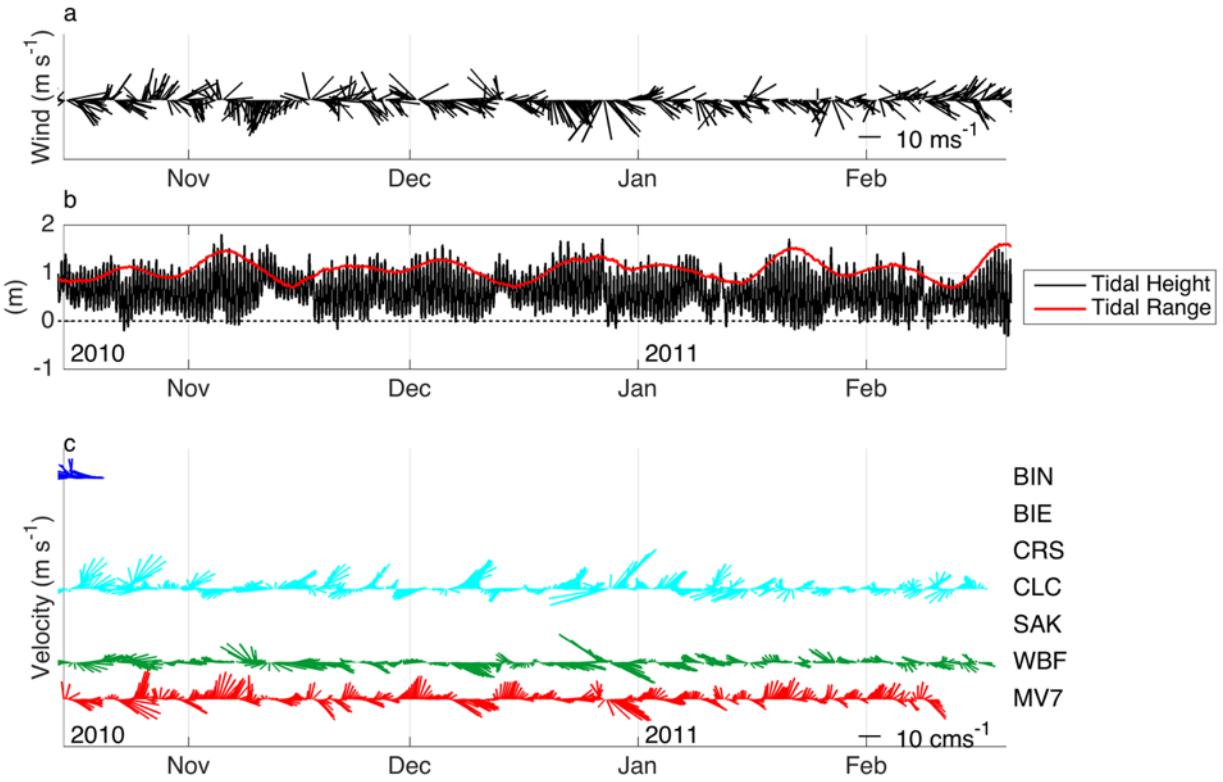

Figure 11: Observations plotted for deployment 3. (a) Wind speed measured at BUZM3 is illustrated as a vector pointing to where the wind is blowing. (b) Tidal height is plotted for the Newport, RI tide gauge and tidal range is indicated with a red line. (c) Station depth-average velocities pointing to where the water is flowing too. Stations are listed on the right side of figure. Months labeled at the start of every month.

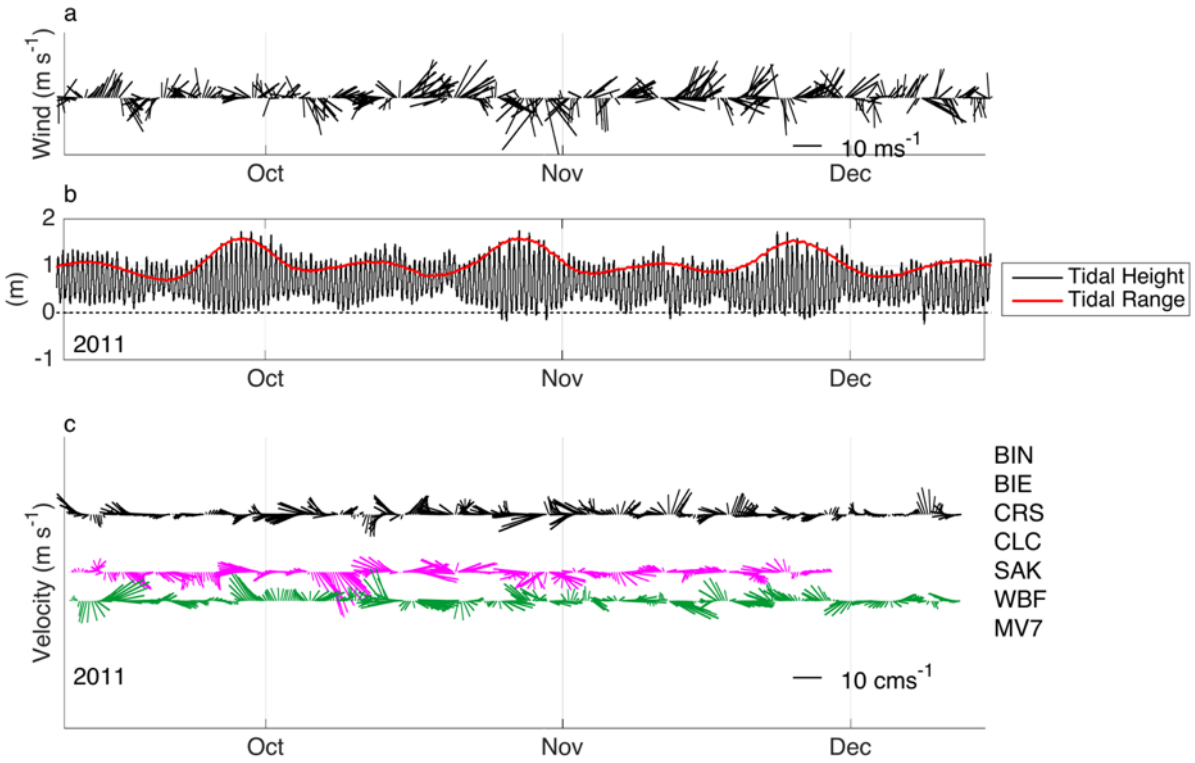

Figure 12: Observations plotted for deployment 4. (a) Wind speed measured at BUZM3 is illustrated as a vector pointing to where the wind is blowing. (b) Tidal height is plotted for the Newport, RI tide gauge and tidal range is indicated with a red line. (c) Station depth-average velocities pointing to where the water is flowing too. Stations are listed on the right side of figure. Months labeled at the start of every month.

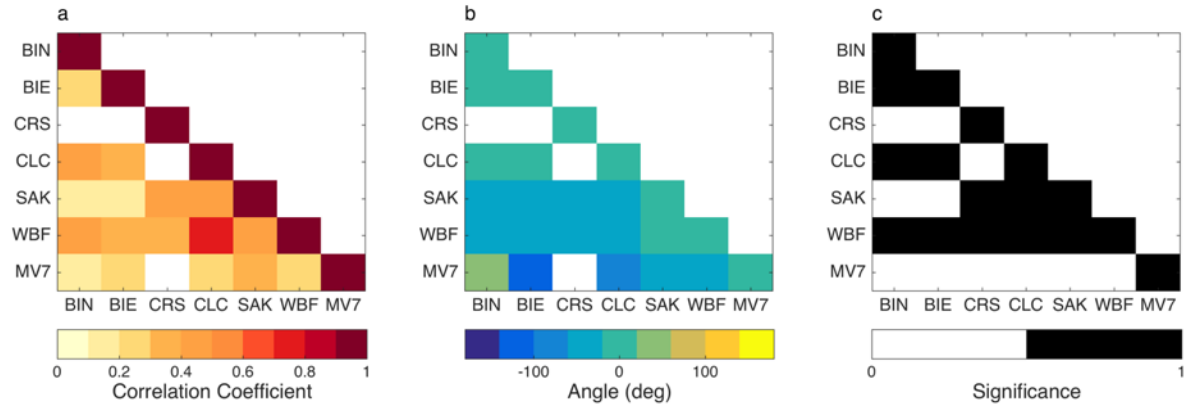

Figure 13: Correlation coefficients for station to station depth-averaged velocities comparison. (a) Absolute value of correlation between complex depth-averaged velocities organized from stations to the west to east. (b) Angle of rotation between the two stations, where positive indicates the station on the x-axis is rotated clockwise relative to the station on the y-axis. (c) Significance of correlation based on an adjusted degrees of freedom due to filtering of data. All time series are filtered using a

33-hour butterworth filter. White spaces in (a) and (b) indicate station pairs with no overlapping data.

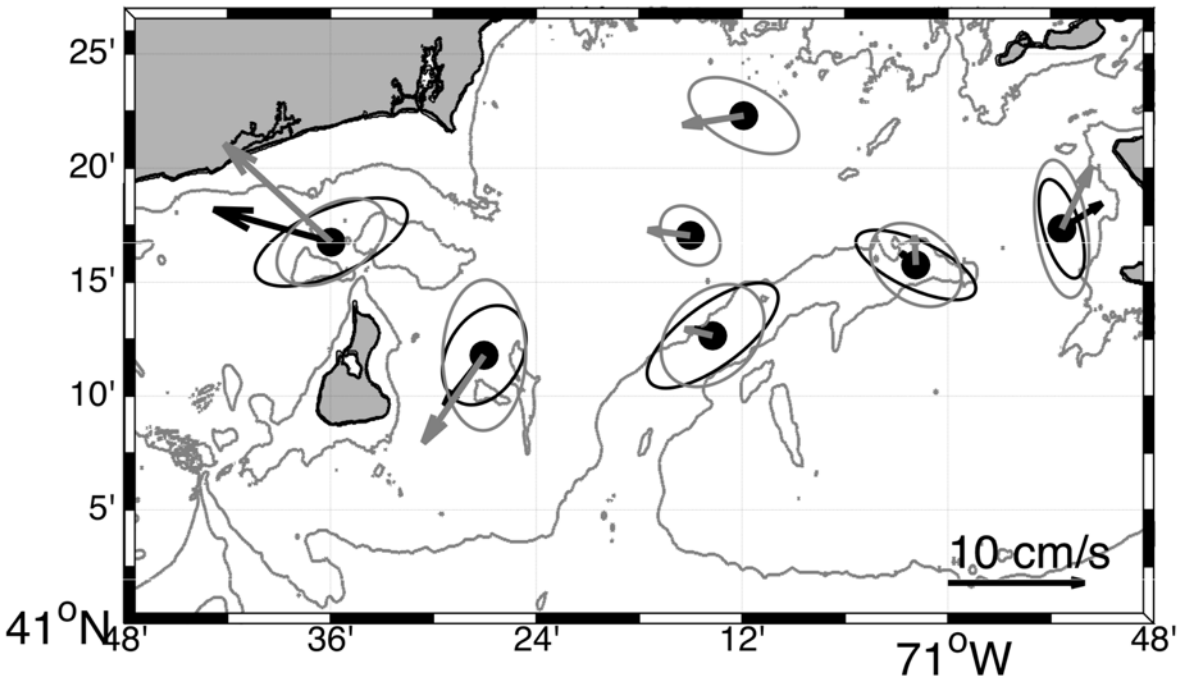

Figure 14: Seasonal averages of depth-averaged residual flow at the moored stations. Summer (July-Sept) is denoted by the grey arrows and winter (Jan-Mar) denoted by the black arrows. The variance ellipses illustrate the scatter of the data sets. Bathymetry contoured every 20 m.

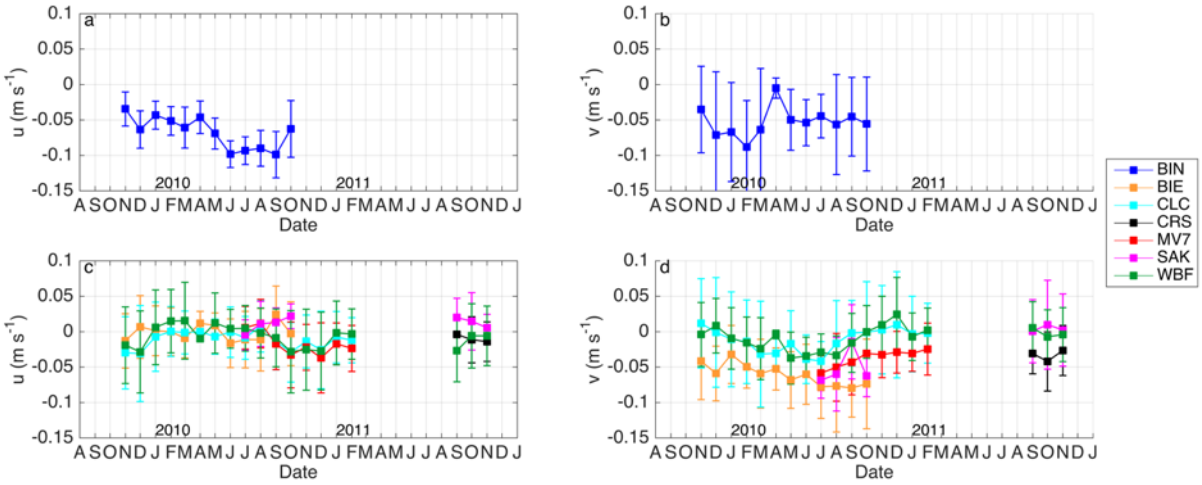

Figure 15: Monthly- and depth-averaged velocities at moored ADCP stations. Colors of stations are same as Fig. 1. Across-shore flow for (a) stations outside of RIS and

(c) inside RIS. Along-shore flow for (b) stations outside of RIS and (d) inside RIS. Error bars indicate one standard deviation of measured velocities.

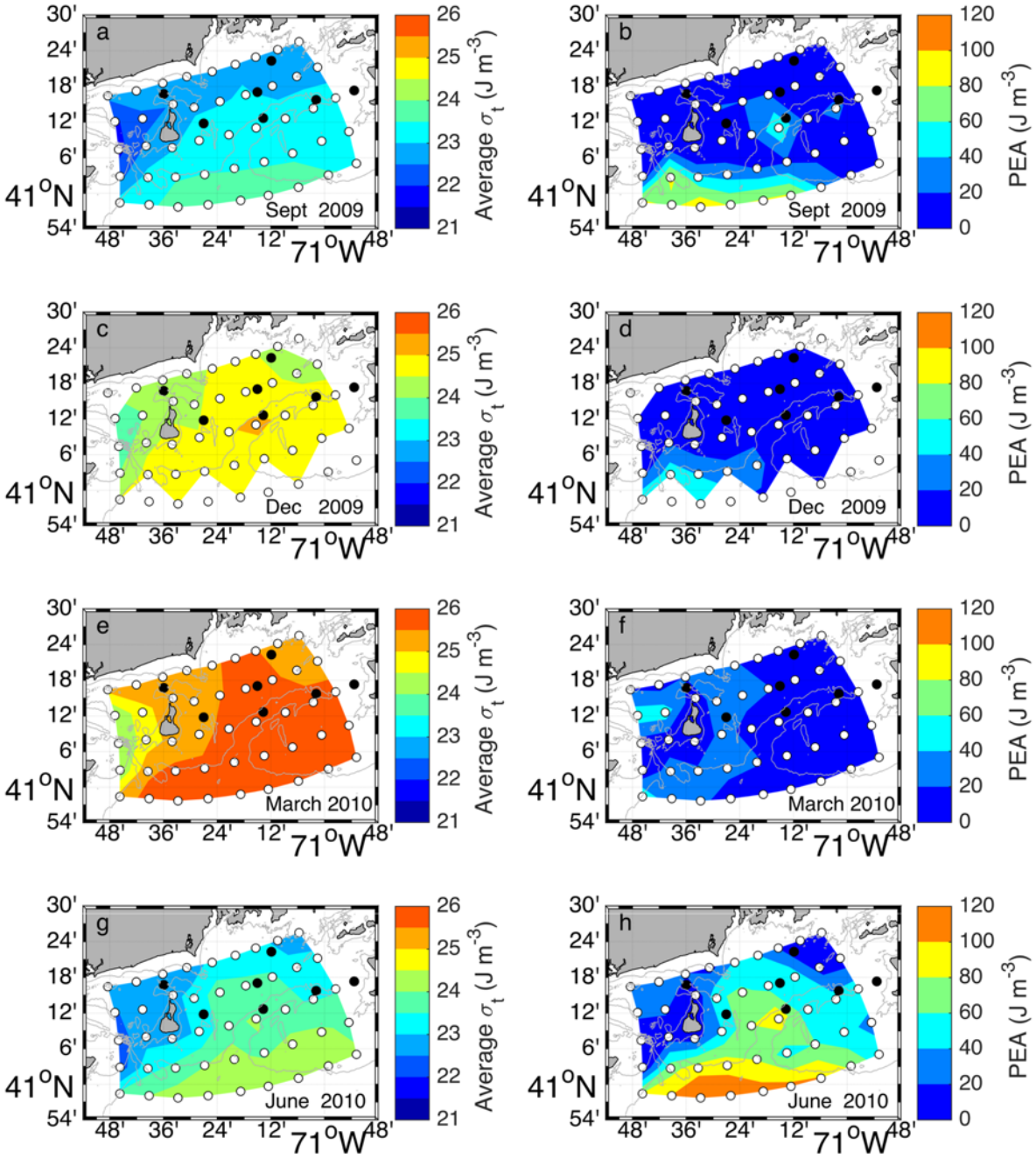

Figure 16: Depth-averaged density (left column) and potential energy anomalies (right column) calculated from four CTD survey deployments. CTD cast locations denoted by white circles. Moored ADCP station location indicated by black circles. Properties are overlain on bathymetric contours spaced every 20 m.

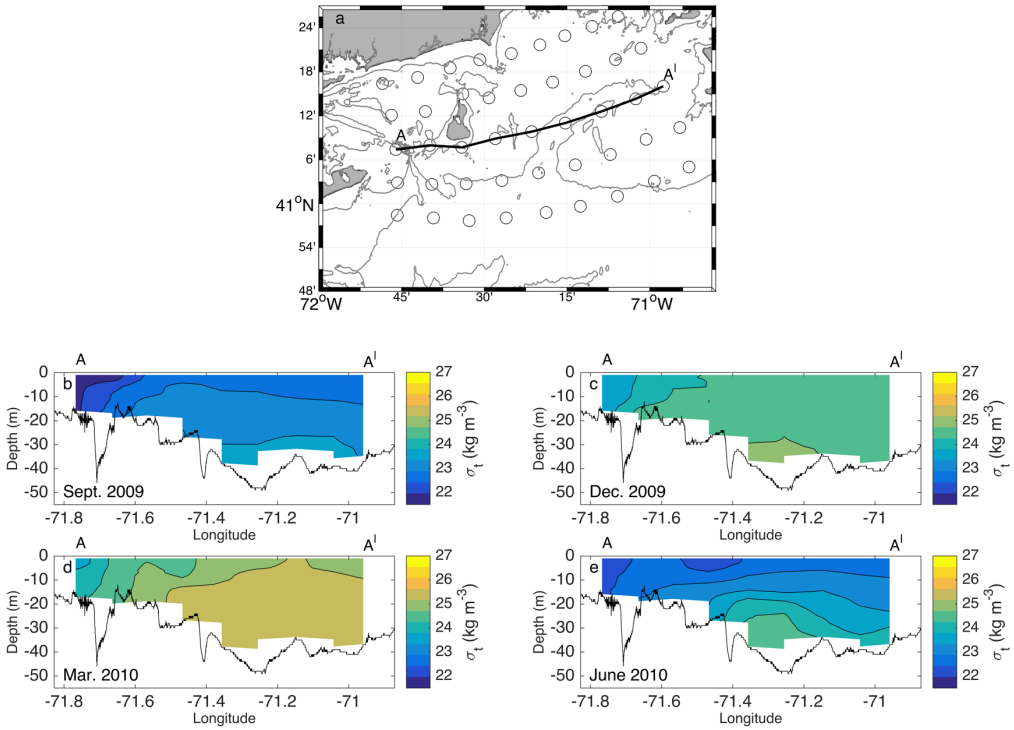

Figure 17: Density cross-section along an east-west transect in central RIS. (a) Location of CTD survey marked with open circles and cross-section line. Density is contoured for surveys taken in (b) September 2009, (c) December 2009, (d) March 2010 and (e) June 2010. Contours are every 0.5 kg m^{-3}.

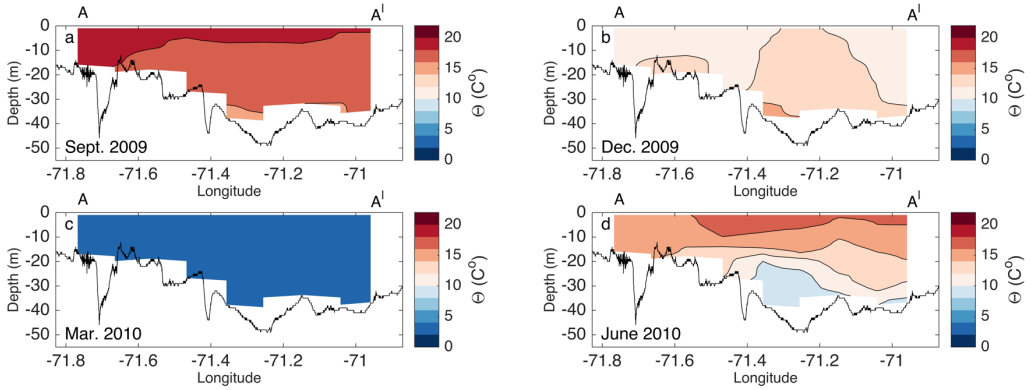

Figure 18: Temperature cross-section along an east-west transect in central RIS at same location as Fig. 17 a. Temperature is contoured for surveys taken in (a) September 2009, (b) December 2009, (c) March 2010 and (d) June 2010. Contours are every 2 °C.

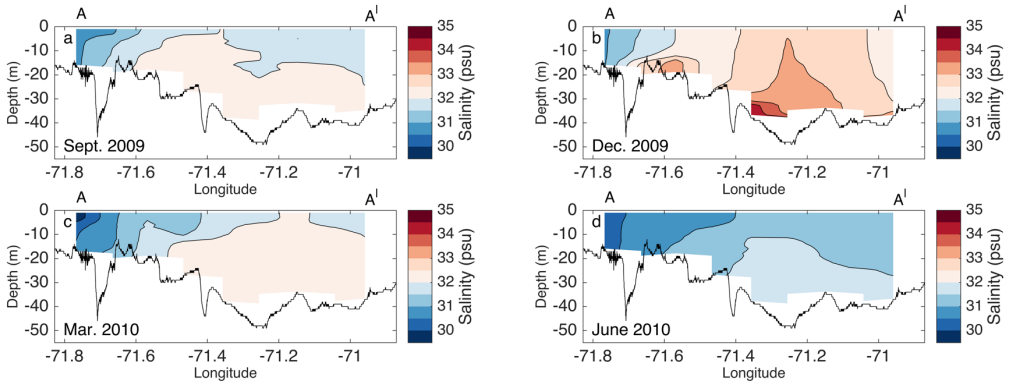

Figure 19: Salinity cross-section along an east-west transect in central RIS at same location as Fig. 17 a. Salinity is contoured for surveys taken in (a) September 2009, (b) December 2009, (c) March 2010 and (d) June 2010. Contours are every 0.5 psu.

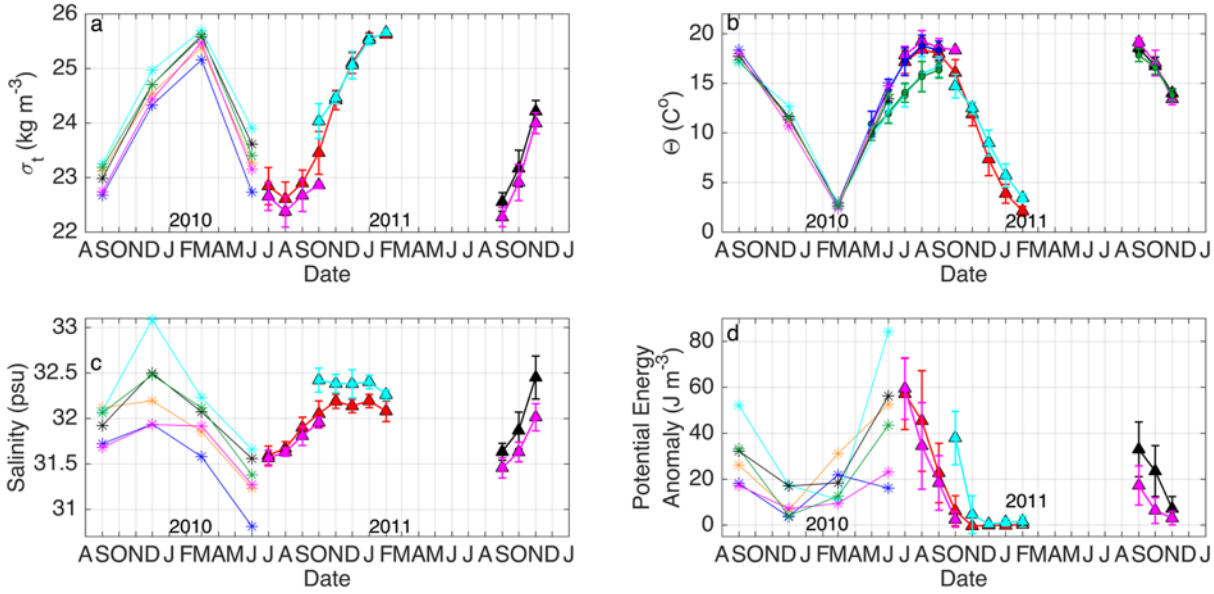

Figure 20: Depth-averaged hydrographic properties from CTD surveys, deployments and thermistor chains. Monthly averages of (a) densities, (b) temperature, (c) salinity and (d) potential energy anomalies calculated from CTD (triangle) and thermistor (circle) chain deployments and interpolated to moored station locations from CTD surveys (star). Standard deviation is provided for CTD and thermistor deployments. Station colors are the same as Fig. 1.

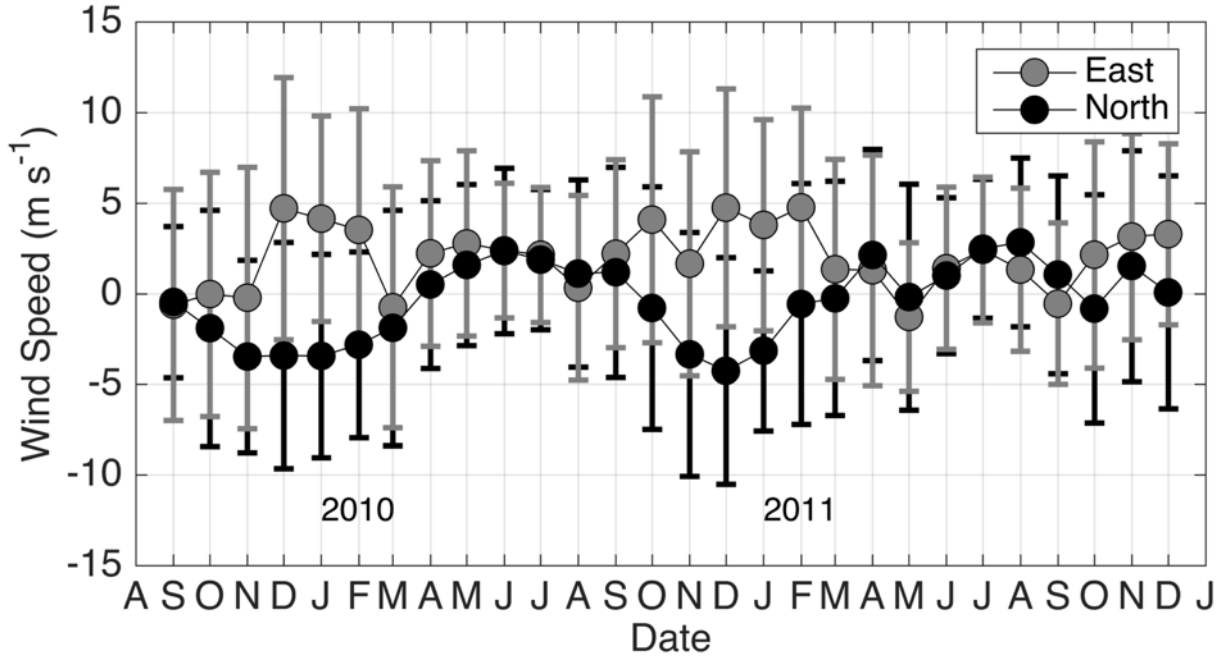

Figure 21: Wind speed estimates calculated at 10 m above sea level at BUZM3. Monthly averages of north (black) and east (gray) are plotted with standard deviation of measurements.

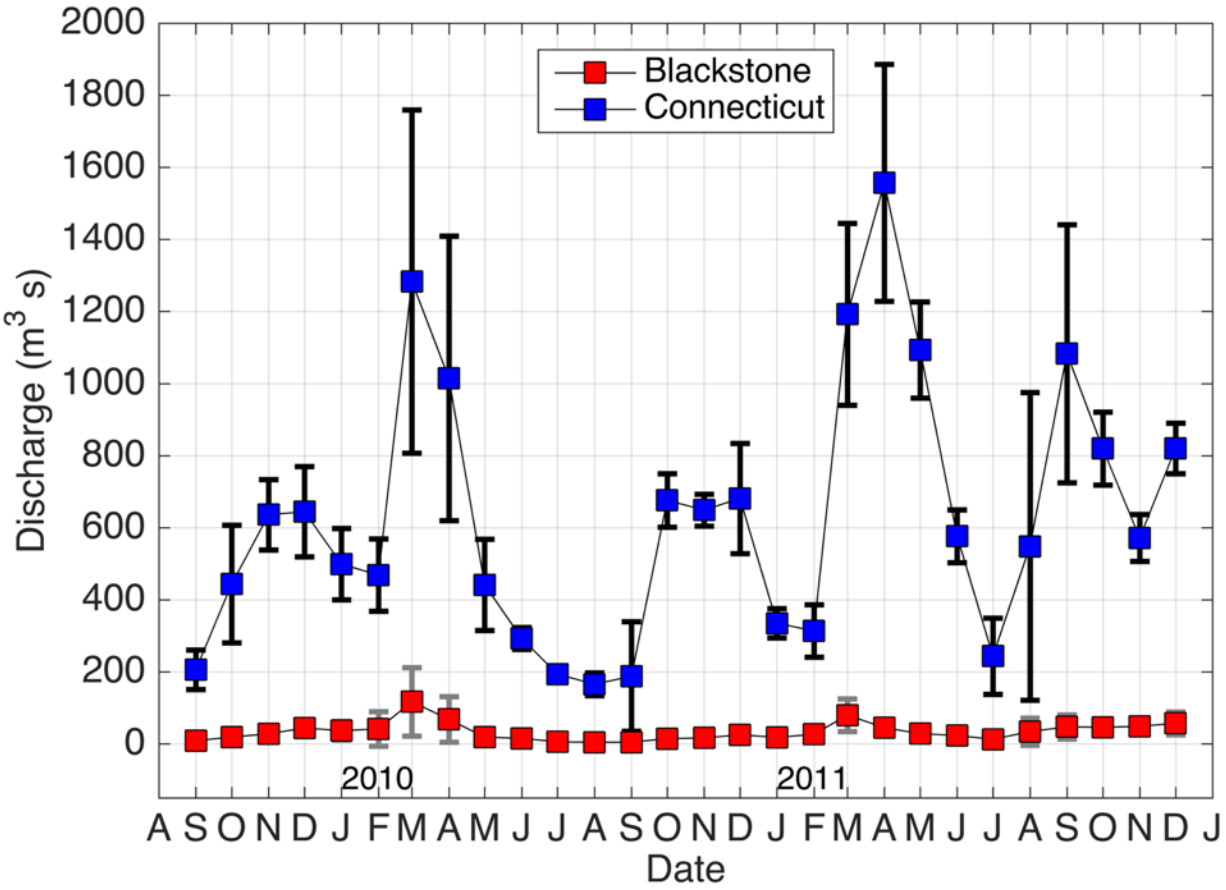

Figure 22: Monthly mean river discharge calculated for the Blackstone (red) and Connecticut (blue) rivers. Error bars indicate monthly standard deviation.

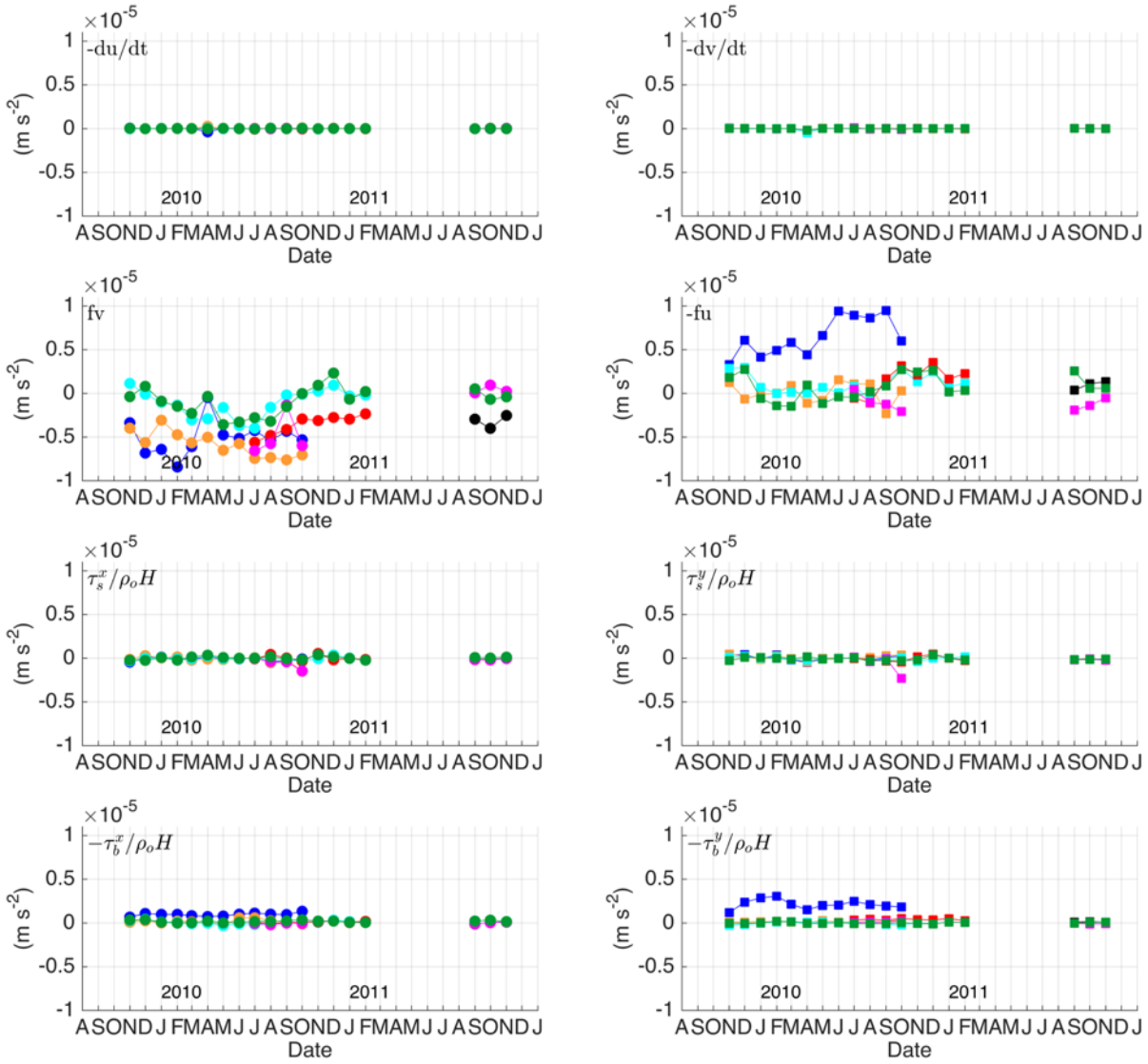

Figure 23: Four terms in the momentum balance are calculated from moored ADCP velocities and wind stress estimates for across- (left column) and along-shore (right column) directions. (a) & (b) The acceleration terms, (c) & (d) the Coriolis terms, (e) & (f) the wind stress and (g) & (h) are averaged monthly. Station colors are same as Fig. 1 and error bars indicate one standard deviation of the data.

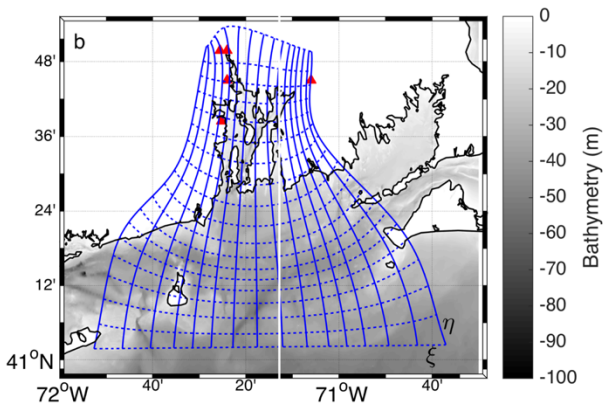

Figure 24: Outline of ROMS grid used. Boxes are every 50 grid nodes in both the ξ (dashed) and η (solid) directions. River inputs, not actual locations of river gauges, are marked with red triangles. Rivers starting from east and moving counter clockwise are the Taunton, Blackstone, Moshassuck, Pawtuxet and Hunt.

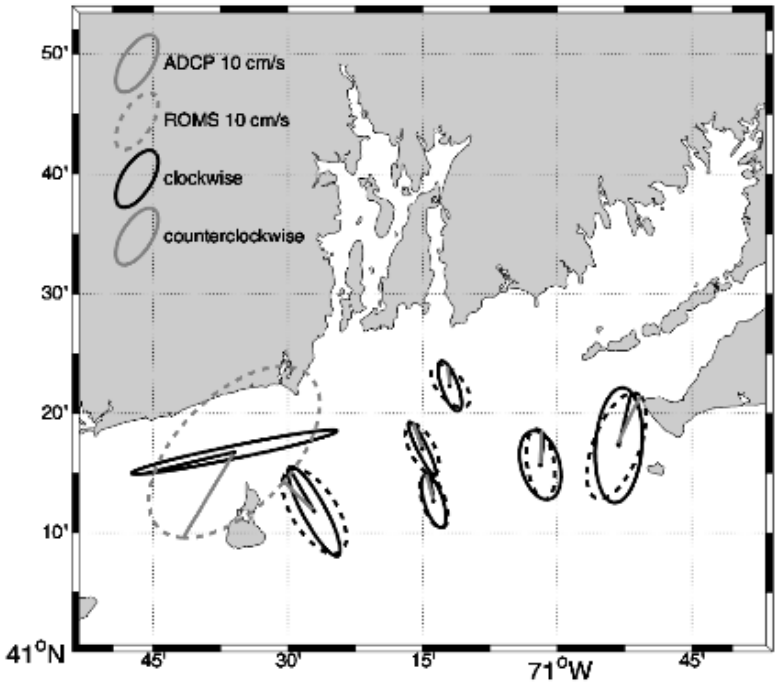

Figure 25: Comparison of depth-averaged tidal ellipses. Observational data (solid) and numerically model (dashed) are centered on moored stations. Clockwise and counterclockwise rotations are distinguished by black and grey lines respectively. Phase of the tidal ellipse is indicated with a line from center of ellipse.

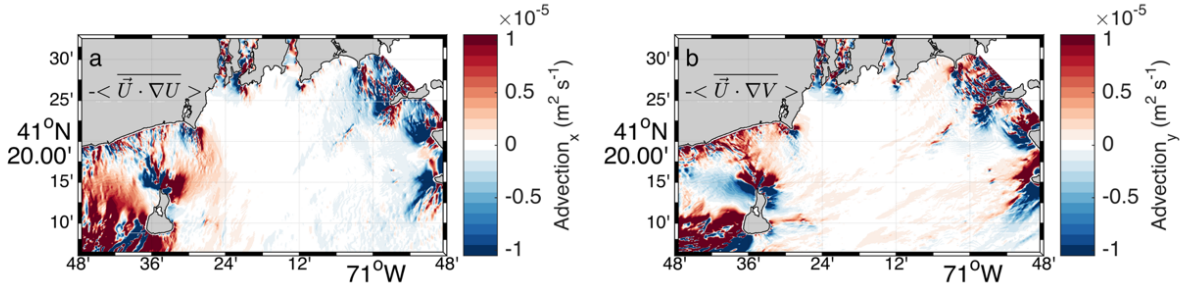

Figure 26: Advective tidal stress calculated from ROMS numerical model using the M2 tidal constituent. (a) Eastward and (b) northward advective tidal stresses colored. Land masked with grey.

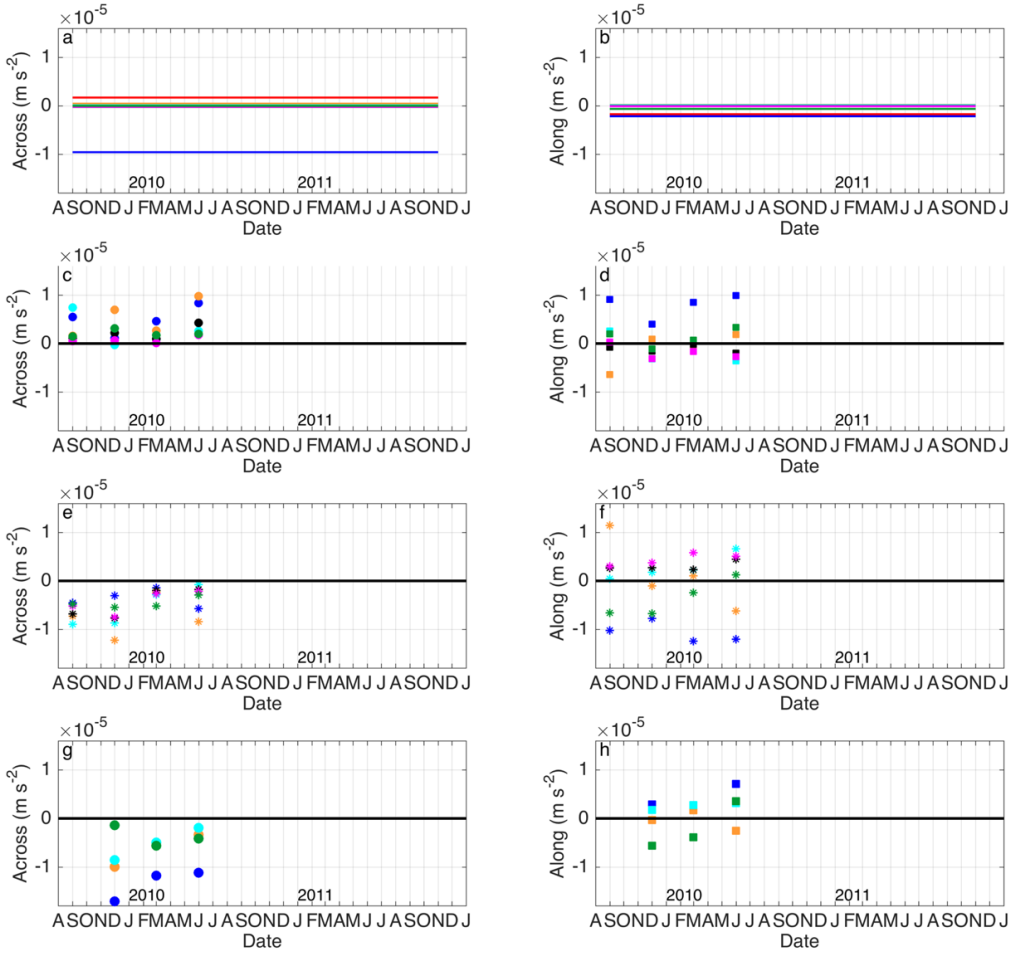

Figure 27: Remaining momentum balance terms. Across- (left column) and along-shore (right column) display calculated (a & b) advective tidal stresses, (c & d) baroclinic pressure gradients, (e & f) barotropic pressure gradients and (g & h) residual terms. Terms are calculated at moored stations and colors are the same as Fig. 1.

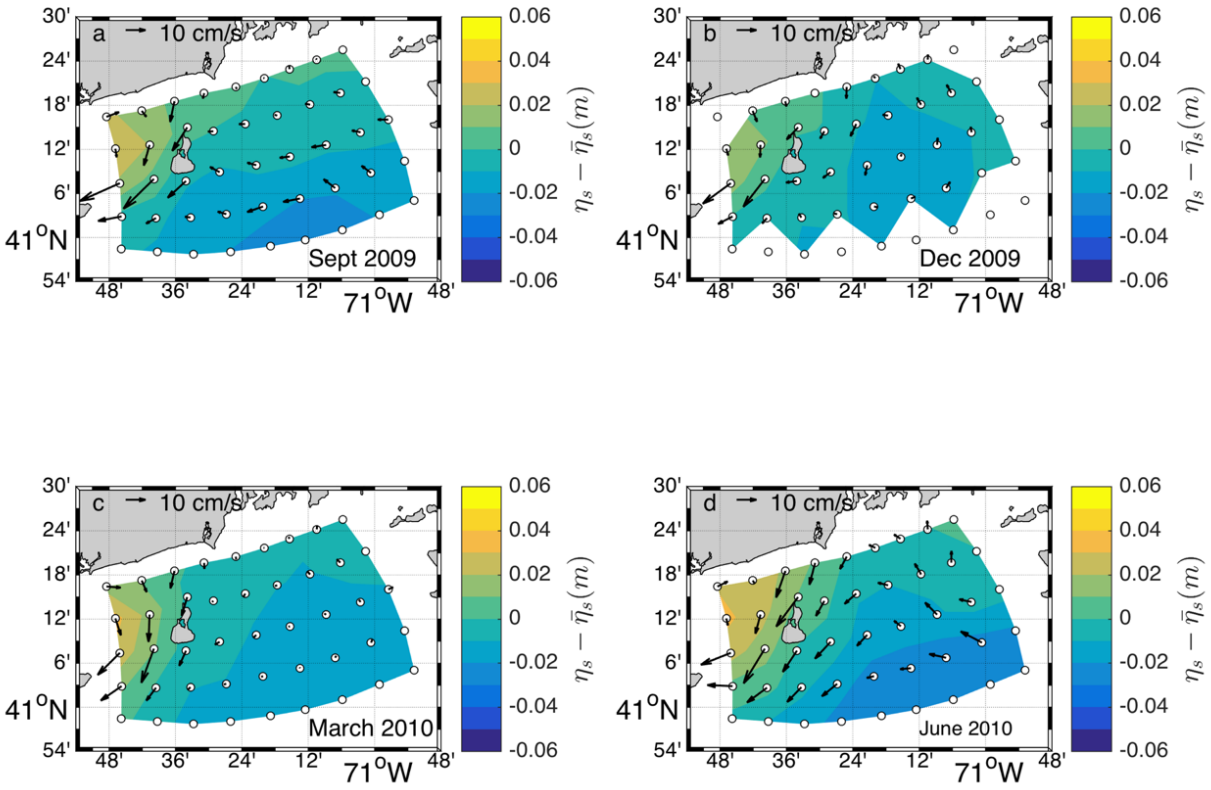

Figure 28: Geostrophic velocity estimates assuming the Coriolis term is balanced by the baroclinic component of the pressure gradient. Depth-averaged geostrophic velocities (arrows) are calculated from data obtained during the (a) September 2009, (b) December 2009, (c) March 2010 and (d) June 2010 surveys. Depth-averaged velocities are displayed on top of contoured relative steric heights.

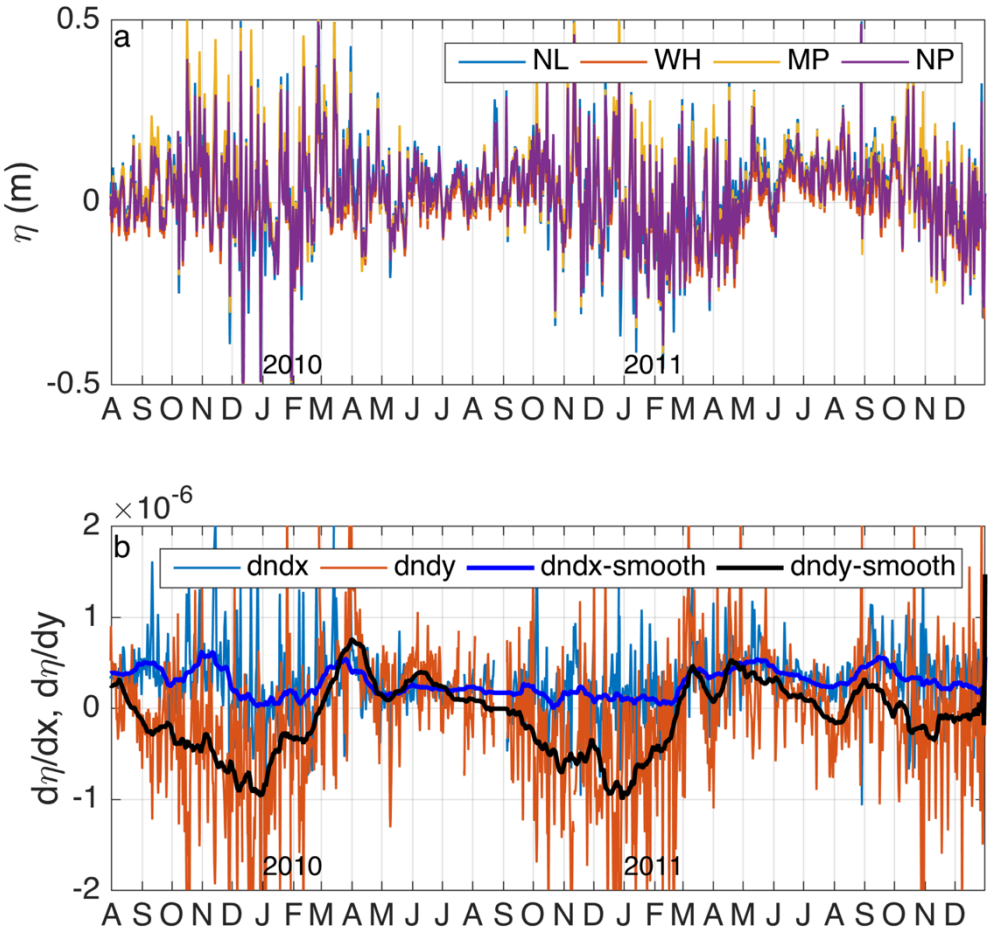

Figure 29: Sea-surface heights and gradients for New London (NL), Woods Hole (WH), Montauk (MP) and Newport (NP) tide gauges. (a) Sea-surface height is referenced to NAVD88 and filtered with 33-hour low pass filter. (b) The east (blue) and north (red) SSH gradients calculated across the region. Dark blue and black lines are smoothed over 30 days.

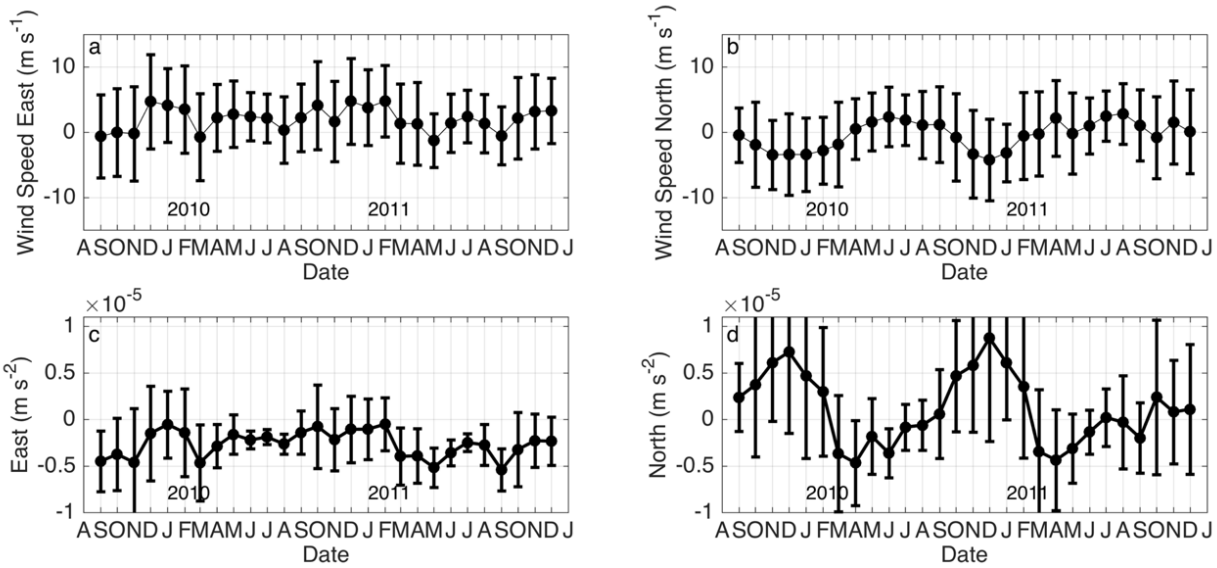

Figure 30: Monthly averages of (a & b) wind from BUZM3 and (c & d) SSH gradients calculated from tide gauge stations. (a & c) are in the eastward direction. (b & d) are in the northward direction. Error bars indicate the standard deviation of data sets.

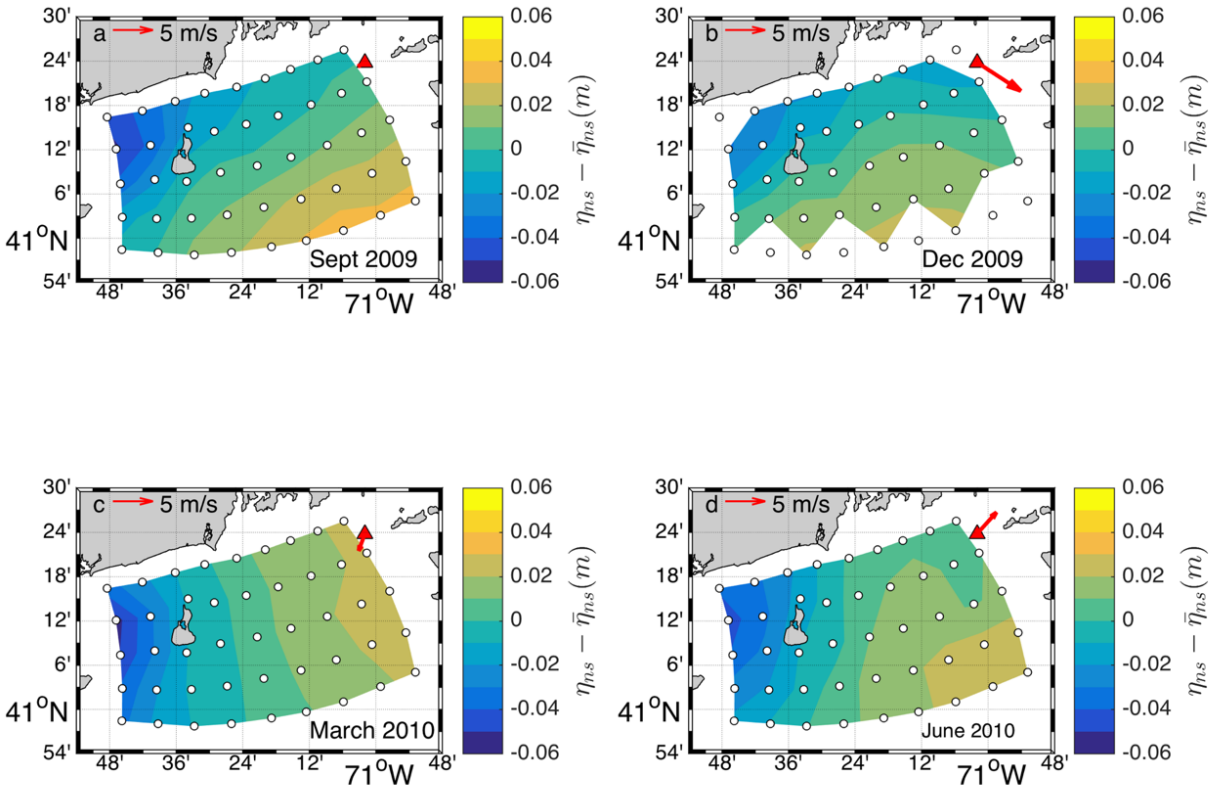

Figure 31: Barotropic relative sea-surface height estimations for each of the four CTD deployments. Average sea-surface height is subtracted from monthly estimations to calculate a relative sea-surface height. (a) September 2009, (b) December 2009, (c)

March 2010 and (d) June 2010. Monthly average wind magnitude and direction is shown by red arrow at station BUZM3 (red triangle).

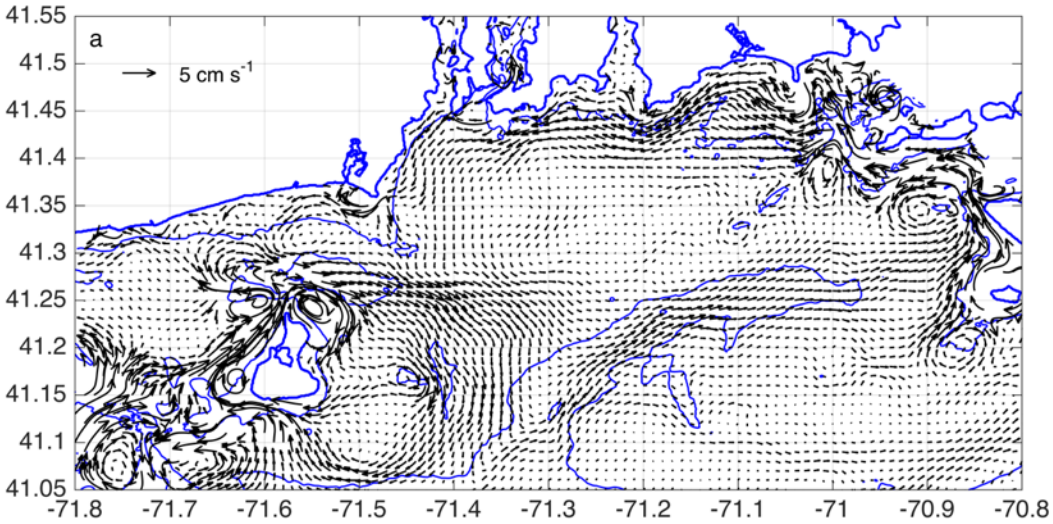

Figure 32: ROMS results for uniform density, no atmospheric forcing, radiative boundary conditions and only the M2 tidal constituent. Depth-averaged velocities are plotted every 12 grid nodes. Velocities are averaged over a tidal cycle. Bathymetry contours (blue) are drawn every 20 m.

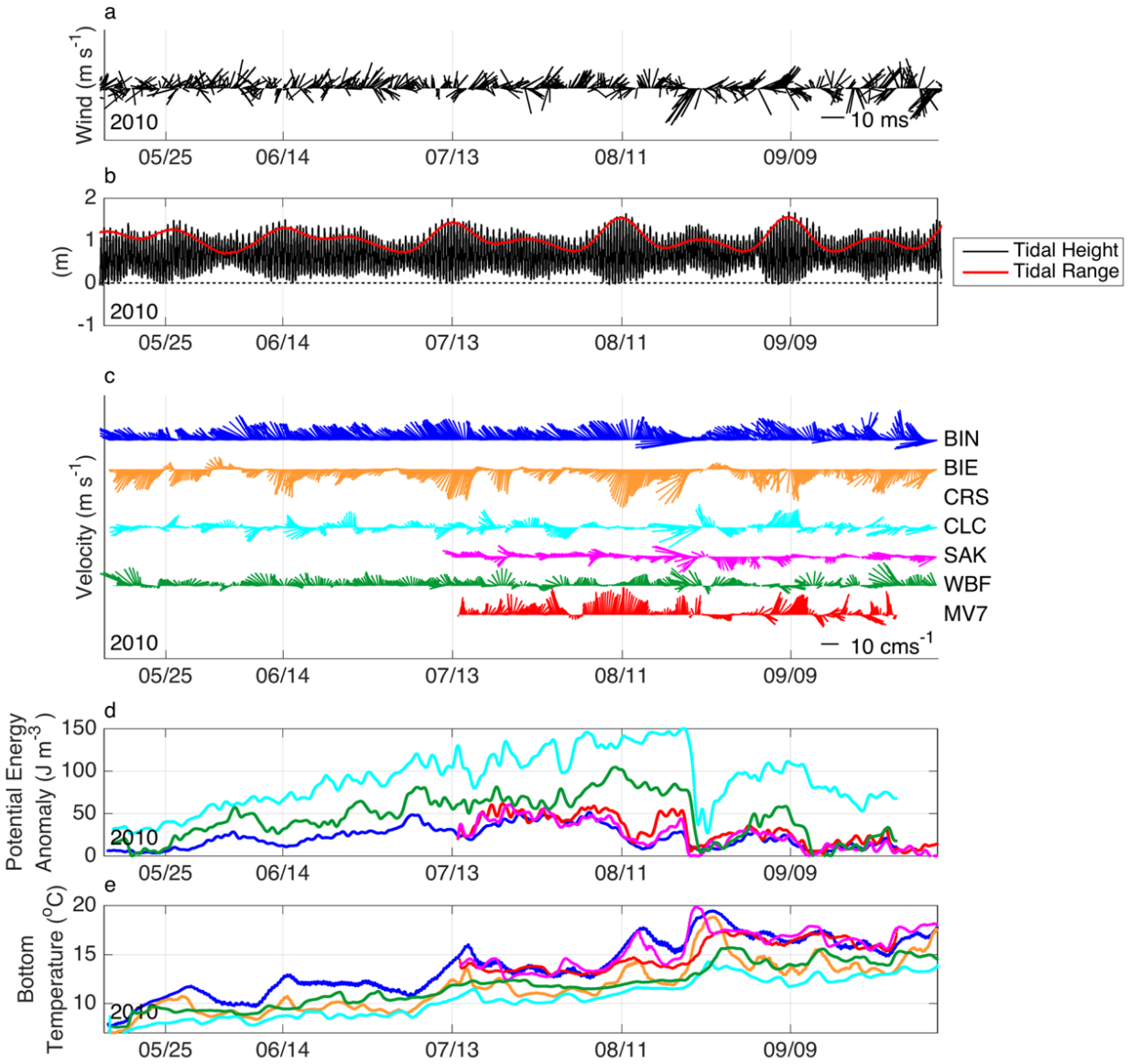

Figure 33**:** Seasonal measurements in RIS. (a) Wind estimates from BUZM3, (b) tidal height and range from Newport, RI tide gauge, (c) depth-averaged velocities at six moored stations, (d) potential energy anomalies for all six stations except BIE, (e) bottom temperature measurements made at ADCP for all six stations. All data is 33-hour low pass filtered except for tidal measurements. Tidal height is not filtered and the tidal range is bandpass filtered between 7 days and 3 months.

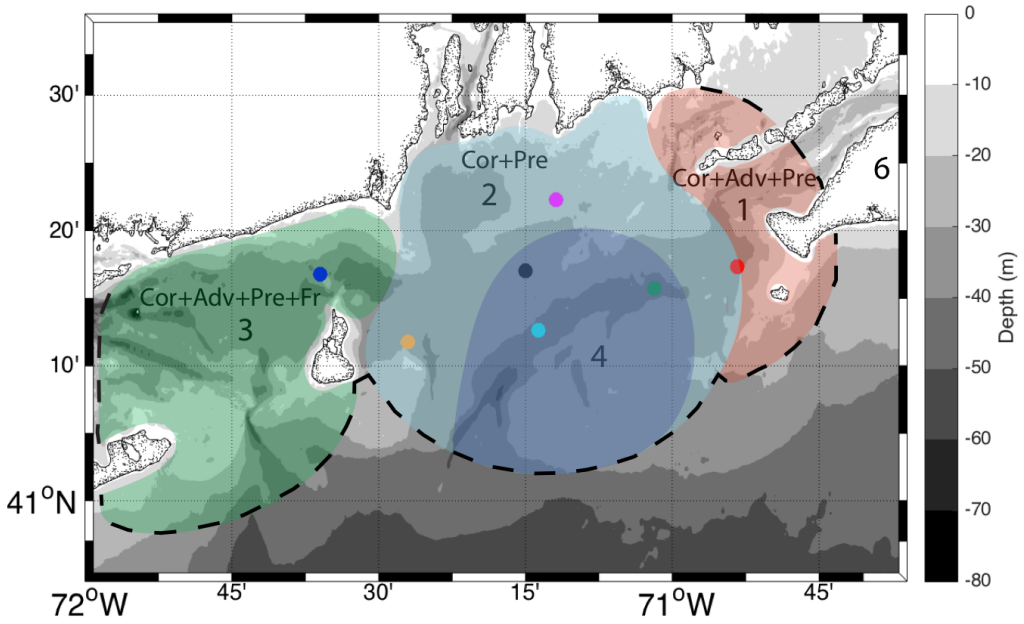

Figure 34: Dividing RIS into four regions based on momentum equation magnitudes. Regions, roughly outlined, are assumed to have similar major momentum forces throughout individual regions. Uncertain boundaries are denoted with dotted lines. Major momentum terms are abbreviated next to each region of interest. Moored ADCP locations are highlighted with circles. Station colors are the same as Fig. 1. Bathymetry is contoured every 10 m.

MANUSCRIPT III

Tidally Driven Stratification Changes in Narragansett Bay

By

Christina A. Wertman[1], David Ullman[1], Christopher R. Kincaid[1], Kathleen Donohue[1] & Robert A. Pockalny[1]

To be submitted to ***Journal of Marine Systems***

---

[1]Graduate School of oceanography, University of Rhode Island, Narragansett, RI 02882, USA.

Abstract

Since 1999, seasonal time series of temperature and salinity measurements have been collected from multiple buoys in Narragansett Bay. These in situ data have provided hydrographic information about the local water column and stratification. In this study, we utilize these data along with numerical modeling to assess the influence of particular environmental factors on stratification. Specifically, we find that tidal height directly correlates with stratification changes at timescales on the order of hours. We set up an idealized simulation with constant freshwater input and no surface fluxes to determine the relative contributions of advection, straining, and differential diffusion from tidal velocities on stratification. We find that, due to the local geometry and bathymetry of Narragansett Bay, the stratification varies both temporally and spatially. Temporal changes are controlled by advection and straining. These common stratification variations can further be characterized into two distinct advection-driven regimes. The location of these regimes depends on the local stratification gradient. The first regime is characterized by advection of more highly stratified water from the north, which produces a maximum in stratification occurring during slack low tide. The second regime results from advection bringing more stratified water from the south into relatively shallow, well-mixed areas. This regime is characterized by the occurrence of a stratification maximum preceding slack high tide.

1. Introduction

Water column stratification plays a major role in biological, chemical and physical processes within estuaries. The degree of stratification regulates the vertical exchange within the water column. Weaker stratification allows for increased vertical

mixing, which leads to more uniform distribution of nutrients, dissolved oxygen and plankton. The vertical exchange between oxygen-depleted deep water and the oxygen-rich surface is reduced as a result of strong stratification, potentially leading to deleterious conditions such as hypoxia and anoxia (Lin et al., 2006). For estuaries, such as Narragansett Bay (NB), stratification has been noted to play an essential role in the regulation of hypoxic events created by algal blooms (Deacutis et al., 2006).

Stratification patterns in estuaries vary over a range of temporal scales. Previous studies indicate that changes in stratification, defined as the vertical difference in density, can be affected by surface heat fluxes (Lund-Hansen et al., 1996), precipitation and evaporation (Nahas et al., 2005), mixing (Burchard and Hofmeister, 2008), straining (Rippeth et al., 2001), and advection (Simpson and Bowers, 1981). Timescales for changes in stratification range from less than an hour, due to mixing and turbulence, to over a year, due to seasonal changes in freshwater input and solar heating.

NB is a unique estuary to study changes in stratification because of its low freshwater input and complex geometry. We use observations and numerical models to answer three questions. First, when and how much does stratification change in NB? The available time series, over 10 years of hydrographic data, allows for the direct characterization of spatial and temporal stratification patterns. The second is why does stratification change? We employ the statistical techniques of spectral and coherence analysis on in situ stratification measurements to determine which environmental parameters contribute to the patterns observed in NB. This analysis focuses on the effects that environmental factors such as solar radiation, river flow,

tides, and wind have on stratification. In addition, we use numerical model simulations to investigate a subset of these external forcing factors in greater spatial and temporal detail than can be accomplished using direct observations. Our last question is how does the stratification change compared to that in other estuaries? We relate our analysis of stratification to larger scale variations in estuarine processes.

2. Narragansett Bay Background

NB is a partially mixed estuary classified geologically as a drowned river estuary (McMaster, 1960). The bay is 40 km long and 15 km wide with an overall north-south orientation. The southern limit of the bay is delimited by Rhode Island Sound and the northern reaches are characterized by the inflow from the Taunton and Blackstone rivers. The bay is littered with embayments and islands resulting in an average channel width of around 5 km. Despite the relatively small channel widths, NB has a Kelvin number of order 1, meaning rotational effects are often important when describing fluid flow (Codiga, 2012; Pfeiffer-Herbert et al., 2015). The average depth is relatively shallow at approximately 10 m relative to mean sea level (e.g. Kincaid et al., 2003). The deepest part reaches up to 50 m in the lower East Passage. Studies of topographic effects in estuaries are wanting, as many numerical models simplify geometry and bottom bathymetry. We add to the understudied area of bathymetrically complex estuaries by examining stratification in NB.

2.1 Sources of Stratification

Several environmental factors including climate, river run-off, and tides control the water column properties and processes in NB in predictable ways. Climate

regulates properties important to stratification, such as precipitation, evaporation, heat flux and wind.

On average Rhode Island and NB receive 10 cm of precipitation per month (*2016 Annual Summary with Comparative Data: Providence, Rhode Island (KPVD)*, 2016). Precipitation is a source of freshwater applied to the surface of NB that increases stratification. In the summer, evaporation exceeds precipitation due to the increase in solar insolation reducing stratification (Fan and Brown, 2003; Pilson, 2008). Surface heat flux also changes the thermal structure of the water column, tending to increase stratification when heat is applied to surface waters.

Another component of the climate in Rhode Island is the seasonal change in wind patterns. During the summer, winds are predominately to the northeast (e.g., Codiga and Ullman, 2010). During the winter, wind direction is more variable, but primarily blows to the east or southeast. Synoptic storms are more common in the winter and blow from the northeast (Kincaid et al., 2008). In addition to direction, winds vary in magnitude. Stronger winds occur during the winter, averaging 10 m s^{-1}. Synoptic weather patterns in the winter tend to be even larger with wind magnitudes up to 25 m s^{-1} (e.g. Codiga and Ullman, 2010) and often lasting 2 to 3 days (e.g. Weisberg and Sturges, 1976). Conversely, the summer season is often characterized by weaker winds, averaging 5 m s^{-1} (e.g. Pilson, 2008). In addition to the seasonal variation in wind magnitude, the summertime winds also exhibit a diurnal periodic variation, known as a sea breeze. The sea breeze effect, producing landward (northward) winds during afternoon hours, is created by diurnal fluctuations in the temperature difference between the land and water (Spaulding and White, 1990).

Not only do winds throughout the year play a role in vertical mixing, but they also induce changes in flow within the bay. Pressure gradients caused by along-estuary winds (axial winds) are an important driver in estuarine circulation, as the winds force flow into or out of an estuary (Geyer, 1997; Li and Li, 2011, 2012; Scully et al., 2005). The axial winds create a buildup of water at the head or mouth of estuaries, creating a pressure gradient resulting from the tilting of the sea-surface. The pressure gradient drives a return flow in the opposite direction of the wind, along the bottom. The resulting circulation induces straining, which changes stratification through the interaction of velocity shear and horizontal density gradients. Often, down-estuary winds create an increase in stratification. The resulting pressure gradient increases estuarine two-layer flow and drives less saline near-surface water over more saline water at depth. Up-estuary winds tend to reduce stratification as pressure gradients oppose estuarine two-layer flow.

Another driver of stratification is the rivers that bring freshwater into NB, primarily from the north. The average freshwater input is estimated to be 93 $m^3 s^{-1}$ (Pilson, 1985). The largest contributions are from the Blackstone and the Taunton rivers, with average fluxes of 22 $m^3 s^{-1}$ and 14 $m^3 s^{-1}$, respectively (*Water-resources data for the United States, Water Year 2010*, 2012a; *Water-resources data for the United States, Water Year 2010*, 2012b). However, the overall freshwater input is relatively small, when compared to estuaries like the Chesapeake Bay (2180 $m^3 s^{-1}$) and Delaware Bay (570 $m^3 s^{-1}$) (Gay and O'Donnell, 2009; Whitney and Garvine, 2006).

River discharge at the head of NB creates a spatial density gradient, with density increasing towards the south (Pilson, 1985). Vertical salinity differences account for approximately 80% of the stratification in the bay and are directly dependent on river discharge (Codiga, 2012). NB usually has some amount of stratification throughout the year, classifying it as a partially mixed estuary.

The highest river discharge is in the spring after seasonal snow melts (Spaulding and Swanson, 2008). Synoptic storms also contribute to the periodic nature of the river flow on shorter time-scales. Storm runoff generates a large peak in river discharge followed by a slower decline in river flux for several days.

2.2 Mechanisms of Changing Stratification

Tides are perpetually a driving force acting on NB. The characteristic tidal range at Newport, RI near the mouth of the bay is 1 meter and increases to 1.3 meters at the head of the bay in Providence, RI (*Tidal Current Tables 2016- Atlantic Coast of North America*, 2016). Hicks (1959) found that the largest tidal component in NB is the M2, the principal lunar tidal constituent, followed by the M4 and M6. The M2 tidal flow interacting with bottom friction and momentum advection produces the overtides at higher frequencies, i.e. M4 and M6.

The observed tides and tidal velocities are representative of a standing wave, with high and low water approximately corresponding to slack velocities (Hicks, 1959). The tidal ellipses, a way of representing the magnitude and direction of tidal flow, are elongated and oriented in a north-south direction. This indicates the influence of forced flow along the axis of NB. Tidal ellipses become more circular with depth, with reduced velocity magnitude due to bottom friction. Changes in tidal

current speed with depth creates a velocity shear during the tidal cycle. This is important as it results in tidal straining.

On time-scales longer than the tides, the general circulation, often called the residual flow, affects stratification through fluid motion. Residual flow is driven by the buoyancy and Coriolis forces in NB (Rogers, 2008). The horizontal density difference, created by the influx of fresh water to the north and salt water to the south, drives a gravitational circulation common in many partially mixed estuaries (Weisberg and Sturges, 1976). Often described as a two-layer system, the fresher upper layer moves seaward to the south, while the saltier lower layer moves landward to the north. Tidal velocities are not strong enough to completely mix away vertical density differences and the gravitational flow acts to stabilize the pycnocline. Average residual velocities in NB are on the order of 10 cm s^{-1} (Kincaid et al., 2003).

The gravitational flow observed in NB is altered by the rotation of the Earth, the Coriolis force. Rotation plays a role in fluid motion in NB as the widths of the channels are on the same order of magnitude as the internal radius of deformation, the internal Rossby radius (2-4 km) (Kincaid et al., 2003). The result of the Coriolis force is a deflection of water to the right in the northern hemisphere. This causes a general counter-clockwise flow around NB and the large islands. A result of this counter-clockwise flow is the deflection of isopyncals horizontally. Spatially, the isopyncals trend northeast to southwest, causing the East Passage to be denser than the West Passage (Hicks, 1959).

The combination of tidal and residual flow results in circulation that changes stratification. Flow changes stratification through advection, straining and mixing.

Two end-members of tidally driven stratification change are pure advection and pure straining. In areas where stratification gradients are large over the length of water parcel tidal excursions, advection primarily modifies stratification (Whitney et al., 2012). This scenario occurs when there are strong tidal velocities and horizontal stratification gradients. Often freshwater input and mixing creates a stratification gradient whereby stratification increases toward the head of the estuary. Advection of the stratified water column, during ebb tides, increases stratification. During flood tides, advection decreases stratification, bringing less stratified water into the estuary. We illustrate this schematically in Fig. 1a. An example of this would be Conway estuary in north Wales (Turrell et al., 1996).

Straining becomes important in estuaries with strong velocity shear and horizontal density gradients. For an estuary with increasing density toward the mouth, differential advection, or straining, created by the sheared ebb current brings freshwater over saltier water, increasing stratification. During flood tides, the differential advection works in the opposite sense, bringing saltier water over fresher water, reducing stratification (Whitney et al., 2012). We illustrate this schematically in Fig. 1b. Along with turbulent mixing, tidal straining is the dominant mechanism in estuaries such as the Chesapeake Bay, the York River, and Liverpool Bay (Li and Li, 2011; Scully and Friedrichs, 2007; Simpson et al., 1990). As most estuaries have spatial variations in stratification, density, depth-averaged velocity and velocity shear both advection and straining participate in changing stratification. We find that in NB straining and advection both play a major role in controlling stratification over a tidal cycle, which we explore in section 6.3.

In areas with strong velocity shear, mixing becomes important. Mixing and diffusion tend to reduce gradients. Vertical mixing, often driven by the bottom friction interacting with a flow field, will homogenize the water column vertically, reducing stratification. Vertical mixing is thought to often dominate mixing in the open ocean and estuaries, especially on shorter time-scales (e.g. Rueda and Schladow, 2009). Typical vertical diffusivity values in the literature range from $10^{-6} – 10^{-1}$ $m^2 s^{-1}$ (e.g. Bowden, 1967; Geyer and Signell, 1992; Li et al., 2005). In our numerical model the grid cells within NB are on the order of 50 m in size and we use a horizontal diffusion coefficient (K_H) for temperature and salinity of 1 $m^2 s^{-1}$. This provides a time-scale over which horizontal diffusion is important of O(1) hour $(\frac{\Delta x^2}{K_H})$. In our model, with a time step of 20 s, vertical diffusion is more important at these shorter time-scales.

3. Data

In this study, we set out to compare stratification with environmental factors in order to assess the major driving mechanisms. High frequency data from moored stations in NB allows for comparison with environmental variables at various time-scales, and is ideal for our analysis. In particular, we focus on how tides are responsible for the periodic changes in stratification. We do this using our idealized numerical experiments and find that our models are consistent with observations. Below are descriptions of the data used, including buoys, environmental observations and our numerical model results.

3.1 Buoy Data

The Narragansett Bay Fixed Site Monitoring Network (NBFSMN) is a collection of sensors that measure temperature, salinity, dissolved oxygen and

chlorophyll in NB (Bergondo et al., 2005; Stoffel and Kiernan, 2009). These buoys have a sensor located 1 m below the surface and another located at 0.5 m above the sediment-water interface (Stoffel and Kiernan, 2009). The buoys are primarily positioned in the northern half of the bay, with most of the stations located in the center or western side of channels and embayments (Fig. 2a).

Data is primarily collected in the warmer months from May through October, with sampling every 15 minutes. The exceptions are stations GB and TW, which have predominantly continuous records during all times of the year (Fig. 3). We choose to perform our numerical experiments during summer months, described below, when we can compare to the majority of the NBFSMN station observations. The NBFSMN data began in 1999, however, the period from 1999 to 2003 is not particularly useful, as only two stations were recording data. Half of the stations were online by 2003, and by 2008 all 10 stations were recording observations. Timelines of data availability, from 1999 to 2014, are shown in Fig. 3.

3.2 Environmental Data

We investigate four environmental factors that contribute to stratification: surface heat flux, river runoff, tides and wind. Surface heat flux is a combination of radiative fluxes, latent heat and sensible heat fluxes. Estimates, for the region around Narragansett Bay, are obtained from NOAA National Center for Environmental Prediction North American Regional Reanalysis (NARR). This model has 1/3 deg resolution and output estimated every 3 hours (*NARR data provided by the NOAA/OAR/ESRL PSD, Boulder, Colorado, USA, http://www.esrl.noaa.gov/psd/)*.

The second environmental factor, river runoff, is measured at several gauges around NB by the United State Geological Survey (USGS). For comparison with NBFSMN observations, we use USGS station 01113895, measuring the Blackstone River, which enters NB at the head of the Seekonk River. Daily measurements of discharge are available from this station starting in 2003. In addition to the Blackstone, we also use observations of three other major rivers, the Moshassuck, Taunton, and Hunt Rivers in our numerical model. Riverine data is obtained for year 2010 and used in our spin-up model to create realistic stratification in NB.

The third environmental factor, tides, are measured at tide gauge station 8452660 at Newport, RI (Fig. 2a). We use data from the time period 1999 to 2014. Tidal heights, referenced to Mean Lower Low Water, are sampled at 6-minute intervals.

Finally, wind velocities, measured 10.6 m above sea level at hourly intervals, are obtained from the National Oceanographic and Atmospheric Administration (NOAA) tide gauge station 8452660 located in Newport, RI. Data is available beginning in October of 1999, providing over 14 years of comparison with stratification data.

3.3 ROMS Model

In addition to water column observations, we use the Regional Ocean Modeling System (ROMS) to characterize spatial variations and quantify changes in stratification to compare with our observations. ROMS is widely used in the coastal modeling community for simulating estuarine flows and is particularly well suited for modeling estuarine exchange, circulation and dynamics (e.g. Kremer et al., 2010;

Lerczak and Geyer, 2004; Li and Li, 2012). We simulate estuarine processes in NB with ROMS due to the spatial limitations of the NBFSN buoys. We use a numerical model to constrain the horizontal variability within NB.

ROMS is a hydrostatic, primitive equation model that uses a structured curvilinear grid. The model domain includes NB and extends into Rhode Island Sound, capturing exchange between the continental shelf and the estuary (Fig. 2b). The grid includes 750 x 900 horizontal nodes, with 15 vertical layers. Bathymetry data from a NOS Hydrographic Survey of Narragansett Bay was obtained from the National Oceanic and Atmospheric Administration's Geophysical Data Center. The vertical levels are stretched with the lowest vertical spacing at the head of the bay (0.10 m) and the largest vertical spacing (7 m) at the open southern end. Horizontal resolution is maximized at the head of the bay, with grid spacing in that region of approximately 40 m. Resolution is reduced in Rhode Island Sound, reaching a maximum grid spacing of approximately 150 m.

There are several numerical parameters influencing mixing in ROMS that are important to our study. Bottom stress is computed assuming a logarithmic near-bed velocity profile, with a roughness length scale of 1 mm. We use the Mellor Yamada Level 2.5 closure scheme for vertical mixing parameterization. Coefficients of horizontal eddy viscosity and diffusivity are both set to 1 $m^2 s^{-1}$. Vertical diffusivity, computed from the closure scheme averaged 4 x 10^{-4} $m^2 s^{-1}$, with a minimum value set to 10^{-7} $m^2 s^{-1}$.

We perform two numerical experiments for this study. The first is a spin-up experiment to obtain reasonable hydrographic properties, and the second is to test how

tides change stratification. In the first experiment, for initiation and validation, the model is forced by tidal constituents, horizontal boundary conditions, river inflow and meteorological surface conditions. Nine major tidal constituents are obtained from the ADvanced CIRCulation model (ADCIRC) (Mukai et al., 2002). Boundary conditions are forced with the results of regional model runs of the northeast U.S. shelf which were made available by the University of Massachusetts, Dartmouth and Woods Hole Oceanographic Institution (*Finite Volume Coastal Ocean Model [Internet]*., 2013). The time series of boundary values are filtered with a 33 hour 4^{th} order Butterworth low-pass filter to remove tidal signals. The model is run from January 1, 2010 until July 31, 2010. The temporal evolution of the depth-averaged density, at NBFSMN locations, is displayed in Fig. 4**.** The depth-averaged density, in NB, decreases in the spring and summer.

Model surface forcing, for the spin-up experiment, includes the net surface radiation, surface air temperature, relative humidity, air pressure and wind speed. Estimates of meteorological forcing are obtained from the Weather Research and Forecasting (WRF) Model run by the University of Massachusetts, Dartmouth and Woods Hole Oceanographic Institution for the Gulf of Maine reanalysis for the year 2010 (*Finite Volume Coastal Ocean Model [Internet]*., 2013). Although the meteorological forcing is spatially variable, we choose to prescribe all parameters uniformly over our domain, except for wind. The 9-km resolution WRF parameters were averaged over our domain, while the wind velocities are implemented at the full 9-km resolution.

We compare output from the spin-up numerical experiment with realistic forcing from January 1, 2010 to July 31, 2010 with NBFMSN buoy data. The purpose of this model run was to initialize summer stratification in the bay, not to represent the buoy stations exactly. We estimate how well our model predicts 2010 buoy data using the Willmott Skill (Willmott, 1982):

$$Skill = 1 - \frac{\sum_{i=1}^{N}(T_{mod} - T_{obs})^2}{\sum_{i=1}^{N}(|T_{mod-}\overline{T_{obs}}| + |T_{obs-}\overline{T_{obs}}|)^2}$$

where T_{mod} is model prediction of a variable, such as temperature or salinity, and T_{obs} are the NBFSMN observations. We calculate the Wilmott Skill for surface and bottom measurements of temperature and salinity as well as the vertical density difference measured at the buoy locations.

Over the time period modeled, we find temperature agrees the best with observations, having the highest Willmott Skill. Both surface and bottom temperature have a station average skill over 0.90. Skills for salinity and vertical density differences are on average greater than 0.55. Codiga (2012) found that the vertical density difference in NB was driven by salinity, therefore, the salinity and the vertical density difference skill should be similar.

One reason the salinity agreements might be low could be our choice of river forcing. We only used 4 rivers, and although, they are the largest, the rivers we chose do not account for the total freshwater input into the bay. Another potential discrepancy might come from the complex bathymetry of NB. Our model only resolves bathymetry variations down to 40 m and small-scale structures (~1 m) could have an influence on fluid flow especially at stations BR and CP, which are located adjacent to channels.

Table 1: Willmott Skill calculated from the January 1 - July 31, 2010 model run.

	BR	CP	GB	MH	MV	NP	PP	QP	SR	TW
Temperature Surface	0.92	0.94	0.99	0.97	0.92	0.95	0.96	0.95	0.93	0.99
Temperature Bottom	0.70	0.74	0.99	0.97	0.88	0.92	0.88	0.93	0.89	0.99
Salinity Surface	0.49	0.50	0.67	0.76	0.68	0.58	0.49	0.73	0.65	0.63
Salinity Bottom	0.71	0.65	0.78	0.71	0.67	0.64	0.77	0.78	0.87	0.57
Vertical Density Difference	0.45	0.48	0.34	0.74	0.68	0.51	0.59	0.81	0.57	0.59

We are most interested in the effects that tides have on stratification, as rivers, wind and solar forcing have been well studied in NB and other estuaries (e.g. Codiga, 2012; Scully et al., 2005; Rippeth et al., 2001; Simpson et al., 1981). Therefore, the second experiment has no sources and sinks of stratification, except for riverine input. Specifically, the ROMS model is run with no boundary forcing, no surface fluxes, no wind stress and only the M2 tidal constituents. We call this our idealized experiment.

The idealized experiment is started during a period when known stratification is present in the bay; i.e. during the early summer, at the end of July. The two major tributaries include the Blackstone and Taunton rivers. The constant freshwater flux is specified as 22 $m^3 s^{-1}$ for the Blackstone and 14 $m^3 s^{-1}$ for the Taunton. Our model provides a valid first order estimation of stratification as these two rivers account for about 55% of the freshwater flux into NB (Ries III, 1990). In addition, all but the M2 tidal constituents are removed to limit the change in stratification due to spring-neap variations in tidal velocities. We let the model come into periodic steady-state. This is determined by running the simulation until velocity, density and stratification are not

changing at periods longer than a tidal cycle. In this way, we can isolate the contributions from the tides.

We confirm that our idealized experiment has a reasonable temperature and salinity distribution by comparing buoy locations in the model with real observations. After our idealized experiment comes into steady state, we plot near surface and near bottom estimates of temperature and salinity, averaged over a tidal cycle (Fig. 5 & 6). We find that our model conditions are closest to June and July averages of NBFSMN temperature and salinity measurements (Fig. 5 & 6). The temperature of our steady-state model is cooler than the July averages as a result of no heat exchange with the surface as well as the interaction with a colder Rhode Island Sound.

Observational data was used from all available years at the buoy stations (Fig. 5 & 6). Observational data tends to be fresher than our model, but our numerical results fall within the standard deviation of the buoy observations for June and July. We expect the model to be saltier than the observations, as our idealized experiment only introduces freshwater at the Blackstone and Taunton, a subset of the total freshwater influx coming into the Bay. At stations in Greenwich Bay, GB and SR, vertical density differences do not agree well with observations. This is likely because our model does not include a freshwater source in or near Greenwich Bay.

4. Analysis

A goal of this study is to better quantify the variability of stratification both temporally and spatially. We do this through a combination of data exploration and comparison with known forcing variables. Our analysis of observations helps identify what scales and forcing conditions are important to study in our numerical model.

4.1 Analysis of Observations

We analyze the time series of both stratification observations and numerical modeling results. Stratification in the observational data specifically refers to the density (sigma-t) difference between the top and bottom NBFSMN sensors. The NBFSMN sensors record temperature and salinity, which is used to calculate sigma-t, with the MATLAB SEAWATER Library. Similar to Codiga (2012), we find that using the Brunt-V*äisälä* frequency, or buoyancy frequency, would be misleading with this data set. This is because the stations are primarily fixed above and below the pycnocline. The Brunt-V*äisälä* frequency could change solely based on the depth at the various stations, making inter-station comparison challenging.

Through temporal analysis of the observed stratification, we characterize the frequency content of the dataset. Since the power spectral densities are calculated with continuous signals, we pad times with missing data with station averages. This may bias some of the high frequency signals but does not affect our analysis. We use the Welch method to estimate the power of a signal at different frequencies. Specifically, the power spectral density is found from using Fast Fourier transforms of the auto-correlated stratification time series (Emery and Thomson, 2001). We use a Hamming window of 2048 points and each time step is 15 minutes. The longer length of the time series window provides us with higher frequency resolution but increases the variance in the spectral density estimate. Overlap of the time series is set at 50%, to reduce the variance (Emery and Thomson, 2001).

Calculating the magnitude squared coherence of stratification with environmental observations helps establish which environmental factors are important.

Magnitude squared coherence determines the frequencies at which two signals are most related. A value of 0 indicates no relation of the two signals, while a value of 1 indicates that the two signals are perfectly and linearly correlated. We use the mscohere function in MATLAB to calculate the coherence, which utilizes Welch's averaged modified periodogram method. The method utilizes the cross-spectral density of two-time series as well as the auto-spectral density of each time series to calculate coherence at each frequency of interest. Welch's average method uses multiple segments of equal length to improve results and reduce variance. The cross-spectral density is a complex number and therefore, can be used to calculate the phase lag between two signals. For each station, we compare and calculate the coherence of the vertical density difference with four data sets; surface temperature, river discharge, tides and northward wind.

We determine the significance of each magnitude squared coherence with a method developed by Bendat and Piersol (2010):

$$\alpha = \sqrt{2}\frac{1 - C_{xy}}{\left|\sqrt{C_{xy}}\right|\sqrt{df}}$$

where C_{xy} is the coherence at a given frequency and df is the degrees of freedom. We calculate the degrees of freedom as $df = \frac{2L}{nfft}$, where L is the total length of the time series and nfft is the length of the Hamming window. If the magnitude squared coherence is greater than α, then the coherence is considered significant at that frequency.

4.2 Analysis of ROMS

We use the numerical output of our two ROMS experiments to develop a stratification scenario and to explore possible causes of stratification change at tidal time-scales. Our spin-up experiment is used for direct comparison with observations for the year 2010. We calculate the stratification as the density difference between near-surface and near-bottom levels at NBFSMN station locations in the model output. Additionally, we explore frequency analysis on the output from our spin-up numerical model to assess the similarity between the observations and model. It is important to note that the numerical spin-up experiment does not produce the exact results observed during the modeled year 2010. What is more important is that the model reproduces the same scale of variation that we observe at NBFSMN stations, which is why spectral analysis is useful.

We use our idealized experiment to predict the change in stratification, to within the capability of our experiment, at a finer spatial scale than our observations. Unlike the observations at moored NBFSMN stations, ROMS allows us to explore the causes of stratification changes $\left(\frac{\partial \mathrm{N}^2}{\partial \mathrm{t}}\right)$ due to the addition of velocity estimates, which are rarely available in NB. Model circulation estimates provide valuable information, and allow for the prediction of $\frac{\partial \mathrm{N}^2}{\partial \mathrm{t}}$ in NB.

We choose to use a definition related to the vertical gradient of density to define stratification. Spatial variability of stratification is explored with the numerical model, which carries out precise calculation of density and velocity. The study of the stratification balance allows for the evaluation of mechanical changes by analyzing advection, straining and differential diffusion (Chen and Sanford, 2009; Li and Li, 2011).

Derivation of the stratification balance begins with the non-linear density conservation equation:

$$\frac{\partial \rho}{\partial t} = \overbrace{-\left(u\frac{\partial \rho}{\partial x} + v\frac{\partial \rho}{\partial y} + w\frac{\partial \rho}{\partial z}\right)}^{advection} + \overbrace{\frac{\partial}{\partial x}\left(K_H\frac{\partial \rho}{\partial x}\right) + \frac{\partial}{\partial y}\left(K_H\frac{\partial \rho}{\partial y}\right) + \frac{\partial}{\partial z}\left(K_v\frac{\partial \rho}{\partial z}\right)}^{diffusion} \quad (1)$$

where ρ is density, $\boldsymbol{u}$ is the velocity vector and K_H and K_v are the eddy diffusivity for the horizontal and vertical, respectively. The rate of change in density is a function of advection, the first three terms on the right-hand side, and diffusion, the second three terms on the right-hand side of eq. (1). We assume that there are no additional sources from heat or freshwater. This assumption is valid for our numerical idealized experiment in which surface fluxes are turned off and rivers are held constant. The exception is at the river nodes, where freshwater comes into the model. We exclude these nodes from our analysis. To find the stratification balance we multiply eq. (1) by $\left(-\frac{g}{\rho_o}\frac{\partial}{\partial z}\right)$ resulting in:

$$\frac{\partial N^2}{\partial t} = \overbrace{-\boldsymbol{u}\cdot\nabla N^2}^{advection} + \overbrace{\frac{g}{\rho_o}\frac{\partial \boldsymbol{u}}{\partial z}\cdot\nabla\rho}^{straining} \quad \overbrace{-\frac{g}{\rho_o}\frac{\partial}{\partial z}\nabla K\nabla\rho}^{differential\ diffusion} \quad (2)$$

$$\frac{\partial N^2}{\partial t} = \overbrace{-u\frac{\partial N^2}{\partial x}}^{advection_x} \overbrace{-v\frac{\partial N^2}{\partial y}}^{advection_y} \overbrace{-w\frac{\partial N^2}{\partial z}}^{advection_z}$$

$$+ \overbrace{\frac{g}{\rho_o}\left(\frac{\partial u}{\partial z}\cdot\frac{\partial \rho}{\partial x}\right)}^{straining_x} + \overbrace{\frac{g}{\rho_o}\left(\frac{\partial v}{\partial z}\cdot\frac{\partial \rho}{\partial y}\right)}^{straining_y} + \overbrace{\frac{g}{\rho_o}\left(\frac{\partial w}{\partial z}\cdot\frac{\partial \rho}{\partial z}\right)}^{straining_z}$$

$$\overbrace{-\frac{g}{\rho_o}\frac{\partial}{\partial z}\left(\frac{\partial}{\partial x}\left(K_H\frac{\partial \rho}{\partial x}\right)\right)}^{differential\ diffusion_x} \overbrace{-\frac{g}{\rho_o}\frac{\partial}{\partial z}\left(\frac{\partial}{\partial y}\left(K_H\frac{\partial \rho}{\partial y}\right)\right)}^{differential\ diffusion_y} \overbrace{-\frac{g}{\rho_o}\frac{\partial}{\partial z}\left(\frac{\partial}{\partial z}\left(K_v\frac{\partial \rho}{\partial z}\right)\right)}^{differential\ diffusion_z} \quad (3)$$

where N^2 is defined as $-\frac{g}{\rho_o}\frac{\partial \rho}{\partial z}$, ρ_o is a reference density and g is the gravitational acceleration. In addition to an advection and differential diffusion term, the stratification balance now includes a straining term. Stratification will change due to straining when a vertical shear is applied to a horizontal density gradient.

ROMS uses the structured Arakawa C-grid and therefore, careful attention must be used when calculating the N^2 balance with a finite difference scheme. Calculations need to consider the volume of the water parcel and the volume of material being advected, strained and diffused into or out of the parcel of interest. Our analysis is based on methods by Li and Li (2011), who describe in detail how to determine the $\frac{\partial N^2}{\partial t}$ finite difference approximations. Our method deviates from Li and Li (2011), as we do not assume N^2 is only a function of salinity. We transform the stratification equation into sigma and curvilinear coordinates, and then depth average:

$$\frac{\partial \overline{N^2}}{\partial t} = -\frac{1}{H}\frac{\partial}{\partial t}\frac{g}{\rho}[\rho(15)-\rho(1)] =$$

$$\overbrace{-\frac{1}{H}\left(\frac{\partial zm}{\partial \xi}uN^2+\frac{\partial zn}{\partial \eta}vN^2\right)\Big|_1+\frac{1}{H}\int_1^{15}\left(\frac{\partial zm}{\partial \xi}\frac{\partial uN^2}{\partial \sigma}+\frac{\partial zn}{\partial \eta}\frac{\partial vN^2}{\partial \sigma}\right)d\sigma}^{\frac{convergence}{divergence}}+$$

$$\frac{1}{H}\int_1^{15}\Bigg(\overbrace{-u\frac{\partial H_z N^2 m}{\partial \xi}}^{depth-avg\ adv\ \xi}-\overbrace{v\frac{\partial H_z N^2 n}{\partial \eta}}^{depth-avg\ adv\ \eta}+\overbrace{\frac{g}{\rho_o}\left(\frac{\partial u}{\partial \sigma}\cdot\frac{\partial \rho m}{\partial \xi}\right)}^{depth-avg\ strain\ \xi}+$$

$$\overbrace{\frac{g}{\rho_o}\left(\frac{\partial v}{\partial \sigma}\cdot\frac{\partial \rho n}{\partial \eta}\right)}^{depth-avg\ strain\ \eta}\Bigg)d\sigma-\overbrace{\frac{1}{H}\frac{gm}{\rho_o}\left(\frac{\partial}{\partial \xi}\left(K_H\frac{\partial \rho m}{\partial \xi}\right)\right)\Big|_1^{15}}^{depth-avg\ diff\ \xi}-$$

$$\overbrace{\frac{1}{H}\frac{gn}{\rho_o}\left(\frac{\partial}{\partial \eta}\left(K_H\frac{\partial \rho n}{\partial \eta}\right)\right)\Big|_1^{15}}^{depth-avg\ diff\ \eta}\overbrace{-\frac{1}{H}\frac{g}{\rho_o}\left(\frac{\partial}{\partial \sigma}\frac{1}{H_z}\left(K_v\frac{\partial \rho}{\partial \sigma}\frac{1}{H_z}\right)\right)\Big|_1^{15}}^{depth-avg\ diff\ \sigma} \qquad (4)$$

The equation is integrated from sigma level 1 to level 15 and divided by the water column height. See Appendix for more details on the transformation. $\xi \; and \; \eta$ are primarily in the cross- and along-estuary directions. Note that the vertical advection and straining terms have canceled. The resulting equation provides an estimate for depth-average stratification rate of change ($\frac{\partial \overline{N^2}}{\partial t}$) on the left-hand side of the equation. $\frac{\partial \overline{N^2}}{\partial t}$ is related to the change in density from the surface to the bottom.

The first two terms on the right-hand side are the divergence of stratification. These terms are a result of tilted bottom bathymetry ($\frac{\partial zm}{\partial \xi}, \frac{\partial zn}{\partial \eta}$). The magnitudes of the divergence terms are only, on average, about 3% of the magnitude of the advective or straining terms and only 10% the magnitude of the estimated error.

The next two terms in eq. 4 are the depth-averaged advection terms calculated in both horizontal directions. The following two terms are the depth-averaged straining terms. The last three terms on the right-hand side of eq. 4 are the differential diffusion terms. Note that these terms are the vertical integration of a vertical gradient. Therefore, the last three terms can be evaluated at the surface and bottom sigma layers. An error estimate is found by subtracting all the calculated terms on the right-hand side of eq. 4 from the estimate of $\frac{\partial \overline{N^2}}{\partial t}$, the left-hand side of eq. 4. Instantaneous values are used to calculate each term on the right-hand side of eq. 4. However, $\frac{\partial \overline{N^2}}{\partial t}$ is calculated N^2 using output every 6 minutes. Therefore, there is a slight error associated with our calculations as $\frac{\partial \overline{N^2}}{\partial t}$ is calculated between output intervals.

5. Observations

5.1 Temporal and Spatial Patterns

Periodic temporal variations in water temperature, salinity and stratification are observed at each NBFSMN station. For discussion, we look at one representative station, CP, and one representative year, 2010 (Fig. 7). The most obvious signal is the seasonal cycle observed in the temperature time series, with the warmest temperatures occurring in late summer and early fall (Fig. 7a). Peak temperatures occur at different times, with the surface maximum in July (26 ^{o}C at CP) preceding the bottom temperature maximum in mid-August (24 ^{o}C at CP). Vertical temperature differences that help drive stratification are present in the spring and are negligible by early fall (Fig. 7b). The maximum vertical water temperature difference was recorded at 10˚ C in July. The water column at CP is nearly uniform in temperature during the fall and winter months. This is true for other stations in NB as well. BR, TW and GB recorded data during winter months and confirm that vertical temperature differences were negligible during the winter.

Salinity is not uniform throughout the year. At station CP, salinity has an annual periodicity with the highest salinity values recorded in September (Fig. 7a). The peak is most likely due to reduced river flow and increased evaporation rates. Because of the importance of salinity on stratification, we look at the vertical salinity differences (Fig 7b). Vertical salinity differences, at station CP in 2010, show a seasonal periodicity with a minimum occurring in September. The largest salinity differences are in the spring, with magnitudes of approximately 5 PSU.

Density exhibits less variability than temperature and salinity, but still shows an annual periodicity. Bottom density at CP is much less variable when compared with

the surface density (Fig. 7c). The station CP data indicate a seasonal trend in stratification that is maximized in late spring and mid fall and minimized during summer months (Fig. 7d & 8). When averaged over individual months, stratification at other stations shows similar patterns, with maximized vertical density differences during the spring months of May and June and minimum values in late summer (Fig. 8).

We calculate the percent contribution of salinity to vertical density differences by dividing the vertical density differences computed with the average temperature at each station with the actual vertical density differences as described by Codiga (2012):

$$\% = 100 * \frac{\Delta\rho[S, \langle T \rangle]}{\Delta\rho[S, T]}$$

where $\Delta\rho$ is the vertical density difference, S is the in situ salinity, T is the in situ temperature and $\langle T \rangle$ is the temporally averaged temperature measured at a given station. Results are listed in Table 2. Contributions of salinity dominate the vertical density differences for warmer months, with percentages ranging from 70 to 88%. Stations in the north such as BR and GB have the highest contribution to stratification from salinity and stations in the south like QP and TW exhibit the lowest. This illustrates the influence of freshwater input from the northern tributaries.

Table 2: Contribution of salinity to the vertical density difference calculated from all available data during May to October.

Station	BR	CP	GB	MH	MV	NP	PP	QP	SR	TW
Contribution by Salinity (%)	88.2	82.6	85.9	78.1	79.7	79.5	76.6	70.7	78.1	74.4

General spatial trends are observed when plotting the average vertical density difference against latitude (Fig. 9). Temporally-averaged vertical density differences at each station are calculated from data collected May through October from all available years. Average stratification increases from under 1 kg m^{-3} at the most southern station, TW, to almost 4 kg m^{-3} at the northernmost station, BR. Stratification increases with latitude. We compared sensor depth difference with average stratification and latitude to confirm that there is not a bias due to individual station configuration. Station sensor depth differences range from 1 m, at GB and SR, up to 9 m, at NP. No trend was found when we compared sensor depth differences with either stratification or latitude. This indicates that the correlation of vertical density differences with latitude is not a result of instrument setup. We conclude that the latitudinal increase in stratification is likely due to the freshwater influx from northern river input.

Lateral variations in stratification may also exist in NB. Stations at similar latitude, between 41.65˚ N and 41.7˚ N, show lateral differences in stratification. Station PP, located in the East Passage, has a larger stratification (2.5 kg m^{-3}) than stations at similar latitude such as MH (2.0 kg m^{-3}) located in Mt. Hope Bay; SR (0.8 kg m^{-3}) and GB (0.6 kg m^{-3}) located in Greenwich Bay; and NP (1.2 kg m^{-3}) located in the West Passage (Fig. 9). These stations could be less stratified compared to PP due to greater differential diffusion and/or the reduced transport of fresh or salty water. Station PP is likely more stratified due to the connection with the mouth of NB and the influx of freshwater from the Providence River Estuary. Comparison of stations at similar latitudes indicates, that of the three passages connected to the mouth of the

bay, the East Passage is the most stratified. This channel is flanked on either side by less stratified areas of the West Passage and Mt. Hope Bay.

5.2 Power Spectral Analysis

To look at higher frequency temporal trends, we perform power spectral analysis on vertical density differences from NBFSMN stations. We plot results in a variance preserving power spectral density to highlight the higher frequencies (Fig. 10). Power spectral density of the stratification reveals several frequencies that have strong influence over the observed signal. Strongest peaks present, from lowest frequency to highest, include a diurnal (1 cpd), M2 (1.932 cpd), M4 (3.865 cpd) and M6 (5.797 cpd) (Fig. 10).

Similar to the observations, the four most prominent frequencies in the spin-up ROMS experiment are diurnal, the M2, the M4 and M6. Spectra computed from the ROMS output sampled at the NBFSMN buoy locations are shown in Fig. 11. The model is resolving mechanisms that change stratification at tidal frequencies.
The spin-up experiment has less variance compared to observations (Fig. 12). This spectral analysis does not conserve variance. Amplitudes of at the M2 frequency are on the O (10^{-2} -10^{-1}) $kg^2\ m^{-6}\ cpd^{-1}$, averaging 0.05 $kg^2\ m^{-6}\ cpd^{-1}$ for observations. The average of the M2 peak amplitude is also 0.05 $kg^2\ m^{-6}\ cpd^{-1}$ for the spin-up experiment output. The amplitude of the higher peak frequencies (M4 & M6) are lower than observations.

5.3 Coherence

To explain the variations observed in the vertical density differences, we compare observed stratification measurements to four key environmental parameters.

Two parameters are sources of stratification (i.e. net heat flux and river discharge) and two are forcing mechanisms (i.e. tides and wind). We assess the likelihood that these mechanisms affect stratification by evaluating their coherence with stratification.

Coherence between vertical density differences and net heat flux, Blackstone River input and northward wind measured at Newport, RI is not statistically significant for most stations. Coherence is determined over periods of 30 minutes to 11 days to encompass the frequency range of the observed spectral peaks. The significance level is calculated by taking into account the degrees of freedom in our analysis (Bendat and Piersol, 2010). The river discharge data is collected daily and linearly subsampled to 15 minutes. While these parameters do not influence vertical density difference over the period band between 30 minutes and 11 days, they likely influence NB stratification on longer time scales. For example, Codiga (2012) has shown the importance of for riverine input at monthly timescales.

The strongest coherence, between vertical density differences and any variable, is obtained when comparing stratification with tidal heights measured at Newport, RI. We highlight the frequencies that are considered significant for each station (Fig. 13). The strongest coherences are measured at the diurnal, M2, M4 and M6; i.e. tidal frequencies. Seven of the ten stations all have their strongest coherence at the M2 frequency and all, but station MH, had significant coherence at this tidal frequency (Fig. 13).

A combination of varied magnitudes across straining, advection and differential diffusion mechanisms can create a stratification maximum at any time during the tidal cycle (Whitney et al., 2012). We explore the timing of stratification by

calculating the phase lag between observed tidal heights and vertical density differences at various frequencies (Fig. 14). A phase lag of 0^o indicates that the tidal height and change in stratification are maximized and minimized at the same time. A phase lag of 180^o or -180^o indicates that the two time series are inversely correlated, so that at high tide, stratification would be minimized and at low tide, stratification would be maximized. The phase lag of stratification behind tidal height varies over the NBFSMN stations. Significant phase lags are red in Fig. 14.

The largest tidal velocities in NB are generated by the M2 tide, on the order of 10's cm s^{-1}, and potentially have the largest impact on stratification. We plot the phase lag for those stations that had significant coherence with tidal height at the M2 frequency (Fig. 15a). This included stations BR, CP, GB, MV, NP, PP, QP, SR and TW. The phase lag is often measured in degrees but can be converted to time by dividing the phase lag by $T/360^o$, where T is the period of interest. Results suggest that the stratification maximum precedes high tide by an eighth of a period (1.5 hours) at southern stations of TW, MV, SR and QP (Fig. 15a). The phase lag increases at the northern stations. At these stations, stratification lags high tide by a half a period (6 hours), around low tide (Fig. 15a).

The tidal wave that proceeds up NB could hypothetically explain the phase lag between southern station and northern stations. For this to be true the tidal height phase lag must be on the order of hours. However, there is only a 15-minute lag in tidal height from the tide gauge stations of Providence and Newport. Therefore, the tidal wave travels too fast to account for the lag of several hours in stratification observed across stations.

A possible explanation for the variations in stratification timing involves straining. Straining-induced stratification suggests that with an increasing density towards the mouth of an estuary, differential advection should maximize stratification during ebb. In this scenario, stratification should lag by half a period behind tidal heights, as stratification should be out of phase with tides (Scully and Friedrichs, 2007). In addition to straining, pure advection could produce the same result, if stratification increases from the mouth of an estuary to the head and mean velocities are strong (Whitney et al., 2012). Therefore, we postulate that either straining or pure advection could be responsible for the stratification maximum near low tide found at the northern stations of BR, CP, GB, PP and NP. We further explore the combination of mechanisms that causes the phase lags for all the NBFSMN stations in following sections**.**

Power spectral analysis shows the dominant frequencies present in our idealized experiment. We identify a peak at the M2 frequency. After calculating the coherence of the vertical density differences with tidal height at Newport, RI, we plot the phase lag for the M2 frequencies in Fig. 15b. This characterizes the lag of stratification behind the tidal height. We plot the phase lag of the same stations as the observational analysis (Fig. 15a) at the M2 frequencies.

Station phase lag between vertical density differences and tidal height at Newport, RI are similar to the observations in Fig. 15a. Stations TW, PP, QP and MV, some of the more southern stations, have very small phase lag. Modeled stratification is thus maximized around high tide. The rest of the stations cluster around low tide. As the phase lags for the M2 are qualitatively similar to our

observations, we are fairly confident our ROMS simulations are resolving the dominant mechanisms that change stratification over tidal time-scales. Stations SR and PP are the least similar to our observations. These stations are located in the center of the bay. This may indicate that additional freshwater inputs are important. Recall that we only included northern tributary sources.

Since the coherence of stratification with tidal heights is present at many stations and at tidal frequencies, we conclude that the tidal flow is likely causing the change in stratification observed at the M2 frequency. The variability in phase lag exhibited across the stations suggests that a combination of tidally-driven advection, straining, and differential diffusion play a role in changing stratification. We explore these mechanisms further in following sections.

5.4 Tides

Dynamic changes in stratification are created by water movement and turbulence. Observations of NBFSMN stratification indicate changes on the order of 0.20 kg m^{-3} per tidal cycle at all stations (Fig. 12). Coherence between stratification and tidal heights at Newport is the strongest amongst the four environmental variables (tides, heat flux, river input and northward wind) compared with stratification. The coherence, along with previous studies on tidal straining (e.g. Scully and Friedrichs, 2007), suggest tidal currents have a large impact on stratification changes in NB.

To further explore the mechanisms that control stratification at tidal frequencies, we use our idealized numerical model to investigate the stratification balance. We analyze the terms in eq. 4 computed for all nodes located in NB.

5.5 General Trends

The depth- and tidally-averaged stratification ($\langle\overline{N^2}\rangle$) is displayed in Fig. 16a. The largest $\langle\overline{N^2}\rangle$, on the order 10^{-2} s^{-2}, is measured near the Blackstone and Taunton Rivers. This is where the freshwater is introduced into the model. Stratification decreases by an order of magnitude towards the mouth of the bay. Shallow embayments, like Greenwich Bay and the northern part of Mt. Hope Bay, also display low stratification.

We characterize the change in depth-averaged stratification ($\Delta\overline{N^2}$) over a tidal cycle by taking the difference between the maximum modeled $\overline{N^2}$ and $\langle\overline{N^2}\rangle$, similar to Whitney et al. (2012). Results are displayed in Fig. 16b. $\Delta\overline{N^2}$ changes over a tidal cycle from 10^{-4} to 10^{-2} s^{-2}, with the largest changes occurring coincident with elevated stratification. We normalize the $\Delta\overline{N^2}$ by the $\langle\overline{N^2}\rangle$ (Fig. 16c). The average percent change is between 10 and 30 %. Stronger variations, up to 90%, are measured in shallow areas such as the periphery of Ohio Ledge or the northern area of Mt. Hope Bay. The strong changes (red in Fig. 16c) around Greenwich Bay are likely not modeled properly due to the lack of local riverine sources in this area.

An $\overline{N^2}$ maximum during the tidal cycle is measured at every position in NB, illustrating the temporal variability throughout the bay (Fig. 16d). To quantify when the maximum $\overline{N^2}$ occurs, we take the cross correlation between $\overline{N^2}$ and the depth-averaged up-bay velocity. The M2 is the largest contribution as seen with the variance preserving power spectral density for most stations (Fig. 11). Therefore, we evaluate the phase lag in the time domain. The phase lag at which the correlation is maximized provides the lag between the two-time series. In our experiment, we divide the phase lag into four categories each 3 hours long, i.e. a fourth of the tidal period.

a) A phase lag of -1.5 to 1.5 hours denotes $\overline{N^2}$ is maximized during maximum flood.

b) A lag of 1.5 to 4.5 hours indicates $\overline{N^2}$ is maximized during slack high tide.

c) A lag of 4.5 to 7.5 hours indicates $\overline{N^2}$ is maximized during max ebb.

d) A lag of 7.5 to 10.5 hours indicates $\overline{N^2}$ is maximized during slack low tide.

Most of the bay has peak stratification during slack low tide but there is a wide range of phases (Fig. 16d).

The large-scale evolution over a tidal cycle can be described through the distribution of salinity, temperature and stratification throughout the four tidal cycle epochs (Fig. 17, 18, and 19):

a) From high tide to ebb, velocities are primarily down bay, bringing freshwater towards the mouth of the bay.

b) During slack low tide, the velocities weaken, and for many areas, this is coincident with a salinity minimum (Fig. 17c). For example, just south of Greenwich Bay along the western side of the west passage the fresh-water tongue reaches it southernmost extent during slack low tide (Fig. 17c).

c) During maximum flood, the tide enters the bay, up-bay velocities are maximized, and the salt front starts to move up-bay (Fig. 17d). Throughout this phase we see stratification start to retreat or dissipate, especially within channels (Fig. 18d). Particularly looking at Ohio Ledge, we see the river plume that was apparent during maximum ebb and low tide start to dissipate.

d) Once NB reaches high tide, most surface salinities are maximized as a result of the intrusion of Rhode Island Sound water and stratification is generally at a minimum

(Fig. 17). Only slight temperature differences were observed throughout the tidal cycle (Fig. 19). Note the high temperatures towards the north are a result of warmer input in rivers, while the high temperatures in Greenwich Bay are a result of the model configuration. Greenwich Bay is an area that has a longer residence time and is shallow, allowing heat to be absorbed in this area during the spring and early summer modeled spin-up period.

5.6 Stratification Driving Mechanisms

We next explore what causes the temporal variations in $\overline{N^2}$ by estimating contributions from advection, straining and differential diffusion. We start with an illustrative location, station Quonset Point (QP), and evaluate the terms from eq. 4. We plot the station's tidal height relative to mean sea level and the up-bay (η) depth-averaged velocity in Fig. 20a. The up-bay velocity precedes high tide by a quarter of a period (3 hours). This is characteristic of a standing wave. Our model suggests that most of NB behaves like a standing wave. Velocity and tidal height measurements from Quonset Point and Fall River tidal and current gauges also suggest a standing wave in Narragansett Bay from observations (*Tidal Current Tables 2016- Atlantic Coast of North America*, 2016). Furthermore, our numerical model indicates that stratification at QP is in phase with the tidal velocity, maximized during flood and minimized during ebb (Fig. 20b).

The mechanisms responsible for $\frac{\partial \overline{N^2}}{\partial t}$ at QP are plotted in Fig. 20c. The major terms, advection, straining and differential diffusion, govern $\frac{\partial \overline{N^2}}{\partial t}$ and vary over a tidal cycle. At station QP, advection has the largest amplitude and dictates when $\overline{N^2}$ is

maximized. When advection is maximized around 0.38 and 0.9 days, $\overline{N^2}$ increases (Fig. 20). When advection is negative around 0.1 and 0.5 days, $\overline{N^2}$ decreases (Fig. 20). It should be noted that straining and differential diffusion play a role in the stratification balance. Straining both increases and decreases $\overline{N^2}$. It also tends to act against advection. Differential diffusion has a smaller variation but always reduces $\overline{N^2}$.

We explore advection and straining terms further at station QP, by plotting the horizontal components of the two terms in Fig. 20d&e. Both mechanisms have contributions from the ξ (cross-bay) and η (up-bay) directions. Straining and advection have largest variance in the up-bay direction. Much of NB is similar to QP, in that advection variation is slightly larger than straining and diffusion variations. This implies advection determines when the change in stratification occurs. Also similar to QP, most of the bay has a larger variance in the η direction for both advection and straining. We explore the size of the three mechanisms in the rest of the bay by determining the variance of terms in the stratification balance.

5.7 Variance

Unlike Simpson et al. (1990), who found that tidal straining in many estuaries was the primary cause of increased (decreased) stratification during ebbing (flooding) tides, we find that a combination of mechanisms is responsible for observed temporal trends in the bay. This is suggested from the modeled $\overline{N^2}$ time series described in the previous section, and further supported here by our variance analysis.

The major contribution to $\frac{\partial \overline{N^2}}{\partial t}$ is from advection, straining and diffusion. Convergence/divergence plays a minor role in changing stratification and our error

estimates are also small. We proceed with our variance analysis by normalizing the major three terms. Normalized variance is calculated by:

$$S_n = \frac{\lambda_n}{\sum_{n=1}^{3} \lambda_n} \tag{5}$$

where λ_1 is the variance of the advection term, λ_2 is the variance of the straining term and λ_3 is the variance of the differential diffusion for any location in NB. By comparing the relative strength of the variance of one component to the total variance, we can determine the relative contribution of each component to the stratification balance over a tidal cycle.

We use ternary diagrams to plot the normalized variance of the three variables. The total variance sums to a constant, in this case $S_1+S_2+S_3=1$. Each component, advection, straining and differential diffusion, is plotted along one side of the triangle. This allows one to represent three variables in two dimensions. Each corner represents 100% of the variance contributed to $\frac{\partial \overline{N^2}}{\partial t}$. by that component. For example, the top corner represents samples that have only variations due to the differential diffusion component; where $S_3 = 1$ (100%), $S_1=0$ is 0% variation in advection and $S_2=0$ is 0% variation in straining. The percentage of any component decreases linearly away from that corner. Therefore, the bottom horizontal edge of the triangle represents 0% variance contributed by differential diffusion.

After calculating the normalized variance for all positions in NB, we plot them on a ternary diagram in Fig. 21a. Warmer colors indicate a higher density of samples. Each sample is a location in NB ROMS model. The ternary diagram illustrates that the largest contribution of the variance of the stratification change is from advection and

straining. Although, on average advection contributes a higher percentage to the variance, the straining contribution is comparable in magnitude.

Variance analysis shows that advection, straining and differential diffusion contribute differently to $\frac{\partial \overline{N^2}}{\partial t}$ at a given location. The ternary diagram (Fig. 21a) illustrates that advection and straining both contribute more than differential diffusion. Our analysis shows that in only about 5% of NB, differential diffusion dominates the balance. The other 95% has either advection (65%) or straining (30%) as the largest contributor to $\frac{\partial \overline{N^2}}{\partial t}$ variance.

5.8 Phase

The variance analysis illuminates which components are changing stratification the most. This analysis does not provide information about when the maximum stratification occurs. To determine the phase of stratification, we utilize cross correlations analysis techniques. Specifically, we cross-correlate depth-averaged stratification $\left(\overline{N^2} = \frac{1}{n+h}\int_{z=-h}^{n} N^2 dz\right)$ with the η depth-averaged velocity $\left(\bar{v} = \frac{1}{n+h}\int_{z=-h}^{n} v dz\right)$ at every location in NB. The maximum correlation provides the timing of the maximum $\overline{N^2}$ and a histogram shows the relative distribution of the timing of maximum $\overline{N^2}$ across the bay in Fig. 22a. Our analysis indicates that peak $\overline{N^2}$ occurs in 41.5% of the bay at slack low tide ($\pm$ 1.5 hours). The next highest peak occurs at maximum slack high tide ($\pm$ 1.5 hours) in 19.5 % of the bay.

To determine what causes the $\overline{N^2}$ maximum we need to determine the phase of advection and straining. We take the depth-averaged advection term and cross-correlate it with the depth-average velocity in the η direction. Correlations indicate the

time during the tidal cycle when advection is maximized. There are two peaks in the 2-D histogram of these results (Fig. 22**e**). One peak occurs at maximum flood, in phase with the tidal velocities and the other peak is right after max ebb**.** This indicates advection is out of phase with the tidal cycle (Fig. 22**e**).

We take the depth-averaged straining term and cross correlate it with the depth-averaged velocity in the η direction. Correlations indicate most of the straining is either maximized at maximum flood or just after maximum ebb (Fig. 22c). The maximum flood peak is larger than the max ebb peak indicating more of the bay has a straining term that is directly in phase with the tidal velocity cycle in the η direction. The two peaks in advection and straining provide valuable information about when the term separately is maximized but do not explicitly explain the distribution of stratification phase lags observed over the bay (Fig. 16d).

Each grid cell in our model represents a sample where we have estimated the timing of maximum $\overline{N^2}$, advection and straining. The comparison of when the $\overline{N^2}$ is maximized against when advection is maximized provides more detail about the dynamics occurring in NB (Fig. 22b). A 2-D histogram of NB timing of maximum $\overline{N^2}$ versus the timing of maximum advection, colored by the density of the number of samples, reveals there are primarily two regimes. One regime occurs when advection is maximized at maximum ebb, resulting in $\overline{N^2}$ being maximized during slack low tide (Fig. 22b). The other regime occurs when advection is in phase with the tide and maximized during maximum flood. $\overline{N^2}$ is maximized just after high tide for this regime (Fig. 22b). Potentially a third regime is noticed where advection is still in phase with the tidal cycle, but $\overline{N^2}$ is maximized during slack low tide.

6. Discussion

Estuaries, such as Liverpool Bay, are dominated by straining (Simpson et al., 1990), while other estuaries have found to have a balance between straining and advection (Whitney et al., 2012). Our study illustrates that there can be multiple regimes within one estuary. In the following sections, we focus on two major regimes within NB.

6.1 Two Advection Dominated Regimes

The two dominant peaks in Fig. 22b suggest there are two coherent regimes controlling $\frac{\partial \overline{N^2}}{\partial t}$ in NB related to advection. The high density of samples indicates that many parts of the bay behave similarly. We explore how advection and straining changes stratification over a tidal cycle by defining two regimes. The first regime is defined as any position in NB with a maximum advection around max ebb and maximum $\overline{N^2}$ occurring around low tide. We call this regime 1 (Fig. 23a). Regime 2 is defined as any position that experiences a maximum advection around max flood and maximum $\overline{N^2}$ around high tide (Fig. 23a). Both regimes use a cut-off sample density of 0.25 counts/deg^2 to define the region. These contours are outlined in the blue and red for regime 1 and 2, respectively (Fig. 23a). It appears that much of the bay's channels are included in regime 1, while embayments like Greenwich Bay or inter-channel areas tend to fall into regime 2 (Fig. 23b).

In NB straining and advection tend to be anti-correlated. This is illustrated in Fig. 22d, where straining and advection are largely out of phase. Therefore, straining works against advection in both regimes. As a result of straining being consistently anti-correlated with advection, we can reclassify major regimes based on one term.

6.1.1 Slack Low Tide Maximum Stratification, Regime 1

Ohio Ledge is an example of regime 1 dynamics. Tidal evolution at Ohio Ledge is shown in Fig. 24. Density profiles are shown at various locations and indicate the steepest gradients during maximum ebb, when the river plume emerges into Ohio Ledge (Fig. 24 c & d). Spatially averaged terms (eq. 4) over Ohio Ledge, indicate that $\overline{N^2}$ is maximized in-between maximum ebb and maximum low tide (Fig. 25 a & b). The contribution from diffusion is always negative at around $-5x10^{-8}$ s^{-3} and convergence and divergence has almost no net effect in eq. 4 (Fig. 25c). Straining balances diffusion in this area and has a positive value with average $5x10^{-8}$ s^{-3}. Straining is positive in this area because of the induced estuarine two-layer flow. The vertical gradient of velocity and the along-estuary horizontal gradient in density are negative, resulting in a net positive straining term. $\frac{\partial \overline{N^2}}{\partial t}$ is thus a result of the advection variation, as straining and diffusion balance one-another. This can be seen in the similarity in phase, magnitude and shape of the advection term (Fig. 25 c) and $\frac{\partial \overline{N^2}}{\partial t}$ (Fig. 25b).

A cross-section through Ohio Ledge (Fig. 26) illustrates that during maximum flood stratification increases up-bay (right of figure) and density increases down-bay (Fig. 26). Maximum flood results in minimum stratification as up-bay velocities move unstratified waters toward the head of the bay (Fig. 26 a & c). During maximum ebb, stratification increases due to the advection of the freshwater plume into Ohio Ledge (Fig. 26 b & d). Although, straining is positive throughout the tidal cycle, it tends to be balanced in this area by differential diffusion, not influencing $\frac{\partial \overline{N^2}}{\partial t}$ greatly.

6.1.2 Slack High Tide Stratification Maximum, Regime 2

The region between Jamestown and Prudence Island, referred to here as inter-channel, represents an area that is characterized as regime 2. In general, $\overline{N^2}$ is maximized at slack high tide as more stratified water advects from the East Passage to the West Passage (Fig. 27). Vertical density differences are larger during flood and slack high tide than during parts of the tidal cycle (Fig. 27 b, d, e, & f). Stratification terms (eq. 4) averaged over this region demonstrate that as water advects from the southeast, advection increases $\overline{N^2}$ (Fig. 28 b & d). Although the magnitude of $\frac{\partial \overline{N^2}}{\partial t}$ (Fig. 28 b) is smaller than the advection term (Fig. 28 c), the phases are similar. Straining, in this location, reduces the effect of advection as it is out of phase with advection (Fig. 28c). Diffusion always reduces $\overline{N^2}$ (Fig. 27c).

A schematic representation of regime 2 illustrates a bottom intrusion in Fig. 29. An imaginary cross-section is drawn northwest (right of figure) to southeast (left of figure), in between the two islands. In this area, the pycnocline intersects the bottom topography. Regime 2 is controlled by the pycnocline moving up-bay during flood which increases $\overline{N^2}$ and similarly, as the pycnocline moves down-bay during ebb $\overline{N^2}$ decreases.

6.3 Advection & Straining

Together, regime 1 and 2 account for 35 % of the bay. In the other areas, the sign and phase of advection is controlled by the direction of the horizontal stratification gradient because tidal velocities are directionally invariant within the model. However, the variance amplitude of the straining term becomes more important in these other areas. Peak $\overline{N^2}$ can occur at any time during the tidal cycle

depending on the magnitude of both straining and advection. We identified the most coherent regimes present in NB, through the phase of $\overline{N^2}$, advection and straining, and note the rest of NB depends on the balance of all terms in eq. 4.

6.4 Comparison to Other Estuaries

Estuaries can be driven by pure advection or pure tidal straining. For example, the Chesapeake Bay, is thought to be dominated by straining (Li and Li, 2011). Advection likely plays more of a role in NB because the stratification gradients change faster over a shorter distance. NB is different from larger estuaries like the Chesapeake, due to its length and shape.

The length of NB, is only a few 10's km, and it has multiple embayments and relatively shallow areas. These factors contribute to juxtaposing regions of high stratification next to areas of low stratification, making advection as important as straining. This is a result of strong horizontal stratification gradients.

Numerical modeling of estuaries has started to explore spatial variations in mechanisms, however there is a lack in documentation through observations (Burchard and Hofmeister, 2008; Giddings et al., 2011). As more estuaries are studied with numerical techniques, variations in mechanisms have been found within one estuary (Whitney et al., 2012). One such case is the Rhine river outflow region (Rijnsburger et al., 2016). Rijnsburger et al. (2016) found that advection and straining are opposing and lead to various timings of the maximum stratification, similar to our NB modeling results.

The analysis of the NBFSMN network observations and NB numerical model has found NB to experience multiple regimes. More detailed studies of other estuaries

may reveal more spatially variant regimes as well. We suggest that it is important, even within the same estuary, to consider different stratification regimes as it effects turbulent mixing, physical, biological, geological and chemical processes.

6.5 Impact on Mixing

Mixing is dependent on stratification and shear (e.g. Whitney et al., 2012; Peltier and Caulfield, 2003). Shear increases turbulence and is commonly maximized during flood or ebb tides, when velocities are often greatest. Stratification can limit turbulence, as it affects the gradient Richardson number Ri (N^2/S^2) and eddy viscosity (K) (Whitney et al., 2012). S^2 is defined as $(|du/dz|)^2$. In addition to tides, wind can also create shear and induce additional mixing. Our numerical model predicts stratification varies over a tidal cycle throughout NB. We postulate that mixing efficiency from wind events lasting a couple hours would result in different amounts of mixing depending on the phase of the tidal cycle.

Ohio Ledge is a good example of an area that experiences large changes in stratification. This area would be susceptible to variable mixing that would depend on the time a wind event occurs in relation to the tidal cycle. During ebb tide we predict most of Ohio Ledge to have a maximum in stratification (Fig. 24b). However, during maximum flood, a small part of the periphery reaches its maximum stratification (Fig. 24d & Fig. 16 d). A strong wind event applied to our model, lasting on the order of hours would be more effective at mixing the periphery during ebb tides than during flood tides. During such a wind event, we would expect stronger residual flows around the periphery due to baroclinic gradients, as the boundary between well mixed and stratification is enhanced.

7. Conclusion

Spatial and temporal stratification patterns in NB are primarily driven by seasonal, synoptic and semi-diurnal variations of environmental parameters including winds, run-off, solar heating and tides. The analysis of the multiple year buoy network in NB and hydrographic numerical modeling of NB have facilitated the characterization of stratification changes. Spatially, there is a latitudinal increase in stratification resulting from the freshwater input from the northern tributaries. This spatial trend is temporally changed due to several environmental factors. Over yearly time-scales, freshwater fluxes control the general stratification with more freshwater increasing stratification in the spring. These observations are in agreement with Codiga (2012), who found that riverine input was the most important source of stratification on monthly time-scales in NB.

On shorter time-scales, we find stratification varies at tidal frequencies. Periodic stratification changes are observed at NBFSMN buoys at diurnal, M2, M4 and M6 frequencies. Power spectral densities of observations reveal stratification changes on the order of 0.5-1 kg m^{-3} at the M2 frequency. Through numerical modeling we found that advection and straining play a key role in controlling stratification changes.

Our model results indicate that in NB stratification is not spatially uniform. NB is a relatively shallow estuary with complex bathymetry. This leads to more mixing especially in shallow areas, and a non-uniform stratification gradient throughout NB. Most of the bay's stratification increases to the north, as a result of tributary freshwater input. However, there are several areas in the bay, such as the area between Jamestown and North Prudence Islands, where local mixing and the influence of a

bottom salt intrusion result in stratification increasing to the south. Advection therefore leads to stratification maximum at different times of the tidal cycle depending on the direction of the stratification gradient. This result is especially important for turbulent mixing, which is dependent on stratification and vertical shear, both of which vary during the tidal cycle.

References

Annual Summary with Comparative Data: Providence, Rhode Island (KPVD) (Local Climatological Data No. ISSN 0198-4594), 2016. National Centers for Environmental Information, Ashville, NC.

Bendat, J.S., Piersol, A.G., 2010. Random data: analysis and measurement procedures, 4th ed. ed, Wiley series in probability and statistics. Wiley, Hoboken, N.J.

Bergondo, D.L., Kester, D.R., Stoffel, H.E., Woods, W.L., 2005. Time-series observations during the low sub-surface oxygen events in Narragansett Bay during summer 2001. Mar. Chem. 97, 90–103. https://doi.org/10.1016/j.marchem.2005.01.006

Bowden, K.F., 1967. Stability Effects on Turbulent Mixing in Tidal Currents. Phys. Fluids 10, S278. https://doi.org/10.1063/1.1762468

Burchard, H., Hofmeister, R., 2008. A dynamic equation for the potential energy anomaly for analysing mixing and stratification in estuaries and coastal seas. Estuar. Coast. Shelf Sci. 77, 679–687. https://doi.org/10.1016/j.ecss.2007.10.025

Chen, S.-N., Sanford, L.P., 2009. Axial Wind Effects on Stratification and Longitudinal Salt Transport in an Idealized, Partially Mixed Estuary*. J. Phys. Oceanogr. 39, 1905–1920. https://doi.org/10.1175/2009JPO4016.1

Codiga, D.L., 2012. Density stratification in an estuary with complex geometry: Driving processes and relationship to hypoxia on monthly to inter-annual timescales: NARRAGANSETT BAY STRATIFICATION. J. Geophys. Res. Oceans 117, n/a-n/a. https://doi.org/10.1029/2012JC008473

Codiga, D.L., Ullman, D.S., 2010. Characterizing the physical oceanography of coastal waters off Rhode Island, Part 1: Literature review, available observations, and a representative model simulation (Technical Report No. 2), Appendix to Rhode Island Ocean Special Area Management Plan. Rhode Island Coastal Resource Mangaement Council, Wakefield, R.I.

Deacutis, C.F., Murray, D., Prell, W., Saarman, E., Korhun, L., 2006. Hypoxia in the Upper Half of Narragansett Bay, RI, During August 2001 and 2002. Northeast. Nat. 13, 173–198. https://doi.org/10.1656/1092-6194(2006)13[173:HITUHO]2.0.CO;2

Emery, W.J., Thomson, R.E., 2001. Data analysis methods in physical oceanography, 2nd and rev. ed. ed. Elsevier, Amsterdam; New York.

Fan, Y., Brown, W., 2003. The Heat Budge for Mt. Hope Bay (Technical Report No. SMAST-03-0801). School for Marine Science and Technology, University of Massachusetts, Dartmouth, MA.

Finite Volume Coastal Ocean Model [Internet]., 2013. Boston (USA): SeaPlan and School of Marine Science and Technology, University of Massachusetts, Dartmouth. Gulf of Main 2010. Available from: http://fvcom.smast.umassd.edu/necofs/.

Gay, P., O'Donnell, J., 2009. Comparison of the Salinity Structure of the Chesapeake Bay, the Delaware Bay and Long Island Sound Using a Linearly Tapered Advection-Dispersion Model. Estuaries Coasts 32, 68–87. https://doi.org/10.1007/s12237-008-9101-4

Geyer, W.R., 1997. Influence of Wind on Dynamics and Flushing of Shallow Estuaries. Estuar. Coast. Shelf Sci. 44, 713–722. https://doi.org/10.1006/ecss.1996.0140

Geyer, W.R., Signell, R.P., 1992. A Reassessment of the Role of Tidal Dispersion in Estuaries and Bays. Estuaries 15, 97–108. https://doi.org/10.2307/1352684

Giddings, S.N., Fong, D.A., Monismith, S.G., 2011. Role of straining and advection in the intratidal evolution of stratification, vertical mixing, and longitudinal dispersion of a shallow, macrotidal, salt wedge estuary. J. Geophys. Res. 116. https://doi.org/10.1029/2010JC006482

Hicks, S.D., 1959. The Physical Oceanography of Narragansett Bay1. Limnol. Oceanogr. 4, 316–327. https://doi.org/10.4319/lo.1959.4.3.0316

Kincaid, C., Bergondo, D., Rosenberger, K., 2008. The Dynamics of Water Exchange Between Narragansett Bay and Rhode Island Sound, in: Desbonnet, A., Costa-Pierce, B.A. (Eds.), Science for Ecosystem-Based Management. Springer New York, New York, NY, pp. 301–324.

Kincaid, C., Pockalny, R.A., Huzzey, L.M., 2003. Spatial and temporal variability in flow at the mouth of Narragansett Bay. J. Geophys. Res. Oceans 108, 3218. https://doi.org/10.1029/2002JC001395

Kremer, J.N., Vaudrey, J.M.P., Ullman, D.S., Bergondo, D.L., LaSota, N., Kincaid, C., Codiga, D.L., Brush, M.J., 2010. Simulating property exchange in estuarine ecosystem models at ecologically appropriate scales. Ecol. Model. 221, 1080–1088. https://doi.org/10.1016/j.ecolmodel.2009.12.014

Lerczak, J.A., Geyer, W.R., 2004. Modeling the Lateral Circulation in Straight, Stratified Estuaries. J. Phys. Oceanogr. 34, 1410–1428. https://doi.org/10.1175/1520-0485(2004)034<1410:MTLCIS>2.0.CO;2

Li, M., Zhong, L., Boicourt, W.C., 2005. Simulations of Chesapeake Bay estuary: Sensitivity to turbulence mixing parameterizations and comparison with observations. J. Geophys. Res. 110. https://doi.org/10.1029/2004JC002585

Li, Y., Li, M., 2012. Wind-driven lateral circulation in a stratified estuary and its effects on the along-channel flow: WIND-DRIVEN LATERAL CIRCULATION. J. Geophys. Res. Oceans 117, n/a-n/a. https://doi.org/10.1029/2011JC007829

Li, Y., Li, M., 2011. Effects of winds on stratification and circulation in a partially mixed estuary. J. Geophys. Res. 116. https://doi.org/10.1029/2010JC006893

Lin, J., Xie, L., Pietrafesa, L.J., Shen, J., Mallin, M.A., Durako, M.J., 2006. Dissolved oxygen stratification in two micro-tidal partially-mixed estuaries. Estuar. Coast. Shelf Sci. 70, 423–437. https://doi.org/10.1016/j.ecss.2006.06.032

McMaster, R.L., 1960. Sediments of Narragansett Bay System and Rhode Island Sound, Rhode Island. SEPM J. Sediment. Res. Vol. 30. https://doi.org/10.1306/74D70A15-2B21-11D7-8648000102C1865D

Mukai, A.Y., Westerink, J.J., Luettich Jr., R.A., Mark, D., 2002. Eastcoast 2001, A Tidal Constituent Database for Western North Atlantic, Gulf of Mexico, and Caribbean Sea (No. ERDC/CHL TR-02-24). U.S. Army Corps of Engineers, Coastal and Hydraulics Laboratory.

Nahas, E.L., Pattiaratchi, C.B., Ivey, G.N., 2005. Processes controlling the position of frontal systems in Shark Bay, Western Australia. Estuar. Coast. Shelf Sci. 65, 463–474. https://doi.org/10.1016/j.ecss.2005.06.017

Navarra, A., Simoncini, V., 2010. A guide to empirical orthogonal functions for climate data analysis. Springer, Dordrecht ; New York.

Peltier, W.R., Caulfield, C.P., 2003. Mixing efficiency in stratified shear flows. Annu. Rev. Fluid Mech. 35, 135–167. https://doi.org/10.1146/annurev.fluid.35.101101.161144

Pfeiffer-Herbert, A.S., Kincaid, C.R., Bergondo, D.L., Pockalny, R.A., 2015. Dynamics of wind-driven estuarine-shelf exchange in the Narragansett Bay estuary. Cont. Shelf Res. 105, 42–59. https://doi.org/10.1016/j.csr.2015.06.003

Pilson, M.E.Q., 2008. Narragansett Bay Amidst a Globally Changing Climate, in: Desbonnet, A., Costa-Pierce, B.A. (Eds.), Science for Ecosystem-Based Management. Springer New York, New York, NY, pp. 35–46.

Pilson, M.E.Q., 1985. On the Residence Time of Water in Narragansett Bay. Estuaries 8, 2. https://doi.org/10.2307/1352116

Ries III, K.G., 1990. Estimating surface-water runoff to Narragansett Bay, Rhode Island and Massachusetts (Report No. 89–4164), Water-Resources Investigations Report.

Rijnsburger, S., van der Hout, C.M., van Tongeren, O., de Boer, G.J., van Prooijen, B.C., Borst, W.G., Pietrzak, J.D., 2016. Simultaneous measurements of tidal straining and advection at two parallel transects far downstream in the Rhine ROFI. Ocean Dyn. 66, 719–736. https://doi.org/10.1007/s10236-016-0947-x

Rippeth, T.P., Fisher, N.R., Simpson, J.H., 2001. The Cycle of Turbulent Dissipation in the Presence of Tidal Straining. J. Phys. Oceanogr. 31, 2458–2471. https://doi.org/10.1175/1520-0485(2001)031<2458:TCOTDI>2.0.CO;2

Rogers, J., 2008. Circulation and transport in upper Narragansett Bay. Narragansett Bay R. I. Univ. R. I. Grad. Sch. Oceanogr.

Rueda, F., Schladow, G., 2009. Mixing and stratification in lakes of varying horizontal length scales: Scaling arguments and energy partitioning. Limnol. Oceanogr. 54, 2003–2017. https://doi.org/10.4319/lo.2009.54.6.2003

Scully, M.E., Friedrichs, C., Brubaker, J., 2005. Control of estuarine stratification and mixing by wind-induced straining of the estuarine density field. Estuaries 28,

321–326. https://doi.org/10.1007/BF02693915

Scully, M.E., Friedrichs, C.T., 2007. The Importance of Tidal and Lateral Asymmetries in Stratification to Residual Circulation in Partially Mixed Estuaries*. J. Phys. Oceanogr. 37, 1496–1511. https://doi.org/10.1175/JPO3071.1

Simpson, J.H., Bowers, D., 1981. Models of stratification and frontal movement in shelf seas. Deep Sea Res. Part Oceanogr. Res. Pap. 28, 727–738. https://doi.org/10.1016/0198-0149(81)90132-1

Simpson, J.H., Brown, J., Matthews, J., Allen, G., 1990. Tidal Straining, Density Currents, and Stirring in the Control of Estuarine Stratification. Estuaries 13, 125. https://doi.org/10.2307/1351581

Simpson, J.H., Crisp, D.J., Hearn, C., 1981. The Shelf-Sea Fronts: Implications of their Existence and Behaviour [and Discussion]. Philos. Trans. R. Soc. Math. Phys. Eng. Sci. 302, 531–546. https://doi.org/10.1098/rsta.1981.0181

Spaulding, M.L., Swanson, C., 2008. Circulation and Transport Dynamics in Narragansett Bay, in: Desbonnet, A., Costa-Pierce, B.A. (Eds.), Science for Ecosystem-Based Management. Springer New York, New York, NY, pp. 233–279. https://doi.org/10.1007/978-0-387-35299-2_8

Spaulding, M.L., White, F.M., 1990. Circulation Dynamics in Mt. Hope Bay and the Lower Taunton River, in: Cheng, R.T. (Ed.), Residual Currents and Long-Term Transport. Springer New York, New York, NY, pp. 494–510.

Stoffel, H., Kiernan, S., 2009. Narragansett Bay Fixed-Site Monitoring Network: Final Report on Activities during 2005-2008 (Final Report). Rhode Island Department of Environmental Management-Office of Water Resources.

Tidal Current Tables 2016- Atlantic Coast of North America, 2016. . NOAA/ National Ocean Services, Silver Spring, MD.

Turrell, W.R., Brown, J., Simpson, J.H., 1996. Salt Intrusion and Secondary Flow in a Shallow, Well-mixed Estuary. Estuar. Coast. Shelf Sci. 42, 153–169. https://doi.org/10.1006/ecss.1996.0012

Water-resources data for the United States, Water Year 2010 (Water-Data Report No. WDR-US-2010, site 01108000), 2012a. . U.S. Geological Survey.

Water-resources data for the United States, Water Year 2010 (Water-Data Report No. WDR-US-2010, site 01112500), 2012b. . U.S. Geological Survey.

Weisberg, R.H., Sturges, W., 1976. Velocity Observations in the West Passage of Narragansett Bay: A Partially Mixed Estuary. J. Phys. Oceanogr. 6, 345–354. https://doi.org/10.1175/1520-0485(1976)006<0345:VOITWP>2.0.CO;2

Whitney, M.M., Codiga, D.L., Ullman, D.S., McManus, P.M., Jiorle, R., 2012. Tidal Cycles in Stratification and Shear and Their Relationship to Gradient Richardson Number and Eddy Viscosity Variations in Estuaries. J. Phys. Oceanogr. 42, 1124–1133. https://doi.org/10.1175/JPO-D-11-0172.1

Whitney, M.M., Garvine, R.W., 2006. Simulating the Delaware Bay Buoyant Outflow: Comparison with Observations. J. Phys. Oceanogr. 36, 3–21. https://doi.org/10.1175/JPO2805.1

Willmott, C.J., 1982. Some Comments on the Evaluation of Model Performance. Bull. Am. Meteorol. Soc. 63, 1309–1313. https://doi.org/10.1175/1520-0477(1982)063<1309:SCOTEO>2.0.CO;2

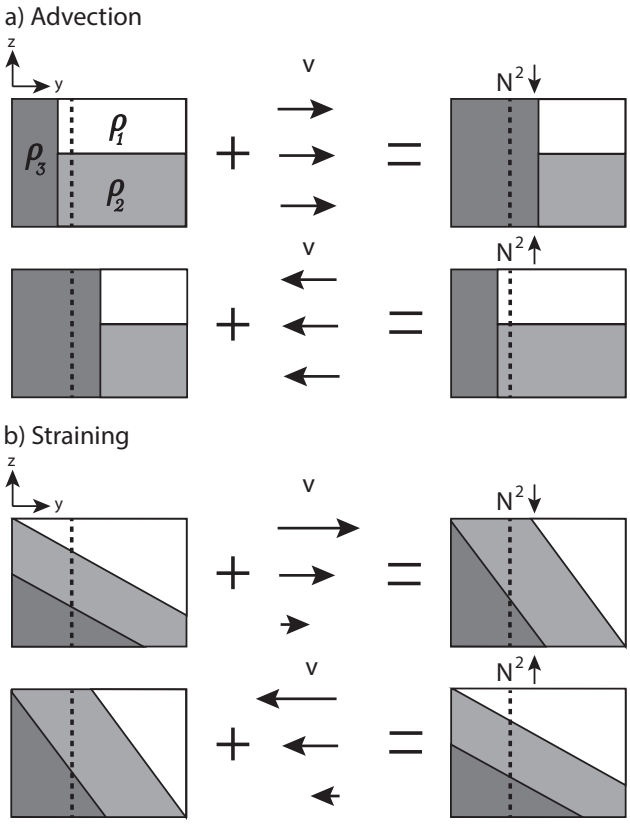

Figure 1: Schematic of physical mechanisms that can change stratification; (a) advection and (b) straining. $\rho_3 > \rho_2 > \rho_1$. Stratification change (N^2 arrow) referenced for dotted line. Adapted from Burchard and Hofmeister (2008).

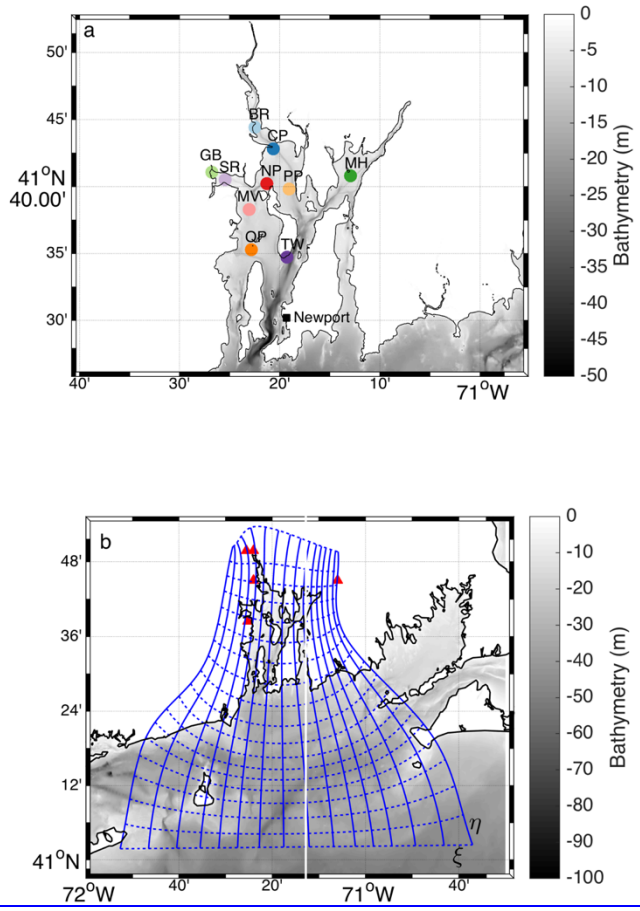

Figure 2: Location of observations and numerical model. (a) Location of Narragansett Bay Fixed Site Monitoring Network (NBFSMN) and Newport tide gauge (black) plotted on bathymetry of Narragansett Bay. (b) Outline of ROMS grid used. Boxes are every 50 grid nodes in both the ξ (dashed) and η (solid) directions. River inputs, not actual locations of river gauges, are marked with red triangles. Rivers starting from east and moving counter clockwise are Taunton, Blackstone, Moshassuck, Pawtuxet and Hunt. All maps in this study use Mercator projections.

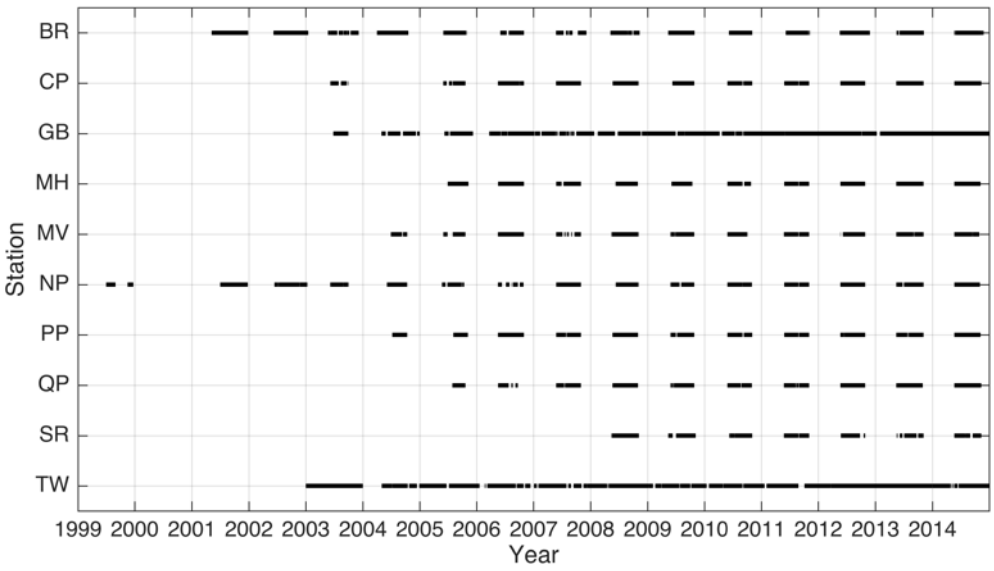

Figure 3: Time of observation of NBFSMN buoys. Black lines indicate periods when instruments were recording data at 15 minute intervals. Locations of stations shown in Fig. 1a.

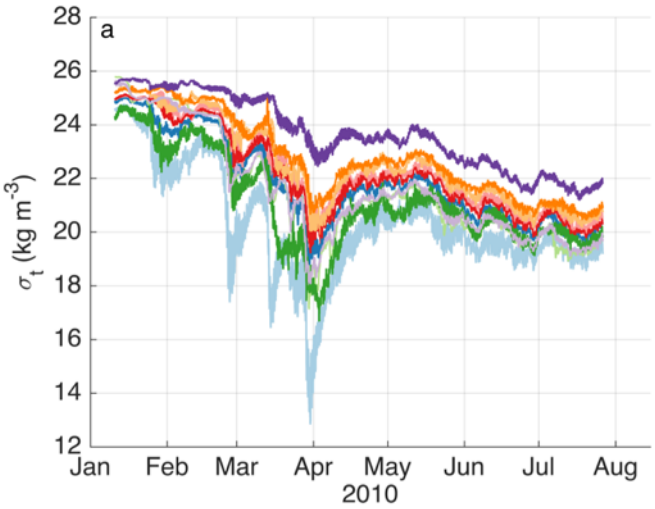

Figure 4: Spin-up ROMS experiment evolution of depth-averaged density at NBFSMN stations. Stations are indicated by color and positions are given in Fig. 2a.

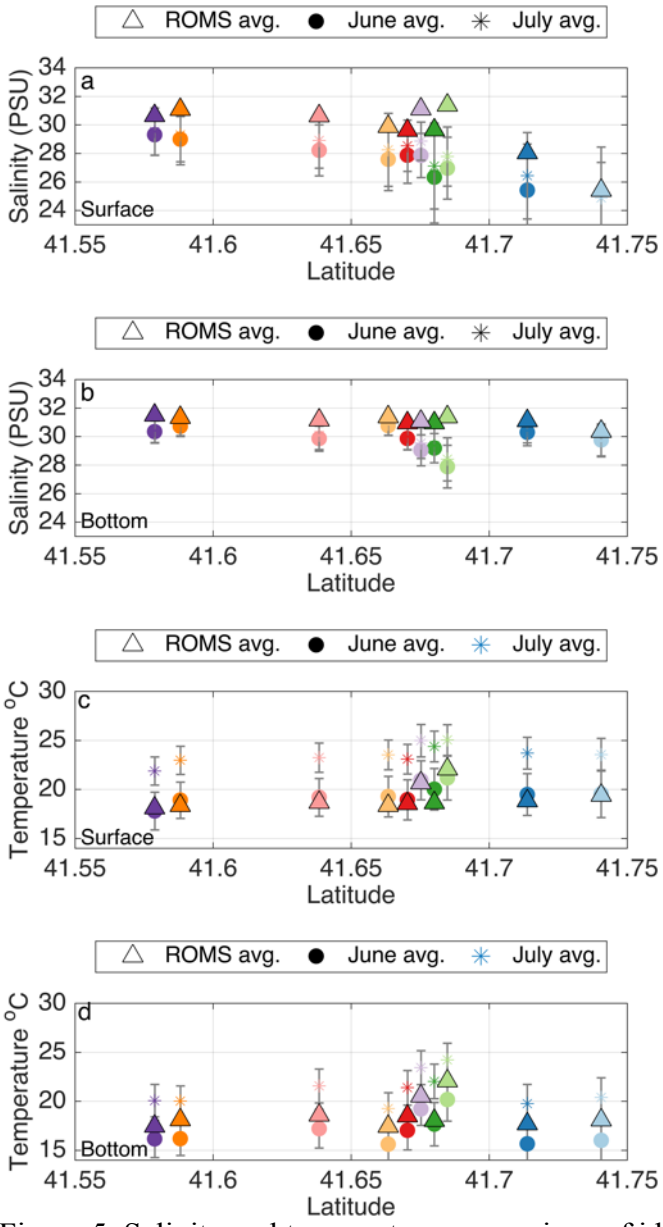

Figure 5: Salinity and temperature comparison of idealized ROMS experiment (triangles) and NBFSMN buoys as a function of latitude. (a) Surface salinity, (b) bottom salinity, (c) surface temperature, and (d) bottom temperature at buoy locations. June (circle) and July (asterisk) averages, over NBFSMN data set, are displayed with standard deviations.

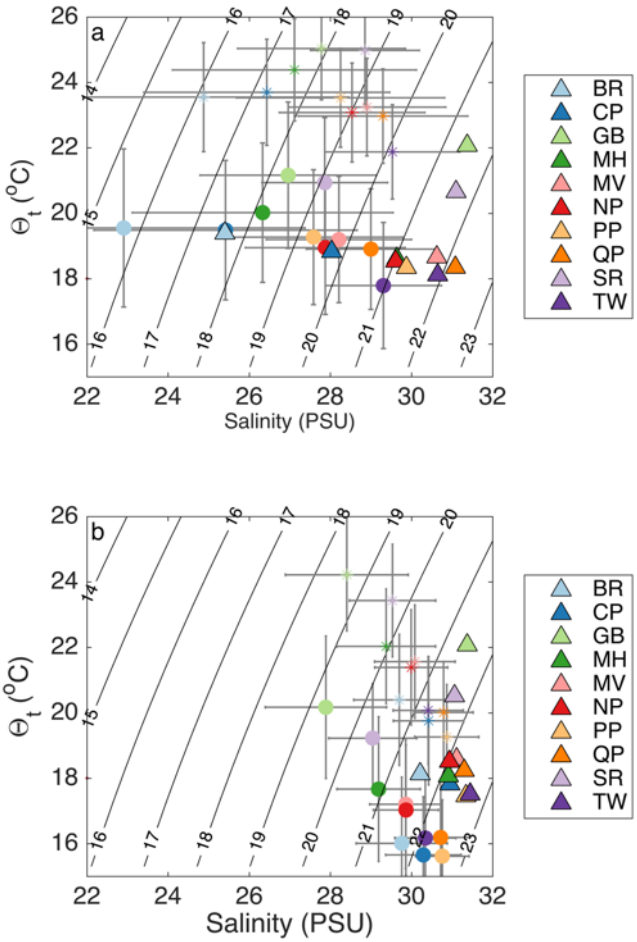

Figure 6: Temperature and salinity plots for (a) 1 meter below surface and (b) 0.5 meters above the seafloor at NBFSMN station locations. Buoy data is averaged from June (circles) and July (asterisk) of all available years. Standard deviation of measurements is plotted as grey error-bars. After our idealized ROMS experiment comes into steady state, station averages of temperature and salinity (triangles) are plotted.

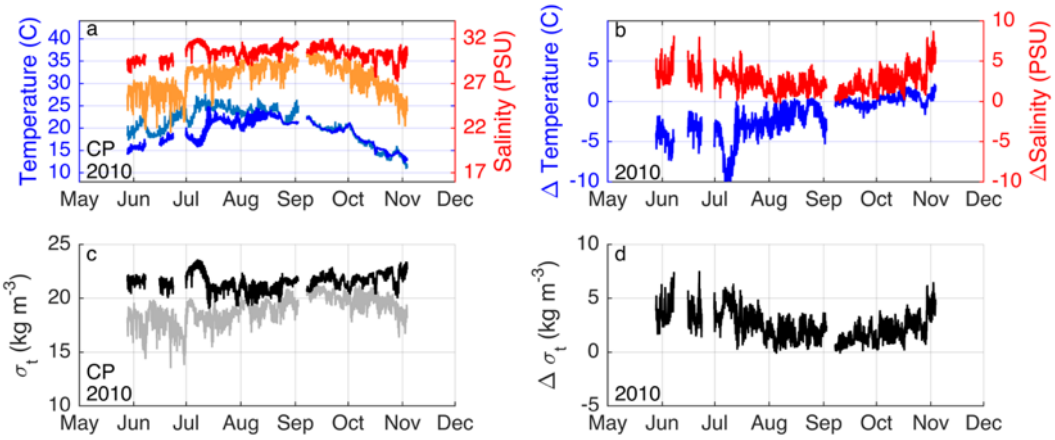

Figure 7: Station CP measurements during 2010. (a) NBFSMN station temperature (blue) and salinity (red) plotted every 15 minutes from May to November of 2010. Top and bottom measurements are displayed in different colors. Dark blue and red are deeper sensors and light blue and orange are near surface sensors. (b) Vertical temperature difference (blue) and vertical salinity difference (red) obtained at station CP. (c) Plotted calculated sigma-t for top and bottom sensor (grey) and (d) vertical density difference (black).

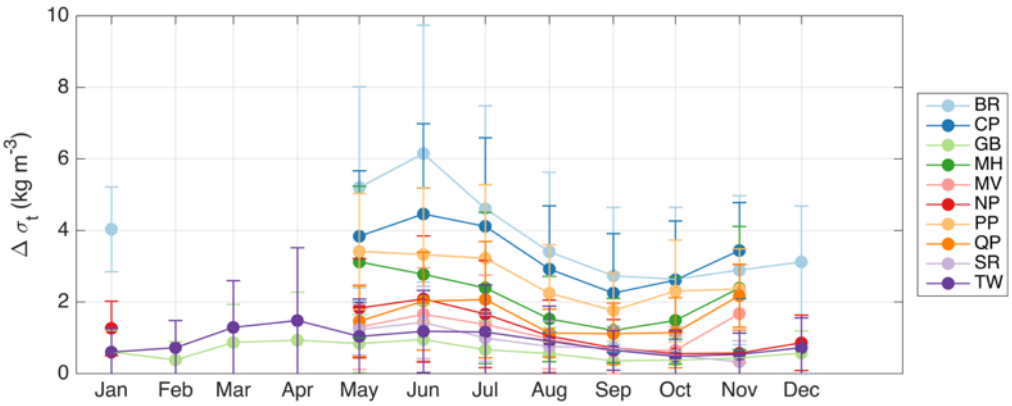

Figure 8: Monthly averaged vertical density differences at NBFSMN buoys. Standard deviation indicated with error bars. All data available was used in monthly averages.

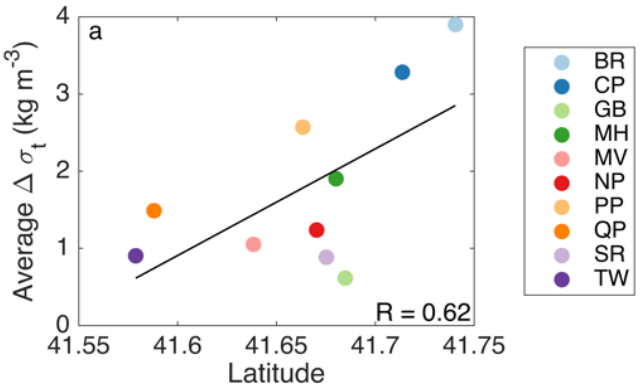

Figure 9: Average vertical density difference vs. latitude. Station data are averaged from May to October of available years. Black line is linear best fit to data, with a R value of 0.62.

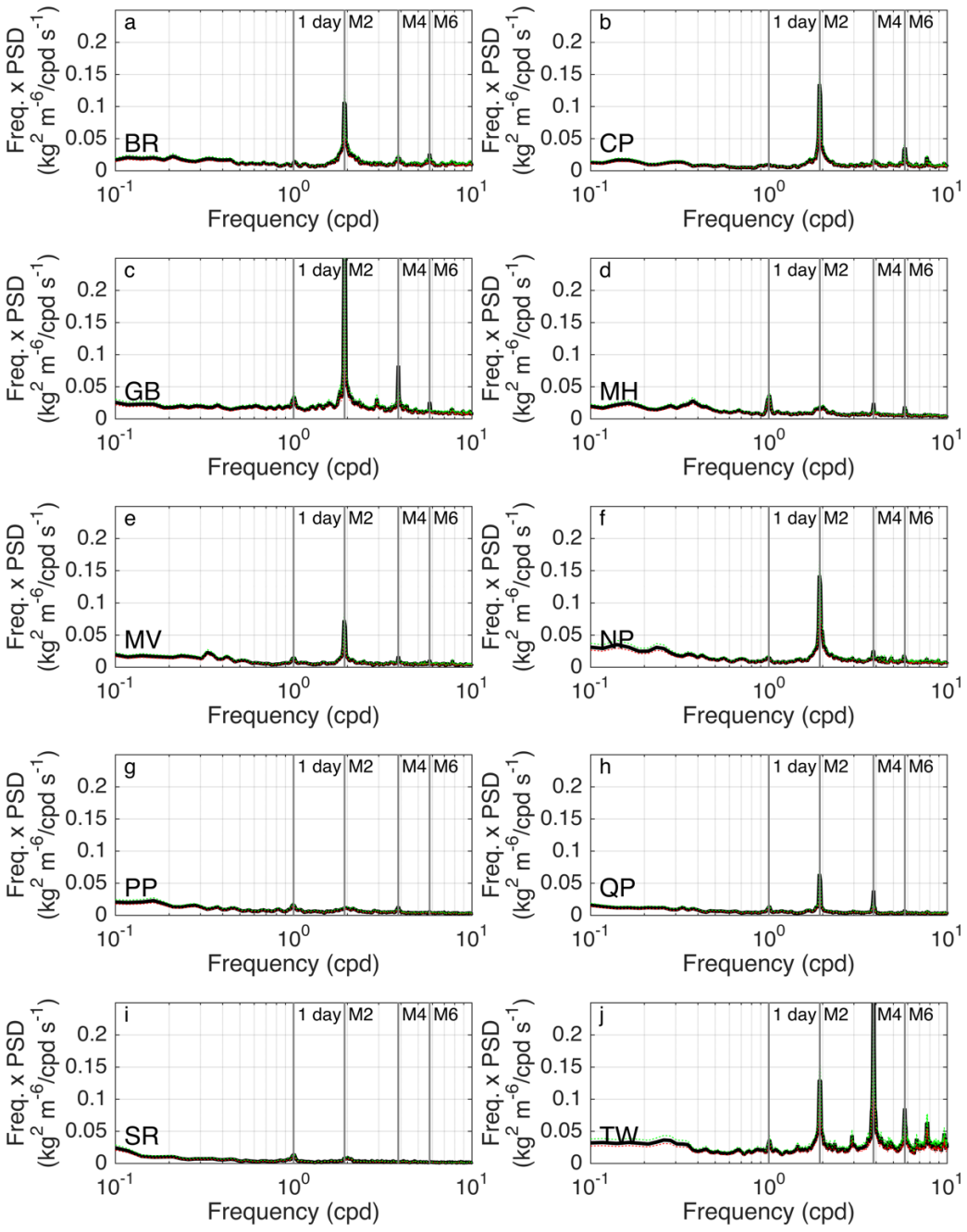

Figure 10: Variance conserving power spectral density of vertical density differences for all NBFSMN station observations. Red and green dashed lines indicate error bars. Diurnal, M2, M4 and M6 frequencies denoted with vertical grey lines. Data used from all available time periods. Missing data were padded with station averages.

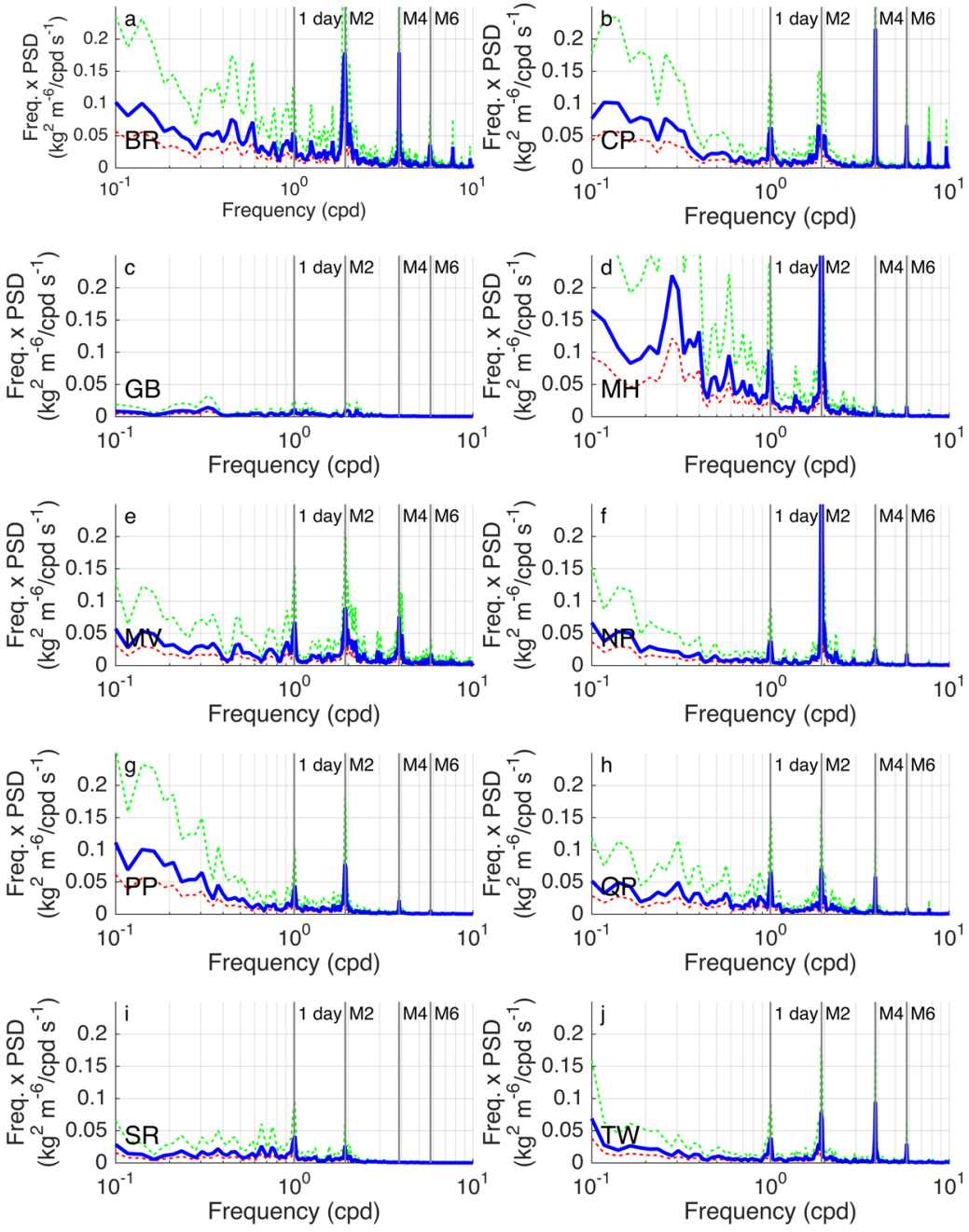

Figure 11: Variance conserving power spectral density of vertical density differences for all modeled NBFSMN stations. Red and green dashed lines indicate error bars. Diurnal, M2, M4 and M6 frequencies denoted with vertical grey lines. Data used from output of ROMS spin-up experiment. Time series starts January 10, 2010 and ends July 31, 2010 for ROMS numerical spin-up.

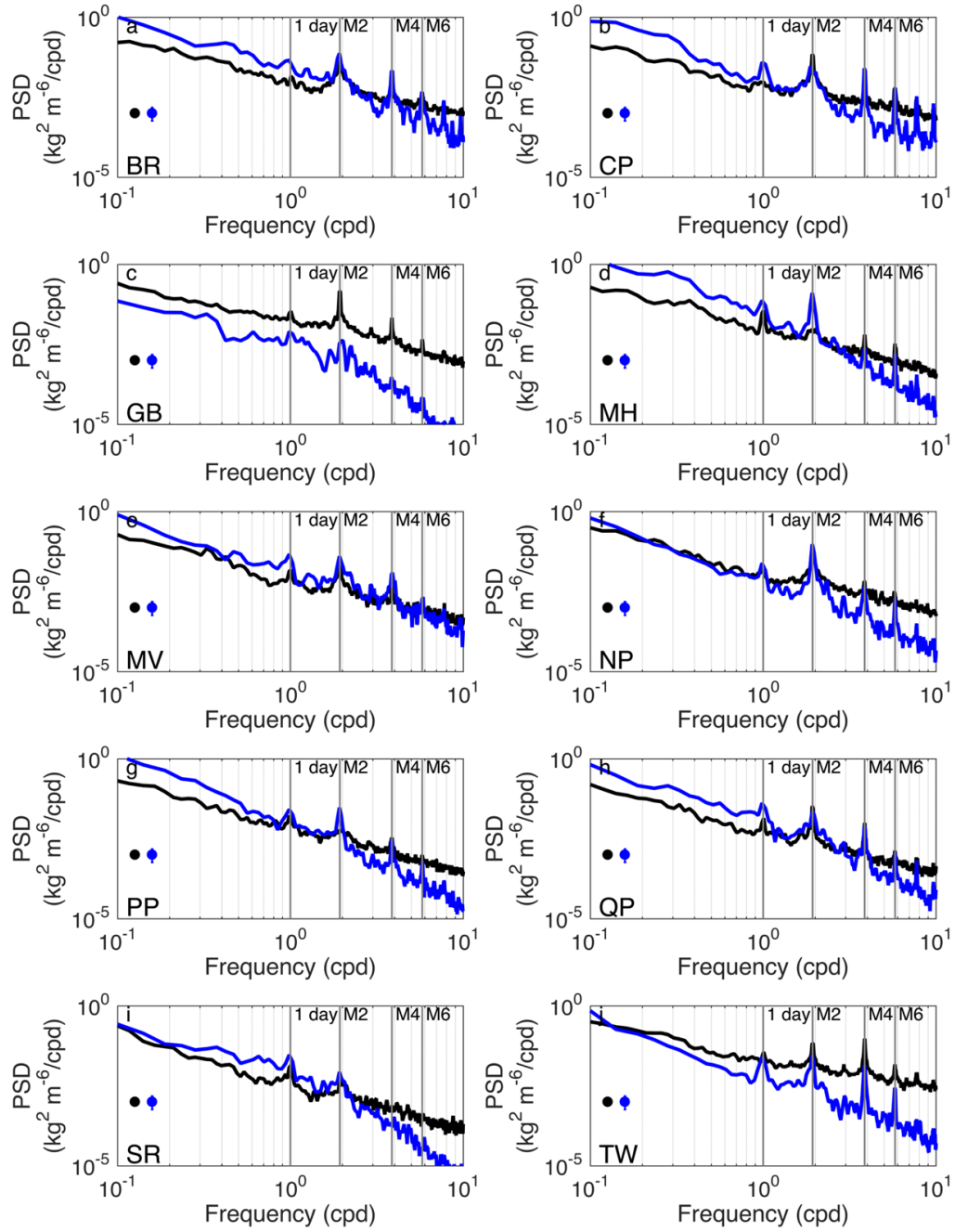

Figure 12: Power spectral density of vertical density differences for observations (black) at NBFMSN station locations as well as in our ROMS spin-up experiment (blue) for 2010. Error bars provided at the black and blue dots for each data set. Time series starts January 10, 2010 and ends July 31, 2010 for ROMS numerical spin-up.

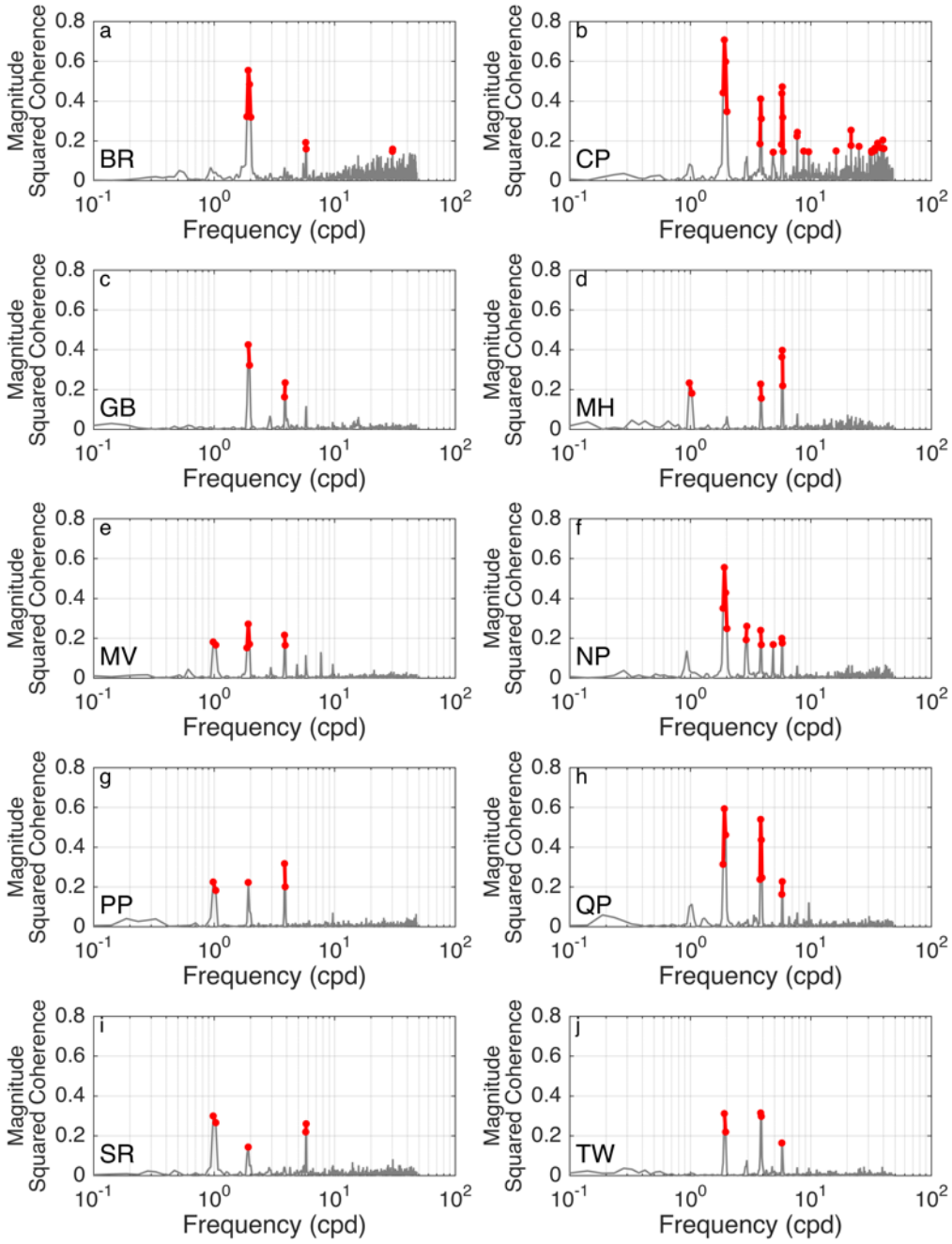

Figure 13: Magnitude squared coherence between observed vertical density difference at NBFMSN stations and tidal height measured at Newport, RI. Red indicates the frequencies of significant magnitude squared coherence.

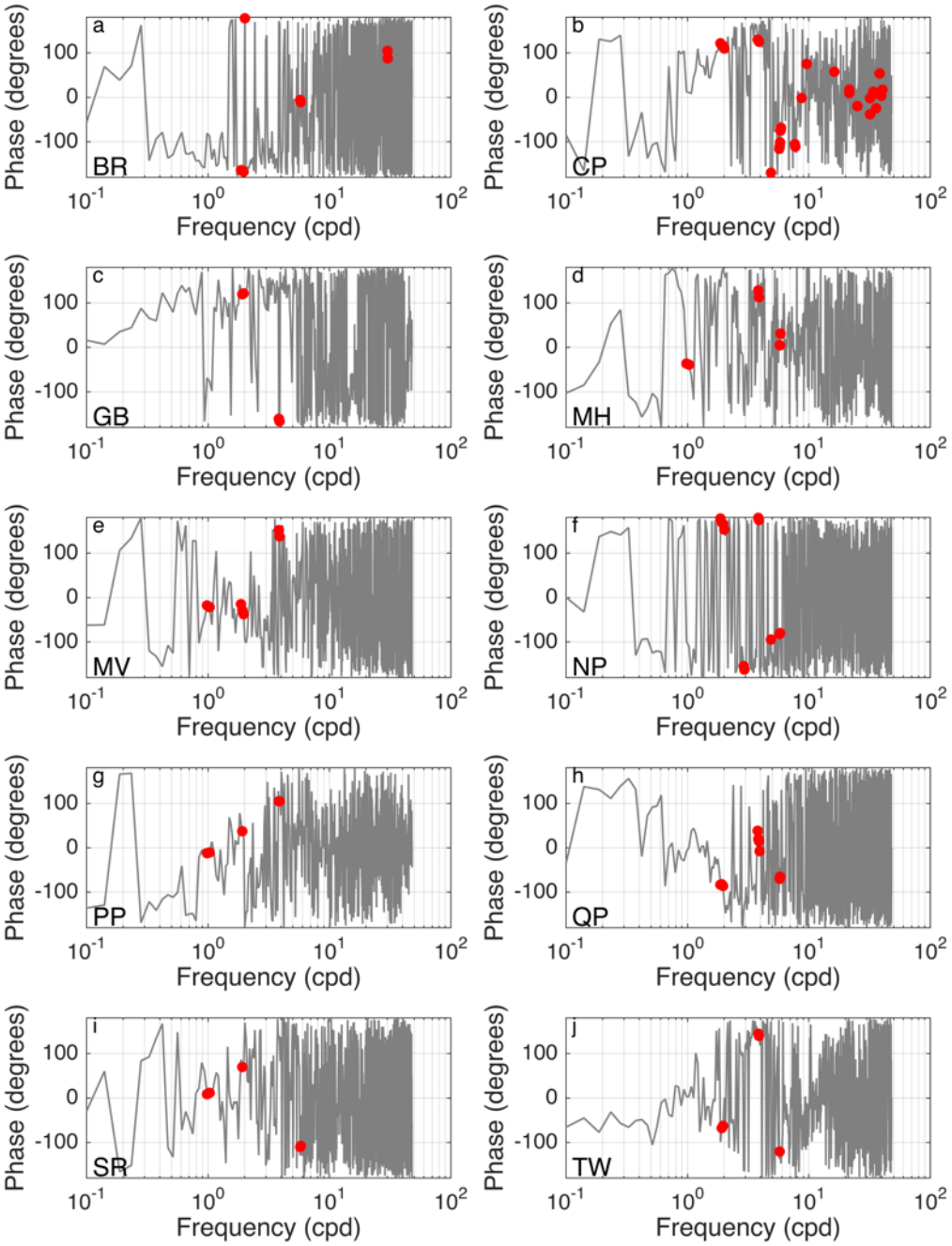

Figure 14: Phase lag between vertical density difference at NBFMSN stations and tidal height measured at Newport, RI. Red indicates the frequencies of the significant phase lag.

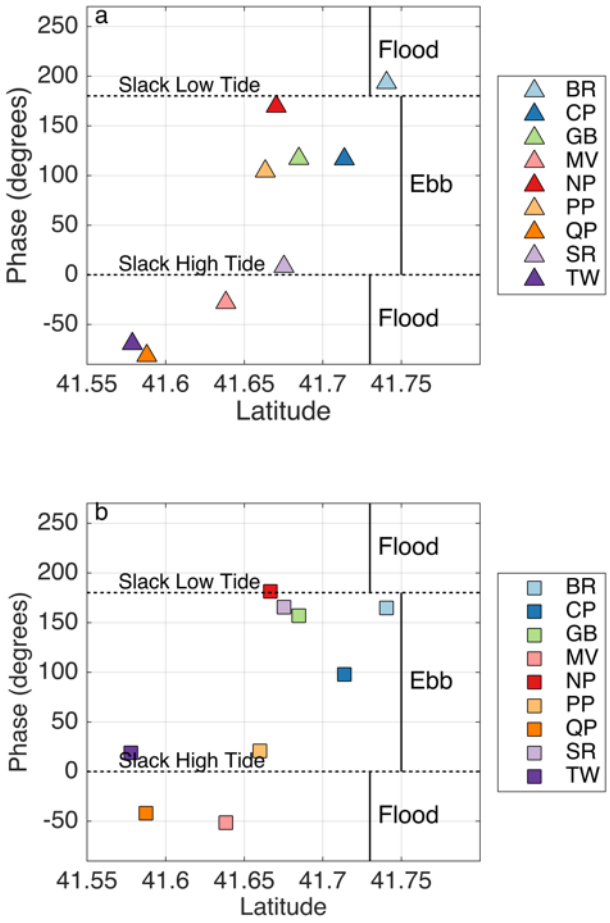

Figure 15: Phase lag of vertical density difference at NBFSMN buoys and tidal height at Newport, RI at the M2 frequency versus latitude. Phase lag is displayed for both (a) observations and (b) numerical model idealized experiment results. Only stations with a significant coherence value of observed data at the M2 frequency are plotted (Fig. 13). The same stations are plotted for our numerical idealized experiment (b).

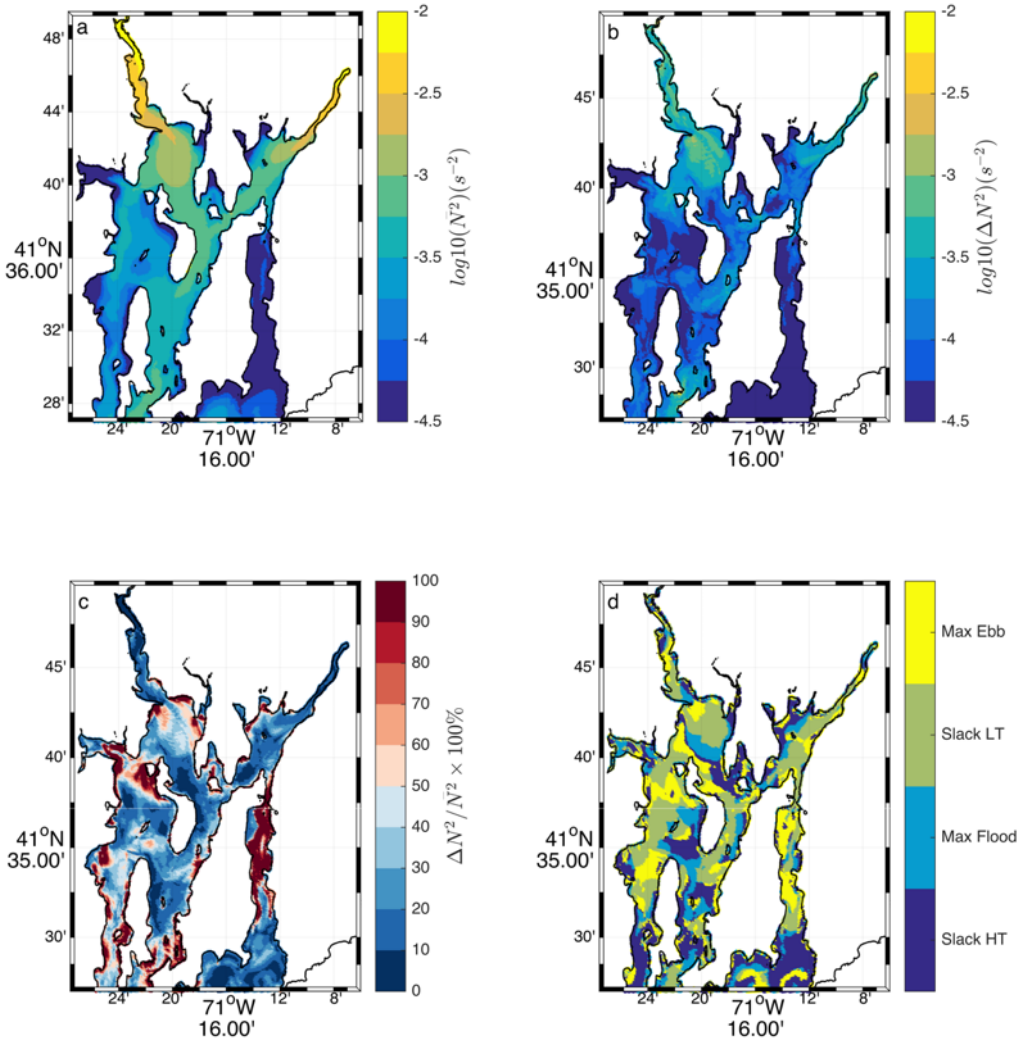

Figure 16: Stratification changes over a tidal cycle from the steady state idealized experiment. (a) Depth- and tidally-averaged stratification. (b) Difference between the maximum depth-averaged stratification and tidally averaged stratification. (c) Percent change of the maximum stratification. (d) Phase of the maximum stratification relative to the tidal cycle, i.e. when stratification is maximized.

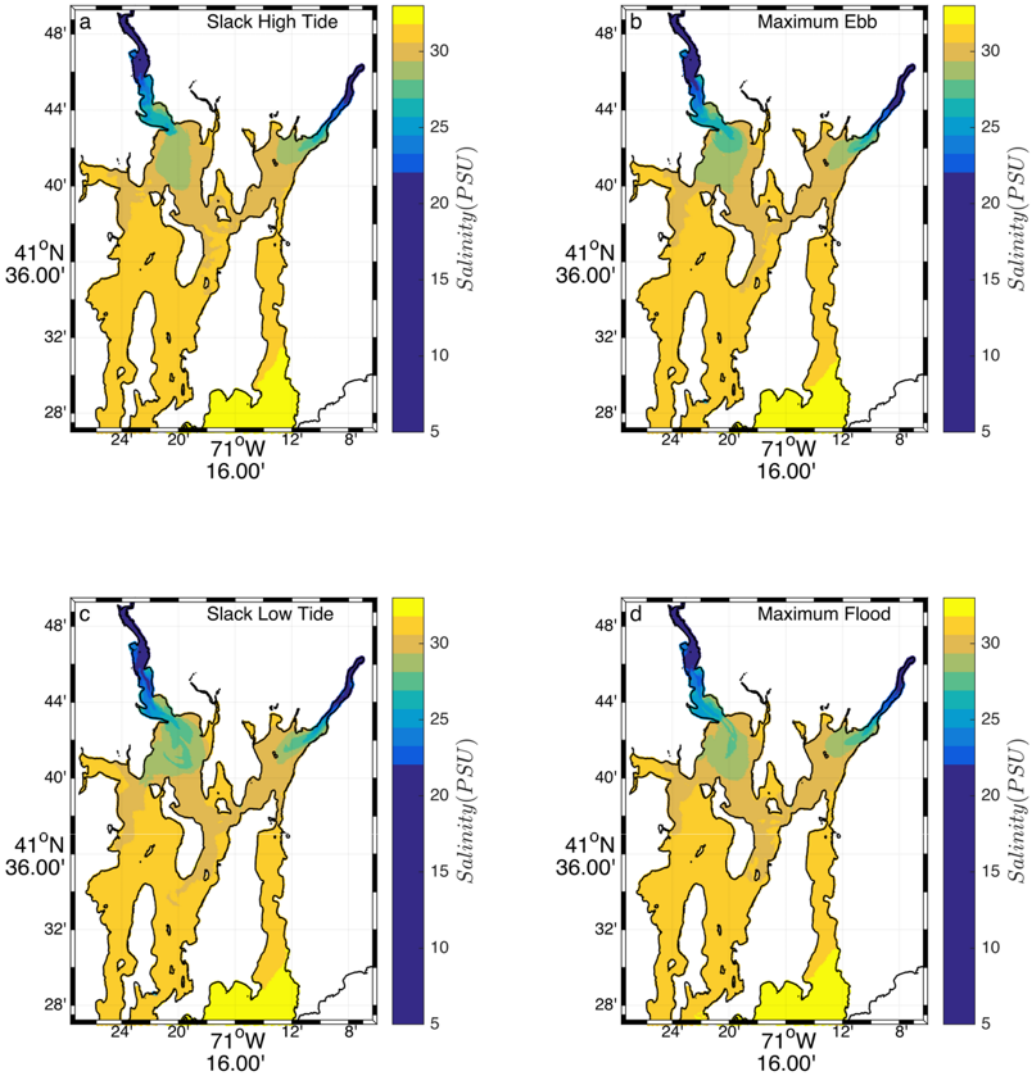

Figure 17: Surface salinity of the ROMS steady state idealized experiment. Surface salinity in PSU displayed for (a) slack high tide, (b) maximum ebb, (c) slack low tide and (d) maximum flood.

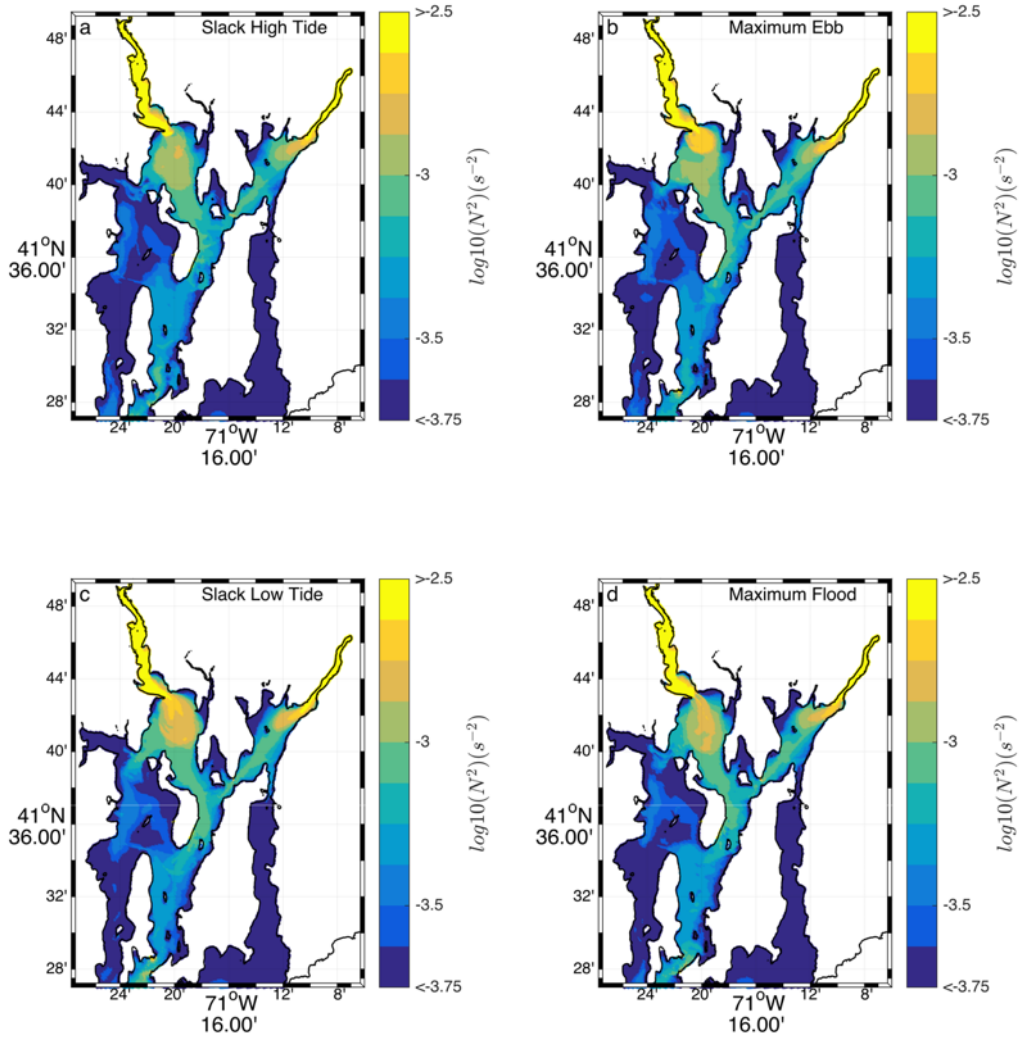

Figure 18: Depth-averaged stratification of the ROMS steady state idealized experiment, at (a) slack high tide, (b) maximum ebb, (c) slack low tide and (d) maximum flood.

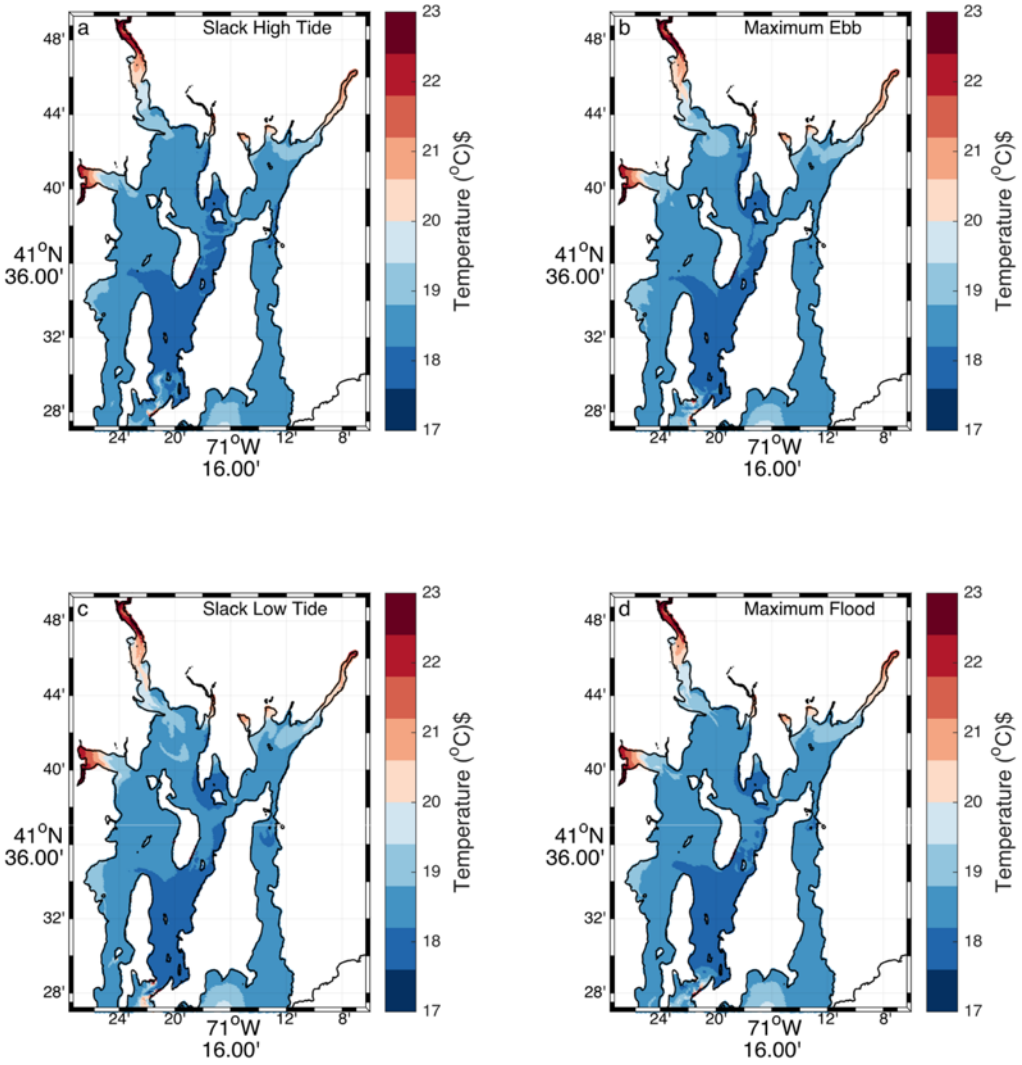

Figure 19: Surface temperature of the ROMS steady state idealized experiment, displayed for (a) slack high tide, (b) maximum ebb, (c) slack low tide and (d) maximum flood.

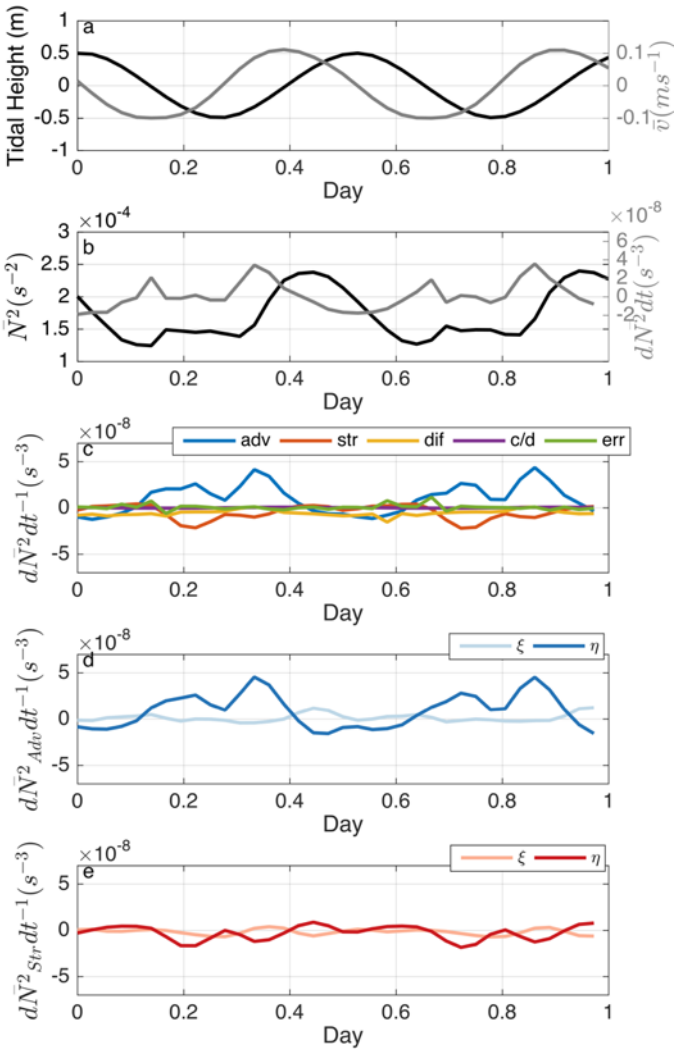

Figure 20: Time series of depth-average properties at station QP from ROMS steady state idealized experiment. (a) Tidal height (black) relative to mean sea level and northward depth-averaged velocity (grey). (b) Depth-averaged stratification (black) and rate of change (grey). (c) Components from eq. 4, including advection (blue), straining (red) and differential diffusion (yellow), convergence/divergence (purple) and error (green). (d) Advection components (eq. 4) broken up into the ξ-direction (light blue), η-direction (darkest blue). (e) Straining components (eq. 4) broken up into the ξ -direction (light red), η-direction (darkest red). ξ and η are primarily in the across- and along-bay directions.

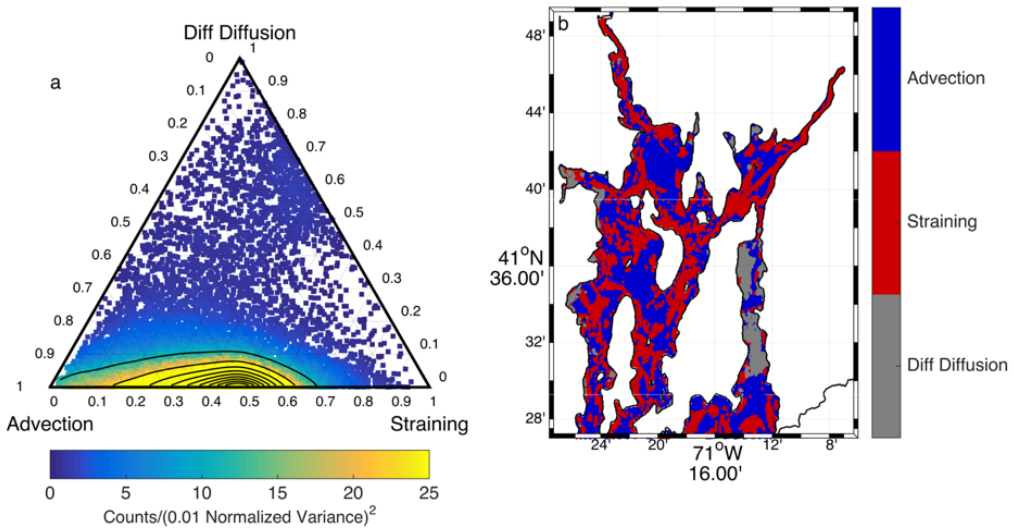

Figure 21: Normalized variance for major depth-averaged components of eq. 4 (a) at every location displayed as a Ternary diagram and (b) locations in NB. Warmer colors indicate high density of samples in (a). Contours are spaced every 5 counts/(0.01 normalized variance)^2. (b) The bay is colored by the term that has the largest variance at any given location.

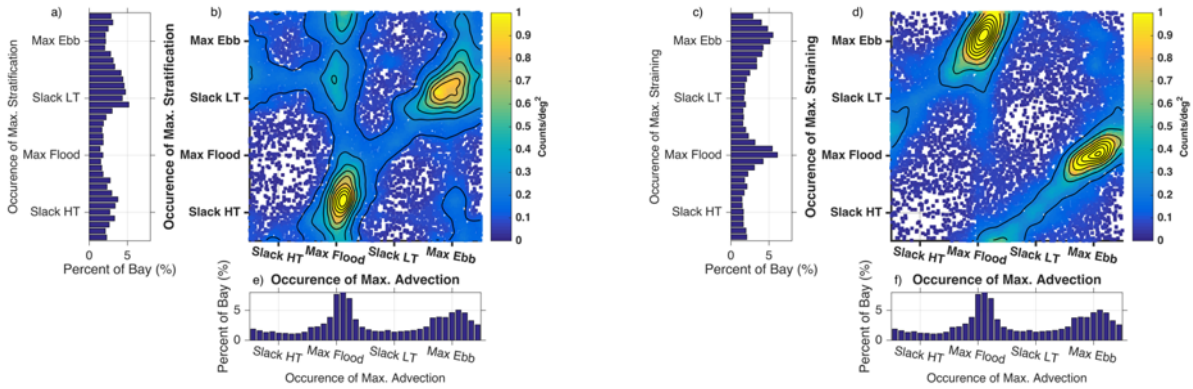

Figure 22: Histogram of occurrence when (a) stratification, (e & f) advection and (c) straining are maximized. Each term compared to the η tidal velocity at the same location. Advection and straining are the sum of the components in the ξ- and η-directions. (b) 2-D histogram of when advection is maximized versus when stratification is maximized. Higher density of samples indicated with warmer colors. (d) 2-D histogram of when advection is maximized versus when straining is maximized.

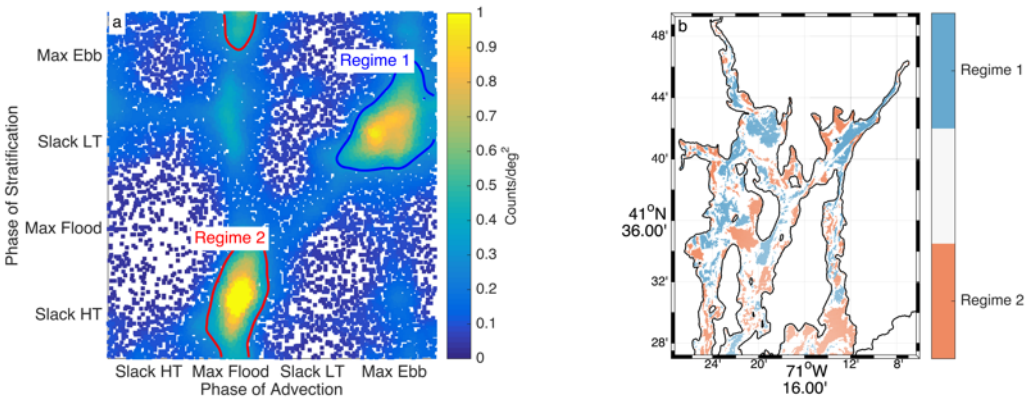

Figure 23: Location and definition of regimes 1 and 2. (a) Displays the definitions of regime 1 (blue contour) and regime 2 (red contour) overlain on the 2-D histogram of the phase of advection and stratification. Contours are outlined at the 0.25 counts/deg2 contour. (b) Physical locations in Narragansett Bay of regime 1 (blue) and regime 2 (red).

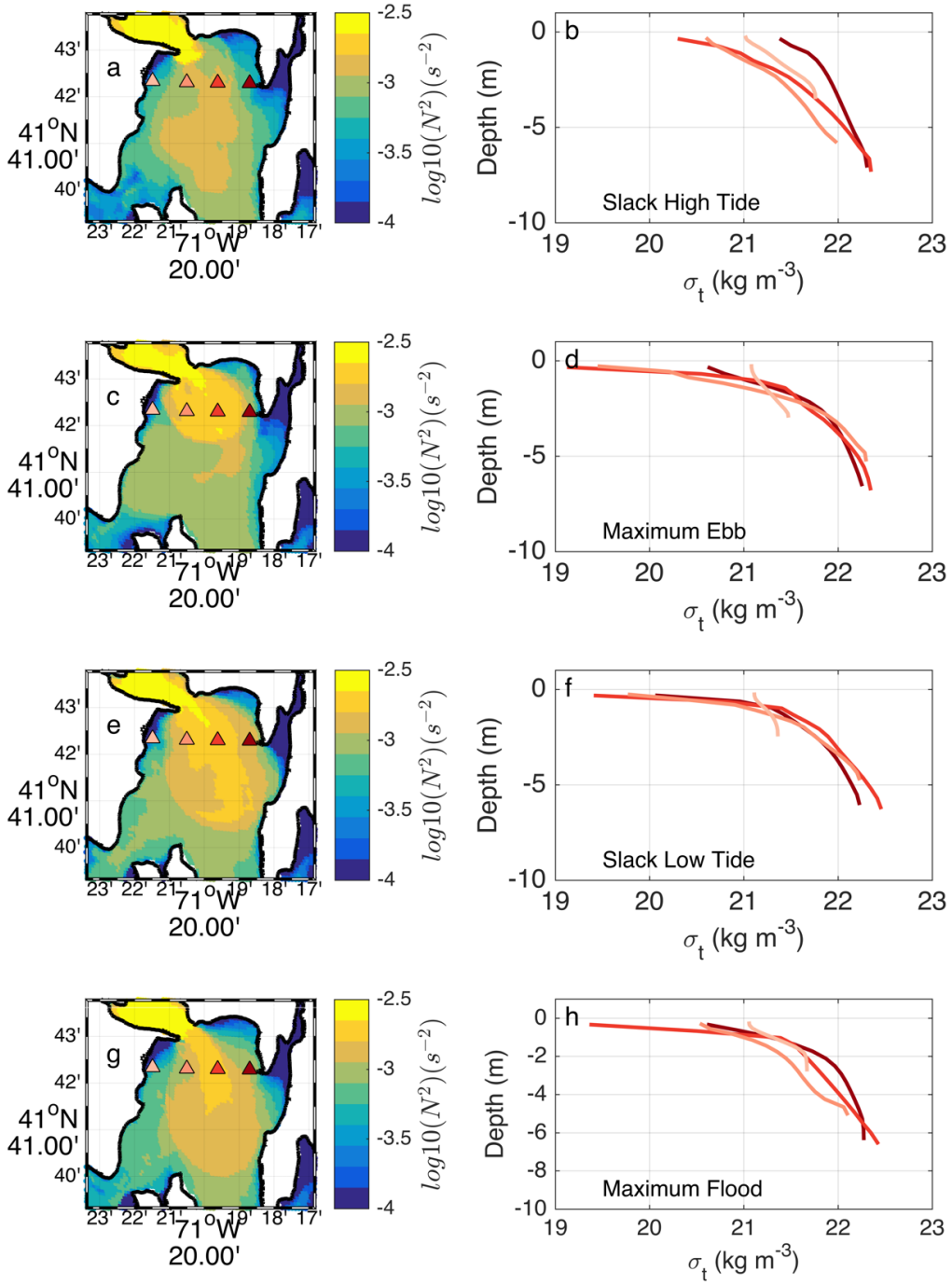

Figure 24: Stratification in the Ohio Ledge region for four stages of a tidal cycle. Left column illustrates the spatial variation of depth-averaged stratification. Right column provides density profiles as a function of depth for positions, shown in the left column. Data are displayed for (a & b) slack high tide, (c & d) maximum ebb, (e & f) slack low tide and (g & h) maximum flood.

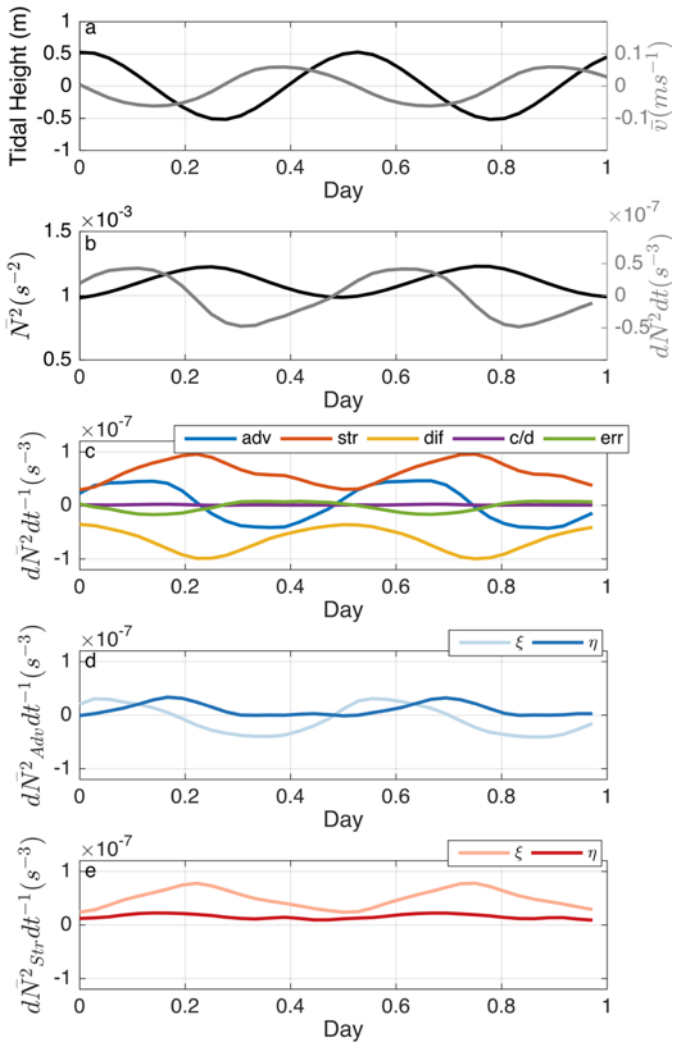

Figure 25: Time series of depth-average properties, averaged over Ohio Ledge, an area shown in Fig. 24. (a) Tidal height (black) relative to mean sea level and η depth-averaged velocity (grey). (b) Depth-averaged stratification (black) and rate of change (grey). (c) Components from eq. 4 including advection (blue), straining (red), differential diffusion (yellow), convergence/divergence (purple) and error (green). (d) Advection components (eq. 4) broken up into the ξ-direction (light blue) and η-direction (darkest blue). (e) Straining components (eq. 4) broken up into the ξ-direction (light red) and η-direction (darkest red).

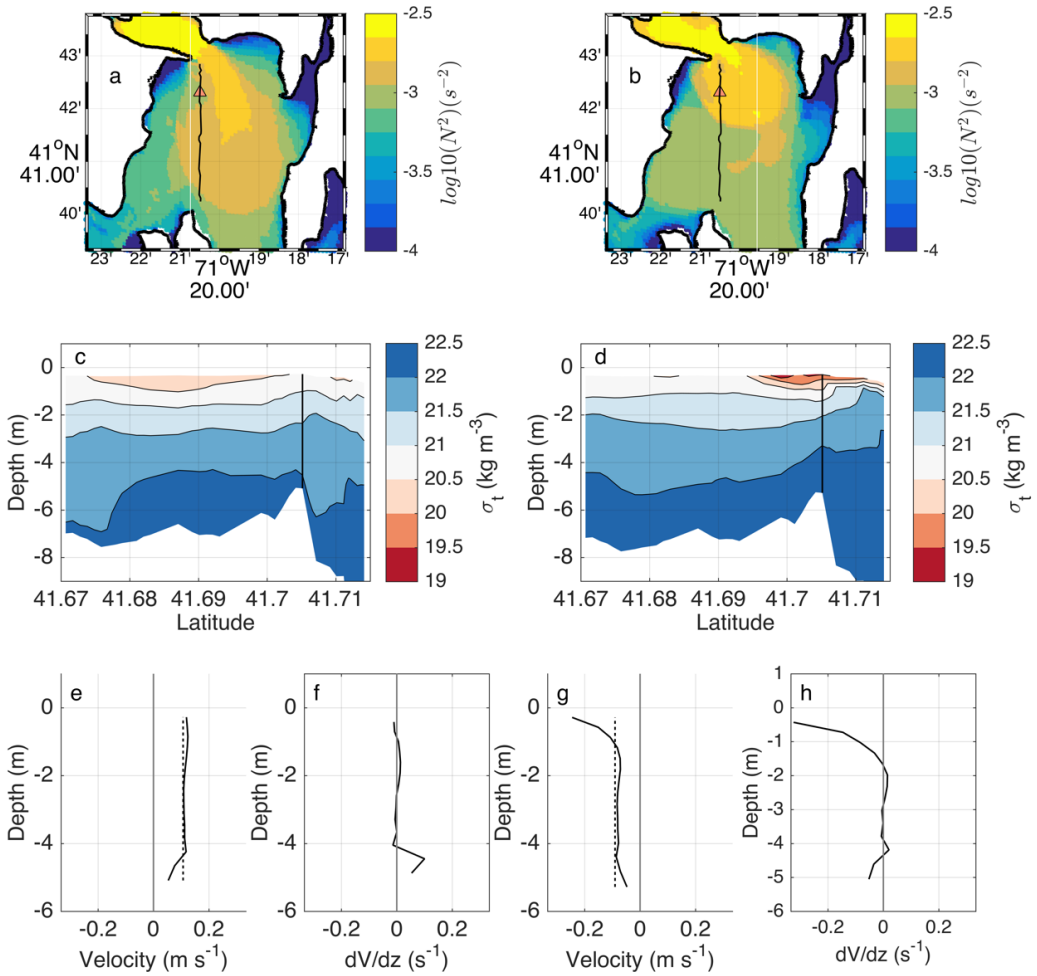

Figure 26: Cross-section through Ohio ledge during maximum flood (a, c, e, f) and maximum ebb (b, d, g, h). (a & b) Map of location and stratification. (c & d) Cross-section of density along marked line in map. Triangle location indicated by vertical black line. (e & g) Northward velocity (black) and depth-average northward velocity (dotted) for location marked with triangle in a & b. (f & h) Vertical gradient of Northward velocity plotted for location marked with triangle.

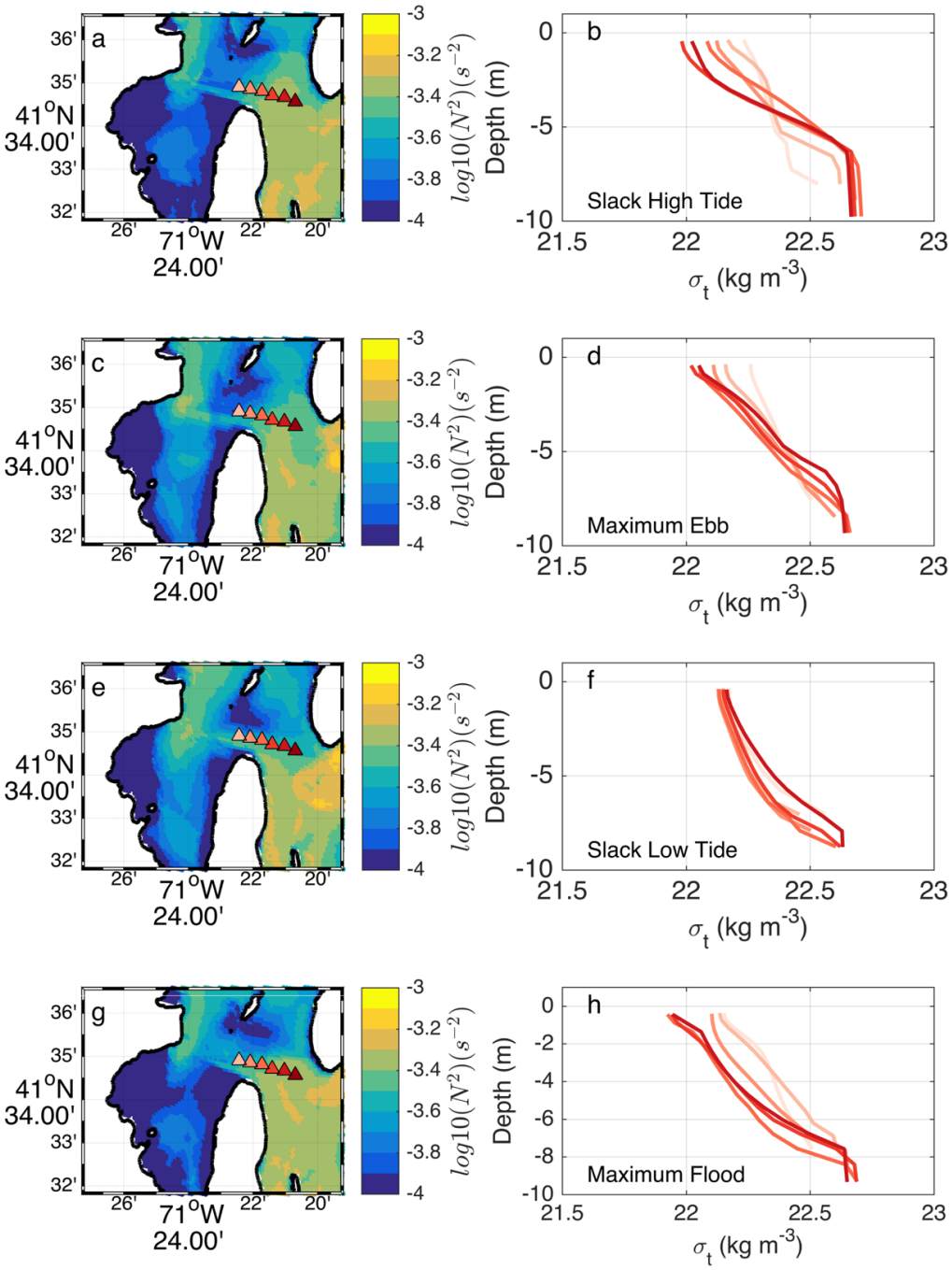

Figure 27: Stratification in an inter-channel over four stages of a tidal cycle. Left column illustrates the spatial variation of depth-averaged stratification. Right column provides density profiles as a function of depth for positions shown in the left column. Data are displayed for (a & b) slack high tide, (c & d) maximum ebb, (e & f) slack low tide and (g & h) maximum flood.

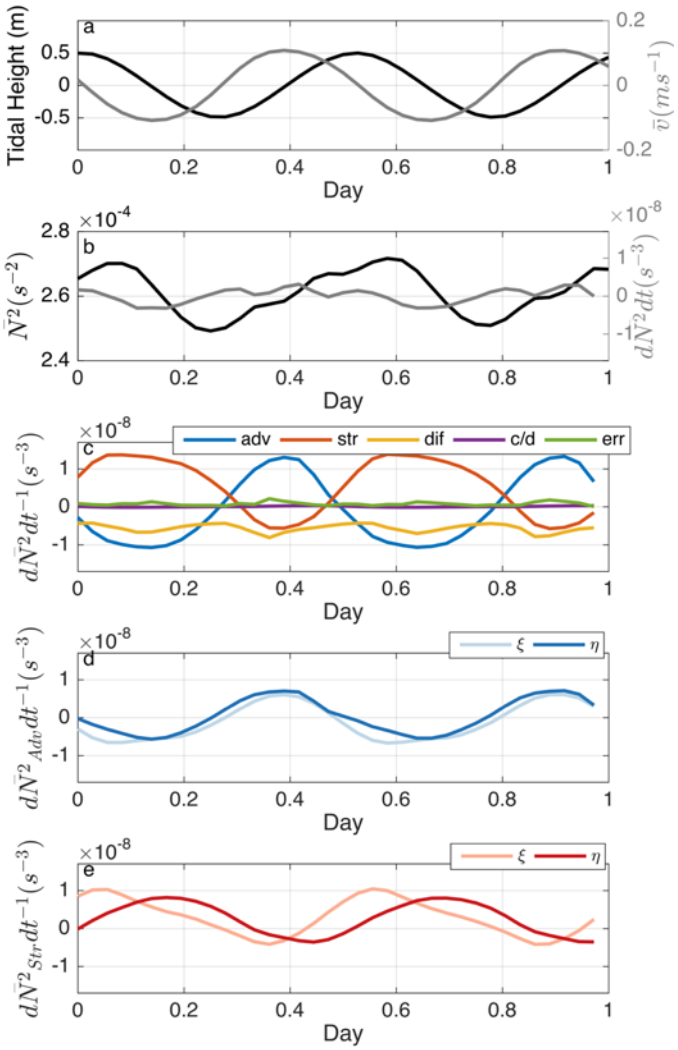

Figure 28: Time series of depth-average properties, averaged over the inter-channel between Jamestown and Prudence Island, an area shown in Fig. 27. (a) Tidal height (black) relative to mean sea level and η depth-averaged velocity (grey). (b) Depth-averaged stratification (black) and rate of change (grey). (c) Components from eq. 4 including advection (blue), straining (red), differential diffusion (yellow), convergence/divergence (purple) and error (green). (d) Advection components (eq. 4) broken up into the ξ-direction (light blue) and η-direction (darkest blue). (e) Straining components (eq. 4) broken up into the ξ-direction (light red) and η -direction (darkest red).

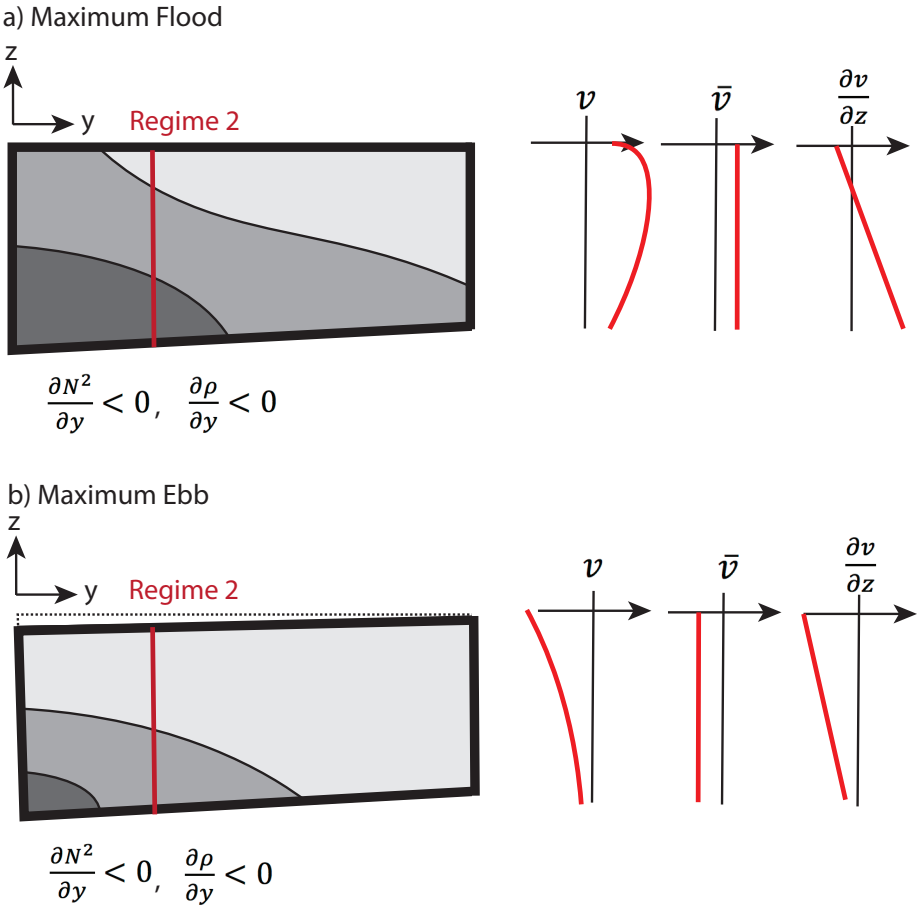

Figure 29: Schematic of isopycnals at (a) maximum flood and (b) maximum ebb for regime 2. Lightest layer is displayed in grey, increasing density is denoted with darker greys and contours of density. Velocity profiles (right column) are show for the location of the solid vertical line.

Appendix A: Depth-Averaged Stratification Equation

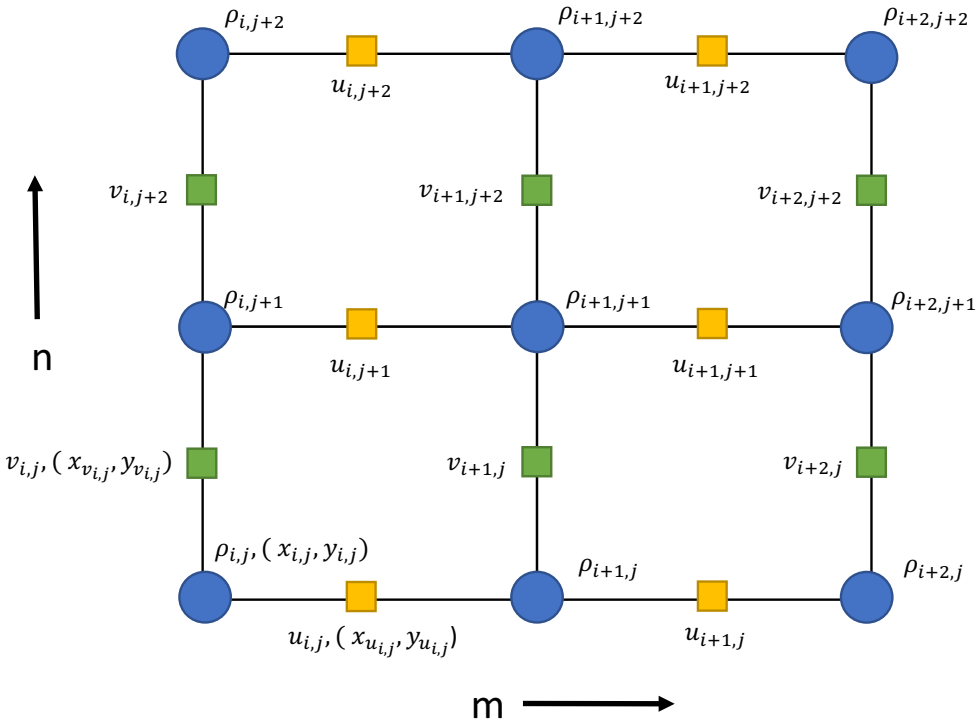

Figure A-1: Schematic of Arakawa C-grid in the horizontal direction.

The stratification equation is given by

(A-1)

$$\frac{\partial N^2}{\partial t} = \overbrace{-u\frac{\partial N^2}{\partial x}}^{advection_x} \overbrace{-v\frac{\partial N^2}{\partial y}}^{advection_y} \overbrace{-w\frac{\partial N^2}{\partial z}}^{advection_z} + \overbrace{\frac{g}{\rho_o}\left(\frac{\partial u}{\partial z}\cdot\frac{\partial \rho}{\partial x}\right)}^{straining_x}$$

$$+\overbrace{\frac{g}{\rho_o}\left(\frac{\partial v}{\partial z}\cdot\frac{\partial \rho}{\partial y}\right)}^{straining_y}+\overbrace{\frac{g}{\rho_o}\left(\frac{\partial w}{\partial z}\cdot\frac{\partial \rho}{\partial z}\right)}^{straining_z}-\overbrace{\frac{g}{\rho_o}\frac{\partial}{\partial z}\left(\frac{\partial}{\partial x}\left(K_H\frac{\partial \rho}{\partial x}\right)\right)}^{differential\ diffusion_x}$$

$$-\overbrace{\frac{g}{\rho_o}\frac{\partial}{\partial z}\left(\frac{\partial}{\partial y}\left(K_H\frac{\partial \rho}{\partial y}\right)\right)}^{differential\ diffusion_y}-\overbrace{\frac{g}{\rho_o}\frac{\partial}{\partial z}\left(\frac{\partial}{\partial z}\left(K_v\frac{\partial \rho}{\partial z}\right)\right)}^{differential\ diffusion_z}$$

where N^2 is the Brunt-V$\ddot{a}is\ddot{a}l\ddot{a}$ frequency, (u, v, w) are the velocities, g is the gravitational acceleration, ρ is density and K_H, K_v are the horizontal and vertical eddy diffusivity respectively. Integration of the equation above and focusing on vertical terms and rate of change yields

(A-2) $$\int_{-H}^{\eta} \frac{\partial N^2}{\partial t} dz = \int_{-H}^{\eta} \left(- w \frac{\partial N^2}{\partial z} + \frac{g}{\rho_o} \left(\frac{\partial \mathrm{w}}{\partial z} \cdot \frac{\partial \rho}{\partial z} \right) + \cdots \right) dz.$$

To evaluate this right-hand term we use Liebnitz rule on time derivative integration. This produces

(A-3) $$\frac{\partial}{\partial t} \int_{-H}^{\eta} N^2 dz - N^2 \frac{\partial \eta}{\partial t}\Big|_{\eta} + N^2 \frac{\partial -H}{\partial t}\Big|_{-H} = \int_{-H}^{\eta} \left(- w \frac{\partial N^2}{\partial z} - \left(\frac{\partial w}{\partial z} \cdot N^2 \right) + \cdots \right) dz.$$

Simplifying (A-3) on the right-hand side becomes

(A-4) $$\frac{\partial}{\partial t} \int_{-H}^{\eta} N^2 dz - wN^2|_{\eta} = \int_{-H}^{\eta} \left(- \frac{\partial w N^2}{\partial z} + \cdots \right) dz.$$

Next we simplify the right-hand side of the integration

(A-5) $$\frac{\partial}{\partial t} \int_{-H}^{\eta} N^2 dz - wN^2|_{\eta} = -wN^2|_{-H}^{\eta} + \int_{-H}^{\eta} (\ldots) dz.$$

Combining the terms that include wN^2, we rewrite (A-5) as

(A-6) $$\frac{\partial}{\partial t} \int_{-H}^{\eta} N^2 dz = -wN^2|_{-H} + \int_{-H}^{\eta} (\ldots) dz.$$

There is no flow perpendicular to the wall and we can therefore rewrite $w_{-H}\ as\ u \frac{\partial H}{\partial x} + v \frac{\partial H}{\partial y}$. There is also no density gradient perpendicular to the wall, and $N^2|_{-H}\ can\ be\ written\ as\ - \frac{g}{\rho_o} \frac{\partial \rho}{\partial z}\Big|_{-H} = - \frac{g}{\rho_o} (\frac{\partial \rho}{\partial x} \frac{\partial H}{\partial x} + \frac{\partial \rho}{\partial y} \frac{\partial H}{\partial y})$.

$-wN^2|_{-H}$ is rewritten as

(A-7) $$-wN^2|_{-H} = -u \frac{\partial H}{\partial x} \frac{g}{\rho_o} \left(\frac{\partial \rho}{\partial x} \frac{\partial H}{\partial x} \right) - v \frac{\partial H}{\partial y} \frac{g}{\rho_o} (\frac{\partial \rho}{\partial y} \frac{\partial H}{\partial y}).$$

where $\frac{\partial H}{\partial x}, \frac{\partial H}{\partial y}$ is usually very small. This causes $-wN^2|_{-H}$ to be very small except for near channels and steep bathymetry.

We rewrite the remaining equations written in sigma coordinates. Starting with the transformations of x, y, z into sigma coordinates:

(A-8) $$(\frac{\partial}{\partial x})_z = (\frac{\partial}{\partial x})_\sigma - \frac{1}{H_z} (\frac{\partial z}{\partial x})_\sigma \frac{\partial}{\partial \sigma}$$

(A-9) $$(\frac{\partial}{\partial y})_z=(\frac{\partial}{\partial y})_\sigma-\frac{1}{H_z}(\frac{\partial z}{\partial y})_\sigma\frac{\partial}{\partial\sigma}$$

(A-10) $$\frac{\partial}{\partial z}=\frac{1}{H_z}\frac{\partial}{\partial\sigma}$$

(A-11) $$m=\frac{1}{\Delta x};\ \ n=\frac{1}{\Delta y}\ ;H_z=\Delta z$$

Combining the above simplifications and transforming coordinate system (A-6) becomes

(A-12)

$$\frac{\partial}{\partial t}\int_1^{15}N^2H_z d\sigma$$

$$=\overbrace{-(\frac{\partial zm}{\partial\xi}uN^2+\frac{\partial zn}{\partial\eta}vN^2)\Big|_1}^{flow\ at\ bottom\ slope\ (-wN^2|_{-H})}$$

$$+\int_1^{15}(\overbrace{-u\frac{\partial N^2m}{\partial\xi}+u\frac{1}{H_z}\frac{\partial zm}{\partial\xi}\frac{\partial N^2}{\partial\sigma}}^{advection_x}\overbrace{-v\frac{\partial N^2n}{\partial\eta}+v\frac{1}{H_z}\frac{\partial zn}{\partial\eta}\frac{\partial N^2}{\partial\sigma}}^{advection_y}$$

$$+\overbrace{\frac{g}{\rho_o}\left(\frac{\partial u}{H_z\partial\sigma}\cdot(\frac{\partial\rho m}{\partial\xi}-\frac{1}{H_z}\frac{\partial zm}{\partial\xi}\frac{\partial\rho}{\partial\sigma})\right)}^{straining_x}$$

$$+\overbrace{\frac{g}{\rho_o}\left(\frac{\partial v}{H_z\partial\sigma}\cdot(\frac{\partial\rho n}{\partial\eta}-\frac{1}{H_z}\frac{\partial zn}{\partial\eta}\frac{\partial\rho}{\partial\sigma})\right)}^{straining_y}-\overbrace{\frac{g}{\rho_o}\frac{\partial}{H_z\partial\sigma}\left(\frac{\partial m}{\partial\xi}\left(K_H\frac{\partial\rho m}{\partial\xi}\right)\right)}^{differential\ diffusion_x}$$

$$-\overbrace{\frac{g}{\rho_o}\frac{\partial}{H_z\partial\sigma}\left(\frac{\partial n}{\partial\eta}\left(K_H\frac{\partial\rho n}{\partial\eta}\right)\right)}^{differential\ diffusion_y}-\overbrace{\frac{g}{\rho_o}\frac{\partial}{H_z\partial\sigma}\left(\frac{\partial}{H_z\partial\sigma}\left(K_v\frac{\partial\rho}{H_z\partial\sigma}\right)\right)}^{differential\ diffusion_z})H_z d\sigma$$

where H_z is the height of each grid cell, m and n are the inverse of the horizontal cell size in the ξ and η directions. There are 15 sigma levels in our experiment. In sigma coordinates the Brunt-V*äisälä* frequency is defined as

(A-13) $$N^2=-\frac{g}{\rho}\frac{\partial\rho}{\partial z}=-\frac{g}{\rho}\frac{\partial\rho}{H_z\partial\sigma}.$$

We rearrange the terms in (A-12)

(A-14)

$$\frac{\partial}{\partial t}\int_1^{15} N^2 H_z d\sigma$$

$$= -\left(\frac{\partial zm}{\partial \xi} uN^2 + \frac{\partial zn}{\partial \eta} vN^2\right)\Big|_1$$

$$+ \int_1^{15} \left(-u\frac{\partial N^2 m}{\partial \xi} - v\frac{\partial N^2 n}{\partial \eta} + \frac{g}{\rho_o}\left(\frac{\partial u}{H_z \partial \sigma}\cdot\left(\frac{\partial \rho m}{\partial \xi}\right)\right)\right.$$

$$+ \frac{g}{\rho_o}\left(\frac{\partial v}{H_z \partial \sigma}\cdot\left(\frac{\partial \rho n}{\partial \eta}\right)\right) + u\frac{1}{H_z}\frac{\partial zm}{\partial \xi}\frac{\partial N^2}{\partial \sigma} - \frac{g}{\rho_o}\frac{\partial u}{H_z \partial \sigma}\frac{1}{H_z}\frac{\partial zm}{\partial \xi}\frac{\partial \rho}{\partial \sigma}$$

$$\left. + v\frac{1}{H_z}\frac{\partial zn}{\partial \eta}\frac{\partial N^2}{\partial \sigma} - \frac{g}{\rho_o}\frac{\partial v}{H_z \partial \sigma}\frac{1}{H_z}\frac{\partial zn}{\partial \eta}\frac{\partial \rho}{\partial \sigma} \ldots \right) H_z d\sigma$$

To simplify further we combine terms related to $\frac{\partial zm}{\partial \xi}$ and $\frac{\partial zn}{\partial \eta}$ under the integral on the right-hand side.

(A-15)

$$\frac{\partial}{\partial t}\int_1^{15} N^2 H_z d\sigma$$

$$= -\left(\frac{\partial zm}{\partial \xi} uN^2 + \frac{\partial zn}{\partial \eta} vN^2\right)\Big|_1$$

$$+ \int_1^{15} \left(-u\frac{\partial N^2 m}{\partial \xi} - v\frac{\partial N^2 n}{\partial \eta} + \frac{g}{\rho_o}\left(\frac{\partial u}{H_z \partial \sigma}\cdot\left(\frac{\partial \rho m}{\partial \xi}\right)\right)\right.$$

$$+ \frac{g}{\rho_o}\left(\frac{\partial v}{H_z \partial \sigma}\cdot\left(\frac{\partial \rho n}{\partial \eta}\right)\right) + \frac{1}{H_z}\frac{\partial zm}{\partial \xi}\frac{\partial uN^2}{\partial \sigma}$$

$$\left. + \frac{1}{H_z}\frac{\partial zn}{\partial \eta}\frac{\partial vN^2}{\partial \sigma} \ldots \right) H_z d\sigma$$

We write terms out in separate integrals

(A-16)

$$\frac{\partial}{\partial t}\int_1^{15} N^2 H_z d\sigma$$

$$= -\left(\frac{\partial zm}{\partial \xi} uN^2 + \frac{\partial zn}{\partial \eta} vN^2\right)\Big|_1$$

$$+ \int_1^{15} \left(\frac{\partial zm}{\partial \xi}\frac{\partial uN^2}{\partial \sigma} + \frac{\partial zn}{\partial \eta}\frac{\partial vN^2}{\partial \sigma}\right) d\sigma$$

$$+ \int_1^{15} \left(-u\frac{\partial N^2 m}{\partial \xi} - v\frac{\partial N^2 n}{\partial \eta} + \frac{g}{\rho_o}\left(\frac{\partial u}{H_z \partial \sigma}\cdot\left(\frac{\partial \rho m}{\partial \xi}\right)\right)\right.$$

$$\left. + \frac{g}{\rho_o}\left(\frac{\partial v}{H_z \partial \sigma}\cdot\left(\frac{\partial \rho n}{\partial \eta}\right)\right) + \cdots\right) H_z d\sigma$$

The first two terms on the right-hand side of (A-16) illustrates the effect due to the bottom slope. Integrating the left-hand side of equation

(A-17) $$\frac{\partial}{\partial t}\int_1^{15} N^2 H_z d\sigma = -\frac{\partial}{\partial t}\frac{g}{\rho_o}\int_1^{15} \frac{\partial \rho}{H_z \partial \sigma}\frac{H_z}{1} d\sigma = -\frac{\partial}{\partial t}\frac{g}{\rho_o}\int_1^{15} \frac{\partial \rho}{\partial \sigma} d\sigma =$$

This shortens to a term relating to the vertical change in density.

(A-18) $$\frac{\partial}{\partial t}\int_1^{15} N^2 H_z d\sigma = -\frac{\partial}{\partial t}\frac{g}{\rho_o}[\rho(15) - \rho(1)]$$

Evaluating the integral of the diffusion term on the right-hand side of (A-16) becomes

(A-19) $$\int_1^{15}\left(-\frac{g}{\rho_o}\frac{\partial}{\partial \sigma}\left(\frac{\partial m}{\partial \xi}\left(K_H\frac{\partial \rho m}{\partial \xi}\right)\right) - \frac{g}{\rho_o}\frac{\partial}{\partial \sigma}\left(\frac{\partial n}{\partial \eta}\left(K_H\frac{\partial \rho n}{\partial \eta}\right)\right) -\right.$$

$$\left.\frac{g}{\rho_o}\frac{\partial}{\partial \sigma}\left(\frac{\partial}{\partial \sigma}\frac{1}{H_z}\left(K_v\frac{\partial \rho}{\partial \sigma}\frac{1}{H_z}\right)\right)\right) d\sigma.$$

The three diffusion terms can be evaluated at the surface and bottom boundaries

(A-20) $$-\frac{gm}{\rho_o}\left(\frac{\partial}{\partial \xi}\left(K_H\frac{\partial \rho m}{\partial \xi}\right)\right)\Big|_1^{15} - \frac{gn}{\rho_o}\left(\frac{\partial}{\partial \eta}\left(K_H\frac{\partial \rho n}{\partial \eta}\right)\right)\Big|_1^{15} -$$

$$\frac{g}{\rho_o}\left(\frac{\partial}{\partial \sigma}\frac{1}{H_z}\left(K_v\frac{\partial \rho}{\partial \sigma}\frac{1}{H_z}\right)\right)\Big|_1^{15}.$$

We can write equation (A-16) including the simplifications of (A-18) and (A-20) as well as dividing by H, the total depth. This provides the depth-averaged stratification equation in sigma coordinates:

(A-21)

$$-\frac{1}{H}\frac{\partial}{\partial t}\frac{g}{\rho}[\rho(15)-\rho(1)] =$$

$$\overbrace{-\frac{1}{H}\left(\frac{\partial zm}{\partial \xi}uN^2+\frac{\partial zn}{\partial \eta}vN^2\right)\Big|_1+\frac{1}{H}\int_1^{15}\left(\frac{\partial zm}{\partial \xi}\frac{\partial uN^2}{\partial \sigma}+\frac{\partial zn}{\partial \eta}\frac{\partial vN^2}{\partial \sigma}\right)d\sigma}^{\text{divergence}}+$$

$$\frac{1}{H}\int_1^{15}\Bigg(\overbrace{-u\frac{\partial H_z N^2 m}{\partial \xi}}^{\text{depth-avg adv }\xi}-\overbrace{v\frac{\partial H_z N^2 n}{\partial \eta}}^{\text{depth-avg adv }\eta}+\overbrace{\frac{g}{\rho_o}\left(\frac{\partial u}{\partial \sigma}\cdot\frac{\partial \rho m}{\partial \xi}\right)}^{\text{depth-avg strain }\xi}+$$

$$\overbrace{\frac{g}{\rho_o}\left(\frac{\partial v}{\partial \sigma}\cdot\frac{\partial \rho n}{\partial \eta}\right)}^{\text{depth-avg strain }\eta}\Bigg)d\sigma-\overbrace{\frac{1}{H}\frac{gm}{\rho_o}\left(\frac{\partial}{\partial \xi}\left(K_H\frac{\partial \rho m}{\partial \xi}\right)\right)\Big|_1^{15}}^{\text{depth-avg diff }\xi}$$

$$-\overbrace{\frac{1}{H}\frac{gn}{\rho_o}\left(\frac{\partial}{\partial \eta}\left(K_H\frac{\partial \rho n}{\partial \eta}\right)\right)\Big|_1^{15}}^{\text{depth-avg diff }\eta}-\overbrace{\frac{1}{H}\frac{g}{\rho_o}\left(\frac{\partial}{\partial \sigma}\frac{1}{H_z}\left(K_v\frac{\partial \rho}{\partial \sigma}\frac{1}{H_z}\right)\right)\Big|_1^{15}}^{\text{depth-avg diff }\sigma}$$

Expanding straining terms for easier calculation along the C-grid, we rewrite the straining terms inside the integral of (A-21) as

(A-22)

$$\frac{g}{\rho_o}\left(\frac{\partial u}{\partial \sigma}\cdot\frac{\partial \rho m}{\partial \xi}\right)+\frac{g}{\rho_o}\left(\frac{\partial v}{\partial \sigma}\cdot\frac{\partial \rho n}{\partial \eta}\right)$$
$$=\frac{g}{\rho_o}\left(\frac{\partial}{\partial \sigma}\cdot u\frac{\partial \rho m}{\partial \xi}-u\frac{\partial}{\partial \sigma}\frac{\partial \rho m}{\partial \xi}\right)$$
$$+\frac{g}{\rho_o}\left(\frac{\partial}{\partial \sigma}\cdot v\frac{\partial \rho n}{\partial \eta}-v\frac{\partial}{\partial \sigma}\cdot\frac{\partial \rho n}{\partial \eta}\right)$$

The stratification balance is thus written as, including the simplifications of (A-20) and (A-22)

(A-23)

$$-\frac{1}{H}\frac{\partial}{\partial t}\frac{g}{\rho}[\rho(15)-\rho(1)]$$
$$=-\frac{1}{H}\left(\frac{\partial zm}{\partial \xi}uN^2+\frac{\partial zn}{\partial \eta}vN^2\right)\Big|_1$$
$$+\frac{1}{H}\int_1^{15}\left(\frac{\partial zm}{\partial \xi}\frac{\partial uN^2}{\partial \sigma}+\frac{\partial zn}{\partial \eta}\frac{\partial vN^2}{\partial \sigma}\right)d\sigma$$
$$+\frac{1}{H}\int_1^{15}\left(-u\frac{\partial H_z N^2 m}{\partial \xi}-v\frac{\partial H_z N^2 n}{\partial \eta}+\frac{g}{\rho_o}\frac{\partial}{\partial \sigma}\cdot u\frac{\partial \rho m}{\partial \xi}\right.$$
$$-\frac{g}{\rho_o}u\frac{\partial}{\partial \sigma}\frac{\partial \rho m}{\partial \xi}+\frac{g}{\rho_o}\frac{\partial}{\partial \sigma}\cdot v\frac{\partial \rho n}{\partial \eta}-\frac{g}{\rho_o}v\frac{\partial}{\partial \sigma}$$
$$\left.\cdot\frac{\partial \rho n}{\partial \eta}\right)d\sigma-\frac{1}{H}\frac{g}{\rho_o}\left(\frac{\partial m}{\partial \xi}\left(K_H\frac{\partial \rho m}{\partial \xi}\right)\right)\Bigg|_1^{15}$$
$$-\frac{1}{H}\frac{g}{\rho_o}\left(\frac{\partial n}{\partial \eta}\left(K_H\frac{\partial \rho n}{\partial \eta}\right)\right)\Bigg|_1^{15}-\frac{1}{H}\frac{g}{\rho_o}\left(\frac{\partial}{\partial \sigma}\frac{1}{H_z}\left(K_v\frac{\partial \rho}{\partial \sigma}\frac{1}{H_z}\right)\right)\Bigg|_1^{15}$$

We rearrange equation (A-23) into

(A-24)

$$-\frac{1}{H}\frac{\partial}{\partial t}\frac{g}{\rho}[\rho(15)-\rho(1)]=-\frac{1}{H}\left(\frac{\partial zm}{\partial \xi}uN^2+\frac{\partial zn}{\partial \eta}vN^2\right)\Big|_1+\frac{1}{H}\int_1^{15}\left(\frac{\partial zm}{\partial \xi}\frac{\partial uN^2}{\partial \sigma}+\right.$$
$$\left.\frac{\partial zn}{\partial \eta}\frac{\partial vN^2}{\partial \sigma}\right)d\sigma+\frac{1}{H}\int_1^{15}\left(-u\frac{\partial H_z N^2 m}{\partial \xi}-v\frac{\partial H_z N^2 n}{\partial \eta}\right)d\sigma+\frac{1}{H}\frac{g}{\rho_o}m\cdot u\frac{\partial \rho}{\partial \xi}\Big|_1^{15}+$$

$$\overbrace{\frac{1}{H}\int_1^{15}\left(u\frac{\partial H_z N^2 m}{\partial \xi}\right)d\sigma}^{\text{-advec }\xi}+\frac{1}{H}\frac{g}{\rho_o}n\cdot v\frac{\partial \rho}{\partial \eta}\Big|_1^{15}+$$

$$\overbrace{\frac{1}{H}\int_1^{15}\left(v\frac{\partial H_z N^2 n}{\partial \eta}\right)d\sigma}^{\text{-advec }\eta}-\frac{1}{H}\frac{gm}{\rho_o}\left(\frac{\partial}{\partial \xi}\left(K_H\frac{\partial \rho m}{\partial \xi}\right)\right)\Big|_1^{15}-\frac{1}{H}\frac{gn}{\rho_o}\left(\frac{\partial}{\partial \eta}\left(K_H\frac{\partial \rho n}{\partial \eta}\right)\right)\Big|_1^{15}$$

$$-\quad\frac{1}{H}\frac{g}{\rho_o}\left(\frac{\partial}{\partial \sigma}\frac{1}{H_z}\left(K_v\frac{\partial \rho}{\partial \sigma}\frac{1}{H_z}\right)\right)\Big|_1^{15}.$$

We expand advective and straining terms so they are easier to calculate across an Arakawa C-grid cell:

(A-25) $$u\frac{\partial H_z N^2 m}{\partial \xi}=\frac{\partial H_z u N^2 m}{\partial \xi}-H_z N^2\frac{\partial u m}{\partial \xi}$$

(A-26) $$v\frac{\partial H_z N^2 n}{\partial \eta}=\frac{\partial H_z v N^2 n}{\partial \eta}-H_z N^2\frac{\partial v n}{\partial \eta}$$

(A-27) $$\frac{g}{\rho_o}m\cdot u\frac{\partial \rho}{\partial \xi}=\frac{g}{\rho_o}m\cdot\frac{\partial u\rho}{\partial \xi}-\frac{g}{\rho_o}m\cdot\rho\frac{\partial u}{\partial \xi}$$

(A-28) $$\frac{g}{\rho_o}n\cdot v\frac{\partial \rho}{\partial \eta}=\frac{g}{\rho_o}n\cdot\frac{\partial v\rho}{\partial \eta}-\frac{g}{\rho_o}n\cdot\rho\frac{\partial v}{\partial \eta}$$

Finally, applying (A-25) through (A-28), the depth-averaged rate of change of stratification becomes

(A-29)

$$\frac{\partial \overline{N^2}}{\partial t}=\overbrace{-\frac{1}{H}\frac{\partial}{\partial t}\frac{g}{\rho}[\rho(15)-\rho(1)]}^{depth-avg\ stratification\ rate}=$$

$$\overbrace{-\frac{1}{H}\left(\frac{\partial zm}{\partial \xi}uN^2+\frac{\partial zn}{\partial \eta}vN^2\right)\Big|_1+\frac{1}{H}\int_1^{15}\left(\frac{\partial zm}{\partial \xi}\frac{\partial uN^2}{\partial \sigma}+\frac{\partial zn}{\partial \eta}\frac{\partial vN^2}{\partial \sigma}\right)d\sigma}^{divergence}+$$

$$\overbrace{\frac{1}{H}\int_1^{15}m\left(-\frac{\partial H_z u N^2}{\partial \xi}+H_z N^2\frac{\partial u}{\partial \xi}\right)d\sigma}^{depth-avg\ adv\ \xi}+\overbrace{\frac{1}{H}\int_1^{15}n\left(-\frac{\partial H_z v N^2}{\partial \eta}+H_z N^2\frac{\partial v}{\partial \eta}\right)d\sigma}^{depth-avg\ adv\ \eta}+$$

$$\overbrace{\frac{1}{H}\left(\frac{g}{\rho_o}m\cdot\frac{\partial u\rho}{\partial \xi}-\frac{g}{\rho_o}m\cdot\rho\frac{\partial u}{\partial \xi}\right)\Big|_1^{15}+\frac{1}{H}\int_1^{15}m\left(\frac{\partial H_z u N^2}{\partial \xi}-H_z N^2\frac{\partial u}{\partial \xi}\right)d\sigma}^{depth-avg\ strain\ \xi}+$$

$$\overbrace{\frac{1}{H}\left(\frac{g}{\rho_o}n\cdot\frac{\partial v\rho}{\partial \eta}-\frac{g}{\rho_o}n\cdot\rho\frac{\partial v}{\partial \eta}\right)\Big|_1^{15}+\frac{1}{H}\int_1^{15}n\left(\frac{\partial H_z v N^2}{\partial \eta}-H_z N^2\frac{\partial v}{\partial \eta}\right)d\sigma}^{depth-avg\ strain\ \eta}$$

$$\overbrace{-\frac{1}{H}\frac{gm}{\rho_o}\left(\frac{\partial}{\partial\xi}\left(K_H\frac{\partial\rho m}{\partial\xi}\right)\right)\Bigg|_1^{15}}^{depth-avg\ diff\ \xi}\ \overbrace{-\frac{1}{H}\frac{gn}{\rho_o}\left(\frac{\partial}{\partial\eta}\left(K_H\frac{\partial\rho n}{\partial\eta}\right)\right)\Bigg|_1^{15}}^{depth-avg\ diff\ \eta}\ -$$

$$\overbrace{\frac{1}{H}\frac{g}{\rho_o}\left(\frac{\partial}{\partial\sigma}\frac{1}{H_z}\left(K_v\frac{\partial\rho}{\partial\sigma}\frac{1}{H_z}\right)\right)\Bigg|_1^{15}}^{depth-avg\ diff\ \sigma}.$$